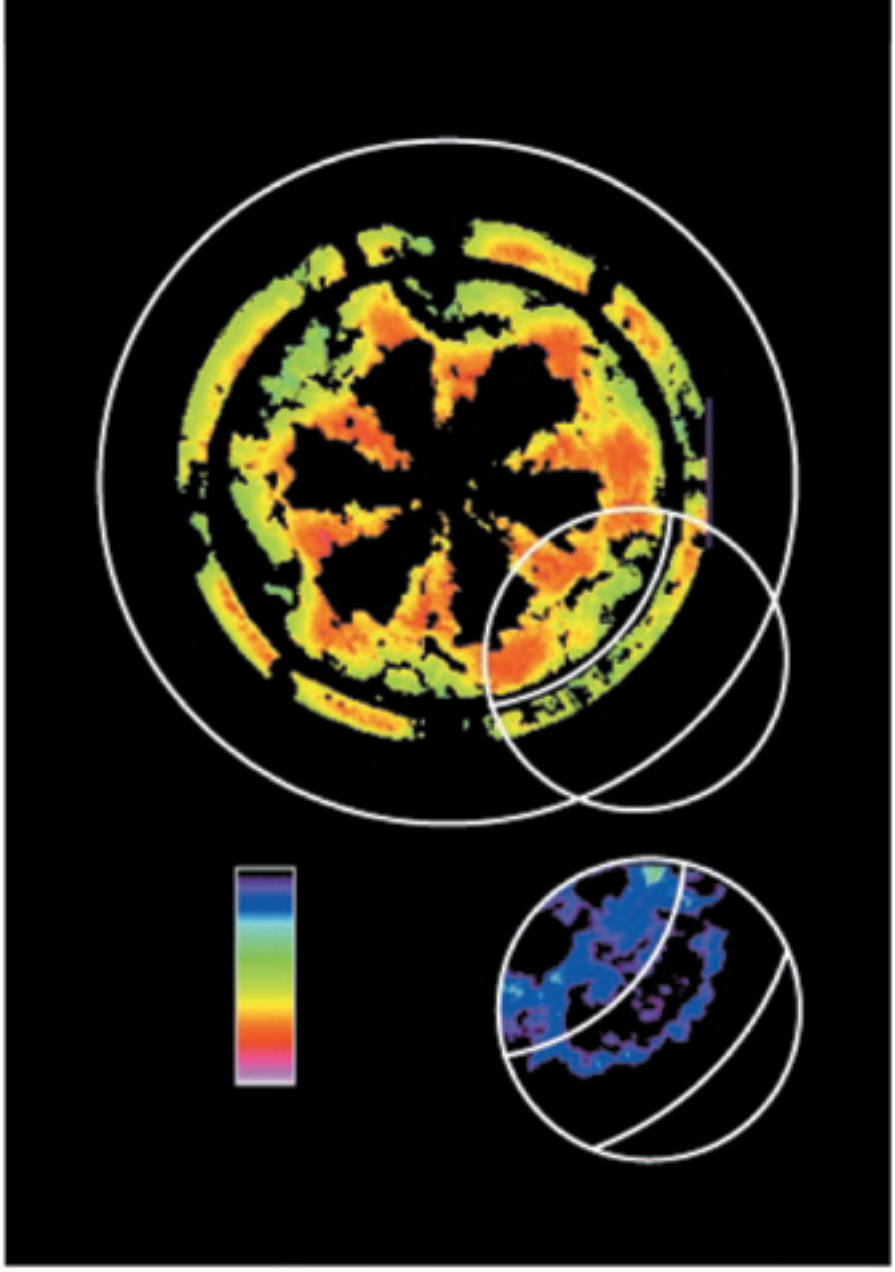

TECHNICAL REVIEW

2003 NO. 15

MITSUBISHI MOTORS FUSO

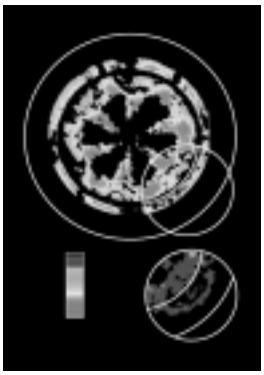

- **Cover Photograph**

The cover photograph shows an image of combustion with the Mitsubishi Innovative Quiescent Combustion System (MIQCS), a new combustion system developed for diesel engines in heavy-duty trucks. The MIQCS realizes a two-stage combustion process that suppresses first-stage combustion by limiting in-cylinder swirl and promotes second-stage combustion by effectively employing air throughout the cylinder. The results are minimal exhaust emissions and maximal fuel economy.

Published by Editorial Committee for the Technical Review
c/o Enviromental & Technical Affairs, Department
MITSUBISHI MOTORS CORPORATION,
16–4, Kohnan 2-chome, Minato-ku, Tokyo 108–8410, Japan
Phone: +81–3–6719–4207
Fax: +81–3–6719–0034

MITSUBISHI MOTORS FUSO

Technical Review 2003 15

TECHNICAL REVIEW

2003 NO. 15

Contents

Previous page
In the 2003 Dakar Rally, which finished on 19 January, Hiroshi Masuoka, driving a Mitsubishi PAJERO EVOLUTION, claimed his second consecutive victory and began a first-second-third-fourth sweep for Mitsubishi Motors. The photos show Masuoka and second-placed driver Jean-Pierre Fontenay powering toward the finish line.

Quality Thesis

New Products

[Company names used in this publication]

On January 6, 2003, Mitsubishi Motors Corporation spun off its truck and bus operations to form a new company, Mitsubishi Fuso Truck & Bus Corporation. This edition of the TECHNICAL REVIEW was jointly produced by the two companies.
Authors of papers in this publication are indicated not only by name and department but also by company. For simplicity, the company names are abbreviated as follows:

Mitsubishi Motors Corporation: MMC
Mitsubishi Fuso Truck & Bus Corporation: MFTBC

New Spirit, Mitsubishi Motors

Rolf Eckrodt
Mitsubishi Motors President & CEO

The start of the new millennium has been accompanied by widespread interest in how technologies should be developed and attempts to predict how technologies will evolve in the future. What course the development of automobile technologies should take is also the subject of considerable debate, for while the automobile brings with it improved quality of life, it also gives rise to other concerns, such as environmental and safety issues. Mitsubishi Motors is working wholeheartedly toward finding solutions to these issues in order to build a prosperous future and give customers the vehicles that they really want. Covering a number of topics, TECHNICAL REVIEW describes the various technical challenges faced in solving these issues.

Tackling a multiplicity of tough problems requires teamwork, such as engineers working together on research and development. Ideally, though, larger scale teamwork in the form of cooperation between companies also has an important part to play. It is the benefits of such teamwork that Mitsubishi Motors aims to achieve through its alliance with DaimlerChrysler. As a member of the Mitsubishi group with a long and well-established reputation in the automobile industry, Mitsubishi Motors has made a valuable contribution to the development of Japanese manufacturing. DaimlerChrysler, meanwhile, has been making automobiles ever since it gave the world the first motorcar at its inception over a century ago. By working together and combining the best of both companies, we are confident of delivering the products that customers want and need. And following the spin-off of the truck and bus division in January to form Mitsubishi Fuso, we are even better placed to create just such high-quality products in collaboration with our partners DaimlerChrysler and the newly formed Mitsubishi Fuso. Doing so naturally requires that numerous reforms be made so as to create the conditions for collaboration with other companies and efficient R&D within the company. That is what the Turnaround Plan now underway is designed to achieve, and indeed considerable progress toward this goal has already been made.

The Turnaround Plan is gradually making its impact felt on the company's automobile design. The eK-WAGON launched in October two years ago, for example, has been widely acclaimed for its utility and innovative design, and has grown to become one of our most popular models, while the new CANTER small truck launched last June has won plaudits for its spacious, comfortable interior. November saw the launch of the new COLT model, the first product to come out of our alliance with DaimlerChrysler. While the original COLT marked a major milestone for Mitsubishi Motors when it first appeared on the market 40

years ago, the new COLT has proved an even greater hit. The appeal of products depends not only on the incorporation of new technologies, but also on close attention to quality and detail in everything from fulfilling customers' needs to quality of service at the sales end of the supply chain. The criticisms leveled at us in the past regarding the quality and specifications of some of our products have imprinted on us all the more firmly the crucial importance of these factors. Enormous strides have been made in quality control thanks to the introduction of the "quality gate" system. Advances have also been made with regard to specifications, as shown by the popularity of our products with customers – and we intend to continue listening to their needs.

At last year's soccer World Cup, the Japanese team made a major impression. This was only a start, however, upon which Japan needs to build at future World Cups. Sustainable progress is the name of the game for Mitsubishi Motors as much as the Japanese soccer team. Under the banner of our brand statement – "Spirited Products for Spirited People" – we intend to bring to market a constant stream of outstanding new products to meet customer needs. Outstanding products require outstanding technologies in every sphere of automobile manufacturing, and these you will find in this and future editions of TECHNICAL REVIEW.

TECHNICAL PERSPECTIVE

Emerging Situation and MMC's Policy on Automobile Recycling – New Technical Issues and Future Activities –

Harushige YAMAMURA* Takehiro ISHIURA** Motokazu KOBAYASHI‡**

Abstract

In order to improve the recycling ratio of end-of-life vehicles, recycling and appropriate treatment of shredder dust from the remains of automobile bodies are indispensable. It is equally important to appropriately handle the chlorofluorocarbons, air bags and hazardous substances. In Japan, a recycling ratio of at least 95 % must be achieved by 2015, by introducing relevant laws and voluntary efforts to tackle the problem. As the recycling of automobiles involves many parties, widespread cooperation is crucial.

Key words: *Discarded Vehicles, Automobile Recycling Law, Shredder Dust, Material Recycling, Thermal Recycling, Gasifying Melting Technology*

1. Introduction

In July 2002, legislation on Recycling End-of-Life Vehicles (hereinafter referred to as the Automobile Recycling Act) was enacted in Japan. Generally speaking, in terms of recycling, motor vehicles are considered the leader compared to other industrial products. Currently, as shown in **Fig. 1**, 70 to 80 % of these vehicles are being recycled. However, the current recycling system in Japan is losing impact as a result of the ever-increasing disposal costs of industrial wastes due to the space restrictions on landfill disposal sites, and the weak price for scrap iron. Further, it is feared that illegal disposals and inappropriate recycling treatments will worsen. This law was enacted as a result.

There are approximately five million motor vehicles de-registered every year, approximately one million of which are exported as used vehicles. The rest, approximately four million units, are dismantled in Japan. The amount of shredder dust, or Automobile Shredder Residue (hereinafter referred to as ASR) discharged is likely to reach 550 to 700 thousand tons. By the law, automobile manufacturers are responsible for the collection and treatment of ASR. As a result, the recycling and/or appropriate treatment of ASR has become quite a big issue for automobile manufacturers.

Under the Promotion of Effective Resource Utilization legislation (amendment enacted in 2001, abbreviated as the 3R Act), automobile manufacturers were also obliged to design and manufacture motor vehicles taking the 3R factors (Reduce, Reuse and Recycle) into consideration. Reducing the environmental impact from the design stage and promoting the manufacturing of motor vehicles which produce the least amount of waste possible are necessary for building a recycling society, in which automobile manufacturers can display their conservation efforts for the environment.

As motor vehicles are a form of international merchandise, they must be designed to comply with not only Japanese regulations, but also European Union (EU) directives regarding those vehicles that have reached the end of their lives. In addition, due to the current situation where nearly one million used vehicles are being exported, it is essential that these vehicles are easy to dispose of anywhere in the world once they have reached the end of their lives. It is also essential that they place only a small impact on the environment.

In this paper, the latest issues to be tackled regarding motor vehicle recycling, motor vehicle recycling trends in Japan, USA and Europe, as well as technical trends on recycling are outlined, and based on these, ways of developing motor vehicles that take into account recycling are discussed.

2. New issues in motor vehicle recycling

2.1 Promotion of ASR recycling

At the moment, the most common method for end-of-life vehicle recycling involves crushing vehicle body remains, after dismantling useful parts from the end-of-life vehicle, by hammer (shredding process), then classifying the metal portions by magnet and/or specific weight for recycling. The residual mixture, once the metal content has been removed, is classified as ASR which, in most cases, is not recycled but disposed of by landfill. Since Japan's land area is so small, the land usable for landfill is limited, resulting in treatment costs increasing year by year. As motor vehicles are, for the most part, constructed from metal, the recycling ratio is already high. At this moment, therefore, promoting the reduction in the amount of ASR and recycling is the most important issue. To achieve this, it is important

* Recycling Promotion Office, Business Dev. Office, MMC
** Material Engin. Dept., Car Research & Dev. Office, MMC
‡* Material Engin. Dept., Research & Dev. Office, MFTBC

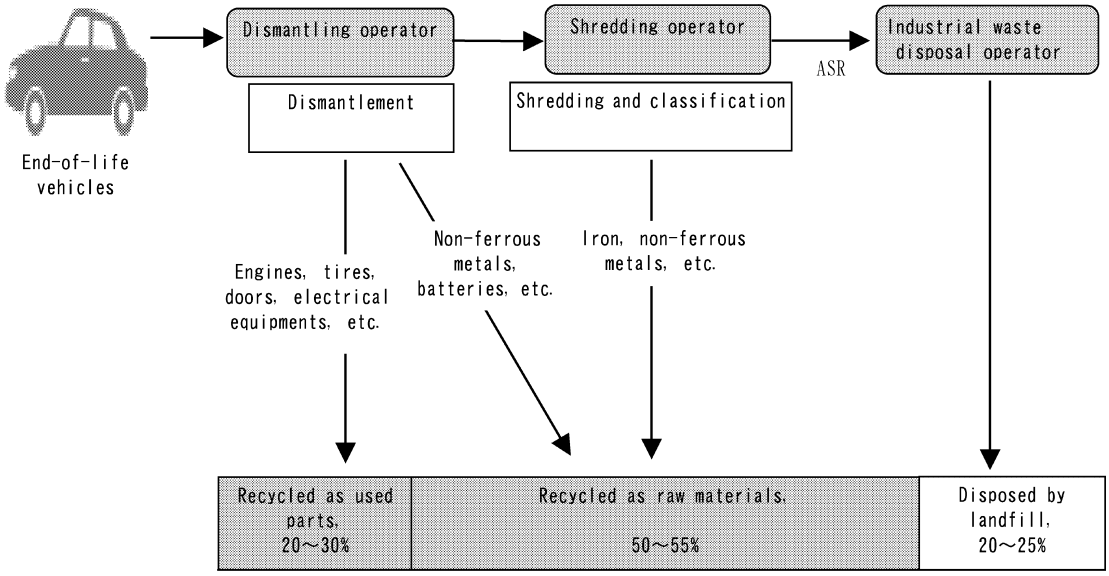

Fig. 1 Current recycling situation for end-of-life vehicles

that technologies is developed that correspond to the requirements in terms of both the treatment infrastructure and automobile manufacturer. Among these it is vital to promote the establishment of more recycling facilities.

2.2 Air bag and similar equipment disposal measures

One new problem is that although an air bag is a device designed to protect passengers in a collision, it may itself cause damage during the recycling process as it contains a gas generator that deploys the bag instantly. It will become more important in the future to remove the deactivated gas generator or intentionally activate it within the vehicle before the vehicle even starts the recycling process.

Air bags have been adopted since the latter half of the 1980's, and, at the moment, almost every new motor vehicle is equipped with them. In the beginning, it was only installed on the steering wheel. Air bags can now be found in the instrument panel in front of the passenger, as well as to the side of the seats.

Nowadays, seat belts with a pre-tensioner (a device that winds the seat belt immediately after collision thus removing the slack in the belt), which also has a gas generator, are increasingly being utilized. From 1998 on a system was installed, which is now standardized across the industry, that activates gas generators on the vehicle (by connecting deploying devices, air bags and pre-tensioners deploy in sequence once a switch is turned, which makes these devices harmless). At the moment, almost every new motor vehicle is equipped with this system. The system ensures the safe treatment of gas generators, the use of which is expected to increase in the future.

2.3 Measures for disposing of chlorofluorocarbon gas (CFCs)

In Japan, preceding the enforcement of the Automobile Recycling Act, the recovery and destruction of motor vehicle air conditioner refrigerant began in October 2002. These actions were obligatory for automobile manufacturers under the Fluorocarbon Recovery and Destruction Law, legislation introduced by Diet members.

From 1994, our company discontinued all use of CFC12, a type of motor vehicle air conditioner refrigerant which destroys the ozone layer, and switched to a CFC alternative – HFC134a. However, since HFC134a has a far higher global warming effect than CO_2, it is necessary to reduce the amount used and ensure a 100 % recovery of the material at the end of the vehicle's life. Each country regulates the amount of CFCs emitted to the atmosphere. As well as recovering and destroying refrigerant for motor vehicle air conditioners, these are enforced under motor vehicle recycling laws and regulations. Furthermore, the introduction of new refrigerant, which at present does not need to be recovered, is progressing.

2.4 Reducing the utilization of hazardous substances

Hazardous substances include heavy metals such as lead, mercury, cadmium and hexavalent chromium, as well as others such as sodium azide, which was once utilized as an agent to generate gas for air bags, etc. Motor vehicle recycling is regulated by various laws and regulations designed to prevent environmental contamination by these hazardous substances. However, if these materials are abandoned illegally, then they will contaminate the soil and/or water. The Japan Automobile Manufacturers Association (hereinafter referred to as JAMA) is already voluntarily tackling the problem of reducing the amount of lead, for example, being used in order to prevent these situations occurring.

As mentioned later, utilizing the four hazardous substances (lead, mercury, cadmium and hexavalent

Table 1 Outline of the Domestic Automobile Recycling Act

Item	Outline
Proclamation and enforcement	• Publicized on 12 July 2002 • Enforcement aimed at December 2004
Type of vehicles to which the Act applies	Four-wheeled passenger vehicles and four-wheeled commercial vehicles (Including all vehicle types, from mini-sized vehicles to large-sized trucks and buses)
Obligations of automobile manufacturers	• Carrying out the recovery and recycling of CFCs, air bags and ASR • Setting up a recycling fee and publicizing it [Responsibility] • Designing and manufacturing motor vehicles considering the environment and recycling • Offering information related to motor vehicle structures and components
Cost	Borne by motor vehicle users

Table 2 Outline of domestic voluntary plans

Item	Outline
Hazardous substance	• Public announcement of the target value of material to be reduced On lead, mercury, cadmium and hexavalent chromium • Applied to the new type of vehicles regulated by the Automobile Recycling Act • Research and development of alternative technology
Body structure of commercial vehicles	• Promoting vehicle designs that make recycling easier • Reducing the use of hazardous substances • Promoting recycling and the appropriate treatment of materials which are difficult to recycle and/or treat • Building a network of cooperating treatment and resource recovery operators
Two-wheel motor vehicles	• Installing facilities that collect and recover resources from end-of-life vehicles • Free take-back of vehicles with recycle markings • Reducing the use of hazardous substances

chromium) is, as a general rule, prohibited under the EU directive on end-of-life vehicles. In Japan, JAMA reconsidered past efforts, which have only been on lead, and announced reduction targets for the above-mentioned materials. Our company, as a part of our green procurement program, promptly introduced a management system, International Electronic Material Data System (IMDS), which is already operating in Europe, to actively tackle the management and reduction in use of hazardous substances.

2.5 Expanded producer responsibility

At the moment, fundamental improvement of the economic aspects of recycling by considering the ease of recycling, starting from the design stage, is required. Expanded Producer Responsibility (EPR) is a motivational method taken very seriously that considers the ease of recycling from design through to manufacture.

This is one concept that aims at promoting recycling, by expanding the responsibility of manufacturers achieving the most economically effective recycling methods, in order to bring product recycling within the decision-making domain of the manufacturer's management structure.

Up to now, the economic fruits of recycling design improvement have gone to recycling operators as increased profit. The manufacturers' efforts in terms of design improvement have only been achieved as a voluntary environmental activity. Under the EPR philosophy, however, the fruits of design improvement will promote effective action that assumes manufacturers' responsibility.

On the other hand, if everything becomes the manufacturers' responsibility, it might create problems. Recycling operators are making efforts to improve efficiency in order to increase their own profitability. This is the reason for the current high recycling ratio. The domain where manufacturers should assume responsibility, should be decided according to the actual state of affairs, that is, depending on which side's efforts, those resulting from the infrastructure or achieved by the manufacturer, will lead to better results. Therefore, the way in which EPR should be applied differs country by country. Information from each country will be described later.

3. Legislative trends related to recycling in various countries and regions

3.1 Japan

The Automobile Recycling Act in Japan was announced in July 2002, the background of which is mentioned in the foreword, and is scheduled to come into effect in December 2004.

The basic philosophy of the Automobile Recycling Act is expressed in the following four points: ① Preventing illegal disposals; ② Continuous operation of recycling and the appropriate treatment of end-of-life vehicles; ③ Minimizing the amount of final landfill disposal, and ④ Achieving the principles of appropriate competition on the basis of making good use and improving the existing infrastructure.

According to the basic philosophy above, and based on the aforementioned EPR philosophy, the Automobile Recycling Act obliges automobile manufacturers to recover, recycle and/or treat appropriately, those CFCs used in motor vehicle air conditioners, air bags and similar equipment as well as ASR, all of which have been difficult to treat appropriately due to the existing infrastructure. The costs necessary for carrying out the recycling and appropriate treatment of these three items will be borne by motor vehicle users as a fee (**Table 1**).

Under this scheme it is necessary to achieve the target of a recycling ratio of end-of-life vehicles of more than 95 % by 2015. This target is stated in the recycling of end-of-life vehicles initiative stipulated by the Ministry of International Trade and Industry in 1997.

Furthermore, recycling of hazardous substances as well as the body structures of commercial vehicles and two-wheeled vehicles, which are currently exempt from the Automobile Recycling Act, will also be carried out voluntarily by the related industries at the same time as enforcement by the Automobile Recycling Act (**Table 2**).

Although the end-of-life motor vehicle recycling system stipulated in the Automobile Recycling Act is the largest one, one which the automobile industry has never experienced, the preparatory work, including the recycling fee deposit system and the manifest informa-

Table 3 Outline of the EU directive on end-of-life vehicles

Item	Outline
Type of vehicles to which the directive applies	Passenger vehicles and commercial vehicles with a gross vehicle weight of less than 3.5 ton
Free take-back of end-of-life vehicles	From 1 July 2002: End-of-life vehicles registered on or after 1 July 2002 From 1 January 2007: All end-of-life vehicles
Locations of facilities where end-of-life vehicles are collected	Equally throughout the EU territory
Actual recycling ratio	Recycle ratio of 80 % (85 % including thermal recycling) shall be achieved by 1 January 2006. Recycle ratio of 85 % (95 % including thermal recycling) by 1 January 2015
Potential recyclability ratio	Achieving 85 % (95 % including thermal recycling) is required to qualify for certification.
Prohibiting the use of hazardous substances	Using lead, mercury, cadmium and hexavalent chromium will be prohibited for those vehicles registered on or after 1 July 2003 (particular parts will be exempt).
Material marking	Material markings shall be attached to parts.
Offering dismantling information	Information necessary for the appropriate treatment of end-of-life vehicle types shall be offered within six months of the launch.

tion management system, are progressing rapidly, driven by JAMA and those concerned as the core group.

3.2 Europe

An EU directive on end-of-life vehicles came into effect in October 2000. This directive stated that each EU member country's legislation had to be completed by April 2002. However, those countries which had already completed legal procedures as of November 2002 were: Germany, the Netherlands, Sweden, Denmark and Austria. The rest of the member countries are expected to enforce this directive in the future even though they will be later than the agreed deadline. The outline of requirements in this directive is shown in **Table 3**.

The principles of this directive include: the producers' responsibility to place a priority on material recycling rather than thermal recycling, which uses combustibles, such as resins, as fuel, promoting the reuse of parts, etc. As a result, the directive has several unique features that differ from Japan's Motor Vehicle Recycling Act, such as free take-back of end-of-life vehicles by motor vehicle manufacturers and recycling ratios with a limited thermal recycle ratio within the recycling process, etc.

On the other hand, for automobile manufacturers complying with the directive, it is important to provide facilities to collect end-of-life vehicles, reduce recycling costs (e.g. developing vehicles which are easy to recycle) and meet hazardous substance regulations. In particular, it is a major issue for automobile manufacturers to provide a network throughout Europe to collect, transport, and dismantle end-of-life vehicles and to offer used parts for sale. Companies are also obliged, when collecting all end-of-life vehicles, to treat ASR by 2007, as well as to provide the funds needed to recycle these vehicles and collect them free of charge. As a result, most Japanese automobile manufacturers are expected to handle this issue by cooperating not only with those companies with which they have a capital relationship, but also with those with which they do not have a capital relationship. Our company, Mitsubishi Motors Corporation, as a part of a total business collaboration, is cooperating with DaimlerChrysler to promote the building of a network for collecting end-of-life vehicles.

3.3 North America

In North America, as in Japan and/or Europe, recycling is conducted using a high recycling ratio. However, although the importance of recycling ASR is recognized, it is not considered to be a great problem. Treatment cost is not particularly high due to the large land area of the nation.

In North America, a large-scale reuse business has developed for making good use of end-of-life vehicles, with numerous end-of-life vehicles now in huge vehicle yards. Whoever needs used parts is able to remove the parts they need from these yards. For dismantling contractors, supplying used parts to service shops is an important part of their business.

Currently, the important issue associated with end-of-life vehicles in North America is the prevention of environmental contamination by mercury in the vicinity of the Great Lakes. In the United States, people are greatly concerned about preserving nature as well as the major problem that mercury from end-of-life products can have on lake and marsh water quality.

In Vermont and Maine, state law has regulated all products containing mercury. Motor vehicles are included among these regulated products. In Maine, automobile manufacturers are obliged to cooperate in terms of the appropriate treatment of parts containing mercury removed from end-of-life products. There is a move in other states and Canada to legislate similar laws.

Reducing the use of mercury has progressed to the stage that no part containing mercury is used in new motor vehicles currently on sale, apart for a few that are related to safety.

4. Recycling technologies

4.1 Recycling technologies for new vehicles

4.1.1 Passenger vehicles

New measures to reduce the environmental impact of end-of-life vehicles are being developed, including improving recyclability and reducing lead usage. They have been promoted based on the recycling end-of-life vehicles initiative. As a result of the legislation of the 3R Act, it is now necessary that a new vehicle is developed which takes into consideration not only "recycling" but also "reducing" and "reusing". Some examples of the actual challenges to improve the ease of dismantling and recycling are introduced in the following section.

Based on the recycling design guideline, we have been working to reduce the number of material varieties

from the design concept stage. We have also been introducing materials that are easy to recycle as well as structures that are easy to dismantle; adopting recycled materials, and striving to apply material coding in order that they are easier to classify by dismantling operators. As a result, we have achieved our voluntary target of a greater than 90 % potential recyclability ratio. This is an index that has been set up to evaluate the effort needed to tackle recycling, for all new vehicles launched in or after the year 2000 (**Fig. 2**).

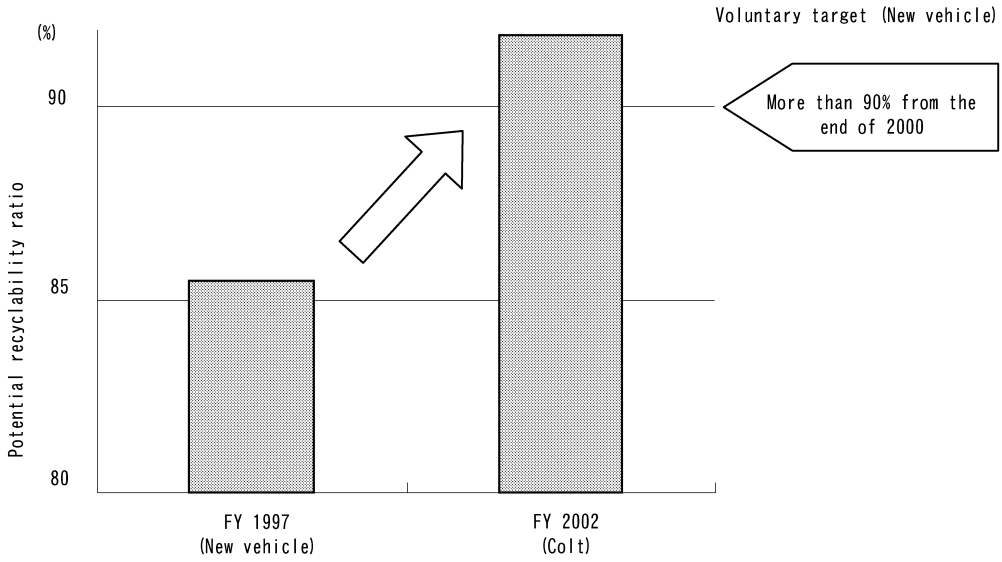

Fig. 2 Potential recyclability ratio of COLT

(1) Measures to reduce resource use

As with "Reduce", which should have the highest priority among the 3Rs, measures to reduce resource use, particularly rationalizing raw material use as well as the longer useful life of materials, are being taken into consideration at the design stage. For example, we are trying to make parts smaller and lighter, as well as reducing their number such as by using aluminum for the structural parts of engine and transmission; using plastics for the intake manifold; adopting tailored blanks or high-tensile steel sheets for body and chassis parts and reducing the number of wires in wiring harnesses, etc. In addition, we are also trying to develop technologies that will increase the useful life of parts, such as enlarging the areas of the vehicle body where galvanized steel sheets, body sealer and/or undercoats are applied to improve anticorrosion performance, as well as developing technologies that will extend the useful lives of rubber parts and lubricants.

(2) Measures for materials

Thermoplastic resins, which are easy to recycle, are adopted for almost all interior and exterior plastic parts, such as bumpers, radiator grill, instrument panel and interior trims (**Fig. 3**). Parts which have been made of rubber, such as weather strips for the front hood and tail gate, as well as air intake and vacuum hoses for engine control can also be substituted by thermoplastic elastomers.

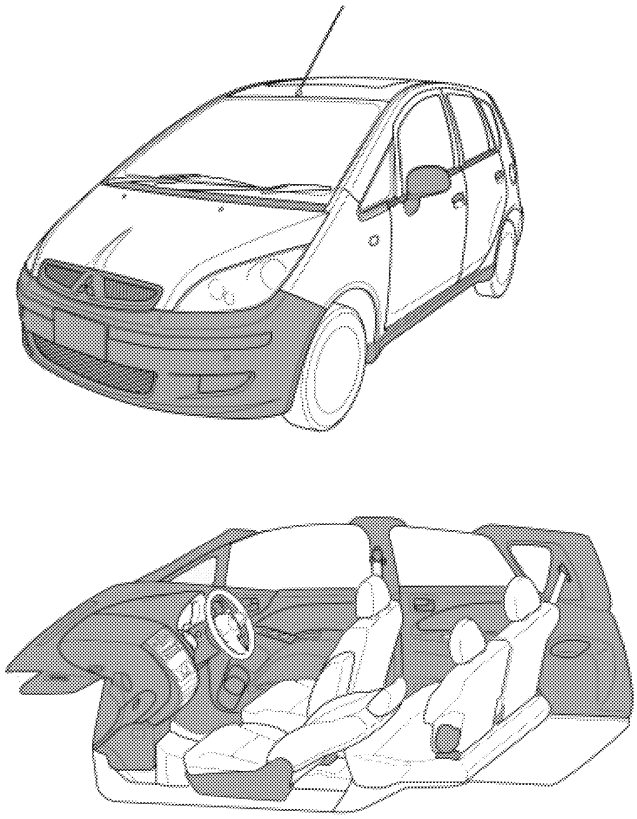

Fig. 3 Recyclable parts of COLT

As for recycling scraps of materials produced in the manufacturing process, those from interior and exterior part materials, such as bumpers and interior trims, can be recycled for the same purpose. Using scraps of carpet material as floor insulation has just begun. Further, we are trying to recycle scrap materials from other industries. Recycled materials from PET bottles for soft drinks are used as carpets, floor mats, engine covers and engine oil level gauges. Further, we are using an air cleaner housing molded that incorporates recycled polypropylene blended with recycled paper. These are produced from recycled polypropylene food containers, and the used paper from paper tubes is used for winding up spun threads (**Fig. 4**).

Another example is the door garnishes made from molded-in-color plastics with high-metallic gloss. By eliminating painting after molding, this material need not have any paint peeled off at the recycling stage. In

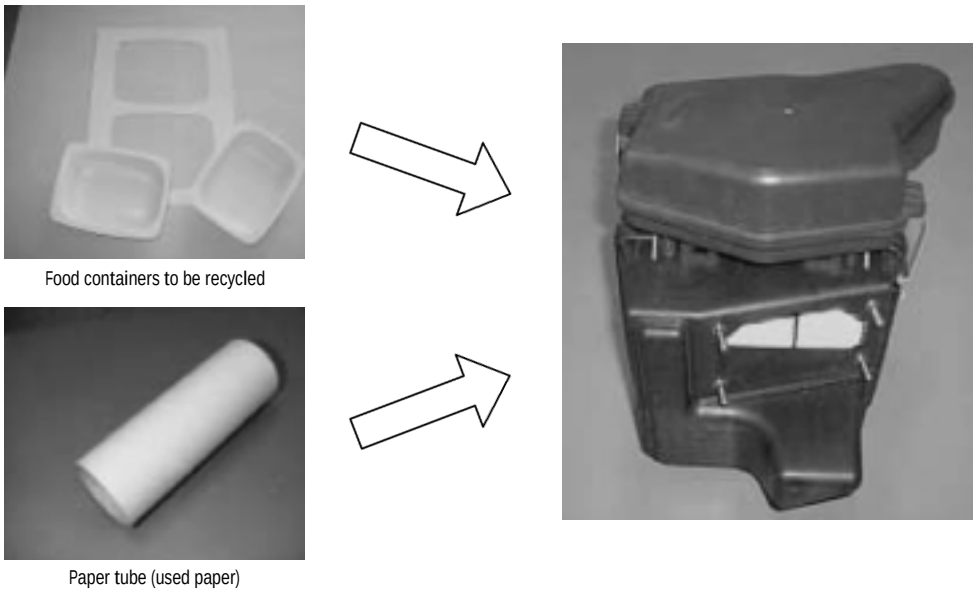

Fig. 4 Air cleaner housing molded with recycled polypropylene blended with recycled paper

addition, we are studying for adopting biodegradable plastics which have a smaller environmental impact on manufacturing, made not from fossil resources but from agricultural renewable resources.

(3) Measures for structures

We are adopting structures which make dismantling and separating easier, such as reducing the number of fasteners or discontinuing adhesion between different materials. As for bumpers, the number of bolts has been reduced to less than one-half by changing, for example, bolted joints to clippings, and metal reinforcements have been discontinued in order to make dismantling easier. At the same time, we are making efforts to integrate multiple parts into one, or to bring multiple parts into a module, such as adopting a plastic intake manifold with the integrated surge tank and resonator. In order to evaluate these efforts as a whole and to adopt them in vehicle development, we are evaluating the ease of dismantling actual vehicles at the vehicle development stage, using our own evaluation standards. Taking into account the time needed to dismantle an end-of-life vehicle is a very important factor.

(4) Material marking

In order to ensure the quality of recycled material within the recycling process, it is mandatory that each material is classified. Therefore, in addition to those plastic parts heavier than 100 g, we are also labeling materials with rubber components. As for large parts such as bumpers, assuming that they will be cut into pieces at the dismantling stage, they are labeled with continuous material marking in a longitudinal direction.

(5) Reducing hazardous substances

We are continually making efforts, through the development of new materials, etc., to reduce the use of hazardous substances.

For example, we are aggressively promoting the adoption of lead-free materials for the radiator, heater core, fuel tank, wiring harnesses, hoses, glass ceramic prints and electrodeposition paints for the vehicle body, etc. Furthermore, as for mercury and cadmium, the amounts used for discharge headlamps and/or liquid crystal panels have already been minimized. For example, with illuminating combination meters, we are aiming for a mercury-free state by adopting light emitting diodes (LEDs) as the backlight.

4.1.2 Trucks and buses

Our recycling efforts with regard to our trucks and buses are operating under the same philosophy as our passenger vehicles. CANTER, our new truck launched in 2002, has achieved a potential recyclability ratio in excess of 90 %. This is our company's voluntary target. Here are some examples of the adoption of recycled materials for trucks and buses, as well as the original development of the artifical wood.

(1) Adopting recycled materials

In the Mitsubishi Fuso Truck and Bus Corporation, when compared to other truck manufacturers, it is relatively easy to obtain material from recycled passenger vehicle bumpers. These bumpers were collected by our sales companies. We are aggressively promoting the adoption of recycled bumper material for exterior parts, etc. At present, the typical parts using recycled material from bumpers are: cab side covers, wheelhouse covers, air cleaner housings, etc.

We are also promoting the effective use of more recycled materials, such as adopting recycled material from containers (i.e. cases used to transport beer bottles); recycled material from other industries, for covers used as cab interior trims or expanded polypropylene boards for gate panels of medium-sized truck cargo beds.

(2) Development of the artifical wood

As trucks and buses use comparatively large amounts of wood, recycling wood is one of the main recycling issues for trucks and buses. Most of the wood

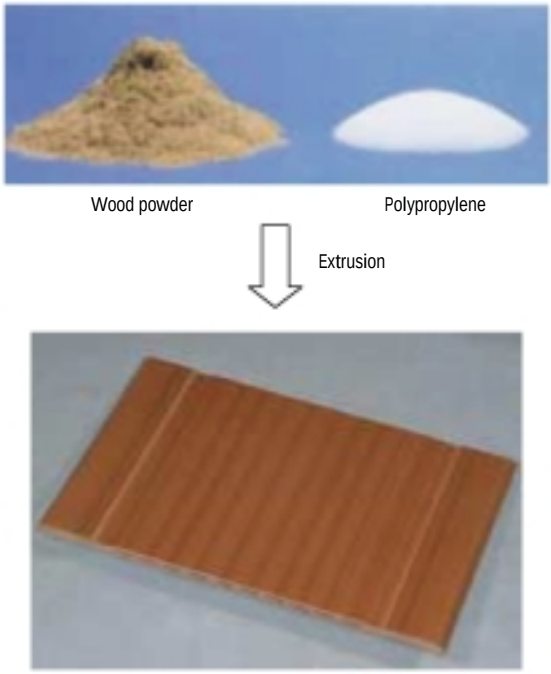

Fig. 5 Artificial wood

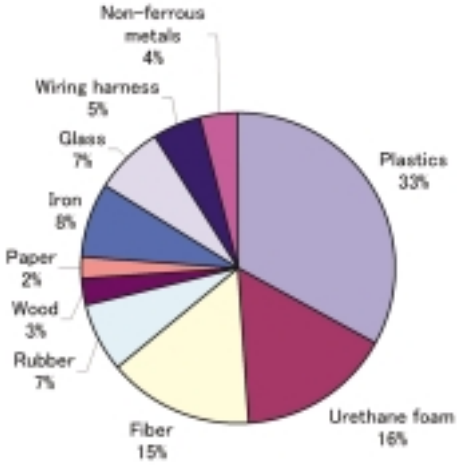

Fig. 6 Composition ratio of ASR

is produced in the tropical rainforests of the South Seas. The indiscriminate cutting down of these trees is now considered to be one of the main causes of environmental destruction leading to global desertification and global warming. Our company is starting to reduce the use of South Seas timber as well as developing recyclable artificial wood.

This artificial wood is made from a mix of polypropylene resin and wood powder (utilizing wood scraps), and is molded by extrusion (**Fig. 5**). This artificial wood has a high degree of recyclability; it can be recycled several times with very little deterioration of its physical properties. We are studying ways of utilizing the material for areas such as front and/or gate panels of truck cargo beds.

This material has the equivalent combustion characteristics of real wood, so that when finally incinerated at the end-of-life vehicle, it will not produce any particularly hazardous substances. It can therefore be treated within the existing infrastructure without difficulty.

4.2 Recycling technologies for end-of-life vehicles

In Japan, the most urgent among the three items which automobile manufacturers are obliged to follow concerning collecting and recycling, is minimizing the amount of ASR to be disposed of by landfill. We will focus here on the technologies needed to treat ASR.

ASR, as shown in **Fig. 6**, consists of three-quarters organic substances, such as resin, expanded urethane, fiber, rubber, etc., and one quarter inorganic substances, such as iron and copper, and glass.

There are many different methods of treating ASR, one emphasizing the importance of recycling the material; another focusing on thermal recycling and a third utilizing refining non-ferrous metals. Some of these methods are already in practice, others are still under study as potential new business models.

For material recycling, there are the following technologies:

(1) Improving the recovery ratio of iron and non-ferrous metals by screening, magnetic separation and/or eddy current, etc. by the shredding operator.
(2) Refining technology of copper (not only utilizing ASR as the heat source in the reverberatory furnace, but also recovering metals such as copper).
(3) Heat carrier bath method (A new recycling method that has been developed by NKK Corporation, in which ASR is dipped in an oil bath of 280 ˚C, recovering resins and the like which float, as well as recycling the recovered precipitates as materials for iron and non-ferrous metal manufacturing).
(4) Recovering urethane foam and fiber from ASR as sound insulation material.

An automobile manufacturer in Germany is studying a technology with which, after separating metals, etc. thoroughly from ASR, resins in ASR are shaped into grains that can be used as a reducing agent blown into blast furnaces. Seat fabrics and urethane foam are then used as desiccating agents for drainage sludge and/or high calorie material for combustion.

Galloo Corporation, a shredding operator in Belgium, is using a technology where, by separating the resinous and non-organic components from ASR, polyethylene, polypropylene, etc. can be recovered from the plastic components and non-organic components can also be effectively utilized.

Behind all these technological developments is the policy underlying the EU regulations which places priority on material recycling and sets an upper limit on the thermal recycling ratio within the total recycling ratio. As a result it is necessary for related industries to develop these technologies.

Thermal recycling technologies are as follows:

(1) Gasification combustion type melting technology (Electric power generation by a boiler utilizing combustion heat of pyrolytically decomposed gas)
    • Floating floor type (Separate type)

- Kiln type (Separate type)
- Shaft type (Integral type)

(2) Gasification reform type melting technology (pyrolytically decomposed gas is recovered as purified gas)
- Thermo-select type (Separate type)
- PKA type (Separate type)

Gasification melting technologies have had several problems when burning ASR only, such as too much variation of conditions, generating too much heat and containing too many low melting point alloys. Nowadays, however, these problems are being overcome. In spite of the high initial investment, this method may be the most practical, if the economic aspects can be improved by co-burning other types of waste.

A taskforce has been set up under the Industrial Structure Council and the Central Environment Council to study the details of an automobile recycling system. Also being studied is the concept and level of the recycling ratio and the standards for facility approval. As with ASR, material recycling is inherently not easy and the status of thermal recycling needs to be clarified.

The shredderless process does not generate any ASR. By pressing the remains of end-of-life vehicles into cubes after removing useful parts and placing them into an electric furnace or a converter, iron material can be recovered. The contents, which usually constitute ASR, are then utilized as fuel. Under Japan's Automobile Recycling Act, through the cooperation of dismantling operators and those iron producers with electric furnaces, an automobile manufacturer may obtain a Total Resources Recovery Approval and, by treating the remains of end-of-life vehicles, may be considered an ASR recycler. Even though not all of end-of-life vehicles will be treated by this method, with efforts by the electric furnace industry, this method may develop in the future.

5. Summary

Even though iron content, which makes up a large amount of the weight within an end-of-life vehicle, is able to recycled, it is not actually returned as high quality material, such as thin steel sheet. Depending on the copper content found in the remains of an end-of-life vehicle, recycled iron may only be used in low-grade products such as steel construction bars. In the future, the steel industry will need to remove the copper content from dismantled end-of-life vehicles in order to obtain high quality iron. Therefore, the automobile industry should make it easier to remove copper parts, such as wiring harnesses and/or motors, etc. High quality recycled iron could be achieved but only through the cooperation of the material suppliers and the automobile industry as users.

As for the treatment of ASR, it is expected that reducing the use of substances containing chlorine such as polyvinyl chloride (PVC) which generate dioxins, will make thermal recycling or treatment using a blast furnace easier. Based on the composition of ASR, it is also important to obtain the cooperation of the non-ferrous metal refining industry. This industry has the technology to recover useful metals such as copper and to stabilize melted slag as well as to recover resources.

Utilizing and improving the existing infrastructure well is very important not only for the dismantling of treatment processes but also for the recycling process as a whole. A recycling-oriented society cannot be achieved without cooperation between the various industries.

We will develop approaches to facilitate ASR treatment and to reduce the amount of ASR itself. This will be done by improving the ease of dismantling and recycling, as well as raw material selection and product designs that reduce the use of hazardous substances from the development stage.

We will therefore integrate each recycling initiative that has been practiced so far, and deploy it as a Design for Environment (DfE) operation. The structure of this operation will be completed within fiscal year 2002, and then applied to mass production vehicles.

We firmly believe that the efforts of automobile manufacturers, which began based on the Recycling Initiative, will increase steadily under the new Automobile Recycling Act and result in a society where a recycling ratio of greater than 95 % could be achieved by 2015.

References

(1) Materials distributed at a joint meeting with METI and MOE regarding Automobile Recycling on 26 November 2002.

(2) Research Report "Future prospects and issues to be resolved concerning end-of-life vehicles", No. 36, p. 43, March 2002, Development Bank of Japan


Harushige YAMAMURA


Takehiro ISHIURA


Motokazu KOBAYASHI

EGR System in a Turbocharged and Intercooled Heavy-Duty Diesel Engine – Expansion of EGR Area with Venturi EGR System –

Hitoshi YOKOMURA* Susumu KOHKETSU* Koji MORI*

Abstract

The EGR system is a very effective technique for reducing NOx emission from a diesel engine, particularly at the high load of engine operation condition where the engine emits more NOx than at other conditions.

In a turbocharged engine, however it is difficult to introduce EGR at the high load because of the high boost pressure in the air intake.

In this study, effective technologies to introduce EGR in a turbocharged engine were evaluated, and the Venturi type EGR system was found to be promising, without penalty of fuel economy caused by the increase of pumping loss.

Key words: *Exhaust Gas Recirculation (EGR), Diesel Engine/Venturi EGR System*

1. Introduction

Diesel emission regulations continue to be tightened in many countries, necessitating diesel engines with the least possible emissions. Exhaust gas recirculation (EGR) is one of the most effective methods for reducing the emissions of nitrogen oxides (NOx) of diesel engines. EGR system has already been used to mass-produced diesel engines, in which EGR is used at the low and medium load of engine operating condition, resulting in effective NOx reduction. In order to meet future emission standards, EGR must be done over wider range of engine operation, and heavier EGR rate will be needed. It is especially important for EGR to be done in a high engine load range since the amount of NOx is larger than the other engine operation conditions.

EGR systems adapted to the diesel engines of trucks usually recirculate exhaust gas utilizing the pressure difference between upstream part of the turbocharger turbine and downstream part of the compressor. This method of EGR needs that the pressure upstream of the turbine (hereinafter referred to as "turbine pressure") is higher than the pressure downstream of the compressor (hereinafter referred to as "boost pressure"), i.e.,

$$\Delta P = (\text{turbine pressure} - \text{boost pressure}) > 0$$

In a turbocharged diesel engine for truck, however, $\Delta P > 0$ is limited to the low load region, while in the high load region ΔP is smaller than zero and EGR is impossible. Several methods have been proposed to achive $\Delta P > 0$ condition even under a high-load condition. For example, some of these systems increase the turbine pressure to obtain a $\Delta P > 0$ condition by means of an exhaust choke valve or a variable geometry (VG) turbocharger, whereas other systems decrease the boost pressure to obtain a $\Delta P > 0$ condition by means of an intake throttle valve or a venturi[(1) – (4)].

This paper discusses the effects of EGR for NOx reduction and evaluates some methods proposed for creating a $\Delta P > 0$ condition. The paper then discusses the characteristics of the venturi EGR system that is the most promising among the proposed and shows that the system is rather effective for expanding the EGR range up to high engine load conditions.

Table 1 Engine specifications

Type	Turbocharged and intercooled direct injection diesel engine
Number of cylinders	6
Bore x stroke	135 x 140 mm
Displacement	12.023 liters
Maximum output	287 kW/2200 rpm

2. Test equipment

2.1 Engine

The engine used for the test was a turbocharged, intercooled direct injection 12-liter diesel engine for heavy-duty trucks. The major specifications of the engine are shown in **Table 1**.

2.2 EGR system

The EGR system used with the test engine was the type that exhaust gas was recirculated from the upstream part of the turbocharger turbine to the downstream part of the compressor. **Fig. 1** shows the configuration of the EGR system. The EGR passage is taken

* Engine Research Dept., Research & Dev. Office, MFTBC

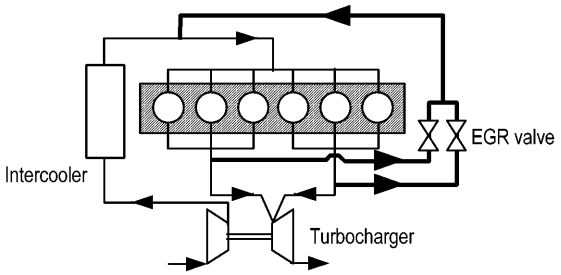

Fig. 1 Original EGR system

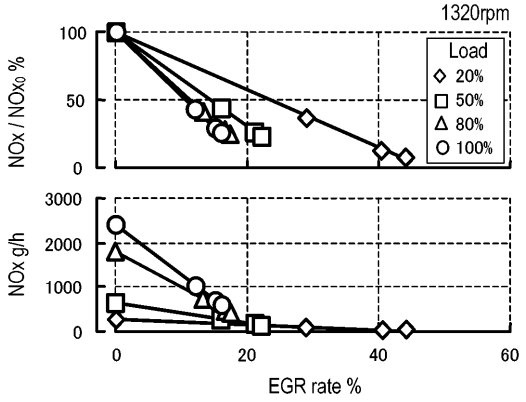

Fig. 2 Relationship between EGR rate and NOx

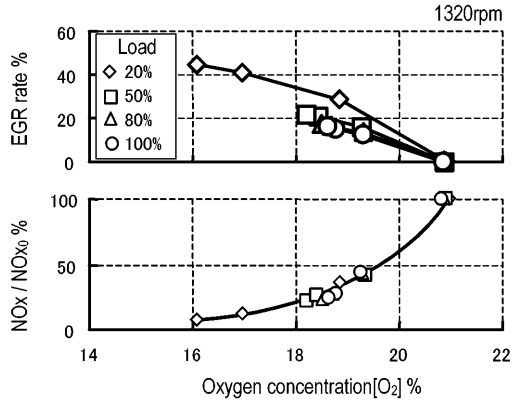

Fig. 3 Relationship between oxygen concentration and NOx reduction

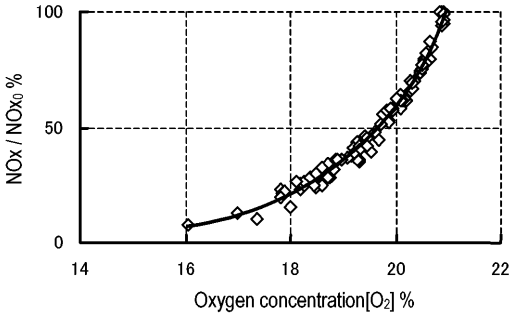

Fig. 4 Relationship between oxygen concentration and NOx reduction

out each manifold which separate front bank cylinder and rear cylinders, and connects to the intake pipe after two pipes connet to a single pipe. On each of the two pipes, an EGR valve is installed as a means of regulating the EGR rate. Each of the two valves has a capacity of 3500 liters/min (at pressure difference of 6.7 kPa).

Experiments were conducted by applying some of the proposed systems to this original EGR system to cause a positive ΔP condition.

3. Experiment results and evaluation

3.1 NOx reduction effect of EGR

Fig. 2 shows the typical NOx reduction effect of EGR at the mid-speed range of the test engine. Under all load conditions, the amount of NOx decreases as the EGR rate increases. The graph also shows that the NOx reduction curves with the 0 % EGR point as the origin slope downward at different angles according to the load; the higher the load, the steeper the angle. In other words, the NOx reduction effect at the same EGR rate increases as the engine load becomes higher.

It is generally known that there are two reasons to reduce NOx by EGR. The first of them is the reduction of combustion temperature. The addition of exhaust gases to the intake air increases the amount of combustion-accompanying gases (mainly CO_2), which in turn increases the heat capacity and lowers the combustion temperature. The second effect is the reduction of oxygen concentration in the intake air, which restrains the generation of NOx. **Fig. 3** shows the NOx emission test results as a function of the concentration of oxygen in the intake air/EGR gas mixture. This graph shows that the NOx reduction rate depends mostly on oxygen concentration, and not on the engine load or EGR rate. **Fig. 4** shows the results of NOx emission tests conducted while varying both the engine operating conditions and EGR rate, in which the test results shown in **Fig. 3** are merged. As in **Fig. 3**, almost all the data are on or in a single curve, indicating that there is a strong correlation between the oxygen concentration and NOx reduction rate. The reason for this is thought to be as follows: In **Fig. 2**, the NOx reduction rate under a certain load is different from that under another load even when the EGR rate remains the same because the difference in load causes a difference in the amount of combustion-accompanying gases and oxygen concentration in EGR gas, which in turn changes the oxygen concentration in the intake gas (mixture of intake air and EGR gas).

Fig. 5 shows the oxygen concentration calculated on the assumption that the EGR rate is increased while keeping the excess air ratio of the intake air and EGR gas mixture constant. The EGR rates and oxygen concentrations are plotted on the graph for each of the excess air ratios $\lambda = 1.5$ to 5 that correspond to the high-to-low engine load range. This graph indicates that, given the same oxygen concentration, the required EGR rate at $\lambda = 1.5$ is less than half of that at $\lambda = 5$. Considering this finding together with **Fig. 4**, we con-

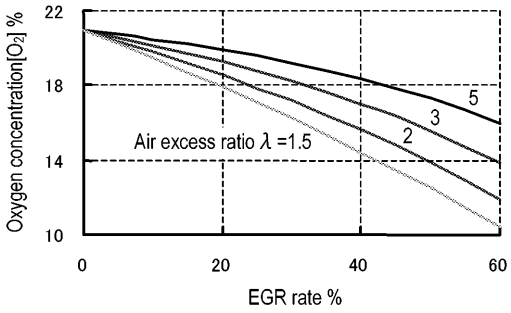

Fig. 5 Relationship between EGR rate and oxygen concentration

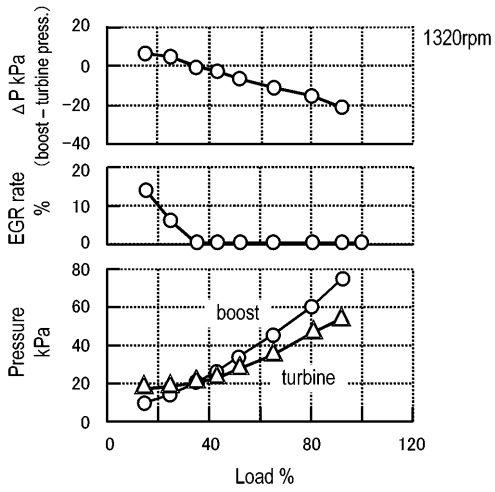

Fig. 6 EGR rate and pressure difference between boost and turbine pressure

clude that EGR operating under a high-load condition will bring about a NOx reduction rate equivalent to that attained under a low-load operation even with an EGR rate lower than that under the low-load condition. Since high-load operation involves a large amount of emissions, even a low rate of NOx reduction will have a very large effect on the overall NOx reduction.

It is therefore essential to extend the EGR-feasible load range to encompass high-load operation in order to reduce NOx emissions from turbocharged diesel engines.

3.2 Methods for expanding EGR-feasible load range

This section discusses two feasible methods for expanding EGR range to the high-load, one by using an exhaust throttle valve and the other by using a VG turbocharger. **Fig. 6** shows the EGR rates by the original EGR system at mid-speed range. The turbine pressure exceeds the boost pressure under low loads of engine operation condition but it goes below the boost pressure as the load increases. This means that the EGR-feasible range is limited only to low-load operations.

Fig. 7 shows the results of the pressure and EGR rate equipped with an exhaust choke in the mid-speed range and under the high-load condition. In this test, the opening of the exhaust choke valve located down-

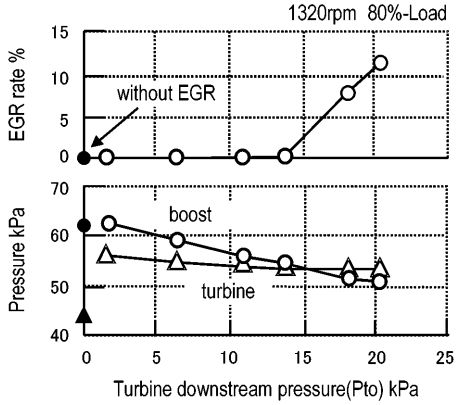

Fig. 7 Turbine and boost pressures and EGR rate in increasing Pto

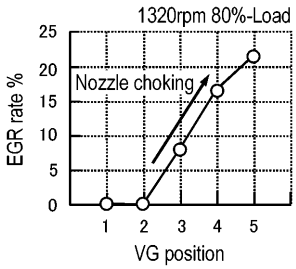

Fig. 8 Relationship between VG position and EGR rate

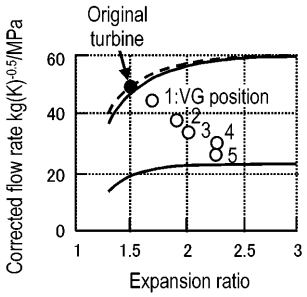

Fig. 9 Characteristics of VG turbocharger

stream of the turbine was changed to increase the pressure there. When the pressure downstream of the turbine is made low, EGR does not take place because the boost pressure exceeds the turbine pressure. Instead, narrowing the choke valve opening increases the pressure downstream of the turbine and EGR can take place as soon as the pressure levels reverse. The resulting situation, however, gives rise to a drop of the excess air ratio due to the decrease in boost pressure, which may increase smoke emissions.

The results of tests conducted using the VG turbocharger are described next. The VG turbocharger used in the test was of the same type as that actually used in large-size diesel engines. **Figs. 8** and **9** show the EGR rates achieved in the mid-speed range under a high-load condition for different turbocharger geometry points created by progressively narrowing the noz-

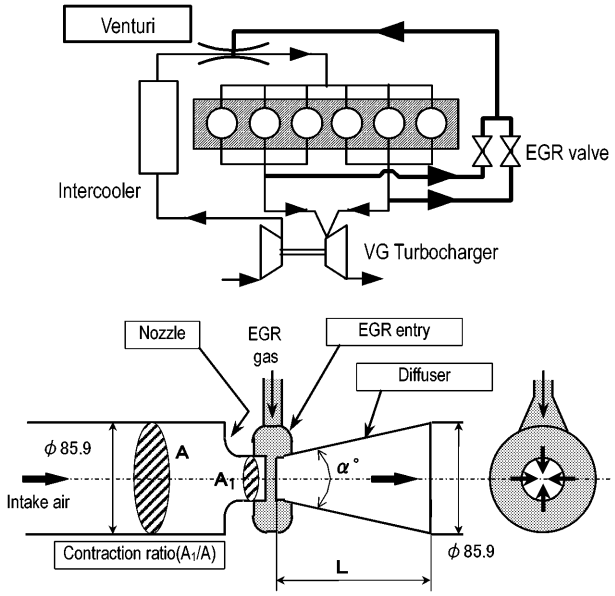

Fig. 10 Schematic of venturi EGR system

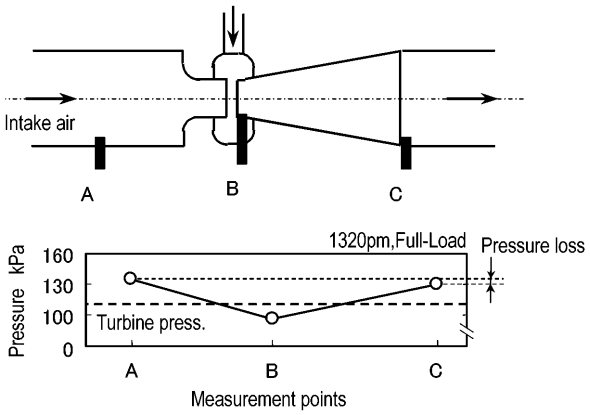

Fig. 11 Pressure distribution of venturi EGR system

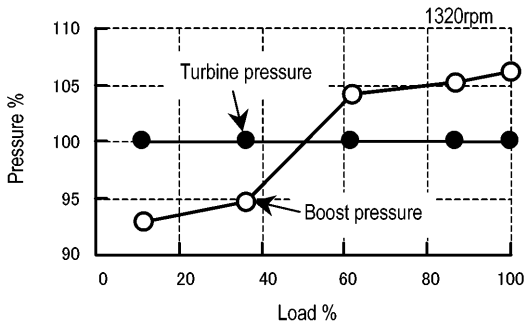

Fig. 12 Relationship between boost pressure and turbine pressure

zle area of the VG turbocharger. The EGR rate increases by narrowing the nozzle area. A maximum EGR rate over 20 % can be attained.

Both the above-mentioned methods certainly make it possible for EGR to take place in the high-load range, but they inevitably involve a higher pumping loss during intake and exhaust strokes because they work on the turbine pressure to make it higher than the boost pressure.

3.3 Venturi EGR system

The venturi system assures a positive ΔP by decreasing the pressure on the intake side only regionally. With this system, the boost pressure is once reduced ($\Delta P > 0$) in the EGR entry section, but a pressure is re-established to the original boost pressure downstream of that section. Therefore it is theoretically possible for this system to expand the EGR-feasible range without increasing the pumping loss. **Fig. 10** shows the configuration of the venturi EGR system. The venturi is located on the intake passage downstream of the intercooler and consists of three sections: a nozzle, an EGR entry section, and a diffuser. Through the gap formed between the nozzle and diffuser, the EGR gas is circumferentially drawn into the intake air stream and mixes with the air. The contraction ratio of the venturi is defined as the ratio of the sectional area of the intake pipe to the sectional area of the nozzle (A_1/A).

Fig. 11 shows the pressure distribution in the venturi area at the mid-speed range under a high-load condition. The pressure at point A on the upstream side of the venturi is higher than the turbine pressure. At the EGR entry section (point B), the pressure drops below the turbine pressure, and hence $\Delta P > 0$. The pressure is then restored downstream of the EGR entry section (point C) to a level almost equivalent to the pressure at point A. From the obtained pressure distribution data, it was confirmed that the venturi EGR system enabled EGR to take place under a high-load condition without being accompanied by pumping losses resulting from a decrease in the boost pressure.

Next, we conducted an investigation for various shapes of the venturi's component sections in order to find the optimum venturi specifications to increase the EGR rate in the high-load operation range with minimum pressure loss. The following section describes the effects of optimizing the shape of each component section based on the results of the investigation, and compares the venturi method with the EGR rate augmentation method that depends on exhaust choking, and identifies its advantages over other methods.

3.4 Effects of venturi geometry

(1) Contraction ratio

Before investigating the effects of the contraction ratio on the EGR rate through tests, it was necessary to roughly select an appropriate range of the contraction ratio of the venturi. The amount of drop of the boost pressure necessary for EGR to take place was therefore derived from the relationship between the boost and turbine pressures in the original EGR system, and then the contraction ratio necessary for attaining that pressure drop was determined assuming the flow through the venturi to be an adiabatic compression flow.

Fig. 12 shows the relationship between boost and turbine pressures in the original EGR system. The engine was operated in the mid-speed range, in which

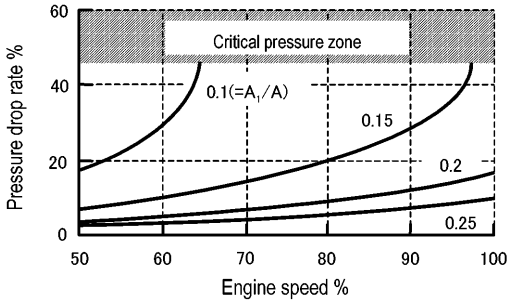

Fig. 13 Estimation of necessary contraction ratio

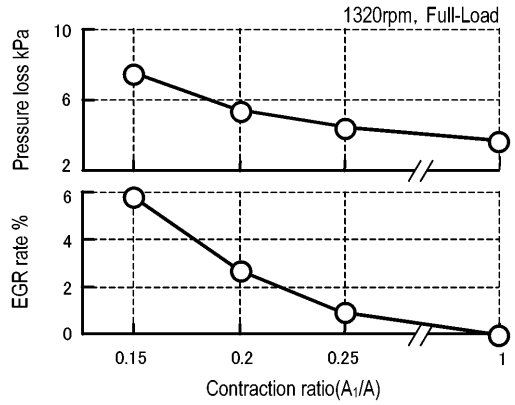

Fig. 14 Effect of contraction ratio

EGR cannot easily occur with conventional systems at the high load. The graph indicates that the boost pressure exceeds the turbine pressure in the mid- and high-load operation ranges, making it difficult to maintain the $\Delta P > 0$ condition. Therefore, EGR can take place when the pressure at the EGR entry section is lowered by using a venturi to less than the turbine pressure. For example, it is necessary to reduce the boost pressure about 5 – 6 % at the full-load point to establish $\Delta P > 0$ condition. **Fig. 13** shows the boost pressure drop rates calculated for different venturi contraction ratios. The indicated pressure drop rates are obtained assuming that the intake gas temperature is 50 ˚C and the contraction ratio is varied from 0.1 to 0.3. The graph indicates that the contraction ratio must be 0.2 or lower to obtain a 5 – 6 % boost pressure drop in the mid-speed range.

In the case of operation at the maximum rated speed with the contraction ratio set at around 0.15, the calculated pressure at the EGR entry section enters the critical pressure zone (a pressure drop rate of 46.5 % was used in the calculation). Based on this estimation, the contraction ratio of 0.2, with which the pressure would not enter the critical zone, was selected as the reference ratio with the next lower ratio 0.15 and next higher ratio 0.25 also selected as contraction ratios for the test of sample venturis.

Fig. 14 shows the test results for the EGR rate and pressure loss with each contraction ratio. The test was conducted at the mid-speed range, full-load condition. In the graph, the contraction ratio of 1 corresponds to

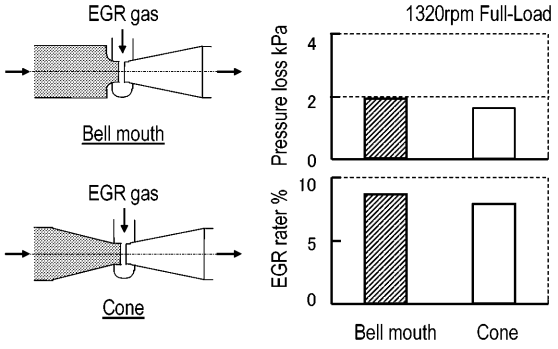

Fig. 15 Effect of nozzle shape

the non-venturi condition. The results confirmed that the EGR rate was influenced by the contraction ratios as expected, and that decreasing the contraction ratio to 0.15 could raise the EGR rate to as high as 6 %. With regard to the pressure loss, it increased slightly as the contraction ratio was decreased but the increase in the pressure loss had almost no effect on the air flow rate and fuel consumption under the operating conditions used in the test. It was also confirmed that intake air flow did not reach to sonic speed even with the contraction ratio at 0.15 and the engine speed at the maximum rated speed. Despite the estimation from the calculation, sonic speed was not actually reached presumably because of the pressure loss.

The test results revealed that the optimum contraction ratio was 0.15.

(2) Nozzle

As shapes of the venturi nozzle, an ordinary cone shape and a bell-mouth shape were selected for the study in order to meet the objectives of compactness and minimum pressure loss.

Fig. 15 shows the study results. There was almost no difference in the EGR rate attributable to differences in nozzle shape. Regarding the pressure loss, both the shapes showed almost the same characteristics although the pressure loss of the cone-shaped nozzle was slightly lower than that of the bell-mouth.

The bell-mouth-shaped nozzle with shorter overall length was finally selected rather than the cone-shaped nozzle because it is easier to install on the engine.

(3) Diffuser

The shape of the diffuser was also studied to achieve compactness and minimum pressure loss. It is well known that the pressure loss largely depends on the expansion angle of the diffuser and an expansion angle of 5.5˚ is optimum because it is associated with the minimum pressure loss[5]. On the other hand, the diffuser can be made more compact by increasing the expansion angle, as its length is inversely proportional to the expansion angle. In the study, diffusers of angles of 8˚, 11˚, and 17˚ were tested because of their compact size in addition to a diffuser of the ideal 5.5˚ angle. Taking the length of the 5.5˚ diffuser as 1, those of the larger angle diffusers are 0.7, 0.5, and 0.3, respectively. If the expected increase in the pressure loss can be properly controlled, the shorter diffusers will signifi-

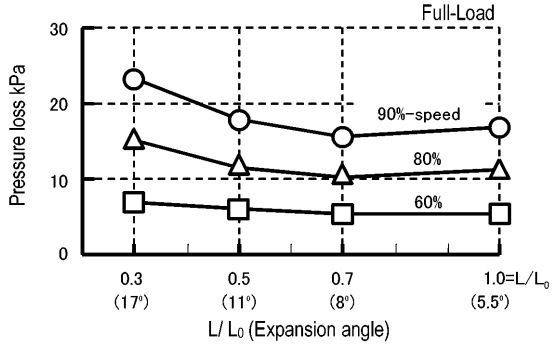

Fig. 16 Effect of diffuser length on pressure loss

Table 2 Optimum venturi geometry

Contraction ratio (A_1/A)	0.15
Nozzle	Bell mouth
EGR entry	Circumferential
Diffuser	Expansion angle $\alpha = 11^\circ$ Overall length L = 273 mm

cantly reduce the size of the venturi.

Fig. 16 shows the pressure loss for each of the expansion angles. Compared with the ideal 5.5° angle, the increase in pressure loss due to an increase in angle is almost negligible up to 11°, but increasing the angle further for shorter length evidently increases pressure loss in the high-speed range of operation. In conclusion, it was determined that the 11° expansion angle was the most appropriate for the diffuser to be adequately compact while being able to control the pressure loss to an appropriately low level.

It was also confirmed that changing the expansion angle from 5.5° to 11° did not cause any substantial change in EGR rate.

(4) Determination of optimum venturi geometry

Based on the findings from the studies conducted with regard to the EGR rate, pressure loss, and compactness, it was found that the geometry specifications shown in **Table 2** corresponded to the optimum characteristics of the venturi.

3.5 EGR rate improvement effect of venturi system

Fig. 17 shows the advantages of the optimized venturi system over the original EGR system in terms of the EGR rate.

With the venturi system, the $\Delta P > 0$ condition is established even in the 50 % or higher load range where ΔP is negative and consequently EGR is impossible with the conventional systems. Furthermore, the EGR-feasible range of the venturi system extends to the full-load engine condition, at which the system attains a 6 % EGR rate. The venturi system also increases the EGR rate by approximately 10 % in the mid-load and low-load ranges regardless of engine speed.

The venturi EGR system involves pressure losses at the nozzle and diffuser sections. The effects of these pressure losses on the fuel consumption of the engine

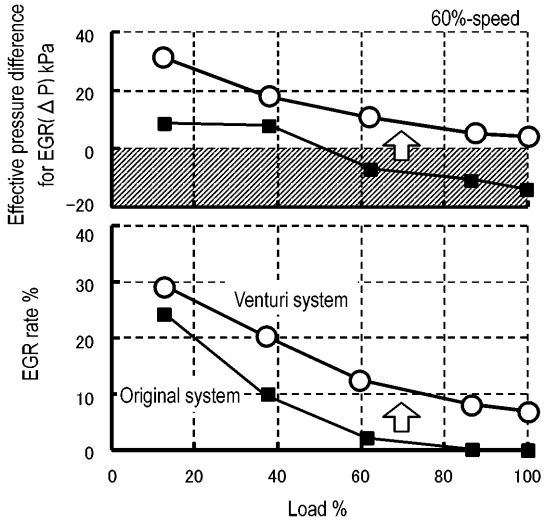

Fig. 17 Advantages of venturi system on EGR

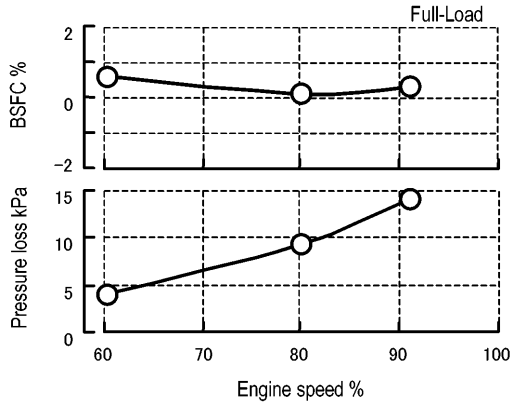

Fig. 18 Effect of pressure loss on fuel consumption

were investigated. **Fig. 18** shows the fuel consumption rates and pressure losses in an engine with the optimized venturi system under the full-load condition. Though the pressure loss increases with increase in airflow as the engine speed becomes higher, the increase in fuel consumption is less than 1 %, indicating that the venturi has almost negligible effect on the fuel consumption.

This study thus confirmed that the venturi can expand the range of EGR without increasing the fuel consumption.

3.6 Comparison with other approaches

In order to verify the effectiveness of the venturi EGR system, it was compared with the system that depended on exhaust choking to expand the EGR-feasible range. **Fig. 19** compares the EGR rate and fuel consumption of the two systems. When the fuel consumption rate of the venturi system is compared with that of the exhaust choke system for the same 6.2 % EGR rate, for example, the fuel consumption of the venturi system is about 4 % better than that of the exhaust choke system. **Fig. 20** is a low-pressure indicator diagram,

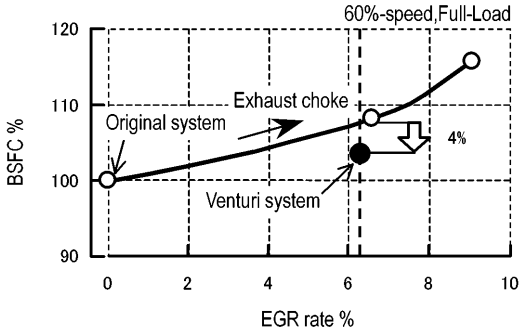

Fig. 19 Comparison of venturi and exhaust choke systems

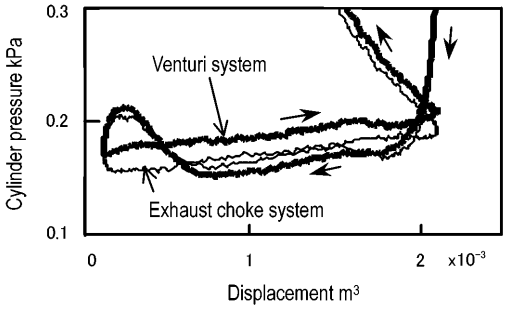

Fig. 20 Analysis of cylinder pressures

which shows why the venturi system is superior to the exhaust choke system in terms of fuel consumption. In the exhaust choke system, creating the $\Delta P > 0$ condition to take place EGR makes the exhaust stroke pressure of the cylinder higher than the intake stroke pressure, which significantly increases the pumping loss. In the venturi system, on the other hand, the intake stroke pressure remains higher than the exhaust stoke pressure throughout the operation, thus making EGR possible, which means that the pumping loss constitutes positive work that enables the unique merits of a turbocharged engine to be achieved. For this reason, the venturi system is superior to the exhaust choke system in terms of fuel consumption.

The pressure indicator diagram shows that the venturi system functions successfully as intended, creating the $\Delta P > 0$ condition in the EGR entry section and allowing the original boost pressure to be restored downstream of that section, so EGR takes place without any increase in pumping loss or fuel consumption.

4. Summary

(1) The application of EGR to diesel engines achieves larger reductions in NOx emissions under a high-load condition than a low-load condition for the same EGR rate. In other words, under the high-load condition, a low EGR rate produces the same NOx emission reduction effect as a high EGR rate under the low-load condition.

(2) It was shown that a method for expanding the EGR-feasible load range to high-load operation is essential when applying EGR to turbocharged diesel engines, and that the venturi EGR system achieves this objective more effectively than the conventional exhaust choke system and VG turbocharger system.

(3) It was shown that the venturi EGR system expands the EGR-feasible range without adversely affecting fuel economy caused by an increase of pumping loss, and it is thus an effective system for turbocharged diesel engines.

References

(1) S. Kohketsu et al.: "Exhaust Gas Recirculation in Turbocharged Diesel Engines", Proceedings of JSAE Convention, 9638266, 1996
(2) G. Graf et al.: SAE Paper 2000-01-0225, 2000
(3) E. Mattarelli et al.: SAE Paper 2000-01-0224, 2000
(4) U. Lundqvist et al.: SAE Paper 2000-01-0226, 2000
(5) Technical Material, "Fluid Resistance in Pipes and Ducts", JMSE

Hitoshi YOKOMURA

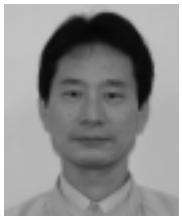

Susumu KOHKETSU

Koji MORI

In-Cylinder Phenomena Diagnostics for Gasoline Engine Development

Kazunari KUWAHARA*

Abstract

Recent advances in technologies for diagnosing in-cylinder phenomena have enabled engine designers to clarify the factors underlying the phenomena such as airflow, air-fuel mixing, and ignition and combustion of the mixture. Such information helps designers to develop and implement methods for optimally designing and controlling the factors. Proper combustion control has been achieved through optimum turbulence control for premixed leanburn gasoline engines and through optimum mixing control for direct injection gasoline engines. For the purpose of even more sophisticated combustion control, it is necessary for designers to keep sophisticating their eyes and insights into in-cylinder phenomena and updating the information.

Key words: *Gasoline Engine, Measurement, Combustion, Leanburn, Direct Injection*

1. Introduction

From the end of the 1980s and throughout the 1990s, Japanese motor vehicle manufacturers promoted the development of premixed lean-burn gasoline engines and direct injection gasoline engines, and were leading motor vehicle manufacturers in the world in regard to gasoline engine technologies. Mitsubishi Motors Corporation was a pioneer in the development of current engine technologies and realized these engines in the form of the MVV engine[1][2] and GDI* engine[3].

* GDI is a registered trademark or a trademark of Mitsubishi Motors Corporation in Japan and other countries.

Contributing to the progress of these engine technologies was the rapid advancement of in-cylinder phenomena diagnostics. During the same period, phenomena diagnostics technologies progressed, supported by the development in related fields, such as laser technology, photoelectron technology, semi-conductor technology, etc. Examples include observation of flows, fuel atomization and combustion by a high-speed video camera, measurement of flows by laser Doppler velocimetry or a laser sheet method, measurement of atomization by phase Doppler particle analysis or a laser sheet method, and measurement of mixing or combustion by a laser induced fluorescence method, etc. The complex in-cylinder phenomena occur within a space whose shape varies with the movement of the piston, fluctuating considerably time-wise as well as space-wise. By making full use of optical diagnostic methods such as using an optical engine with the transparent cylinder and piston crown, and with an observation window in the combustion chamber, analysis of these phenomena has become possible.

As understanding of the phenomena deepens, ideas for controlling combustion and measures to bring these ideas to reality are being contemplated. However, even it is admitted that once combustion has started, it is difficult to control. The alternative is to control the phenomena before combustion starts, such as flows, atomization or mixing. Thus, depending on a purpose of combustion control, an approach called "phenomena design" is being examined, in which the phenomena occurring before combustion is controlled for optimization.

Typical examples of this approach were for the combustion control for the MVV and GDI engines. The combustion control for the MVV engine was realized by controlling turbulence and that for the GDI by controlling mixing. Basic concepts of the combustion control were formulated by carefully working out ideas of the phenomena design and measures for realizing them, starting with clarification of features of the phenomena through diagnosis.

In the present paper, typical diagnostic technologies that contributed to building these concepts, and findings of the phenomena and points of the phenomena design obtained by these diagnostic technologies will be introduced.

2. Typical diagnostic technologies

2.1 Laser color sheet method

An effective means of clarifying structure of flows is to look for instantaneous spatial distribution of flow velocity vectors. Although the two-dimensional flow structure could be captured with a laser sheet method[4], in order to enable analysis of the complicated flows, some contrivance is necessary to locate the velocity vectors with high data density. In 1990, the author et al. developed "two-color laser sheet method", which makes it possible to measure two-dimensional distribu-

* Advanced Powertrain Dept., Car Research & Dev. Office, MMC

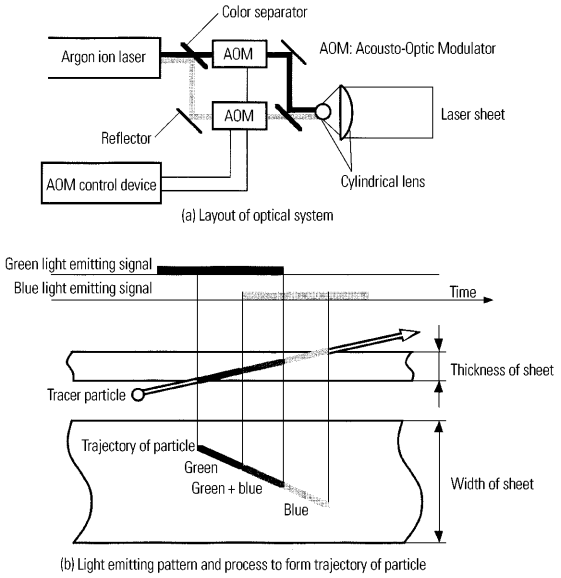

Fig. 1 Principle of two-color laser sheet method

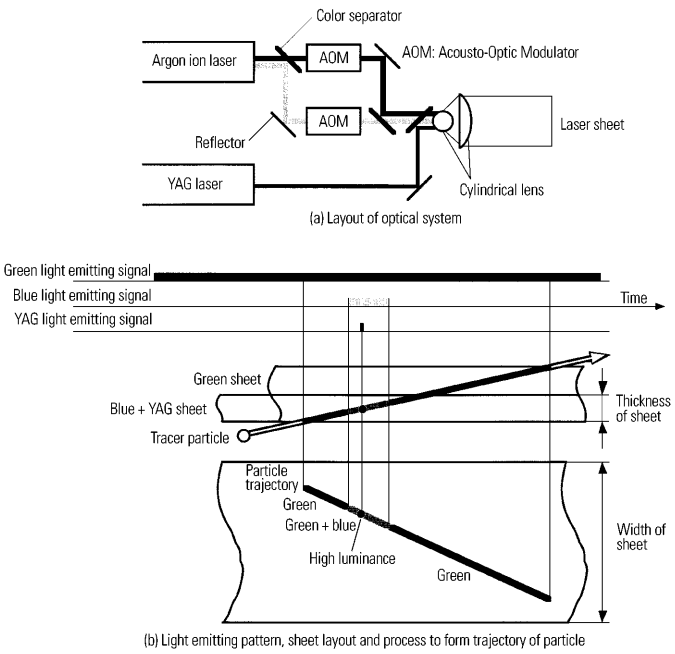

Fig. 2 Principle of three-color laser sheet method

tion of two-dimensional velocity vectors with high data density[5]. However, it would be more effective if the instantaneous three-dimensional flow structure would be measured. In 1993, the author et al. developed another measurement method named "three-color laser sheet method", enabling the measurement of two-dimensional distribution of three-dimensional velocity vectors[6].

Fig. 1 shows the principle of the two-color laser sheet method. Blue (wavelength of 488 nm) and green (wavelength of 514.5 nm) beams are separated from an argon ion laser beam oscillated in multi-mode. After these beam are modulated with rectangular waves at different timings using acousto-optic cells, they are brought together again, then directed to a cylindrical lens to transform to a sheet. By causing the laser sheet to emit light of green, green + blue (cyan blue) and blue alternately in this order, and by photographing a tracer particle flowing in the sheet, the particle trajectory structured with green, cyan and blue portions could be obtained. The velocity vector in and parallel to the sheet could be obtained by the length of the cyan portion, taking the green portion as the starting point, and the light-emitting duration of the cyan portion. A trajectory with imperfect color pattern is removed as an ineffective one that are shown when a particle passes through the laser sheet during the light-emitting duration. By relying on the color pattern, even when two trajectories cross, they could be easily separated, so that velocity vectors could be obtained at high density.

Fig. 2 shows the principle of the "three-color laser sheet method". Blue and green beams are separated from an argon ion laser beams and these beams are modulated with rectangular waves at different timings by acousto-optic cells. By adding a single shot at the second harmonic wavelength of an Nd-YAG laser (532 nm) to those beams, a laser sheet with a two-layer structure is formed, piled up with one layer composed of the three colors and the other layer of only the green color of the argon ion laser. Although the second harmonic shot of the Nd-YAG laser is in a kind of green hue, its energy density is far higher than that of the argon ion laser green, so high as to be beyond comparison, they could be distinguished by the luminances of them. The green sheet of the argon ion laser is made to emit light for the time duration sufficient for a particle passing through the sheet, and the blue sheet is made to emit light for the short period in between. A marking is placed with the Nd-YAG laser in the time duration of the light emission of the blue sheet, so that the duration is divided into 2 unequal segments. A search is then initiated for a velocity vector in and parallel to the sheet using the layer composed of the three colors. That is, the velocity vector could be obtained from the length of the cyan portion of a particle trajectory, its duration of the light emission and the marking by the Nd-YAG laser. The component of the velocity vertical to the sheet are searched for using the entire two-layer structured sheet. By comparing the color pattern of the trajectory with the time pattern of the light emission, it is possible to extract the trajectory of a particle that has dashed into and then passed through the sheet during the light-emitting duration of the green sheet. The time needed for this particle to pass through the sheet is obtained by deviding the total length of the trajectory by the length of the cyan portion. The value of the vertical component of the velocity is obtained from the time and the thickness of the sheet. By deciphering the color pattern, it can be determined whether the particle has dashed into the sheet from above or from below. There are many cases in which the directions of particles could be decided even from the trajectories of the particles that have not passed through the sheet. However, it is difficult to expect high-density

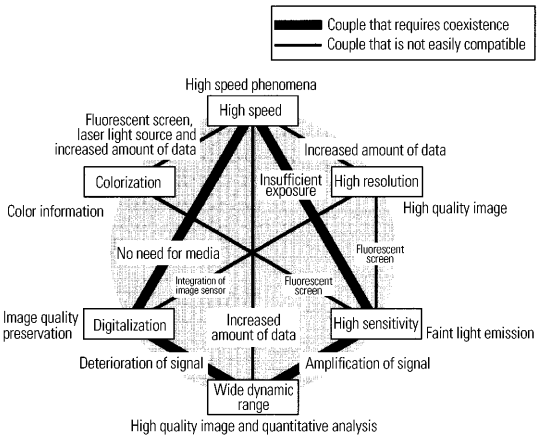

Fig. 3 Requirements on image measurements

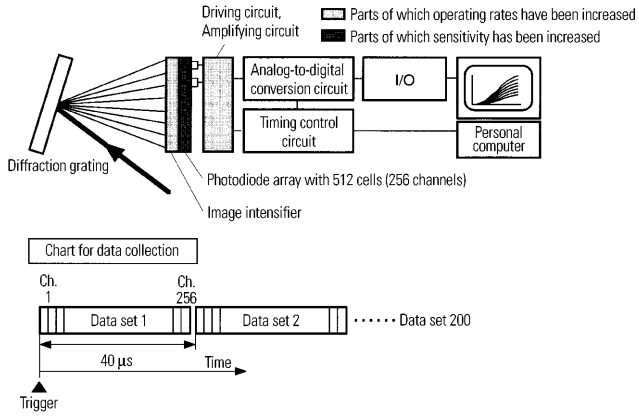

Fig. 4 High-speed optical multi-channel analyzer

data because of the complexity of the principle and the following fundamental contradiction. The accuracy of the measurement may decrease because, as the velocity component vertical to the sheet become larger and as the angle at which the particle dashes into the sheet becomes larger, the trajectory is shortened.

Structure of flows could be successfully clarified by combining results of both the laser color sheet methods, making the best use of each advantage, namely the high-density data and three-dimensional information.

2.2 High-speed video camera

A high-speed video camera[7], which made an appearance in 1993, played a major role in developing insight into the phenomena. The camera, which has a framing rate of 4500 frames/second at full frame with a spatial resolution of 256 x 256, or 40500 frames/second at segmental frame with 64 x 64, provides immediate playback by once taking image data into D-RAM with the 8-bit luminance resolution. With the smart method of splitting one frame into 16 parts and parallel scanning, the camera realized the epoch-making framing rate for those days. Although the spatial resolution and luminance resolution is not necessarily high, the quality of the images was sufficient if the data was shown as a "moving picture" not still ones. There are many requirements for image measurement, such as higher speed, higher spatial resolution, higher luminance resolution, higher sensitivity, wider dynamic range, digitalization and colorization; however, as shown in **Fig. 3**, it is difficult to realize all these requirements at one time. A certain couple out of these requirements are not compatible, and other couple require coexistence with each other. Higher speed restricts higher resolution, which requires longer scanning time corresponding to an increased amount of data. When a level exposure becomes insufficient because of the realization of higher speed, higher sensitivity is required, and, if an image intensifier is incorporated in order to compensate the exposure, because of characteristics of the fluorescent screen of the intensifier, the requirements for higher resolution and wider dynamic range are restricted. Presumably, the camera was designed to attain the optimum balance among these requirements with a technical level available at that time.

With the introduction of this camera, it became easier to visually grasp the phenomena and, by combining the visual data with quantitative data measured by other measurement methods, clarification of features of the phenomena has progressed considerably. Most of the vortices born in the cylinder, where flows fluctuate time-wise as well as space-wise, will be deformed or crushed before turning over. When they are captured as a still picture, these vortices look no different than curved flows; therefore, it is difficult to recognize their existence. However, if captured as a moving picture, the existence of gyrating vortices could be confirmed and, consequently, still pictures taken with the laser color sheet methods could be analyzed effectively.

Connecting the camera to a band pass filter and a high-speed ultraviolet-responsive-type image intensifier, faint chemical light emission from a flame in a premixed lean-burn gasoline engine was visualized, and, by performing quantitative and statistical analysis of the luminance of the light emission, the structure of the lean combustion flame was clarified[8].

In order to clarify the structure of a stratified charge combustion flame in a direct injection gasoline engine, chemical light emission in a ultraviolet wavelength range and luminus-flame light emission in a visible wavelength range were observed at the same time, using an image separation optical system with a half mirror and 2 units of a band pass filter and the camera, one of which was combined with the high-speed ultraviolet-responsive-type image intensifier.

2.3 High-speed optical multi-channel analyzer

In 1994, the author et al. actualized a high-speed optical multi-channel analyzer capable of collecting spectra of light emission at every one degree of the crank angle[10]. **Fig. 4** shows the device. In addition to increasing a operating rate of each part, with a contrivance to shorten a scanning time while simultaneously securing a level of exposure, of connecting a pair of adjacent cells of the photo diode array with 512 cells to use the array as a 256-channel one, 256 spectra could be collected at the maximum sampling rate of

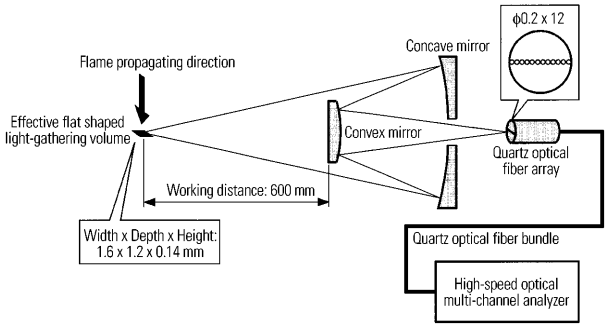

Fig. 5 Cassegrain optical system with optical fiber array

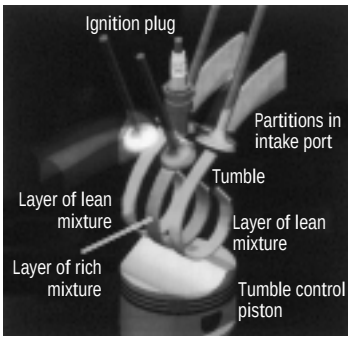

Fig. 6 Four-valve MVV engine employing combustion control concept of barrel stratification

40 microseconds.

The clue, which initiated development of the idea for this device, was that, even though the sampling rates of optical multi-channel analyzers available at that time were only in millisecond order, considering that the 2-dimensional sensor scanning of the high-speed video camera had already been in sub-millisecond order, it was assumed that there would be no reason that scanning a 1-dimensional sensor at a much higher rate would not be possible.

By capturing spectra of discharge light emission that accompanies the spark ignition using this optical multi-channel analyzer, a measuring method to estimate the concentration of an air-fuel mixture at the ignition plug was developed, based on a fact that a shape of the spectra distribution was affected by the air-fuel mixture concentration.

Connecting the optical multi-channel analyzer to a Cassegrain optical system as shown in **Fig. 5**, spectra of local flame light emission were captured[11]. Although setting a larger light-gathering volume was desirable in order to secure a level of exposure, the larger volume would inevitably result in lower spatial resolution. Therefore, for securing a level of exposure as well as at least the resolution of the flame propagating direction, a flat shaped light-gathering volume, which focused on the optical fiber array connected to the light receiving side of the optical system, was placed parallel to the propagating flame front. Results of this measurement and of the image analysis were combined to clarify characteristics of combustion.

3. Phenomena design of MVV engine

One important point of combustion control for a premixed lean-burn gasoline engine is to increase a turbulent burning rate in order to rapidly burn a lean mixture, of which the laminar burning rate is fundamentally low. For this purpose, it is necessary to preserve the kinetic energy that is given to the intake air during the intake stroke, through the compression stroke as a large-scale gyrating flow, which is difficult to attenuate, then to convert it rapidly into turbulence just before the start of combustion. Another point is whether or not it is intended to slightly stratify an air-fuel mixture and enrich the part of the mixture in the vicinity of the ignition plug in order to stabilize the early stage of combustion. If this is the intention, a degree of the mixture stratification should be optimized, considering a trade-off relationship between the expansion of a lean limit of combustion and an increase in NOx emission with the increased degree of the stratification.

Mitsubishi Motors Corporation proposed a combustion control concept named “Barrel stratification” and, based on the concept, announced the three-valve MVV engine in 1991[1]. Then, in 1993, the concept was developed further to the four-valve MVV engine[2], which is shown in **Fig. 6**.

The barrel stratification utilizes a gyrating flow called “tumble”, of which the gyration axis is perpendicular to the axis of the cylinder. Furthermore, utilizing a characteristic that the velocity in the direction of the gyration axis of the tumble is low, and, therefore, there is the limited movement of air and fuel in this direction, the concept promotes the mixture stratification of an air-fuel mixture along that direction. In the concept of the four-valve MMV engine, by using the tumble control piston with a curved top surface, the conversion of the tumble to turbulence is promoted. Furthermore, by supplying fuel to the space caught between two partitions within the intake port, the gentle air-fuel mixture stratification that places a slightly richer mixture in the middle layer of the cylinder, is realized.

In the following sections, flow and turbulence control using this concept will be noted. The process in which the idea of the tumble control piston was worked out, based on diagnostic results in the case of a usual piston, will be described in detail.

3.1 Characteristics of flows and combustion

Although the tumble maintains a distinctive structure just like a barrel being rolled while there is a wide space within the cylinder, when the space becomes flatter as the piston goes up, the structure is deformed and, finally, it is crushed. **Fig. 7** shows the flow structure at 15 degrees before the top dead center of the compression stroke, obtained by the three-color laser sheet method. The velocity component vertical to the horizontally placed sheet, has been classified only into 3 levels: upward, almost parallel to the sheet and downward. At this timing, as the crush of the tumble has

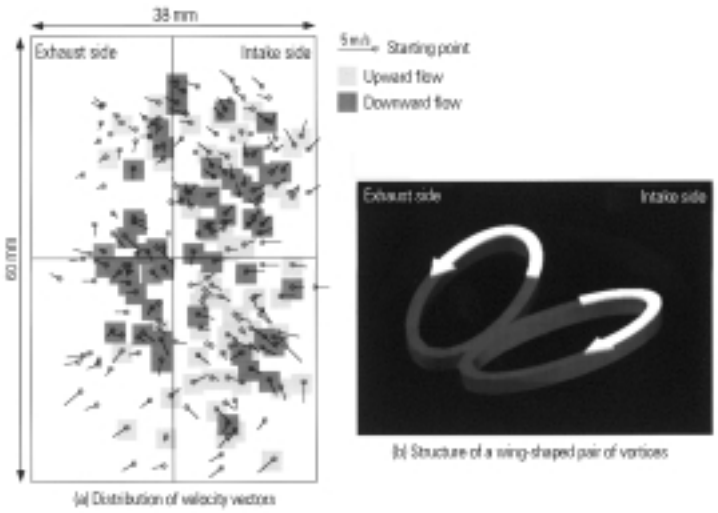

Fig. 7 Three-dimensional flow structure at 15˚BTDC (bore x stroke: 85 x 88 mm; 1000 min^{-1}; WOT; tumble ratio: 2.5; on horizontal plane below sparkplug; with three-color laser color sheet method)

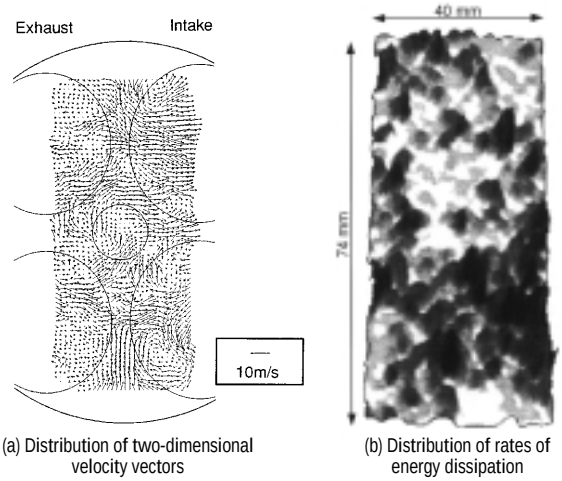

Fig. 8 Flow structure at TDC (1000 min^{-1}; WOT; tumble ratio: 2.5; on horizontal plane 8 mm below sparkplug; with two-color laser sheet method)

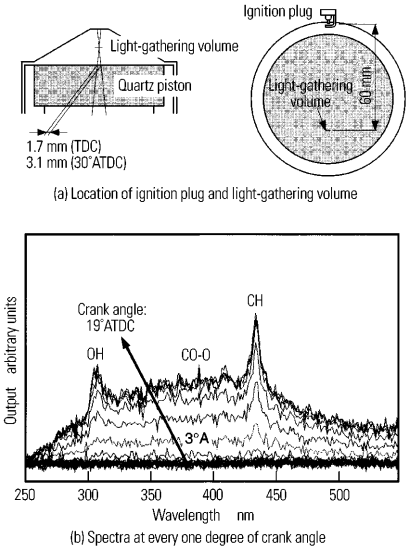

Fig. 9 Local light emission spectra of premixed lean combustion flame (1000 min^{-1}; partial load; propane; equivalence ratio: 0.65; ig. timing: 20˚BTDC)

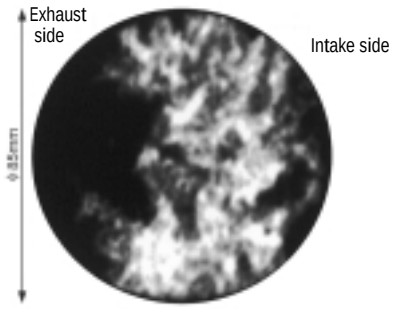

Fig. 10 Structure of premixed lean combustion flame (1500 min^{-1}; partial load; propane; equivalence ratio: 0.61; center ignition; ig. timing: 25˚BTDC; wavelength range: 350 – 390 nm; image acquisition timing: 11˚ATDC)

already started, it appears that the flow structure is characterized by a wing-shaped pair of vortices.

Fig. 8 shows the 2-dimensional flow structure at the compression top dead center obtained by the two-color laser sheet method. One is a result of the distribution of velocity vectors at every 1 mm pitch, interrogated with some 1000 raw data in a picture taken by the horizontally placed sheet, and the other is the result of the distribution of the rates of energy dissipation estimated from the first result[5].

The structure of flows at this timing is governed by numerous vortices with scales ranging from a few mm to some 10 mm, which have considerable local fluctuation. It is assumed that, along with the energy dissipation, turbulence is generated in the vicinity of the vortices.

Fig. 9 shows spectra distributions of local flame light emission collected at every one degree of the crank angle. In the experiment, in order to trace a change of the spectra when a sufficiently-grown propagating flame is passing through the measuring point, the ignition plug was installed on a side wall of the combustion chamber, and the plug and the mesuring point were set rather far apart. The flame light emission is constructed mainly with light emissions of OH radical, CH radical and CO-O recombination. These light emissions were detected over a fairly long time, more than 15 degrees of the crank angle after the flame surface had passed through the measuring point.

Fig. 10 shows one frame from visualized data of the light emission of CO-C recombination in a near-ultraviolet wavelength range of 350 to 390 nm. The spark ignition was executed at the center of the combustion chamber. Light emitting zones is widely distributed

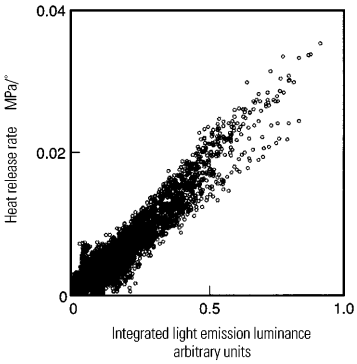

Fig. 11 Relationship between totally integrated light emission luminance and heat release rate (1500 min^{-1}; partial load; propane; equivalence ratios: 0.74, 0.61; center ignition; ig. timing: 25°BTDC; wavelength range: 350 – 390 nm)

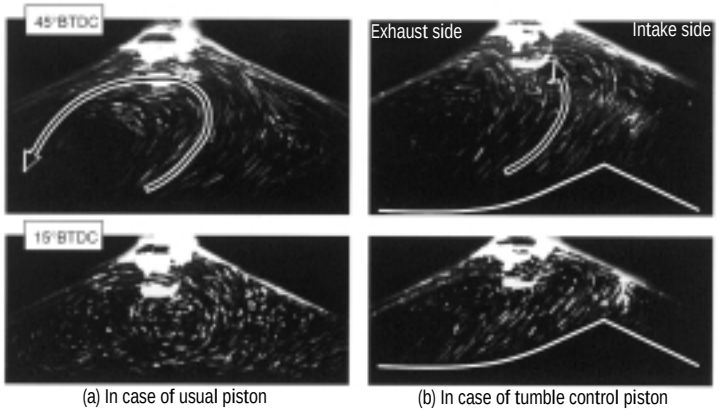

(a) In case of usual piston (b) In case of tumble control piston

Fig. 12 Influence of tumble-control piston on flow field structure at 45°and 15°BTDC (1000 min^{-1}; WOT; on central vertical plane with laser color sheet method)

behind the flame front. This finding is consistent with the finding from the fixed-point measurement with the optical multichannel analyzer that the flame light emission was detected over the long time after the flame front had passed through the measuring point. In large-scale analysis with several thousand frames of the data[8], a linear correlation between the totally integrated value of the local luminance of this light emission throughout the light emitting zones and the heat release rate obtained by pressure-indicator analysis could be found, as shown in **Fig. 11**. The conclusion drawn from this correlation is that the local luminance of the light emission could be an index for evaluating local combustion activity. When the light-emitting zones is assumed to be burning zones, the widely distributed burning zones are characterized by streak patterns with the scales of the numerous vortices that govern the flow field at the end of the compression stroke.

3.2 Turbulence control

As an induction period of a lean air-fuel mixture from the spark ignition to the beginning of combustion is long, it is necessary to ignite at the timing as early as 45 degrees before the top dead center. This timing is before the tumble starts crushing, in the case of a usual piston. Before the tumble is crushed, the ignition plug is exposed to a flow from intake valves to exhaust valves, that is, the flow at the outer circumference of the tumble. When igniting within this flow, a stretch of the arc, multiple discharge and a blow-out of the flame kernel occur, which may become a cause of misfire or unstable combustion[2].

In comparison of the spatial average luminance of the light emission of CO-O recombination between the cases in which an appropriately strong tumble is formed and a weaker one is formed, although a difference of the luminance in the first half of flame propagation is quite small, the luminance with the stronger tumble becomes larger in the latter half of propagation[12]. This fact means that during the first half of flame propagation, the tumble does not necessarily participate effectively in the activation of combustion. The tumble is converted to a wing-shaped pair of vortices, then to numerous vortices at the end of the compression stroke. The fact that the tumble is not directly converted to turbulence presumably sets a limit to the effect of the tumble on the activation of combustion.

It is assumed that the laminar burning rate of a lean air-fuel mixture with an equivalence ratio approaching 0.6, which is close to the lean limit of combustion, decreases to approximately 0.2 m/sec. A condition of combustion in a premixed lean-burn engine, which gives the lean mixture turbulence with an intensity of a few m/sec to 10 m/sec, has already stepped into the regine of the combustion diagram where it is no wonder that the flame is quenched[13], according to the existing turbulent combustion theory. Nevertheless, combustion exists in the engine. In order to explain this fact, along with the result, that burning zones are widely distributed behind the flame front, it is reasonable to assume the following combustion mechanism: in the engine, although flame quenching is occurring in places of local flame elements, when the confined space of the combustion chamber is filled with the numerous vortices, there are opportunities for quenching zones to restart the combustion, being entrained into burning zones by the vortices. Turbulence with scales of sub-millimeters affect the structure of a local flame surface, and are able to increase a turbulent burning rate. On the other hand, the vortices with scales ranging from a few mm to 10 mm are able to mix the field of combustion more effectively than the turbulence.

For contemplating the above-mentioned issues and ideas, it is important to optimize the structure of flows in the following way: to hasten the crush of the tumble, then convert the tumble quickly into the numerous vortices and turbulence, without remaining bulk flows such as the wing-shaped vortices, and distribute the numerous vortices throughout the combustion chamber.

One measure to meet these requirements, is the tumble control piston[2]. **Fig. 12** shows results of photographing flows on the central vertical section of the

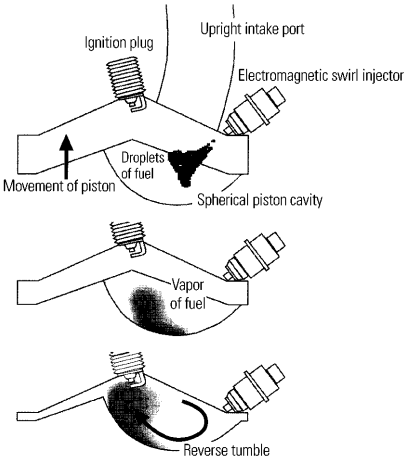

Fig. 13 Combustion control concept of GDI engine

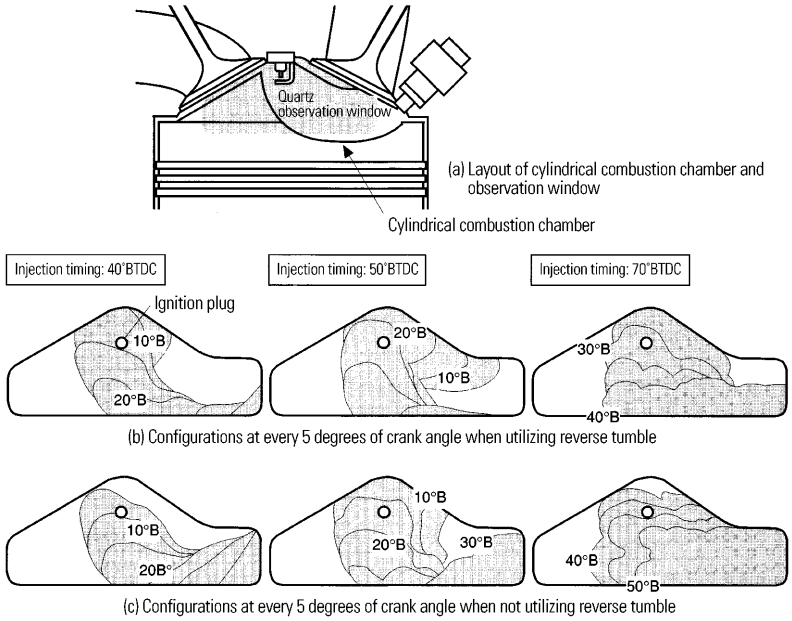

Fig. 14 Influence of reverse tumble on stratified mixture motion (bore x stroke: 85 x 88 mm, 1000 min^{-1}; WOT; air excess ratio: 2.3; inj. timing: 40°, 50°and 70°BTDC; with shadowgraphy)

cylinder by a laser sheet method. At 45 degrees before the top dead center, the gyrating structure of the tumble remains in the case of the usual piston, whereas it appears that the crush of the tumble has already started in the case of the tumble control piston. No gyrating flow could be found and, therefore, a flow in the vicinity of the ignition plug is suppressed with the tumble control piston. It is also assumed that, due to the collision of an upward flow along the top of the tumble control piston to the ceiling of the combustion chamber, the generation of turbulence is promoted. As a result of the suppression of misfire and the activation of combustion by these effects, a lean limit of combustion could be extended.

4. Phenomena design of GDI engine

In combustion control for a direct injection gasoline engine, under a premise of enabling the formation of both a uniform air-fuel mixture and a stratified mixture, it is important to realize the controlled mixture stratification of providing the appropriately rich mixture within a limited place of the vicinity of the ignition plug and at a limited time of the ignition timing. **Fig. 13** shows a combustion control concept, based on which the GDI engine was developed[3]. Utilizing upright intake ports, a swirl injector and the spherical cavity of the piston, and by placing the injector and the ignition plug apart from each other, the mixture stratification was successfully realized. Fuel is injected into the cavity of the piston while the piston is moving upward during the latter half of the compression stroke. The shape of the cavity is so designed that, utilizing the motion of a fuel spray rebounding from the cavity wall and air flows generated by the spray motion, the fuel is guided to the ignition plug. The upright ports form a gyrating flow named "reverse tumble", which gyrates in the reverse direction to that of the tumble. The reverse tumble travels in the same direction as the fuel spray traveling to the ignition plug, and assists in transporting the fuel to the ignition plug. As mixing of the air and fuel progresses along the long path from the injector to the ignition plug, the air-fuel mixture in the vicinity of the ignition plug is suppressed from becoming too rich.

To attain uniform air-fuel mixing, fuel is injected at an appropriate timing during the first half of the intake stroke. The fuel spray follows the piston moving downward, so that the spray will not collide with the piston. By the penetration of the spray toward an expanding space as the piston moves downward, the fuel spreads to the entire space in the cylinder.

Requirements for the shape of the fuel spray are different between the cases of the formation of the uniform mixture and the stratified mixture. In the case of the uniform mixing, it is necessary to form a widely spreading shape in the cylinder, and, in the case of the mixture stratification, a compact shape that could be kept in the cavity is required. The swirl injector alone could conform to these requirements by making good use of a difference between air densities at the injection timings[3].

In the following sections, diagnostic results in the case of the mixture stratification will be shown. In addition, a model of in-cylinder combustion worked out, based on these results and the earlier-mentioned results from the premixed lean-burn gasoline engine, will be described. New combustion control methods which were worked out, starting from this combustion model, and by utilizing multiple fuel injection inherent in direct injection, will be also introduced.

4.1 Characteristics of air-fuel mixing

Fig. 14 shows visualized results of the behavior of the fuel spray and air-fuel mixture by the shadowgraph

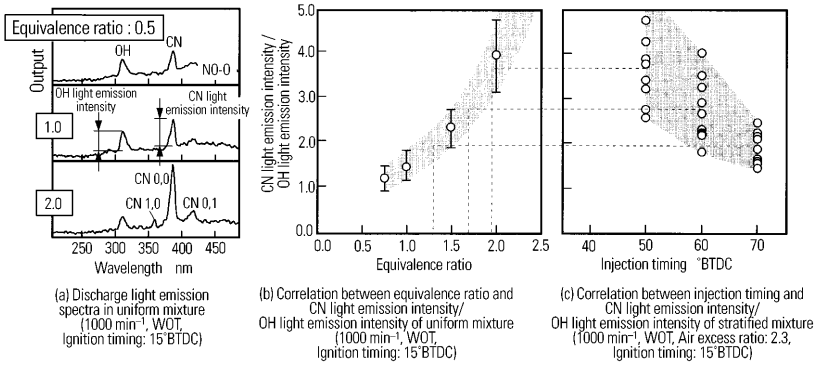

(a) Discharge light emission spectra in uniform mixture (1000 min^{-1}, WOT, Ignition timing: 15°BTDC)

(b) Correlation between equivalence ratio and CN light emission intensity/ OH light emission intensity of uniform mixture (1000 min^{-1}, WOT, Ignition timing: 15°BTDC)

(c) Correlation between injection timing and CN light emission intensity/ OH light emission intensity of stratified mixture (1000 min^{-1}, WOT, Air excess ratio: 2.3, Ignition timing: 15°BTDC)

Fig. 15 Mixture strength measurement at spark plug using discharge light emission spectra

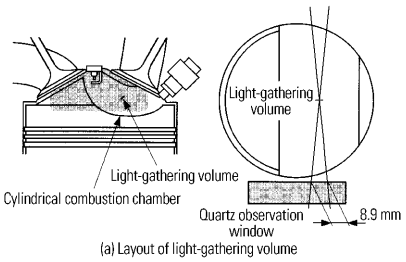

(a) Layout of light-gathering volume

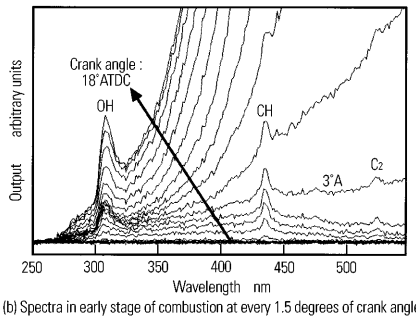

(b) Spectra in early stage of combustion at every 1.5 degrees of crank angle

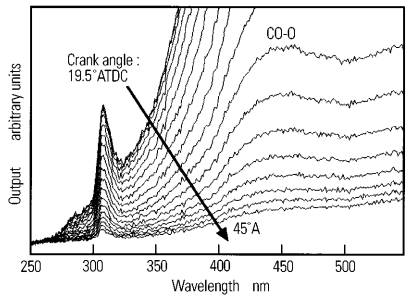

(c) Spectra in latter stage of combustion at every 1.5 degrees of crank angle

Fig. 16 Local light emission spectra of stratified mixture flame in GDI engine (1000 min^{-1}; WOT; air excess ratio: 2.0; inj. timing: 50°BTDC; ig. timing: 15°BTDC)

method, using the high-speed video camera. The figure shows the configurations at every 5 degrees of the crank angle, in comparison between the cases of utilizing the reverse tumble and not utilizing it. In order to provide access to phenomena in the cavity, it was necessary to change the shape of the cavity from a spherical hollow to a cylindrical indentation. When the reverse tumble is formed and the ignition timing is set at 15 degrees before the top dead center, the delay limit of the injection timing, at which the injected fuel is able to reach the ignition plug by the ignition timing, is 40 degrees before the top dead center. The advance limit, at which the injected fuel could be captured within the cavity, is 70 degrees before the top dead center. By setting the injection timing between these crank angles, the intended mixture stratification could be realized. When the reverse tumble is not formed, a range of the injection timing becomes narrower. The fuel injected at 40 degrees before the top dead center will not reach the ignition plug by the ignition timing, and the fuel injected at 70 degrees before the top dead center will diffuse outward the cavity.

If mixture formation rely only on the motion of a fuel spray, an imbalance between the momentum of the spray, which is constant regardless of the engine revolution speed, and the momentum of flows, which increases almost in proportion to the revolution speed, may narrow a range of the revolution speed within which appropriate mixture formation could be realized. This concept, on the other hand, realizes the intended mixture formation in a wide range of the engine revolution speed, because, although the motion of the fuel spray rebounding from the cavity wall and air flows induced by the spray motion, become the main factors, a contribution of the reverse tumble to the mixture formation increase as the engine revolution speed increases.

Fig. 15 (a) shows instantaneous spectra distributions of the discharge light emission that follows the spark ignition in uniform air-fuel mixtures. The discharge light emission consists mainly of light emissions of OH radical, CN radical and NO-O recombination. The figure shows, the spectra at the moment when the light emission of CN radical reaches the peak, selected from data at every 0.5 degrees of the crank angle. In analysis of the spectra at this moment, a clear correlation between the equivalence ratio of the mixture and the ratio of light emission intensities of CN radical and OH radical, as shown in **Fig. 15 (b)**. **Fig. 15 (c)** shows a result, by applying this correlation to stratified mixtures, of estimating the local equivalence ratio at the spark plug. When the injection timing is advanced from 50 degrees to 70 degrees before the top dead center, the local equivalence ratio decreases from 1.9 to 1.3 on average. It becomes clear that a degree of the mixture stratification could be controlled by changing the injection timing.

The fact that the intended mixture formation could be realized in a wide range of the injection timing and the revolution speed, and that a degree of the mixing could be controlled, confirms that the combustion control concept has a high degree of freedom of mixing.

4.2 Characteristics of combustion

Fig. 16 shows spectra distributions of local flame light emission at every 1.5 degrees of the crank angle. Although the flame light emission is governed mainly by a light emission of OH radical and thermal radiation from soot generated in rich parts of the mixture, when

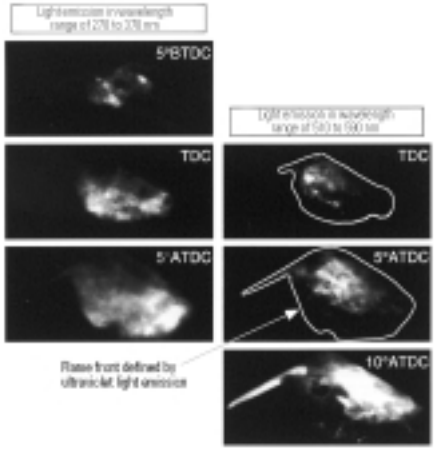

Fig. 17 Propagation of stratified mixture flame in GDI engine (1000 min^{-1}; WOT; air excess ratio: 2.0; inj. timing: 40°BTDC; ig. timing: 15°BTDC)

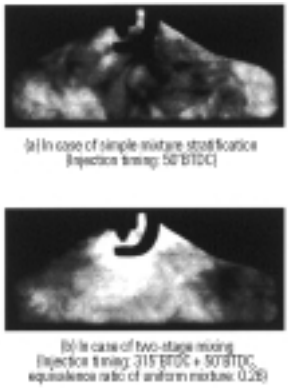

Fig. 18 Soot clouds in latter stage of expansion stroke (1000 min^{-1}; medium load; air excess ratio: 0.95; inj. timing: 50°BTDC for simple stratified mixing and 315°BTDC + 50°BTDC for two-stage mixing; with light extinction method)

the flame front passes through the measuring point, light emissions of CH radical, C_2 radical and CO-O recombination could be recognized. The light emission of CO-O recombination is also recognized in the latter stage of combustion, together with the thermal radiation.

Fig. 17 shows simultaneously visualized data of the light emission in an ultraviolet wavelength range of 270 to 370 nm, most of which consists of the light emissions of OH radical and CO-O recombination just behind the flame front, and the light emission in a visible wave length range of 510 to 590 nm, the main component of which is the thermal radiation. The first flame front, defined by the ultraviolet light emission, rapidly propagates throughout the combustion chamber, and then the second luminus flame, accompanied by the thermal radiation, propagates toward an area behind the first flame front. In the macroscopic view, a flame in a usual gasoline engine propagates toward a air-fuel mixture, and a luminus flame in a diesel engine propagates toward the air surrounding a fuel spray. However, the second luminus flame in the direct injection gasoline engine, propagates toward the area filled with not only the air and fuel, but also various radicals and CO generated by the first flame. Soot generated in a local rich mixture will burn up in this activated area. This mechanism of combustion is considered to play an important role in activating the burn-up of the soot and completing the combustion.

4.3 Combustion control utilizing freedom of mixing

In a simple combustion system, steps of combustion such as vaporization of fuel, air-fuel mixing, low temperature oxidation reaction, e.g. isomerization or peroxidization, thermal ignition, reation toward thermal equilibrium and burn-up of soot, progress in this sequence. Products generated at one step are separated from those at another step time-wise as well as space-wise. However, in an engine, as shown so far, products at a step frequently meet those at an earlier or later step and are mixed. The author et al. named this mechanism of mixing "Time Domain Mixing". This mechanism is considered essential for describing combustion in an engine.

By adopting the direct injection technology, it has become possible for a gasoline engine to provide various conditions of mixing. Either a uniform mixture or a stratified mixture could be appropriately used, or a degree of the mixture stratification could be controlled by changing the injection timing. By dividing fuel injection into multiple times, a condition of both a uniform mixture and a stratified mixture combined could be realized. The principal advantage of a direct injection engine is the freedom of mixing.

Considering the time domain mixing as the starting point, and by contemplating what kind of mixing condition, and what kind of accompanying combustion could be realized by utilizing the freedom of mixing, new combustion control methods named "two-stage mixing" and "two-stage combustion" were achieved.

The two-stage mixing is a method to suppress knocking, which is realized by performing fuel injection twice, first during the early half of the intake stroke and second during the latter half of the compression stroke, in order to place a stratified mixture inside a very lean uniform mixture[14]. The uniform mixture is lean beyond the lean limit of self-ignition. For the stratified mixture formed immediately before the combustion, there is not enough time to proceed to self-ignition. This is effective for advancing the ignition timing under a condition of low engine revolution speed and high load. What is noted is a fact that, in spite of burning the stratified mixture without any excess air, no soot is emitted. **Fig. 18** shows soot clouds in the combustion chamber visualized by the light extinction method, in comparison between cases of the simple mixture stratification and the two-stage mixing. By the two-stage mixing, the residual soot at the latter stage of the expansion stroke is drastically reduced. It is assumed that a mechanism of combustion exists in which the soot generated in the stratified mixture becomes stable ignition sites that leads even the very lean mixture to

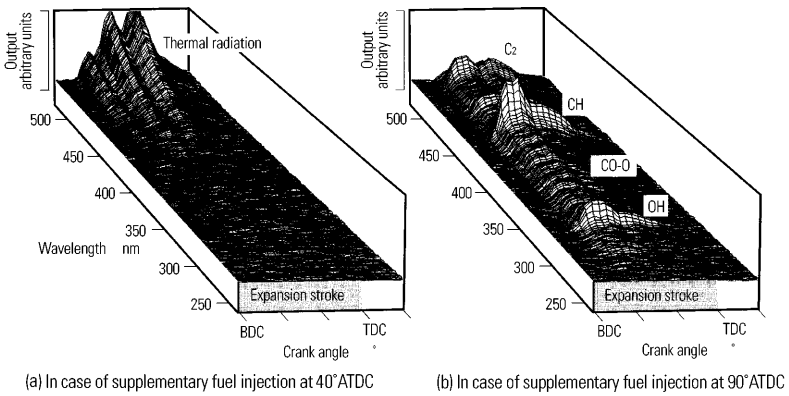

(a) In case of supplementary fuel injection at 40°ATDC (b) In case of supplementary fuel injection at 90°ATDC

Fig. 19 Light emission spectra of flame in exhaust port with two-stage combustion (1000 min^{-1}; WOT; air excess ratio of main combustion: 2.3; inj. timing of main combustion: 55°BTDC; ig. timing: 5°BTDC; total air excess ratio: 1.0; supplementary inj. timing: 40°ATDC and 90°ATDC; 140 mm downstream of exhaust valves; gates at 10°crank angle intervals)

ignition, and the soot burns up rapidly, supported by the combustion of the lean mixture.

The two-stage combustion is a method to warm up a catalyst quickly by providing a burned gas of a stratified mixture, which contains much residual oxygen, and by igniting the fuel supplemented during the latter half of the expansion stroke in the burned gas to raise a temperature of the exhaust gas[15]. The combustion of the supplemented fuel proceeds in the cylinder to the exhaust passage. When the fuel is supplemented during the early stage of the expansion stroke, a significant amount of soot is generated and emitted; however, by supplementing the fuel during the latter stage, the soot emission could be suppressed.

Fig. 19 shows light emission spectra of a flame belched into the exhaust port, collected at the gate of every 15 degrees of the crank angle. Although the flame light emission, in the case of the fuel being injected during the early stage of the expansion stroke, is governed by thermal radiation from the soot, when the fuel is injected during the latter half, the flame light emission is composed mainly of light emissions of OH radical, CH radical, C_2 radical and CO-O recombination. In the case of the fuel injection during the early stage, the fuel injected into a residual flame immediately ignites. In the case of the fuel injection during the latter half, ignition of the fuel occurs through slow precombustion reaction in the burned gas that has an appropriately high temperature. It is assumed that, under nonuniformity of concentration and temperature in the cylinder and slow precombustion reaction, a condition is realized in which products at each step of combustion coexist and, in this condition, the soot rapidly burns up.

5. Summary

When contemplating, as a whole, the findings of the phenomena in the premixed lean-burn gasoline engine and the direct injection gasoline engine, clarified by utilizing the results of the phenomena diagnostics, and a question of why an engine could sustain combustion even under a condition of a high engine revolution speed approaching 10000 min^{-1} where the turbulence intensity would presumably become some 10 times higher than that at a low engine revolution speed[16], it is indispensable to describe the phenomena by the time domain mixing.

An important matter for the evolution of a gasoline engine in the future is finding out new requirements of flow or mixing, taking the time domain mixing as a premise. For this purpose, it is important to further sharpen insight into in-cylinder phenomena, by utilizing information obtained by diagnostic technologies.

References

(1) Kiyota, et al.: Concept of Lean Combustion by Barrel Stratification, SAE Paper 920678 (1992)
(2) K. Kuwahara, et al.: Optimization of In-Cylinder Flow and Mixing for a Center-Spark Four-Valve Engine Employing the Concept of Barrel-Stratification, SAE Paper 940986 (1994)
(3) T. Kume, et al.: Combustion Control Technologies for Direct Injection SI Engine, SAE 960600 (1996)
(4) D. L. Reuss, et al.: Instantaneous Planar Measurements of Velocity and Large-Scale Vorticity and Strain Rate in an Engine Using Particle-Image Velocimetry, SAE Paper 890616 (1989)
(5) K. Kuwahara, et al.: TDC Flow Field Structure of Two-Intake-Valve Engines with Pentroof Combustion Chamber, JSME International Journal, Series B, Vol. 36, No. 4, p. 688 – 696 (1993)
(6) Kuwahara, et al.: Three-Dimensional In-Cylinder Flow Field Structure Measurement by Three-Color Laser Light Sheet Method (in Japanese), Proceedings of 11th Internal Combustion Engine Symposium, p. 567 – 572 (1993)
(7) Takeharu Eto: High Speed Video Camera of 4500 pps (in Japanese), Journal of the Institute of Television Engineers of Japan, Vol. 46, No. 5, p. 543 – 545 (1992)
(8) Kawai, et al.: Statistical Analysis of Leanburn Flame Behavior by Random Access Large Scale Image Data Base (in Japanese), Proceedings of 69th Kansai Branch Annual Meeting, JSME, p. 211 – 213 (1994)
(9) Kuwahara, et al.: Mixture Formation and Flame Propagation in a Gasoline Direct Injection Engine (in Japanese), Internal Combustion Engine Symposium Proceedings, p. 115 – 120 (1997)
(10) Kuwahara, et al.: A Study of Combustion Characteristics in a Direct Injection Gasoline Engine by High-Speed Spectroscopic Measurement (in Japanese), Proceedings of 13th Internal Combustion Engine Symposium, p. 145 – 150 (1996)
(11) K. Kuwahara, et al.: Time-Series Spectroscopic Analysis of the Combustion Process in a Gasoline Direct Injection Engine, Proceedings of 4th International Symposium on Internal Combustion Diagnostics, AVL, p. 131 – 136 (2000)

(12) K. Kuwahara, et al.: Analysis of Barrel-Stratified Lean Burn Flame Structure by Two-Dimensional Chemiluminescence Measurement, JSME International Journal, Series B, Vol. 37, No. 3, p. 650 – 658 (1994)
(13) K. Kuwahara, et al.: Influence of Flow Field Structure after the Distortion of Tumble on Lean-Burn Flame Structure, Proceedings of International Symposium COMODIA94, p. 89 – 94 (1994)
(14) K. Kuwahara, et al.: Mixing Control Strategy for Engine Performance Improvement in a Gasoline Direct Injection Engine, SAE Paper 980158 (1998)
(15) K. Kuwahara, et al.: Two-Stage Combustion for Quick Catalyst Warm-up in Gasoline Direct Injection Engine, Proceedings of International Symposium COMODIA98, p. 293 – 298 (1998)
(16) Yasuhiko Ota: Probable Approaches to Innovative Engine Combustion (in Japanese), No. 12-00 Symposium, JSAE (2000)

Kazunari KUWAHARA

Sensibility Analysis of Vibration Transfer Path and Control of Input Force for Reduction of Acceleration and Deceleration Shock

Tadashi TAKEUCHI* Kyoung-Gon CHOI*
Shoji KAN* Kazuhide TOGAI*

Abstract

In order to reduce acceleration and deceleration shocks, a new method of designing optimized vibration transfer path as well as control of the source of generating vibration torque, using a virtual vehicle, has been studied. Vibration sensibility corresponding with the change of design parameters has been examined using a mechanical system simulation software, which enables a model of the major parts in the vibration transfer path to be created, reflecting their three-dimensional position information. A control system for removing vibration-generating components from the engine torque has been adopted, using command shaping based on the vibration prediction model. The vibration suppressing effects of the method proposed here have been investigated by simultaneous simulations of the vehicle mechanical system model and the engine control model, as well as by actual vehicle testing.

Key words: *Acceleration and Deceleration Shocks, Mechanical System Simulation Software, Vibration Sensibility Analysis, Compensator, Command Shaping, Model-Based Prediction*

1. Introduction

When an accelerator is rapidly depressed for acceleration, torque is produced in a stepped manner such that unpleasant shock can be felt. One realistic countermeasure, which can be taken in a vehicle that has an automatic transmission, is to minimize vibration by employing a torque converter in which lockup does not take place.

Another realistic countermeasure, which can be taken if the vehicle has an electronically throttle, is to avoid rapid torque delivery by opening the throttle valve slowly. Unfortunately, these countermeasures are not ideal with regard to fuel economy (which is affected by transmission efficiency) and acceleration performance.

Vibration-reducing solutions become easier to conceive if the issue of vibration-generating sources and the issue of transfer path sensibility are considered separately. Also, it becomes possible to clarify whether it is more beneficial to focus countermeasures on vibration-generating sources or on the vibration transfer path if different frequencies are considered separately. The results can be used for design optimization not only in the early stages of a vehicle's development but also later in the development process.

Acceleration and deceleration shock is caused mainly by the powerplant's torsional vibration and has low frequencies in the order of 2 – 10 Hz, but it differs from typical powertrain noise, vibration, and harshness phenomena in that it is a transient phenomenon that occurs within a few seconds. As a phenomenon, it is similar to a robot manipulator or a crane (each a motion control system in which an endpoint mass is attached to a flexible arm); vibration-suppressing methods used with robot manipulators and cranes are valuable for reference. Given that electric motors and internal combustion engines operate according to different principles, however, it is essential to take into account the relatively large torque-generation dead time that occurs with an internal combustion engine.

Sensibility analysis of the vibration transfer path employing a mechanical system model and a proposed engine torque control method based on the model are described in this paper for the purpose of powertrain vibration suppression.

2. Sensibility analysis of vibration transfer path using mechanical system model

2.1 Passenger car acceleration vibration transfer path model

In a passenger car, an engine and tires (these represent relatively large inertia moments) are located at the ends of driveshafts and act as a mass-spring kinetic system that is supported by the suspension and engine mountings (**Fig.1**, **Fig.2**). The driveline's torsional vibration makes a significant contribution to acceleration shock[1][2].

A vibration transfer path model was constructed from a drive system torsion model, which covers the

* Powertrain Dev. Dept., Car Research & Dev. Office, MMC

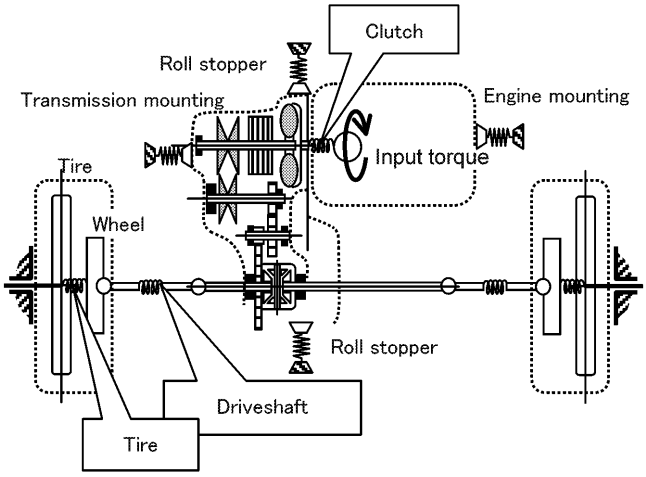

Fig. 1 Powertrain elements

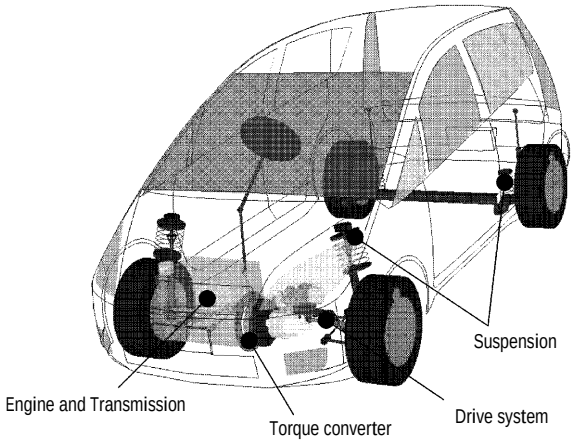

Fig. 3 Appearance of powertrain model

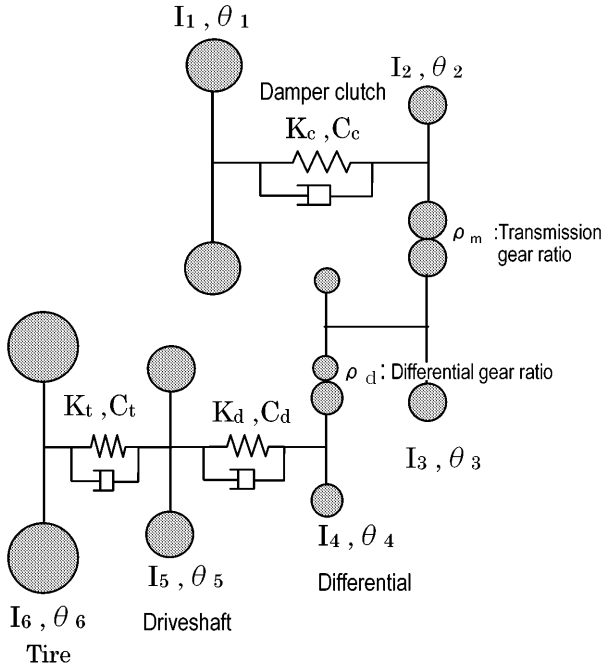

Fig. 2 Drive system torsion model

drive system in terms of the engine, transmission, and tires, and a vehicle dynamic model, which takes into account the mountings and suspension components that transmit the drive system's torsional vibration to the body. The constructed model is a two-dimensional nonlinear model with a total of 10 degrees of freedom. The flywheel, gears, and tires each have one degree of freedom; the suspension has one degree of freedom; and the powerplant and rigid body each have three degrees of freedom (longitudinal, vertical, and rotational)[(2)]. The matrix equation (with damping factors taken into account) is as follows:

$$[M]\{\ddot{X}\}+[C]\{\dot{X}\}+[K]\{X\}=\{F\} \quad (1)$$

where
[*M*]: 10 x 10 inertia matrix
[*C*] : 10 x 10 damping matrix
[*K*] : 10 x 10 stiffness matrix
{*F* } : 10 x 1 force vector
{*X* } : 10 x 1 displacement vector

2.2 Vehicle mechanical system analysis model

The vibration transfer path of a vehicle is basically a multi-body structure with a mass-spring configuration, but it is distributed in three dimensions. Transfer characteristics are significantly influenced not only by the coupling relationships of elements but also by the spatial configuration of elements (particularly the mountings and other support points). These factors can, of course, be described by means of equations of motion, but directly reflecting the positional relationships on an actual vehicle in equations of motion is not an easy task. A vehicle mechanical system model for the COLT was constructed using ADAMS mechanical system simulation software. If this model is used to express motion, it is possible to describe the factors without being concerned about the complex relationships between the coefficients of co-ordinates and expressions; intuitive expression of the vehicle in three dimensions is possible, so verification of positional relationships is easy. Consequently, the model has the merit of enabling computation with constraints to be performed efficiently when mounting-position revisions are included in optimization parameters.

2.3 Simulation results

Simulation results can be expressed in the form of three-dimensional moving animations, and behavior at user-selected co-ordinate points in the vehicle model can be observed. Results for longitudinal acceleration and vertical acceleration at the seat-riser position during operation of the accelerator pedal by the driver in a stepped (tip-in/tip-out) manner are shown in **Fig. 4**. Here, the vehicle's longitudinal vibration with the torque converter's damper clutch locked up can be compared with the vehicle's longitudinal vibration with the

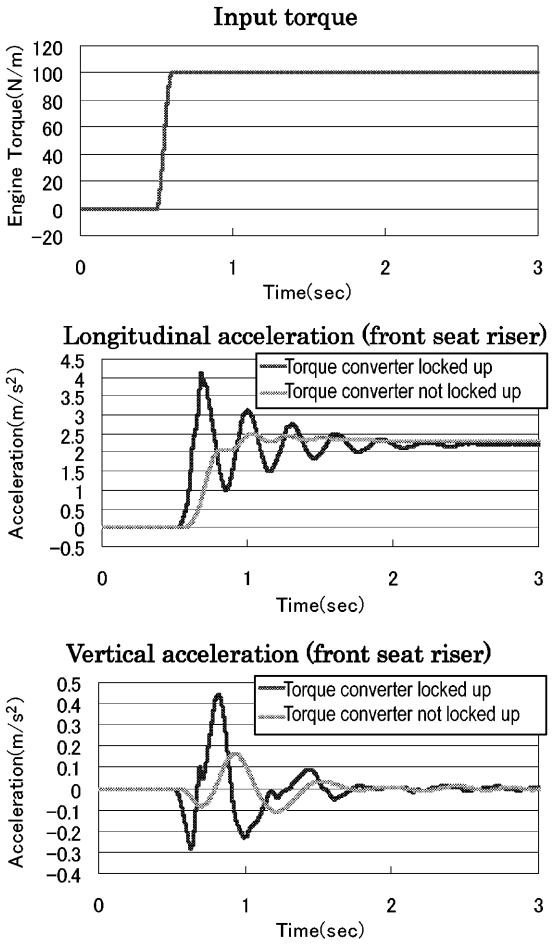

Fig. 4 Tip-in/tip-out analysis

Table 1 Vibration reduction measures: effects and limitations of elements

Vibration reduction method	Components and characteristics	Limitations
Alteration of fundamental resonant frequency; reduction of amplitude	Increase in driveshaft stiffness	Increased weight; cost
Addition of low-pass filter; addition of damping	Prevention of damper clutch lockup	Reduced fuel efficiency
Reduction of amplitude	Increase in powerplant mounting stiffness; alteration of powerplant mounting locations	Increased idling vibration; increased booming noise; increased sensibility of road-surface inputs

torque converter's damper clutch not locked up.

2.4 Sensibility analysis

Using the mechanical system analysis model, it is relatively easy to perform transfer sensibility analysis with respect to parameters including positions.

For the tip-in/tip-out example, the qualitative effects and limitations of elements with respect to vibration transfer are shown in **Table 1**. The results of parameter studies performed for the purpose of reducing vehicle longitudinal vibration are shown in **Figs. 5** – **7**. Even with components that cannot be made the prototype

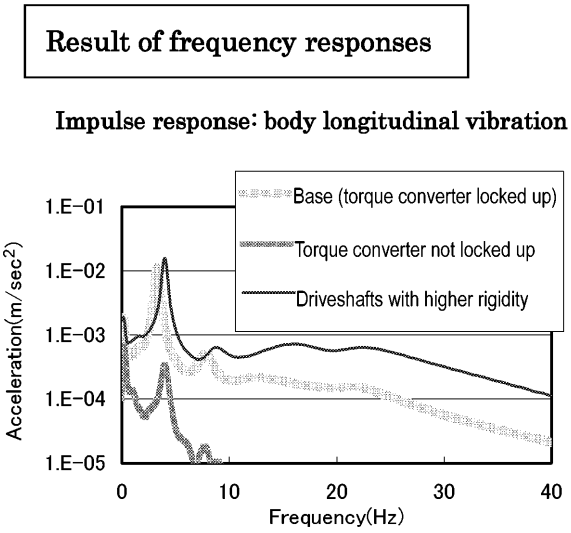

Fig. 5 Results of parameter study (1)

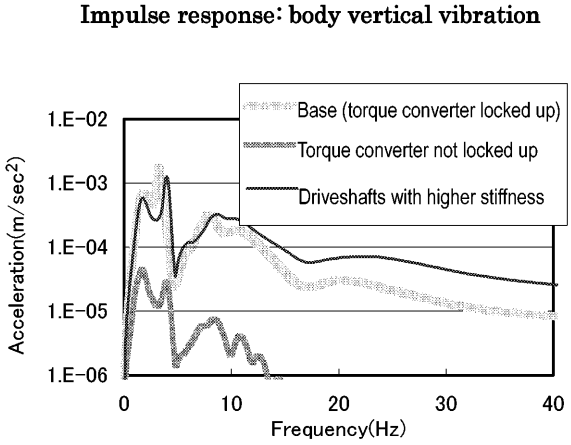

Fig. 6 Results of parameter study (2)

easily unless time is devoted to prototype trials, parameter studies performed using the mechanical system model enable optimal component characteristics for the goal of the analysis to be derived. In addition, the effects of those characteristics on factors other than the goal of the analysis (in this example, the effects of tip-in/tip-out optimization on idling vibration and booming noise) can be determined.

3. Vibration-suppressing control of vibration-generating sources

Vibration can be reduced if components that are amplified in the vibration transfer path are removed from the engine's output torque waveform (a vibration-generating source). Online vibration model predictions based on a driver's accelerator inputs were used to create an algorithm that generates engine output torque targets for the purpose of suppressing vehicle vibration without detracting from acceleration feel.

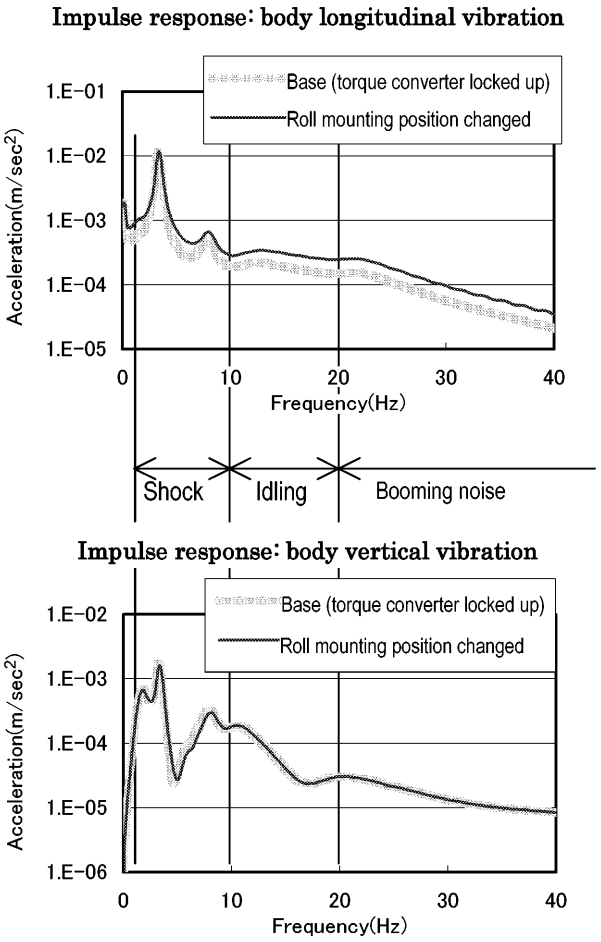

Fig. 7 Results of parameter study (3)

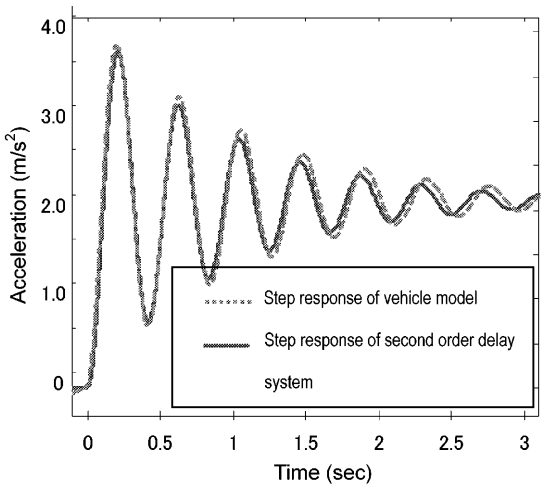

Fig. 8 Approximation of high-order system by second-order system

3.1 Reduction of order of model

Although torque produced by the engine is manifested as body longitudinal vibration via a complex transfer path, the output waveform of body longitudinal acceleration (or driveshaft angular acceleration) resulting from stepped torque variations can, because of its characteristics, be approximated as a second-order delay system (**Fig. 8**). Using the body longitudinal acceleration transfer function $G(s)$, approximation is possible using the following equation:

$$G(s) \approx \frac{K_p \cdot \omega_n^2}{s^2 + 2\varsigma\omega_n s + \omega_n^2} \quad (2)$$

Here Kp is proportional gain, and ς and ω_n are the body longitudinal vibration's damping coefficient and natural resonance frequency (basic order), respectively.

3.2 Study of engine torque control method

A multi-body system consisting of multiple springs and mass points (as seen in, for example, a robot manipulator) is similar to the transfer path of an automobile powerplant. With regard to control of this kind of system, a two-degree-of-freedom control system has been proposed as a benchmark problem for robust control[3]. Despite the similarity in terms of transfer pathes, the use in an automobile of an internal combustion engine (rather than an electric motor) as a torque source means that the effects of dead time caused by stroke delay must be taken into account in design of control arrangements. (**Fig. 9**).

With a reciprocating internal combustion engine, there is a mechanical delay between a control action and torque generation because torque generation takes place following the intake, compression, and expansion strokes. If the engine has four cylinders, the delay is approximately 1.5 revolutions (approximately 75 ms at 1,200 rpm). With respect to 5 Hz vibration, 1/4 of a cycle equates to a delay of 50 ms. Also, with regard to the engine speed, variations occur within 1/2 of a revolution, meaning that the engine speed is not established until 1/2 of a revolution is completed. These factors together mean that there is a delay of approximately two revolutions, so a control based mainly on feedback is difficult to achieve. Damping achievable by means of speed feedback was investigated with respect to a simple second-order vibration system with a damping coefficient ζ of 0.1 and with the ratio of dead time to vibration frequency treated as an index (**Fig. 10**). Increases in dead time were accompanied by decreases in the effectiveness of feedback, indicating that vibration cannot be suppressed by means of feedback alone.

3.3 Compensator configuration: command shaping[4][5]

With a system that is prone to be oscillatory, vibration is excited when there are vibration frequency components in the input. The control problem was considered in terms of command shaping (application of target commands to prevent vibration without any effect on target performance).

3.3.1 Filter-type compensator (frequency domain realization)

With a model of a motion control system that is prone to be oscillatory, the transfer function has ampli-

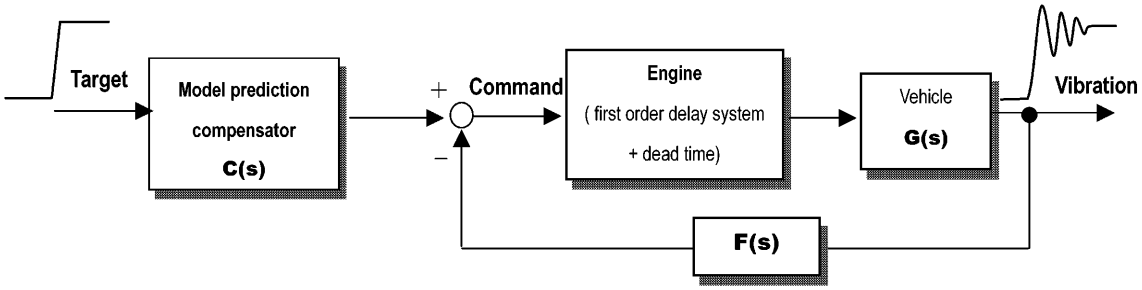

Fig. 9 Concept of Engine torque control

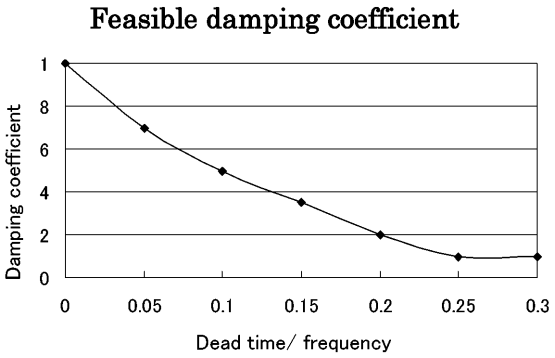

Fig. 10 Equivalent dead time and feasible damping

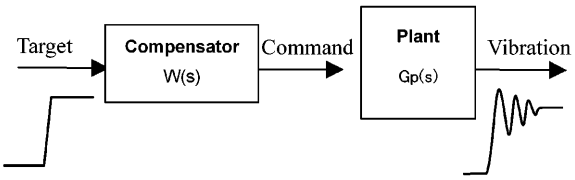

Fig. 11 Command shaping compensator

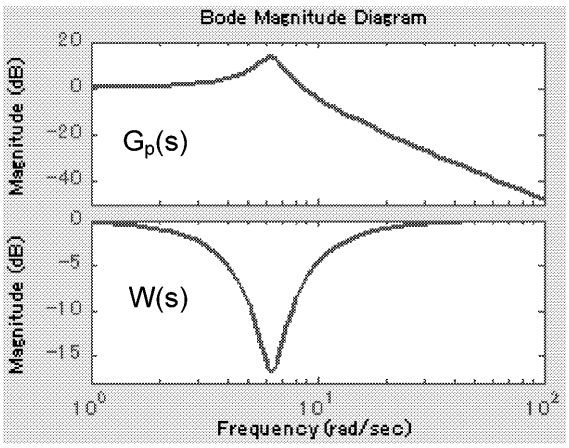

Fig. 12 Compensation by filter

tude peaks at resonant frequencies in the frequency response. A preliminary compensator was considered as a means of reducing the amplitude peaks to realize desirable frequency characteristics. A bandpass filter capable of reducing resonant frequencies can be realized by means of a finite impulse response (FIR) filter or infinite impulse response (IIR) filter. If the denominator of the transfer function of the plant is cancelled by the numerator, desirable characteristics can be substituted[6][7] (**Fig. 12**).

Plant transfer function: $$G_p(s) = \frac{K\omega_p^2}{\left(s^2 + 2\zeta_p\,\omega_p\,s + \omega_p^2\right)}$$

Compensator transfer function:

$$W(s) = \frac{\omega_m^2\left(s^2 + 2\zeta_p\,\omega_p\,s + \omega_p^2\right)}{\omega_p^2\left(s^2 + 2\zeta_m\,\omega_m\,s + \omega_m^2\right)}$$

3.3.2 Model predictive compensator (time domain realization)

A method for modification of target values by time domain response prediction was created. The dead time element of the plant transfer function can be relocated behind the plant by means of equivalent transformation, so dead time is not taken into account in prediction. (The phase of the vibration is shifted in proportion to the dead time, but the amplitude of the vibration is not changed.)

Since dead time is not included by the prediction compensator, various controller constructions are feasible between target and prediction. For instance, arbitrary damping can be added via pole assignment with state feedback. The relationship between accelerator operation and torque generation with an automobile engine contains nonlinearity. In such a case, a simple method for adding damping (that is, speed feedback to torque) can be constructed. In **Fig. 13**, $C(s) = 1$ and $K(s) = Ks$.

3.4 Application to suppression of acceleration vibration

3.4.1 Control targets

Acceleration targets with the compensator must satisfy the following conditions (**Fig. 14**):

(1) Shock reduction: Since the target acceleration acts

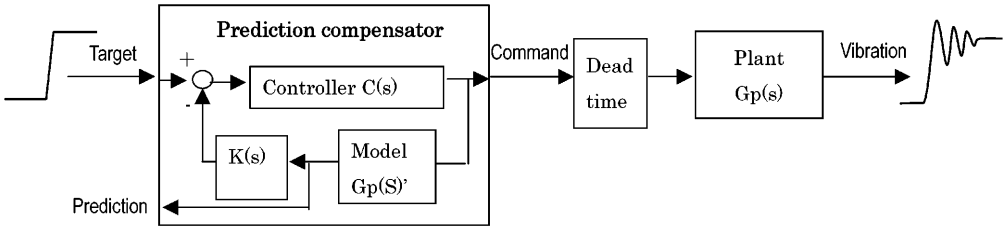

Fig. 13 Concept of prediction model compensator

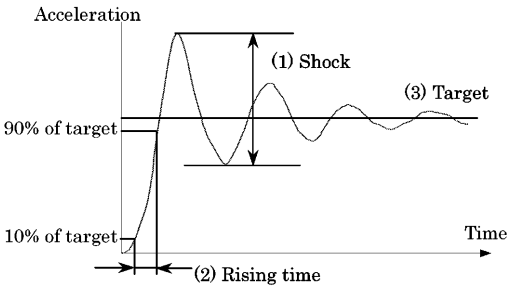

Fig. 14 Determination of acceleration target

in the negative direction (in opposition to the driver's intended acceleration), damping is required to limit its amplitude to 0.1 G (0.98 m/s^2)[8] to prevent driver discomfort.

(2) Rise time: The rise time (defined as the time from 10 % to 90 % of the target value) is a factor contributing to the acceleration feel, so it must be as short as possible.

(3) Tracking to target: This is a requirement for behavior consistent with the driver's accelerator operation. To save the driver from having to take action to compensate for inadequate acceleration targets, the acceleration resulting from the control process must, with an acceptable delay, match that indicated by every accelerator input.

3.4.2 Design of prediction model compensator

The prediction model compensator described in part 3.3.2 of this paper can be constructed with equation (2) as the prediction model. A feedback control system of the type shown in **Fig. 15** is conceivable.

The closed loop transfer function from the input signal $r(s)$ to the output signal $y(s)$ is

$$\frac{y(s)}{r(s)} = \frac{K_p \cdot \omega_n^2}{s^2 + 2\left(\varsigma + K/2\omega_n\right)\omega_n s + \omega_n^2} \qquad (3)$$

In equation (3), it is possible to place the following equation:

$$\varsigma' = \varsigma + K/2\omega_n \qquad (4)$$

By adjusting the gain K, therefore, it is possible to add new damping factor ς' to the plant (vehicle).

3.5 Simulation using online vehicle model

The effects of the compensator shown in **Fig. 15** were verified by means of simulation. To improve the profile, a complete engine performance characteristics map and delay elements were used as the engine model. Changes in the amount of air entering the cylinders in response to throttle changes (intake delays) were treated as first-order delays. They were converted into torque with a three-stroke delay from intake to the combustion stroke[9] (**Fig. 16**).

Methods for controlling torque include ignition timing control and throttle control. Ignition timing control yields excellent responsiveness, but its applicability is limited by exhaust emissions issues and by the range in which stable control is possible. Consequently, adequate controlled torque cannot be achieved with this method. Throttle control, on the other hand, allows a wide range of controllable torque. However, the air amount cannot immediately track throttle changes with this method, meaning that response is inferior to that yielded by ignition timing control. Torque control can also be achieved by control over the fuel injection amount, but this method can be applied only to engines with direct injection. In consideration of these factors, the throttle control method, which has relatively few limitations, was selected for torque control.

The vibration-suppressing effectiveness of the compensator was investigated by means of simulation. With acceleration using the highest gear ratio (the gear ratio most prone to acceleration shock), the input torque was limited to the range in which the relationship between the throttle opening and the steady-state engine torque had more or less linear proportionality. And for simplicity, the target throttle opening was applied in place of the target torque.

The input throttle opening was stepped from the idling position to the target value in a period of 0.1 s as shown in **Fig. 17**, and the vibration-suppressing effect was verified. From the results, it was seen that body longitudinal vibration was greatly reduced by insertion of the compensator (**Fig. 18**).

3.6 Influence of modeling error

The proposed compensator does not use feedback of actual signals, so it is essential that the precondition of accurate verifiability of the body longitudinal resonant frequency corresponding to each gear ratio be fulfilled. Error-induced deterioration in the compensator's performance was studied.

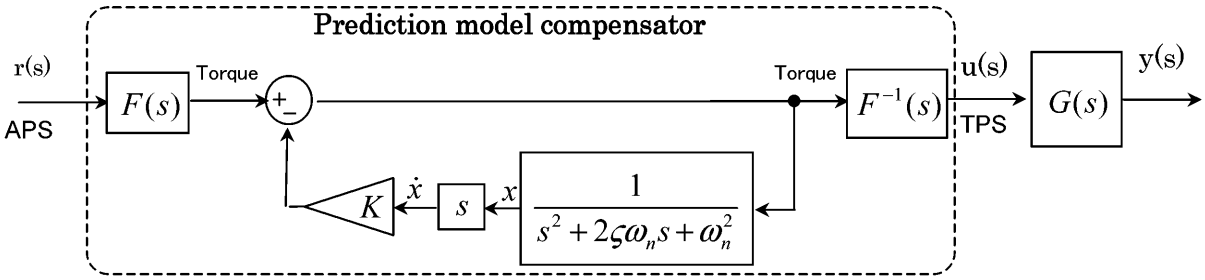

Fig. 15 Prediction model compensator

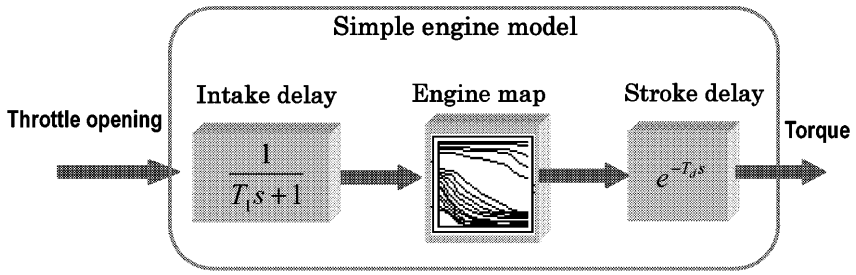

Fig. 16 Concept of simple engine model

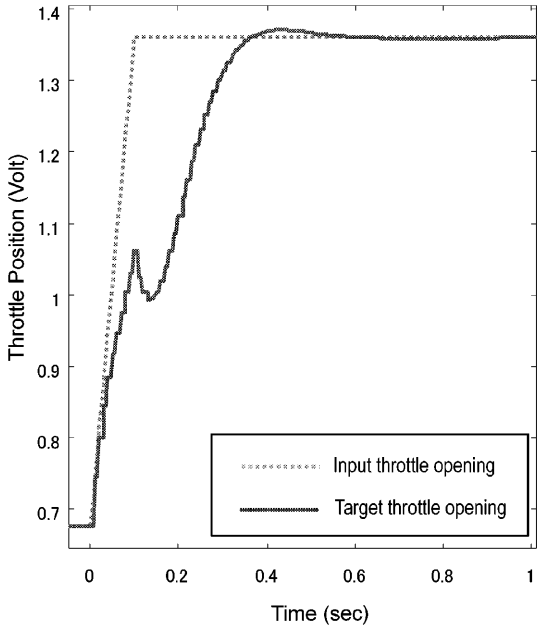

Fig. 17 Change in throttle opening

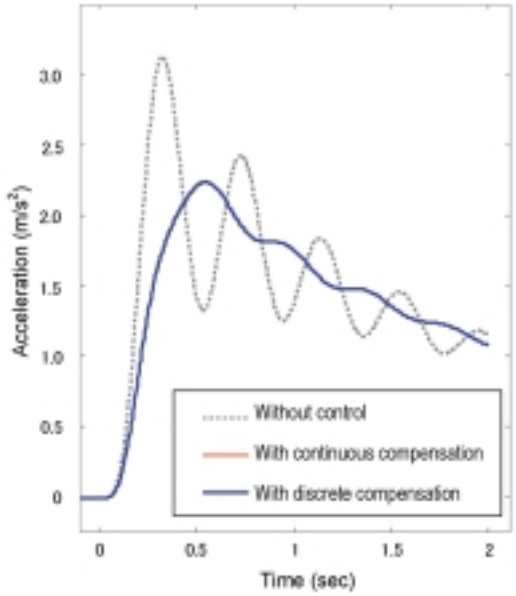

Fig. 18 Change in body longitudinal vibration

Changes in resonant frequencies resulting from an increase in vehicle weight of 260 kg (the combined weight of four passengers with an assumed weight of 65 kg each) were simulated (**Fig. 19**). Notwithstanding the influence of the weight increase on acceleration performance, the results showed that the change in resonant frequency was smaller than 2 % with each gear ratio.

Next, errors ranging from –30 % to +30 % of actual resonant frequencies (caused by measurement errors and other disturbances) were assumed and deterioration in the performance of the discrete compensator was investigated (**Fig. 20**). From the results, it was seen that deterioration in performance was, with acceleration performance taken into account, smaller with errors on the '+' side, i.e., with measured resonant frequencies higher than actual resonant frequencies. Also, it was seen that the insertion of the compensator did not make the system unstable even when there was a

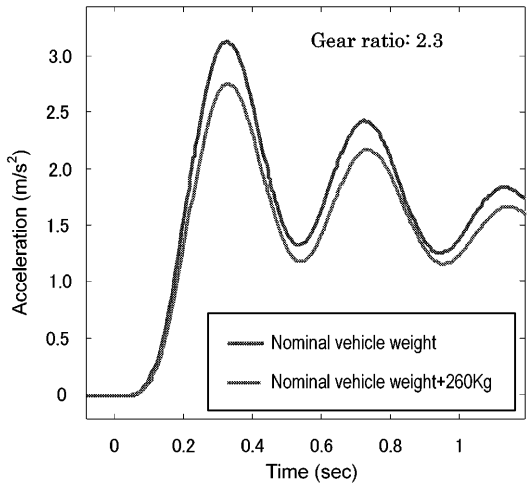

Fig. 19 Change in natural vibration

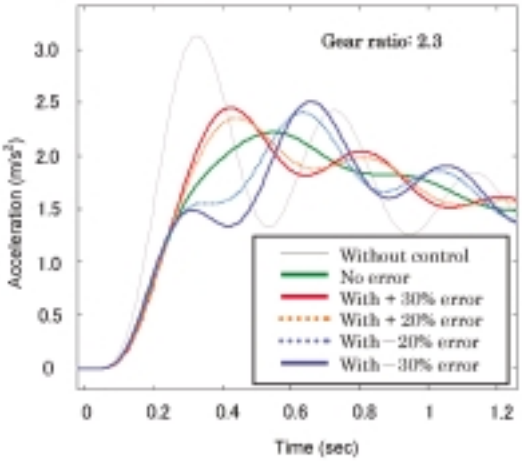

Fig. 20 Effect of vibration frequency error

considerable degree of error.

3.7 Co-simulation of mechanical system model and control algorithm

The ADAMS mechanical system simulation software constructs models from three-dimensional CAE co-ordinate information, making it possible to create a detailed vehicle model without needing to be aware of complex body dynamics. However, it is necessary to use a programming language to describe a controller that includes feedback elements, meaning that the task is not simple. On the other hand, MATLAB/Simulink is a widely used industry standard among control system design tools. Controllers are easy to describe with this tool. However, to express a complex vehicle model it is necessary to describe dynamics as a formula model, meaning that users must have extensive knowledge. An optimization study for the vehicle and controller was achieved with relative ease by means of co-simulation employing the respective merits of ADAMS and Simulink.

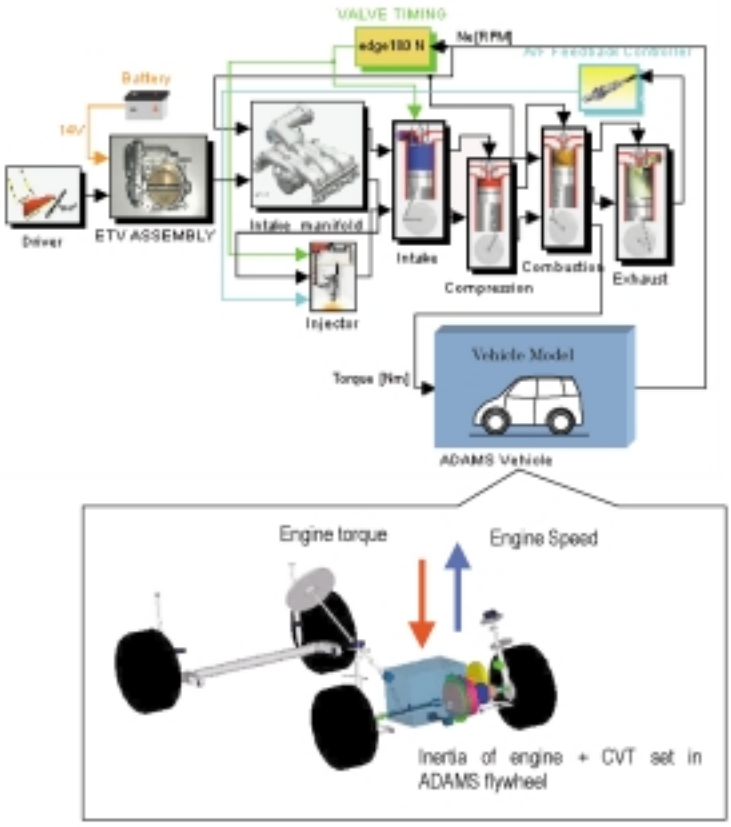

Fig. 21 Co-simulation model

3.7.1 Configuration of simulation

ADAMS/Controls was used for co-simulation. This software made it possible to represent an ADAMS-generated vehicle model as a subsystem in Simulink. The created model consisted of the driver, the controller, the engine (a detailed model), and the vehicle. The vehicle's input was the engine torque, and its output was the engine speed (**Fig. 21**).

3.7.2 Co-simulation results

Simulation results can be represented as three-dimensional moving animations using the post-processing functions of ADAMS. Also, it is possible to observe behavior at arbitrarily selected co-ordinate points of the vehicle model. By way of example, the engine torque and the longitudinal acceleration at the vehicle's center of gravity following stepped depression of the accelerator pedal by the driver are shown in **Fig. 22**.

4. Verification of vibration suppression in actual car

The effects of the control method were verified by means of tests with an actual car. The transmission was kept in its highest gear ratio (the gear in which acceleration shock is greatest (gear ratio: 2.3)). After gentle deceleration, it was confirmed that the lockup clutch was engaged, and when the engine speed reached 1,200 rpm the car was re-accelerated. At that time, the

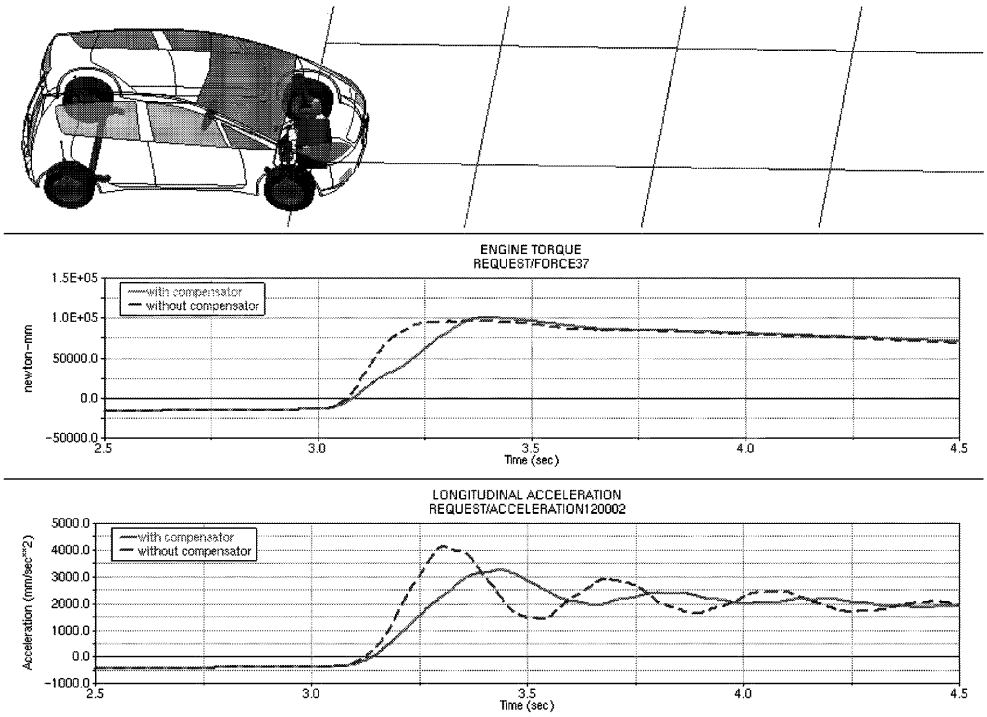

Fig. 22 Results of co-simulation

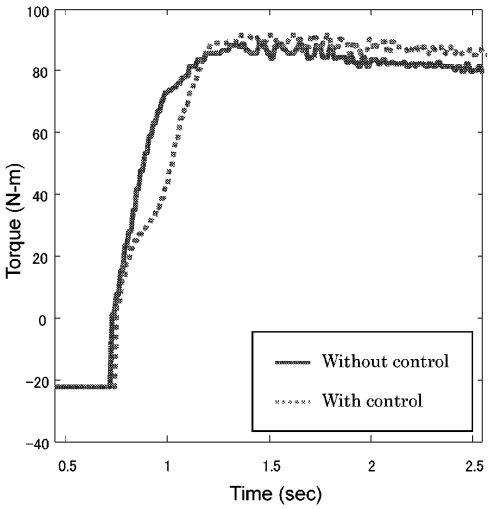

Fig. 23 Change in engine torque profile

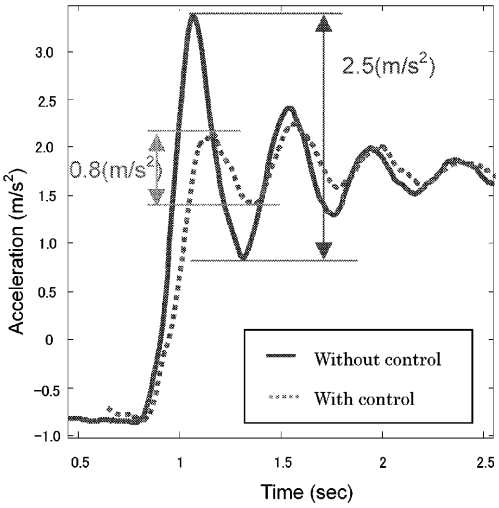

Fig. 24 Change in acceleration level

target throttle opening was determined such that the torque remained within a linear range and the accelerator pedal was operated such that the target throttle opening was achieved in a period of 0.1 s.

Fig. 23 shows the changes in engine torque, and **Fig. 24** shows the body longitudinal acceleration. From the results, it was seen that the proposed control method reduced shock to one third of its original level without detracting from acceleration performance. However, damping did not reach the target value because the target throttle opening was determined using only the torque's steady-state characteristics, meaning that time-constant changes in the amount of air flowing through the throttle when the pressure ratio (manifold pressure / atmospheric pressure) reached or exceeded the critical level were not taken into account

5. Summary

Vibration-reducing techniques were separately analyzed with respect to the issue of vibration-generating sources and with respect to the issue of transfer path sensibility, and an optimal design method was proposed. It was found that if an ADAMS mechanical sys-

tem simulation software, into which three-dimensional data during on-vehicle use can be incorporated without modification, is used for analysis of transfer path sensibility, design parameter changes and their effects can be analyzed with ease. In engine control with respect to vibration-generating sources, where dead time is significant, it was found that command shaping by means of a prediction compensator is effective. For this compensator, an algorithm that generates target output torque values from accelerator commands by means of an online vibration model was proposed.

The proposed methods were verified by means of co-simulation using an ADAMS model and a Simulink (control) model and by means of tests in an actual car. These methods' effectiveness was confirmed, so Mitsubishi Motors Corporation plans to use them in future vehicle development to concurrently meet demands for fuel economy, performance, and ride comfort.

6. Afterword

The ADAMS model was provided by Mr. Sugiura of the Dev. Planning Dept., Office of Passenger Car Dev. & Engin., Mitsubishi Automotive Engineering. Also, co-simulation using ADAMS and Simulink was made possible by co-operation from the engineering IT Dept. of Mitsubishi Motors Corporation. The authors wish to express their gratitude to everyone who co-operated with them.

References

(1) JSAE (Editor): Automotive Technical Handbook 1 (The Basics and Technology), 315/320 (1990)
(2) Furukawa, Magoshi, Tanaka: Vibration Analysis of Engine Mounting, JSAE journal, Vol. 39, No. 12, P1414 – 1421 (1985)
(3) T. Hara, et al.: Benchmark Problem for Robust Control, (I), Journal of SICE, Vol. 34, No. 5 & No. 6, 403/409 and 498/507 (1995)
(4) Lila French et al.: An Expert System for The Design of Input Shapers, Proceedings of the 1999 IEEE 713/718
(5) Derek Lewis et al.: Comparison of Command Shaping Controllers for Suppressing Payload Sway in a Rotary Boom Crane, Proceedings of the 1999 IEEE 719/7724
(6) M. Matsuyama, et al.: Development of Control System for Limiting Drive Systems's Torsional Vibration Using Electronic Throttle System, Proceedings of JSAE Convention, No. 9 – 99, 5/8, 1999
(7) T. Sekozawa et al.: An Adaptive Engine Control Algorithm for Acceleration Response, SAE 910256, 1991
(8) D. E. Goldman: Effect of vibration on man, "Handbook of Noise Control", chap. 11 McGraw-Hill(1957)
(9) Danno, Togai et al.: Powertrain Control by DBW System: Strategy and Modeling, SAE 890760
(10) Togai, Choi, Takeuchi: Vibration Suppression Strategy With Model Based Command Shaping: Application to Passenger Car Powertrain, SICE 02 – 607, 2002

Tadashi TAKEUCHI

Kyoung-Gon CHOI

Shoji KAN

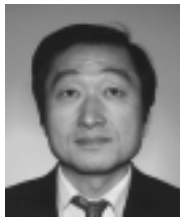

Kazuhide TOGAI

Development of Disc Brake Rotors for Heavy- and Medium-Duty Trucks with High Thermal Fatigue Strength

Junichiro YAMABE* Masami TAKAGI* Toshiharu MATSUI*

Abstract

A new method has been developed to evaluate thermal fatigue by a simulating high-speed braking test using an actual disc brake rotor. Thermal fatigue strength is confirmed to be improved with increasing graphite number in the microstructure. It is also confirmed that the graphite number increases in proportion to the amount of nickel added, and that the inoculation of cerium, a rare earth element, produces an effect similar to that of adding nickel. Based on this approach, a new, low cost material for disc brake rotors for heavy- and medium-duty trucks is developed using both nickel and cerium.

Key words: *Brake, Durability, Fatigue, Heat Resistance*

1. Introduction

Today, disc brakes are the most popular brakes for passenger cars, light-duty trucks and other small-sized vehicles, while mainly drum brakes are used in heavy- and medium-duty trucks. Brakes on heavy- and medium-duty trucks sustain thermal and mechanical loads that are much greater than on small-sized vehicles, which discourages manufacturers from employing disc brakes in heavy- and medium-duty trucks for durability reasons. However, the recent trend toward greater engine output and higher performance in heavy- and medium-duty trucks compels the manufacturers to use brakes with high braking performance and superior safety features such as anti-fade characteristics for which disc brakes are more promising than drum brakes[1][2].

Graphite flake cast iron has long been used as the material for disc brake rotors (hereinafter referred to as "rotors") because of its overall excellence in thermal fatigue strength, anti-squeak and anti-vibration characteristics, and wear resistance. In the case of small-sized vehicles, high carbon graphite flake cast iron[3] with high thermal conductivity is widely used to reduce the thermal load on rotors.

As rotors for heavy- and medium-duty trucks are subjected to a larger thermal load than rotors for small-sized vehicles, they require higher thermal fatigue strength. For this reason, graphite flake cast iron with nickel (Ni), molybdenum (Mo) and chromium (Cr) additions is widely used as the material for truck's rotors, although some rotors use cast steel[4].

Our company uses a material equivalent to JIS FC250 for the rotors of light-duty trucks and FC250-based graphite flake cast iron with 1.2 % Ni plus Mo and Cr for the rotors of large- and medium-duty trucks for increased thermal fatigue strength (for simplicity, the currently used material for rotors of light-duty trucks is referred to as "FC250" and that for rotors of large- and medium-duty trucks as "current material" hereinafter). The current material is excellent in thermal fatigue strength as it has been proven to be more than four times stronger than FC250 in high-speed braking tests using actual rotors, but the substantial amount of Ni that it contains boosts the material cost.

In the research presented here, rotor materials were experimentally produced with the goal of achieving cost reduction (hereinafter these materials are referred to as "experimental materials"). The experimental materials contained reduced amounts of Ni and inoculated Ce (cerium), a rare earth element having a graphite refining effect similar to Ni, and were subjected to rig tests that simulated actual vehicle high-speed braking tests. Based on the test results that clarified the relationship of the thermal fatigue strength to the mechanical and physical properties as well as to the microstructures of the current and experimental materials, a new, low-cost rotor material with thermal fatigue strength equivalent to the current material was developed.

2. Process of initiation and propagation of heat cracks

Braking by disc brakes consists of a process in which the brake pads (hereinafter referred to as "pads") are pressed against a rotating rotor to convert the vehicle's kinetic energy into thermal energy before releasing it into the air. Extremely hot heat spots at temperatures higher than the AC_1 transformation temperature (approximately 750 ˚C) are caused in a very shallow layer under the friction surface of the rotor. Due to the consequent local temperature gradients, the friction surface of the rotor undergoes compressive yield accompanied by plastic deformation. When the rotor subsequently cools down, it undergoes residual tensile stress generated in these spots. Repetition of this thermal stress

* Material Engin. Dept., Research & Dev. Office, MFTBC

Table 1 Chemical composition of sample materials

[wt. %]

Material	C	Si	Mn	P	S	Ni	Cr	Mo	Cu	Ce
Current material	3.35	2.16	0.67	0.028	0.023	1.25	0.32	0.30	0.32	tr
FC250	3.35	2.10	0.68	0.026	0.025	tr	0.20	tr	0.30	tr
Experimental material No. 1	3.26	2.04	0.70	0.030	0.050	tr	0.50	0.27	0.65	0.023
Experimental material No. 2	3.40	2.20	0.71	0.031	0.030	0.30	0.42	0.31	0.52	tr
Experimental material No. 3	3.28	2.02	0.70	0.030	0.047	0.38	0.47	0.29	0.48	0.019
Experimental material No. 4	3.43	2.20	0.71	0.031	0.031	0.64	0.40	0.29	0.23	tr

cycle causes heat cracks to initiate in the friction surface.

The rotor comes under not only the above-mentioned local temperature gradient but also the temperature gradient that occurs between the friction surface average temperature (some 500 ˚C) and the rotor inside temperature. In contrast to the local temperature gradient, this surface/inside temperature gradient is a macroscopic or average temperature gradient. Repeated thermal stress caused by this average temperature gradient has an effect of propagating heat cracks. The thermal stress caused by local temperature gradients is presumed to be much greater than that caused by the average temperature gradient.

As reported in past research, heat cracks initiate at a very early stage of brake application[3]. The life of a rotor, therefore, is considered to be governed by the propagation life of heat cracks after they have initiated.

3. Philosophy of thermal fatigue strength improvement

A heat crack initiates and propagates through repetition of local and average thermal stress cycles. The thermal fatigue strength of a rotor, therefore, can be improved if the propagation of heat crack is properly controlled. Reducing the amount of thermal stress is one way to achieve this purpose and improving the material's resistance against crack propagation is another. More practically, improving the thermal conductivity and increasing resistance against compressive stress at high temperatures will reduce the amount of thermal stress, while resistance against crack propagation may be improved by reducing the amount of graphite crystallization[5], increasing the number of eutectic cells and, in addition, refining the graphite grains, although this is not yet supported by well-established theory.

Metallurgically speaking, however, increasing the thermal conductivity is a trade-off with improving high-temperature compressive yield strength and resistance against propagation of cracks. Concurrently improving all of these characteristics is impracticable. In fact, adding high carbon will improve the thermal conductivity because of the increased amount of graphite crystals in the material structure, but on the other hand, it will reduce the high-temperature compressive yield strength, which will in turn reduce the resistance against propagation of cracks. Similarly, adding Ni as an alloy element is a promising method for reducing the thermal stress because it improves the high-temperature compressive yield strength and for improving the resistance against propagation of cracks because it promotes refining of graphite, but on the other hand, it will reduce the thermal conductivity. For this reason, finding the optimum combination of component elements that yields the best balance among thermal conductivity, high-temperature compressive yield strength and resistance against development of cracks is essential for the improvement of thermal fatigue strength. The high-temperature compressive yield strength is difficult to measure, but its value is generally believed to be about twice as large as the value of tensile yield strength. Since the tensile yield strength of graphite flake cast iron is 10 – 30 % smaller than its tensile strength, it is possible to roughly estimate the high-temperature compressive yield strength of a material from the high-temperature tensile strength. In this research, the tensile strength at high temperatures was substituted for the high-temperature compressive yield strength when comparing one material with another with regard to the effect of high-temperature compressive yield strength on thermal fatigue strength.

4. Simulation tests

4.1 Sample materials

The sample materials used for the tests were the current material, FC250 and experimental materials Nos. 1 to 4. The amounts of Ni and Ce contents in the experimental materials were varied as parameters. All of them were produced with production molds using a similar casting design. The chemical compositions of the sample materials are shown in **Table 1**, the mechanical and physical properties in **Table 2**, and the temperature dependence of the tensile strength in **Fig. 1**. The microstructures of all the sample materials comprise A-type graphite distributed in a pearlite matrix. The microstructures of the current material and FC250 are shown in **Fig. 2**.

When the current material and FC250 are compared in terms of the chemical composition, general properties, and microstructure, there is a large difference in the amount of Ni content with regard to the chemical composition, there is no significant difference with regard to general properties, and there is a large difference in the shape of graphite with regard to the microstructure. The difference in the thermal fatigue

Table 2 Mechanical and physical properties of sample materials

Mechanical and physical properties			Current material	FC250	No. 1	No. 2	No. 3	No. 4
Tensile strength	(MPa)	Room temperature	290	260	420	265	436	252
Thermal conductivity	(W/m·˚C)	Room temperature	45.8	52.6	50.0	53.3	51.0	53.1
		500 ˚C	37.2	38.2	37.8	39.0	38.4	38.8
Coefficient of thermal expansion	(x 10^{-5}/˚C)	100 – 500 ˚C	1.32	1.33	1.35	1.35	1.37	1.34
Young's modulus	(GPa)	Room temperature	114	113	117	113	117	112

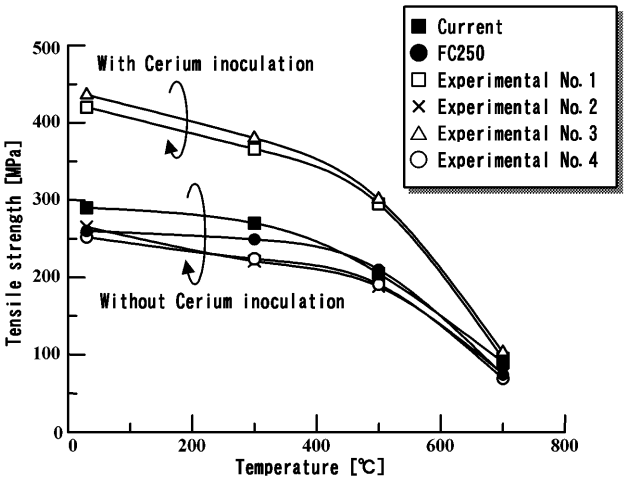

Fig. 1 Temperature dependence of tensile strength

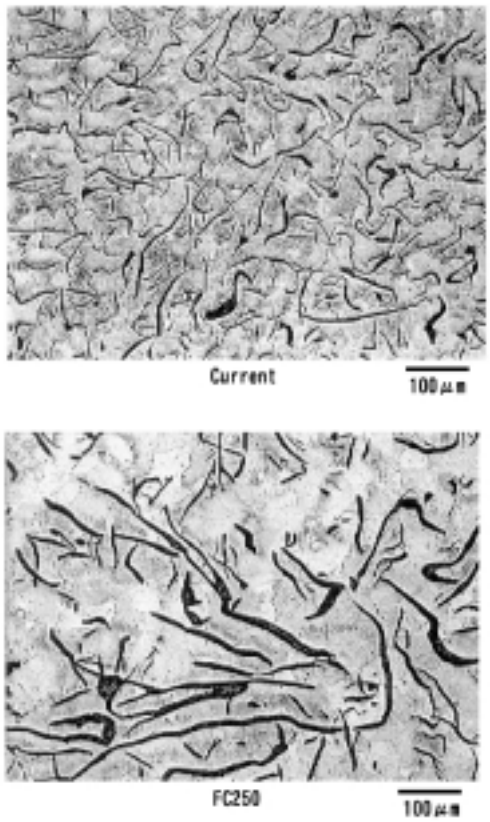

Fig. 2 Microstructure of current material and FC250

strength between the current material and FC250 mentioned above is attributable to the difference in minuteness of distributed graphite grains, which is finer in the current material than in FC250. Finer graphite grains in the current material presumably result from the graphite refining effect of Ni. This point will be discussed in detail in Section 4.5.

In line with the above presumption, an Ni reduction method by inoculation of Ce[(6) – (8)] into the experimental materials was considered with the expectation of increased graphite nucleus and a consequent graphite refining effect as substitution for the above-mentioned effect of Ni. As a study for giving shape to this concept, the effect of Ni and Ce on graphite refining was investigated using the amount of Ni as well as the presence/absence of Ce inoculation as parameters. The amounts of material components other than Ni and Ce were set at the same levels as in the current material in order to retain the anti-squeak characteristics, braking effectiveness, wear resistance and other required properties in addition to the thermal fatigue strength.

The tensile strength of the sample materials at room temperature with Ce inoculation were higher than in the ones without Ce inoculation, presumably due to a combination of the effects of Ce inoculation, such as increased number of eutectic cells, refined graphite grains, and densification of the pearlite matrix structure.

The temperature dependence of tensile strength was nearly the same for all the sample materials, i.e., the tensile strength of each material showed a gradual decline up to 500 ˚C, and beyond that temperature, it declined sharply. At 700 ˚C, the tensile strength of all the materials became nearly the same, showing no recognizable effect of the Ce inoculation.

The thermal conductivity of experimental material No. 2 was the highest and that of the current material was the lowest, although the difference between them was as small as around 15 %. The coefficient of thermal expansion and Young's modulus were not very different among all the materials.

4.2 Test method

The simulation tests were conducted using a test rig that imitated a high-speed braking test on a chassis dynamometer using actual rotors. **Figs. 3** and **4** show the specimens and the schematic of the test rig. Specimens of rotors and pads used in the tests were cut from the actual rotors and actual semi-metallic pads. The test rig was a pin-on-disc type wear test machine with necessary modification, and the tests were conducted by making the pad specimen rub against the

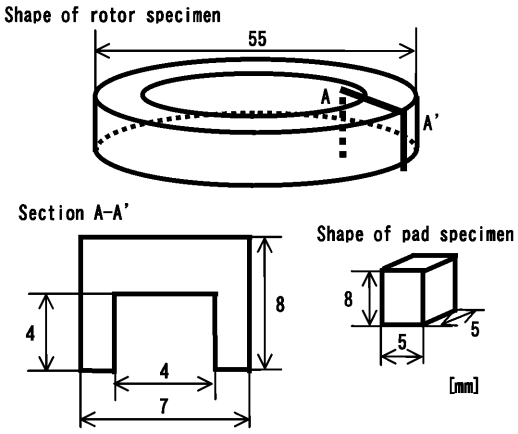

Fig. 3 Shape and dimensions of specimen

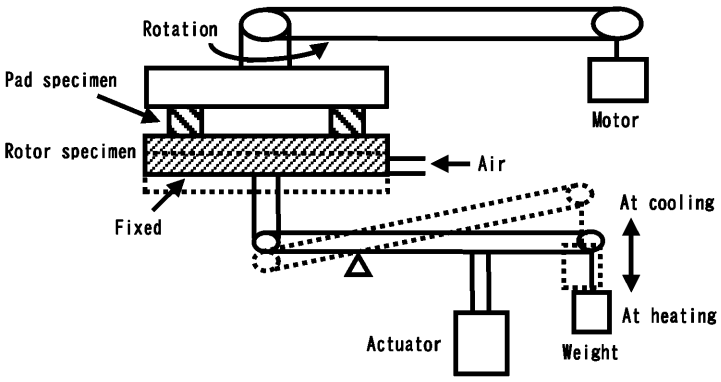

Fig. 4 Schematic of simulator

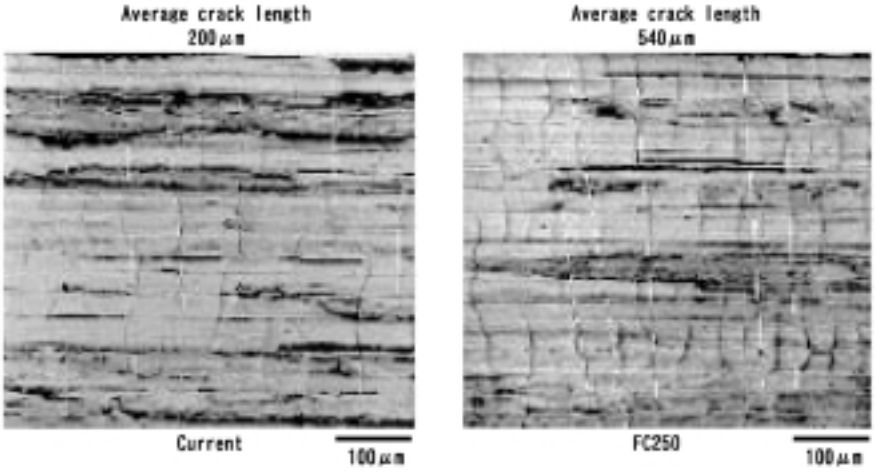

Fig. 5 Crack condition of rotor surface after 120 cycles at simulation test

fixed rotor specimen at a constant surface pressure so that heat cracks would initiate by friction-caused heat. Friction heating was continued until the temperature of the rotor specimen's friction surface reached the same temperature as that experienced by actual rotors, and then the underside of the rotor specimen was cooled by blowing air. Air was continually blown in a small amount against the underside surface of the rotor specimen even during friction heating to create a temperature difference between the friction surface and underside surface. The temperature difference was 240 ˚C with the current material, while it was 230 ˚C even with the experimental material No. 2 that had the highest thermal conductivity. The temperature differences, therefore, were nearly at the same level for all the sample materials. The CAE calculation result of the compressive strain predicted to occur along each rotor's circumference at the highest temperature was nearly the same for all the sample materials; all the differences fell within a 6 % range. Each heating and cooling cycle consisted of 40 seconds for friction heating and 100 seconds for air cooling.

4.3 Verification of the correlation between the simulation test and high-speed braking tests using an actual rotor

Fig. 5 shows the cracks that developed in the surfaces of the current material and FC250 after 120 cycles of simulation tests. The size of each crack is represented by its length measured on the friction surface. Indicated above each photograph is the average of the five longest heat cracks within the field of view determined using an image processing system. The manner of crack development is apparently different between the current material and FC250. Cracks in the current material are shorter in length and smaller in number than those in FC250.

Fig. 6 shows a fractograph of a crack in FC250 under a scanning electron microscope (SEM). The photograph on the left shows the actual surface near the initiation point of the crack, and the photograph on the right shows the inside of the rotor. An intergranular cracking is obvious in the vicinity of the crack's initiation point and there is a conspicuous lamellar pattern in the inside. As the intergranular cracking is characteristic of a high-temperature and high-stress state, while a lamellar pattern is an indicator of (general) fatigue, the former can be associated with the crack initiation caused

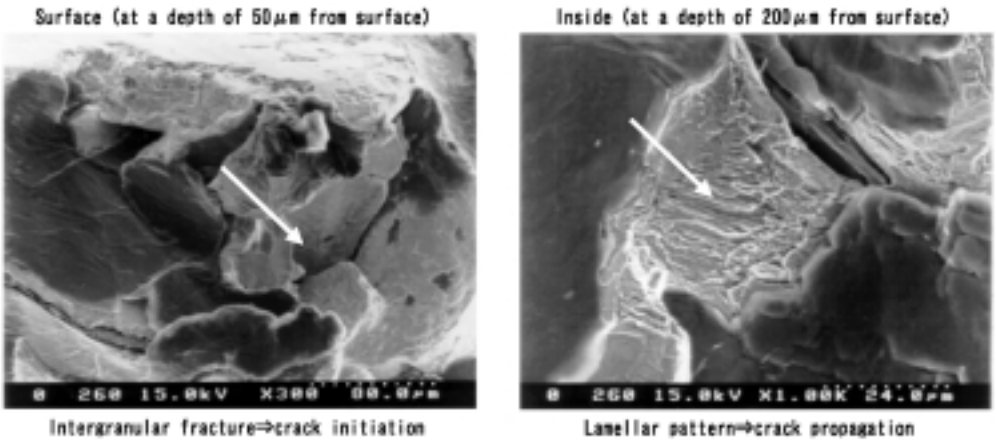

Fig. 6 SEM fractograph of crack surface after 120 cycles at simulation test (FC250)

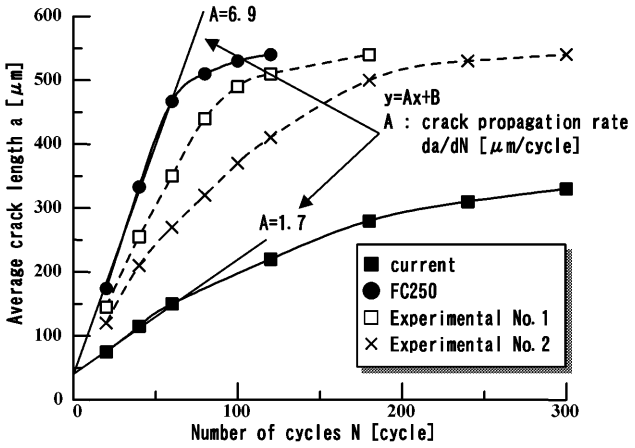

Fig. 7 Relationship between average crack length and number of cycles at simulation test

by a local temperature gradient present in a heat spot and the latter with the crack propagation due to an average heat gradient present throughout the entire rotor. While past researches report that cracks initiate in rotors at an early stage of their use, the results of our research also indicate that cracks initiate in a few initial cycles (1 – 5 cycles) in all the sample materials.

Fig. 7 shows the averages of the heat crack lengths measured at certain simulation cycle points between 20 and 300 cycles. The graph shows the data for the current material, FC250 and experiment materials No. 1 and 2. The crack length of each material propagates at a rate nearly in proportion to the number of cycles up to 60 cycles, but the propagation rate of cracks in FC250 rapidly decreases when the number of cycles exceeds 60, and the average crack length stops increasing when the crack length reaches around 500 μm. This can be explained by the following reasoning: the thermal stress acting on the top of the crack becomes smaller as the crack depth increases, ultimately rendering ineffective the compressive yield stress at high temperatures and the residual tensile stress during cooling. All the sample materials share this phenomenon. Regardless of the type of material and the number of cycles, heat stress stops acting on the top of a crack when the crack length exceeds 500 μm and thus the crack propagates no further.

According to the above-mentioned finding, all the sample materials were evaluated using the data collected in the simulation up to 60 cycles during which cracks propagate almost linearly in proportion to the number of cycles. More particularly, the average length of heat cracks measured at certain simulation cycle points up to 60 cycles are approximately represented by a line for each material, the inclination of the line is defined as the crack propagation rate, and the crack propagation rate of each sample material is used as the parameter representing the thermal fatigue strength of that material.

The heat crack propagation rates of the current material and FC250 determined using the above-mentioned method are 1.7 μm/cycle and 6.9 μm/cycle, respectively, the rate of the current material being one quarter that of FC250. In other words, the crack propagation life of the current material is four times as long as that of FC250, which corresponds fairly well with the heat fatigue life ratio between the two materials derived from the results of the high-speed braking test using actual rotors. The results signify that the number of cycles required before the crack initiation has little contribution to the thermal fatigue strength (or thermal fatigue life) of rotors but the crack propagation life following the crack initiation has a direct bearing on the fatigue strength. Therefore, the thermal fatigue life of a material can be evaluated using the above-mentioned crack propagation rate.

The intercept of the approximative line is about 50 μm, or nearly equal to the average heat crack length, for both the current material and FC250. As this length is approximately the size of a grain (the diameter of a grain in the left picture of **Fig. 6** is 50 – 100 μm), it is reasonable that the intercept correspond to a crack initiation caused by intergranular cracking.

4.4 Comparison of crack propagation rates

Fig. 8 shows the results of simulation tests conducted for the sample materials. In this graph, the crack

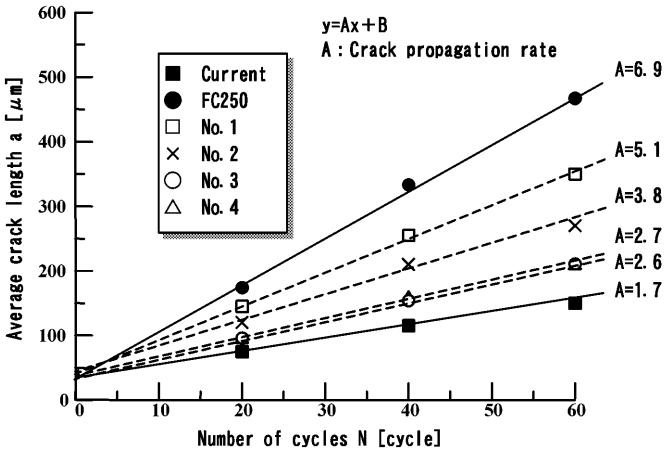

Fig. 8 Relationship between average crack length and number of cycles at simulation test

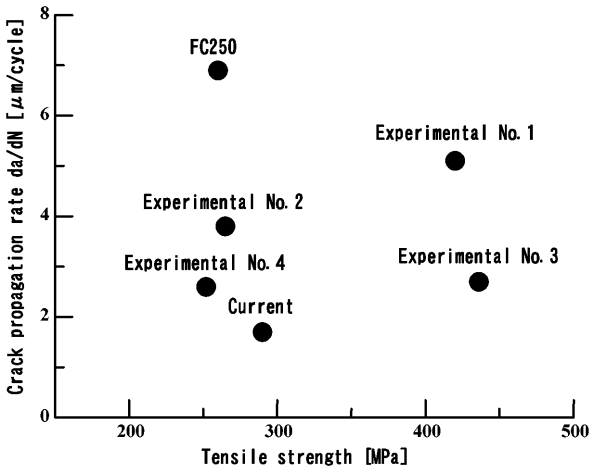

Fig. 10 Relationship between crack propagation rate and tensile strength at room temperature

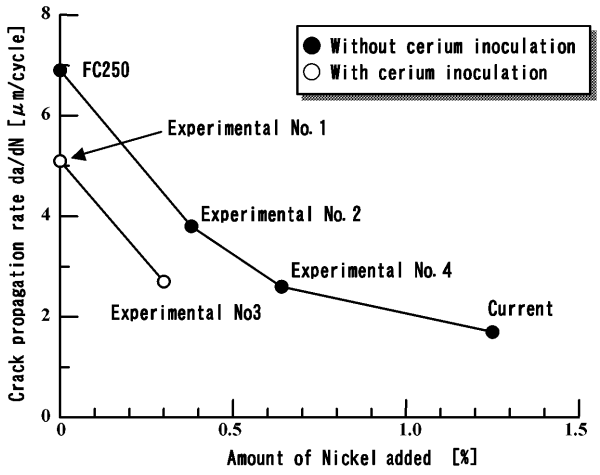

Fig. 9 Relationship between crack propagation rate and amount of Ni added, with and without Ce inoculation

propagation rates represented by the approximative lines derived from average heat crack length measurements up to 60 cycles are also indicated. The test results show that the crack propagation rates of experimental materials No. 1 to 4 are between those of the current material and FC250, i.e., all of them are more rapid than that of the current material. This means that, as far as thermal fatigue strength is concerned, the current material is the best material. From what **Fig. 9** shows about the effect of Ni and Ce on the crack propagation rate, both increasing the amount of Ni content and inoculating Ce slow down the crack propagation rate. This indicates that the Ce inoculation as well as the Ni addition is effective for improving thermal fatigue strength.

4.5 Relationship between crack propagation rate, material properties and Ni addition/Ce inoculation

From the discussion in the preceding section, it becomes clear that Ni addition and Ce inoculation improve the thermal fatigue strength. In order to elucidate the effects that Ni and Ce have on the propagation of heat cracks, this section describes examinations conducted to study the relationship between the crack propagation rate and various properties of each material (mechanical/physical properties and microstructures) and the relationship between these properties and Ni addition and Ce inoculation.

With regard to the relationship between the crack propagation rate and the mechanical/physical properties, this study is limited to its relationship with the tensile strength because, as seen from **Table 2**, none of the property factors show any conspicuous differences among the sample materials except for the tensile strength. **Fig. 10** shows the relationship between the propagation rate and tensile strength of each sample material at room temperature. As shown in the figure, there is no clear correlation between the propagation rate and tensile strength. This is also true of the relationship between the materials at high temperatures. These results suggest that the thermal fatigue strength of rotors would not be improved by only using the material with high tensile strength at room and high temperatures.

The relationship between the propagation rate and the microstructure of the materials was studied next. The matrix hardness, number of eutectic cells, average length of graphite, areal ratio of graphite and number of graphite grains were selected as the parameters representing the characteristics of microstructure. **Table 3** shows the values of these parameters. As shown in the table, the areal ratios of graphite are nearly the same for all the sample materials. In the following discussion, therefore, the areal ratio of graphite is assumed to be the same for all the sample materials.

The parameters of microstructure were compared between the sample materials. Experimental materials No. 1 and No. 3 with Ce inoculation showed the highest matrix hardness values. With regard to both the eutectic cell and graphite grain numbers, which were increased by Ni addition and Ce inoculation, the current material showed the highest values. The average

Table 3 Parameters of microstructure of sample materials

Parameters of microstructure		Current material	FC250	No. 1	No. 2	No. 3	No. 4
Matrix hardness	(HV50gr)	301	289	373	302	367	302
Number of eutectic cells	(grains/cm^2)	318	82	202	117	244	153
Average length of graphite	(μm)	53	113	96	105	75	85
Areal ratio of graphite	(%)	21.6	22.6	17.3	18.9	19.1	19.9
Number of graphite grains	(grains/mm^2)	200	78	83	92	112	116

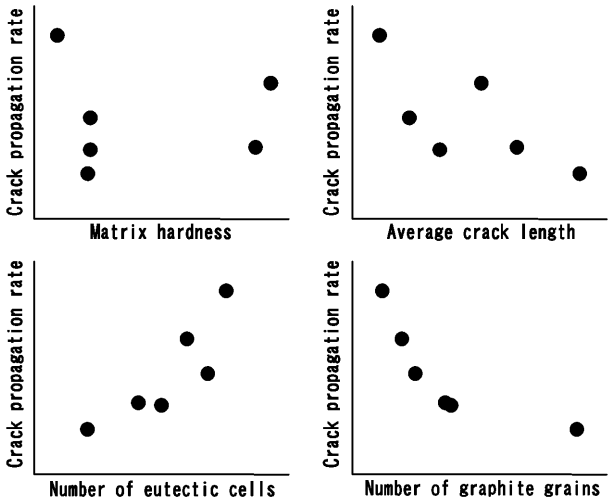

Fig. 11 Relationship between crack propagation rate and parameters of microstructure

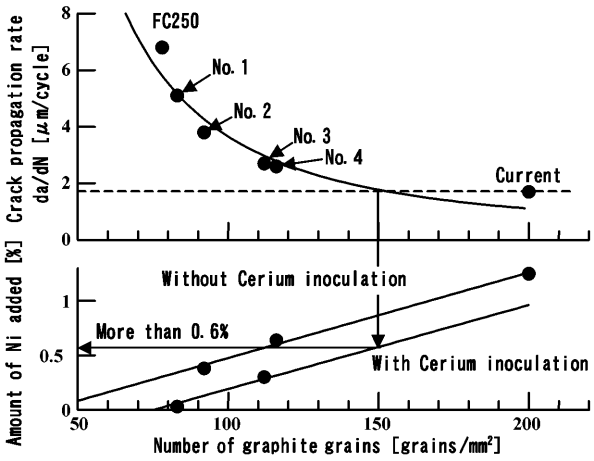

Fig. 12 Relationship between crack propagation rate, amount of Ni added and graphite number

graphite length was inversely related to the graphite grain number, and became shorter as the graphite grain number increased.

Fig. 11 shows the relationship between these microstructure parameters and the crack propagation rate. Among the microstructure parameters, the number of graphite grains shows the highest correlation with the crack propagation rate. Although the average length of graphite and the number of eutectic cells seem correlative with the crack propagation rate, the reason behind it may be a correlation between these parameters and the number of graphite grains.

The upper graph of **Fig. 12** shows the relationship between the crack propagation rate and number of graphite grains, and the lower graph shows the relationship between the number of graphite grains and the amount of Ni addition and presence/absence of Ce inoculation. Both the upper graph and the lower graph have the horizontal axis scale in common, against which the number of graphite grains is plotted. This figure indicates that the crack propagation rate is inversely proportional to the number of graphite grains. Therefore, this relationship can be approximated by the following expression:

$$y = A/x^2 + B$$

where A and B are constants.

The contribution rate derived from calculation using the formula is high ($R^2 = 0.93$). Although the physical validity of this expression is now under study, several previous papers[9][10] support the crack retardation effects of the graphite, and its crack propagation rate retardation effect can be qualitatively explained as follows:

(1) When a crack develops close to a graphite grain, microcracks initiate around the graphite grain, and the microcracks absorb the crack propagation energy.

(2) A large number of graphite grains present in the material deflects crack propagation paths and causes each path to branch out into multiple paths, thus dispersing the crack propagation energy.

In the lower graph showing the relationship between the amount of Ni, presence/absence of Ce inoculation and number of graphite grains, the data on the materials without Ce inoculation indicates that the number of graphite grains increases nearly in proportion to the amount of Ni within the range between 0.3 to 1.2 % in the Ni amount (90 to 200 grains in a square millimeter). Also, the effect of Ce inoculation on the increase in the number of graphite grains can be determined by comparing the data of the Ce-inoculated material (experimental material No. 3) and that of the non-Ce-inoculated material (experimental material No. 2), both containing almost the same amount of Ni.

From these results, it becomes evident that the greater the number of graphite that is distributed in the microstructure in refined grains, the slower the crack propagation rate, and that Ni addition and Ce inoculation have the effect of creating finer graphite grains.

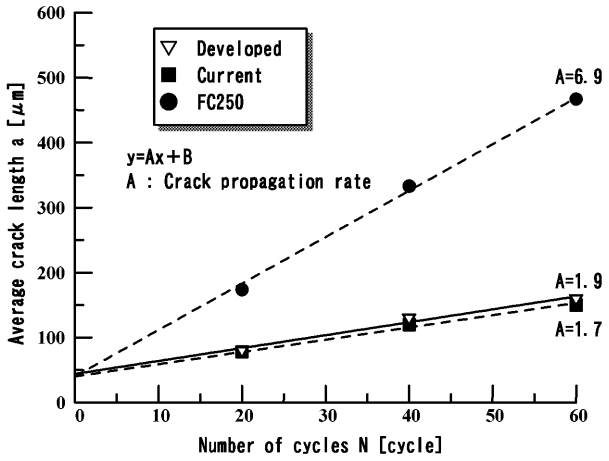

Fig. 13 Relationship between average crack length and number of cycles at simulation test

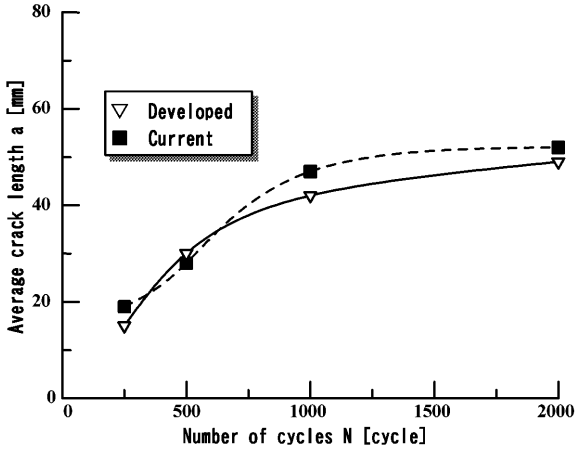

Fig. 14 Relationship between average crack length and number of cycles at high-speed braking test

Table 4 Chemical composition of developed material

[wt. %]

Component	C	Si	Mn	P	S	Ni	Cr	Mo	Cu	Ce
Developed material	3.36	1.92	0.70	0.030	0.050	0.58	0.50	0.37	0.50	0.023

Table 5 Mechanical and physical properties of developed material

Mechanical/physical properties			Developed material
Tensile strength	(MPa)	Room temperature	440
Thermal conductivity	(W/m·˚C)	Room temperature	43.8
		500 ˚C	37.2
Coefficient of thermal expansion	(x 10^{-5}/˚C)	100 – 500 ˚C	1.33
Young's modulus	(GPa)	Room temperature	117

Table 6 Parameters of microstructure of developed material

Parameters of microstructure		Developed material
Matrix hardness	(HV50gr)	394
Number of eutectic cells	(grains/cm^2)	288
Average length of graphite	(μm)	57
Areal ratio of graphite	(%)	19.9
Number of graphite grains	(grains/mm^2)	153

5. Development of a low-cost rotor material

As evident from **Fig. 12**, both Ni and Ce certainly have substantial effects on the crack propagation rate, thus Ce inoculation makes it possible to achieve a crack propagation rate as low as that of the current material even with a smaller Ni amount than the current material. In other words, Ce inoculation enables development of a low-cost rotor material with the same level of thermal fatigue strength as the current material. The amount of Ni added in the newly developed material can be established by first determining the number of graphite grains corresponding to the current material's crack propagation rate from the approximative curve in the upper graph of **Fig. 12**, and then selecting the amount of Ni to be added using the Ce-inoculated material's approximative line in the lower graph. According to the prediction based on this method, a crack propagation rate equivalent to the current material would be realized with graphite grains of more than 150 grains per mm^2 in number and addition of Ni of more than 0.6 %. The Ce-inoculated material's approximative line used in this prediction was the non-Ce-inoculated material's approximative line shifted in parallel for adaptation to the Ce-inoculated material on the assumption that there was no synergistic effect by the simultaneous addition of both Ni and Ce.

Based on the prediction, the particulars of the newly developed material were set up as follows: Ce-inoculated effected, 0.6 % added Ni, and all the other components the same as in the current material. The chemical composition, various properties and parameter values of microstructure of the newly developed material are shown in **Tables 4** to **6**, respectively. The chemical composition, including the amount of Ni, is almost as targeted. The tensile strength, like other Ce-inoculated materials, is as high as 1.5 times that of the current material, and the thermal conductivity and areal ratio of graphite are equivalent to the current material. Including the number of graphite grains of 153 grains/mm^2, the newly developed material fulfills almost all the target properties.

Fig. 13 shows the results of simulation tests of the developed material. As in **Figs. 7** and **8**, the crack propagation rate was determined from the inclination of the approximative line representing the average heat crack lengths at different cycles. The crack propagation of the developed material thus determined is 1.9 μm/cycle, and is almost at the same level as the current material.

Figs. 14 to **16** show the results of the high-speed braking tests conducted using rotors made of the newly

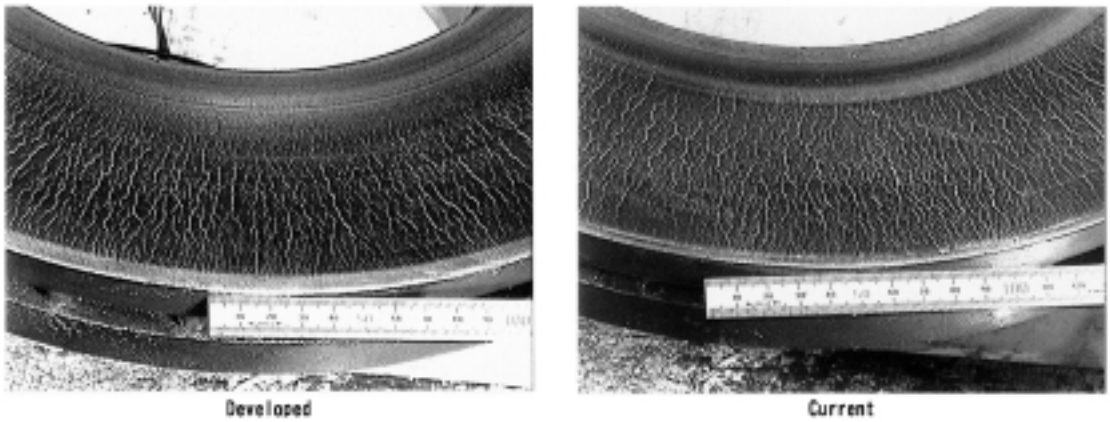

Fig. 15 Crack condition of rotor surface after high-speed braking test

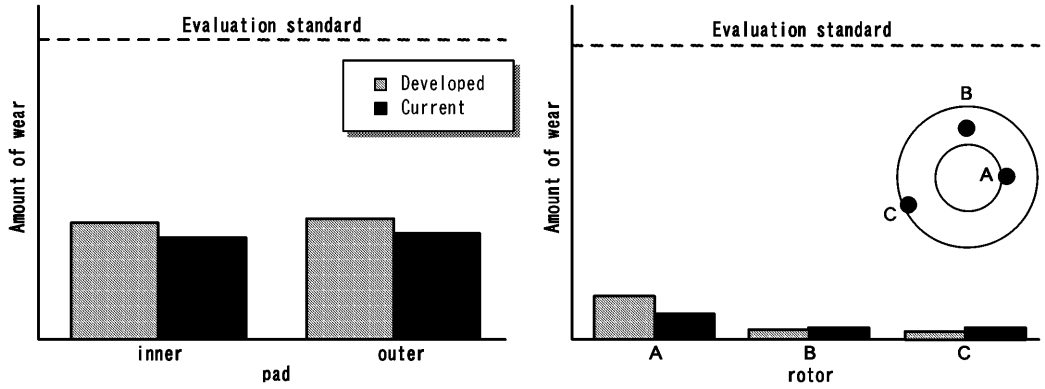

Fig. 16 Wear condition of pad and rotor after high-speed braking test

developed material. **Fig. 14** shows the average heat crack lengths at different cycles, the photographs in **Fig. 15** show the condition of heat cracks developed in the friction surfaces, and **Fig. 16** shows the amount of wear of pads and rotors. In both the rotors made of developed material and current material, each crack propagates not only by itself but also through branching into other cracks. The heat crack lengths for certain numbers of cycles of both materials are similar to each other, and the initiation of heat cracks on the rotor friction surfaces are also quite similar. From all of these facts, it is reasonable to consider the thermal fatigue strength of the developed material to be at the same level as the current material. The new material does not involve any problems associated with resistance to wear, as the amount of wear is small enough to satisfy the standard. It was also confirmed that anti-squeaking, braking effectiveness and other important characteristics are at the same level in the new material as in the current material, so there are no problems involving actual application.

6. Summary

The results and achievements of this research are summarized as follows:

(1) A low-cost disc brake rotor material has been developed, which has thermal fatigue strength at a level equivalent to that of the current material.
(2) A method for evaluating the thermal fatigue strength using specimens has been established, imitating a high-speed braking test of an actual rotor.
(3) The thermal fatigue life of a disc brake rotor is affected very little by the number of cycles at which cracks initiate, but depends on the crack propagation life after the crack initiation.
(4) The greater the number and the more refined the graphite grains distributed in the structure, the more the crack propagation is retarded.
(5) The number of graphite grains in the metal structure increases by Ni addition and Ce inoculation.

We express our deep appreciation for the generous cooperation of Mitsubishi Motors Techno-Metal Corporation and our colleagues in the related departments.

References

(1) Endo, Takahashi and Hara: Development of a Disc Brake Rotor Material for Heavy-Duty Trucks, Presentation Material 20015120 at the Congress of Society of Automotive Engineers of Japan.
(2) Katori, Iwasaki, Fukuda and Akita: Development of a Rotor Material with Excellent Heat Crack Resistance, Presentation Material 20025247 at the Congress of Society

of Automotive Engineers of Japan.
(3) Jimbo, Mibe, Akiyama, Matsui, Yoshida and Ozawa: Development of High Thermal Conductivity Cast Iron for Brake Disc Rotors, SAE Paper 900002.
(4) Sakamoto, Nakata, Yamamura, Kusumoto, Hirayama and Toyama: Development of Brake Disc for High Speed Motor Vehicles, Sumitomo Metal Technical Revue Vol. 45-6 (1992), p. 13 – 22.
(5) Matsuoka, Shiota and Komatsu: Effects of Graphite Shape on Behavior of Fatigue Crack Propagation of Ferritic Gray Cast Iron, Castings 67-3 (1995), p. 197 – 202.
(6) Horie, You, Konisiki, Sugai, Yamada and Senda: Properties of Tenacious Cast Iron utilizing Chill-Reduction Effect of Rare Earth Elements, Castings 64-10 (1992), p. 694 – 698.
(7) Horie, You, Konishiki, Hiratsuka, En and Shoubusawa: Effects of Rare Earth Elements and Sulfur on Chill-Reduction Tendency and Tensile Strength of Flake Graphite Cast Iron, Castings 63-2 (1991), p. 143 – 148.
(8) Konishiki, Horie, Hiratsuka and Sato: Effects of Rare Earth Elements on Chilling and Mechanical Properties of Flake Graphite Cast Irons with different Carbon Equivalence, Cast Engineering 68-10 (1996), p. 865 – 869.
(9) Nozue, Miyake and Okubo: On the Spot Observation of Fatigue Crack Propagation of Spheroidal Graphite Cast Iron within the View of a Scanning Electron Microscope, Journal of Japan Institute of Metals 62-10 (1998), p. 919 – 924.
(10) Kato, Hirose and Suzuki: Effect of Microstructure on Fatigue Crack Propagation Strength of Steel and Cast Iron, Transaction of Japan Society of Mechanical Engineers (A Edition) 51-464 (1979), p. 1161 – 1167.

Junichiro YAMABE

Masami TAKAGI

Toshiharu MATSUI

TECHNICAL PAPERS

Fatigue Strength Prediction of Truck Cab by CAE

Shinichi CHIBA* Kimihiko AOYAMA* Kenji YANABU**
Hideo TACHIBANA** Katsushi MATSUDA** Masashi UCHIKURA**

Abstract

In order to accurately predict the fatigue strength of a truck cab, it is necessary first to estimate the input load history from cab mounts, then with the estimated value, to accumulate the damages from the stress time history generated by the input load, and finally to calculate the fatigue life. This paper introduces the method of combining cab input load estimated by multi body simulation and fatigue life estimation by FEM analysis and fatigue life analysis, and one example of the analysis of the change mechanism of input mode and fatigue life according to the changes of test condition.

Key words: *Fatigue, Body, Numerical Analysis, CAE*

1. Introduction

In the conventional vehicle development, the fatigue strength of a truck cab must be evaluated by conducting physical tests. This is because in the conventional analysis, forces acting on the vehicle body are represented mainly by such static inputs as torsional and vertical bending forces, and the analysis results must be compared with the results of physical tests conducted on prototypes and actual vehicles before the fatigue strength can be assessed. In order to reduce the development period and number of prototypes, a technique is required that depends on so-called virtual prototypes at the drawing stage of development, not on physical prototypes.

Thanks to recent improvements in computer performance and the appearance of multi-purpose fatigue life analysis applications on the market, engineers can conduct fatigue strength analyses that take into account even the stress history and multiaxial stress field, thus making predictions more accurate[(1)]. The truck cab is usually fitted on the frame via four front and rear mounts, through which it receives random inputs, suggesting that in order to predict the fatigue strength, the stress history of composite inputs in a multiaxial stress field must be considered.

As the first step toward the ultimate goal of fatigue strength prediction based on computer aided engineering (CAE) assuming rough-road durability test situations, the fatigue strength evaluation method presented in this paper assumes bench durability test situations and combines schemes for predicting cab input loads and those for predicting fatigue strength. The paper also describes the cases of using the method to investigate the causes of cracks in a light-duty truck during the development stage.

2. Approaches for assessing cab fatigue strength

2.1 Durability test approach

The fatigue strength of the cab is generally assessed through both rough-road durability tests (drive tests) and bench durability tests. In a bench durability test, the displacement history of a hydraulic shaker is first determined using, as a target signal, the frame acceleration rates obtained through experimental rough-road driving, and then oscillation inputs equivalent to those experienced by an actual vehicle are applied by the shaker using the displacement history thus determined. In actual bench tests, however, the history is usually amplified in order to shorten the test time. A typical test rigging is shown in **Fig. 1**, in which the cab is fitted on the frame, the suspension and unsprung components including tires are removed, and the end of each actuator on the shaker is attached to the corresponding spring hanger. The shaker generates vertical vibrations along four axes. Although the shaker cannot generate horizontal inputs, its functions are considered sufficient for evaluating the cab's fatigue strength since the vertical vibration can be regarded as dominant among the effects the inputs to the cab have on the fatigue strength.

2.2 CAE simulation approach

Fig. 2 shows the flow of the CAE method used in this research for predicting the cab fatigue strength. The following two items are not supported by the conventional analysis but can be supported by this CAE method that is capable of predicting the fatigue strength taking the history of composite stress inputs through cab mounts into account.

(1) Quantitative history of cab input loads
(2) Fatigue life calculation based on stress history

The CAE method combines the solvers and predic-

* Engin. Administration Dept., Research & Dev. Office, MFTBC
** Function Testing Dept., Research & Dev. Office, MFTBC
** Cab Design Dept., Research & Dev. Office, MFTBC
** Material Engin. Dept., Research & Dev. Office, MFTBC

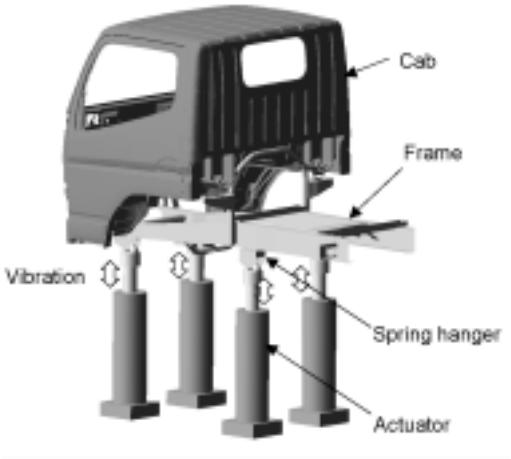

Fig. 1 Bench test conditions

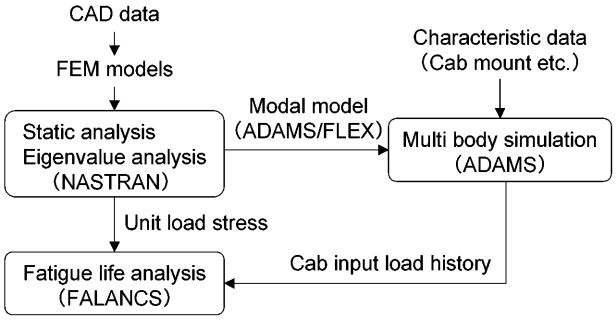

Fig. 2 Flowchart of fatigue strength simulation method

tion schemes offered by multiple applications, including static analysis and eigenvalue analysis by NASTRAN, multi-body simulation by ADAMS, and fatigue life analysis by FALANCS. The calculation process is as follows:

First, a finite element model of the cab is created using CAD data and then an eigenvalue analysis is performed on that model using NASTRAN. The results of the eigenvalue analysis are then converted into an ADAMS's modal model using ADAMS/FLEX. At the same time, the mounts and related parts are modeled using actual measurement data. The models thus created are combined and ADAMS's multi-body simulation is performed on them to derive the cab input load history. This history is then combined with the results of NASTRAN's static analysis to obtain a stress history, from which the fatigue life of each component is calculated.

This prediction method was developed as part of the development program for a full model-change of the Mitsubishi CANTER light-duty trucks, which was completed in June 2002.

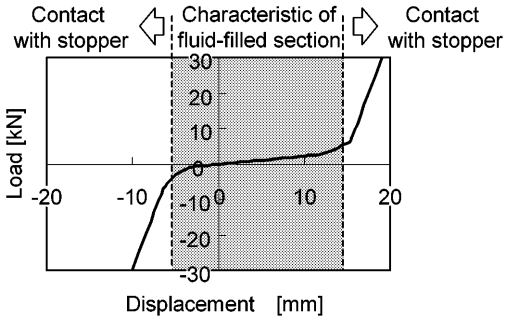

Fig. 3 Static characteristics of cab mounts

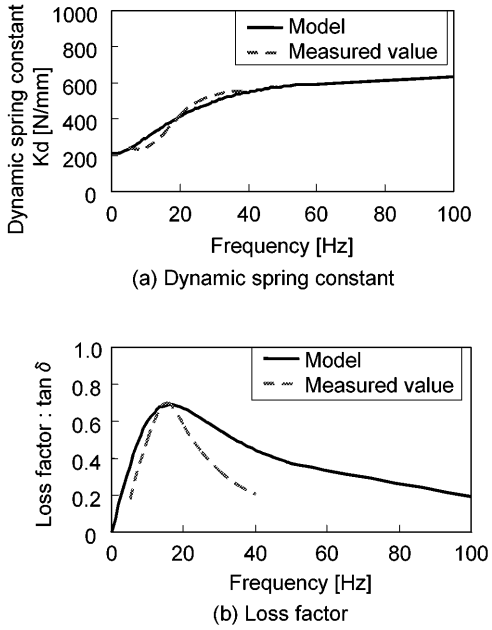

Fig. 4 Dynamic characteristics of cab mounts

3. Analysis of inputs to cab

3.1 Modeling method

3.1.1 Cab mount modeling

The cab is fitted on the frame via cab mounts. The cab mounts of the trucks under development were of a hydraulic damping type filled with a fluid, which features high damping force and low spring constant. **Fig. 3** shows the static characteristics and **Fig. 4** shows the dynamic characteristics of the hydraulic damping mounts, both for the vertical movements of the mounts. The central portion of the curve in **Fig. 3** corresponds to the characteristic of the fluid-filled section of each mount. When the amount of input is above or below the limits, the mount comes in contact with a stopper and the spring constant of the mount suddenly increases. Since the amplitude of inputs is magnified in bench durability tests in order to shorten the test time, the spring constant values after making contact with the stopper are significant. The dynamic characteristics of the cab mount are expressed by a dynamic spring con-

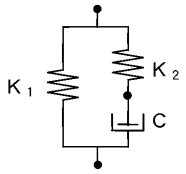

Fig. 5 Hydraulic damping mount modeling

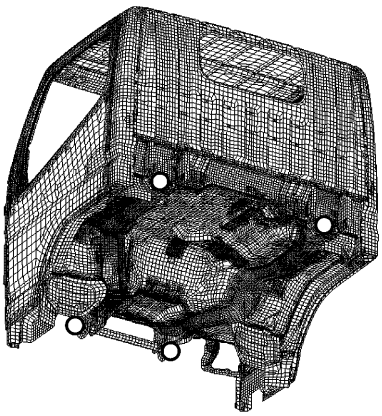

(a) Cab

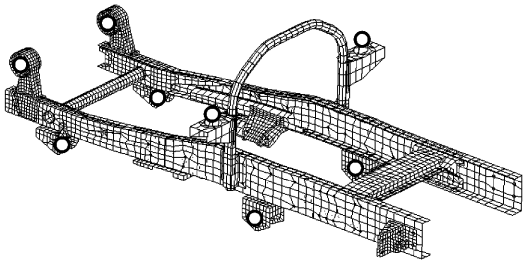

(b) Frame

Fig. 6 Finite element model and constraint points

stant and loss factor for each vibration frequency.

Fig. 5 is a model of the hydraulic damping mount represented by a combination of springs and a dashpot[(2)]. The static characteristics can be expressed by directly substituting an actual measurement value for K_1 and the dynamic characteristics can be expressed by adjusting the values of K_2 and C. As shown in **Fig. 4**, the calculated dynamic constant roughly agrees with the actual measurements, while the calculated and measured loss factor curves also agree in terms of the resonance frequency and peak values although they are somewhat different in the high vibration frequency range. The model is therefore also capable of expressing the dynamic characteristics.

3.1.2 Input analysis model

Rigid structure models have been the most commonly used type of model for motion analyses. However, as the truck's cab and frame are elastic structural bodies, elasticity characteristics should be considered when an accurate analysis is expected. The development team therefore used a modal model based on the constrained mode method as the structural model.

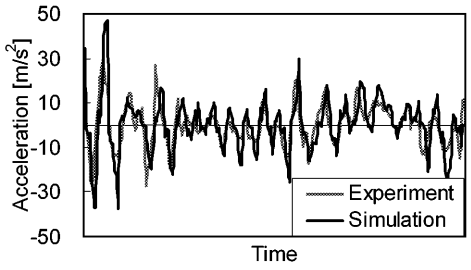

(a) Front

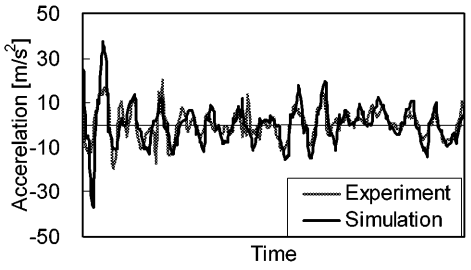

(b) Rear

Fig. 7 Comparison of frame acceleration between experiment and simulation

Fig. 6 shows the finite element models of the cab and frame and the constraint points on them. The constraint points on the cab correspond to the four cab mount locations; those of the frame are a total of eight locations consisting of the four mount locations and the four actuator attaching locations. The number of modes taken into account is 30 (including 24 for the constrained mode) for the cab and 54 (including 48 for the constrained mode) for the frame.

The input analysis model is configured by adding to these cab and frame models the models that represent the shaker's actuators and mounts.

3.2 Verification of simulation results

The simulation was performed by applying the history determined through experiments to the actuators of the shaker, and the results of the simulation were verified in terms of the cab mount displacement and the acceleration rates of several parts through comparison with the experiment results.

Fig. 7 compares the calculated and experimentally measured frame acceleration rates. The simulation results are approximately consistent with the experiment results. The small disagreements may be primarily due to inadequate representation of the elasticity characteristics of the connections between the frame and shaker. To improve the accuracy of the results, therefore, incorporating the elasticity characteristics of the connections is essential.

Fig. 8 shows the simulated cab mount displacement compared with the experimental measurements. The figure indicates that the simulation outputs are sufficiently accurate for practical use, as the amplitudes are almost equivalent to the experimental measurements although the history includes some discrepancies.

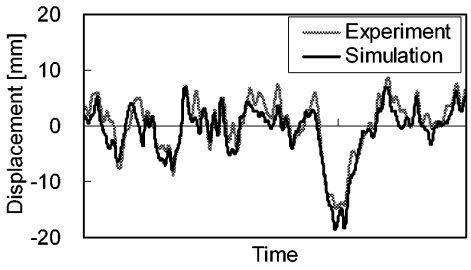

(a) Front

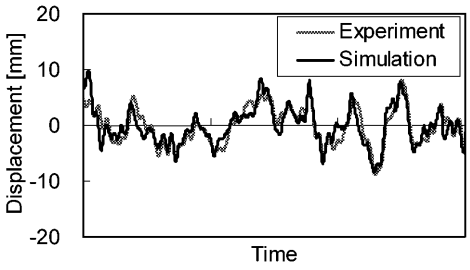

(b) Rear

Fig. 8 Comparison of cab mount displacement between experiment and simulation

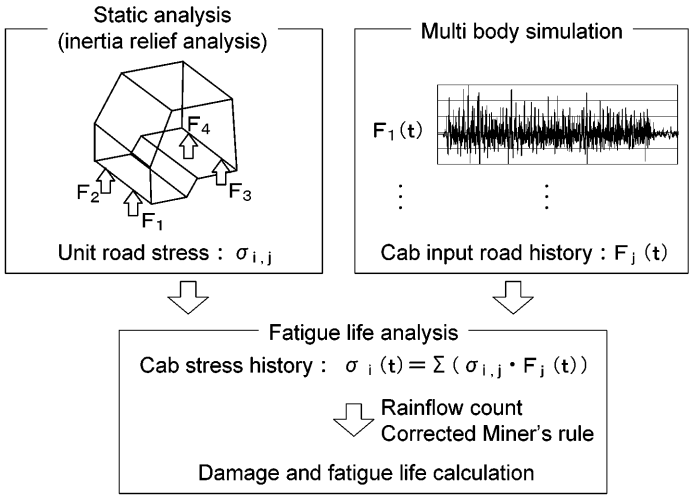

Fig. 9 Procedure of fatigue life analysis

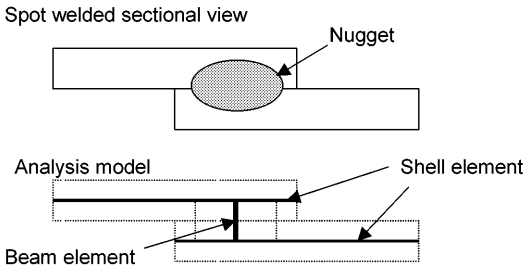

Fig. 10 Spot-weld modeling

4. Fatigue life prediction

4.1 Calculation method

4.1.1 Fatigue life prediction incorporating stress history

Stresses that occur in various areas of the cab are combinations of the following two types of stress:

① Static stress, the generation of which depends on the balance with input loads

② Dynamic stress, the generation of which depends on the vibration characteristics of the cab

The following methods can support the stress history in calculation of the fatigue life and applicable to the above stress types, respectively.

① Linear superposition method based on static analysis stress and input loads

② Modal superposition method based on the proper mode analysis and modal displacement

Since the experimental data collected so far show that static inputs such as torsional forces and vertical bending forces are dominant among the inputs to the truck cab, only method ① was adopted in the research. This method is based on the following principle: the stress condition at a given time can be determined by the linear superposition of stresses that result from the input conditions, while the history of the stress condition is determined by multiplying together the stress resulting from a unit load and the input load history. The process of predicting the fatigue life is as follows (see also **Fig. 9**):

(1) The value of the stress resulting from a unit load applied to each of the four cab mounts is calculated. Since shaking of the cab is a kind of constraint-free loading, NASTRAN's inertia relief analysis program is used for the calculation.

(2) The stress value derived from (1) above is multiplied by the history of cab input load through each mount (calculated from multi-body simulation), and the stress value and load are superposed for all the input cases to create a time history of the stress.

(3) Damage is calculated using rainflow accounting from the stress-time history created in (2) above and the fatigue life is calculated using the corrected Miner's rule.

4.1.2 Calculation of stress in spot welds

In general, a truck cab is formed of a number of sheets of metal attached by spot welding. Since loads acting on the cab are transmitted through these welds to various parts, stress concentrates on the welds and so they are often the most vulnerable points in terms of strength.

FALANCS supports the LBF approach which was proposed by Rupp et al.[3] as a method of analyzing the fatigue life of spot welds. This approach expresses a spot weld as two sheets of shell elements and a beam element (including rigid elements and multi-point constraints (MPCs)) and calculates stresses from element forces (axial force, moments, etc.) to derive the fatigue life. **Fig. 10** shows how a spot weld is modeled. The model is configured by two parallel shell elements and a beam element that joins the shell elements. As to the distance between the shell elements and the angle of

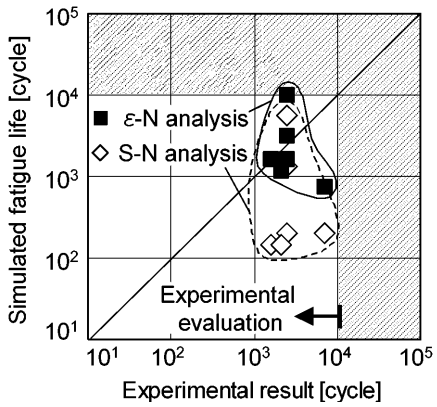

Fig. 11 Comparison of fatigue life at body panel between experiment and simulation

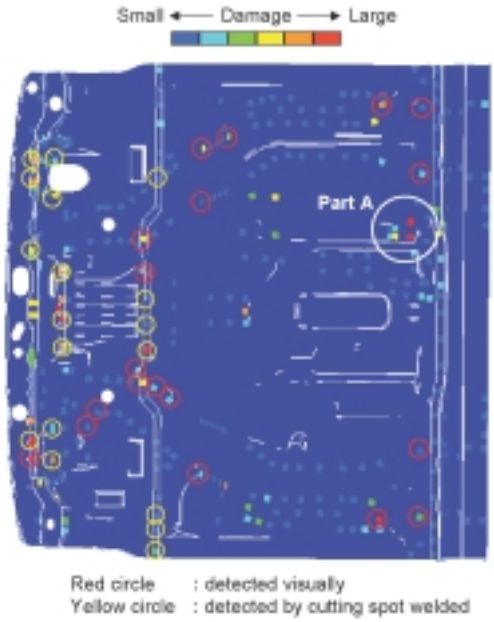

Fig. 12 Damage distribution of spot-welds

the beam element (both are important factors that significantly influence the element forces), the model assumes that the shell element is at the mid-plane of each shell and the beam element is perpendicular to the shell elements.

4.2 Verification of simulation results

The fatigue life simulation results were verified by comparing them with the experimental measurements on the prototype that was fabricated in the initial stage of development of the vehicle. Since vibration inputs within the evaluation standard range did not cause cracks in a sufficient number of locations for a significant comparison, a marginal durability test was conducted by applying inputs of magnitudes beyond the standard range and a number of cracks sufficient for the comparison were produced. The evaluation was performed separately on non-welded panel sections and spot welds.

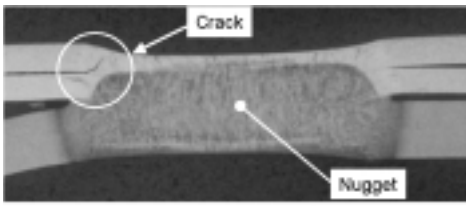

Fig. 13 Crack initiation of spot-weld

4.2.1 Non-welded panel sections

Fig. 11 compares the calculated and experimentally measured fatigue lives. In the calculation, the data length corresponding to one history iteration is regarded as one vibration cycle. The fatigue-life calculation based on the S – N analysis predicted all the cracks that also occurred in the physical experiment, but the calculated fatigue life was much shorter than the experimental result. This discrepancy may be primarily because the calculation did not support the plastic stress (strain). In fact, the fatigue life calculation that was performed based on ε – N analysis using an ε – N curve obtained by a simplified method in which the material's tensile strength and Young's modulus were used[4], showed closer agreement between the calculation and physical experiment. This implies that data on basic material properties must be accumulated in the future for accurate prediction of fatigue life by CAE simulation.

4.2.2 Spot welds

The fatigue life calculation results were compared with the results of the experiment conducted for spot welds on the floor panel. The damage distribution calculated by the fatigue life simulation is shown in **Fig. 12**. The circled points in the figure correspond to the locations where cracks occurred in the experiment. The calculation result indicates major damage in many of these locations. The points indicated by red circles correspond to the locations in which cracks were detected visually, while those indicated by yellow circles correspond to the locations where cracks were found by cutting spot welds after the experiment. **Fig. 13** is a photograph showing the cross section of a spot weld. The crack in the weld has not yet progressed to the surface, so it cannot be detected visually.

There were several locations where cracks actually occurred in the experiment but calculated damage was rather slight. One possible cause for this discrepancy is that the calculation did not support changes in the stress distribution caused by the occurrence of cracks in certain welds, and this might have prevented the simulation from predicting the high stress areas that would have consequentially occurred. Another cause may be the use of an fixed value as the coefficient when calculating the stress from the separation load and bending moment although this method requires the coefficient be varied according to the shape of the part around the weld. Other factors contributing of the discrepancy may include the effects of variation in diameter among spot welds and the initial stresses resulting from welding

that were not supported by this method that calculates the stress from the beam element forces.

Part A in **Fig. 12** is a spot weld for which the simulation predicted major damage but the physical test produced no crack. This weld spot is liable to be affected by contact. The linear-analysis-based simulation, which cannot support contact, may have created an impractically large damage output.

Many issues remain to be solved before the method can be made sufficiently accurate for quantitatively predicting fatigue life, nevertheless the present stage of the simulation can predict crack locations with reasonable accuracy.

Fig. 14 Roof deck installation

5. Application of the simulation method

The company's practice of bench durability tests for truck cabs includes, as one of the standard evaluation items, the fatigue strength under the load of a roof deck installed on the cab (including the mass of cargo on it). A cab with roof deck installed is shown in **Fig. 14**. Physical durability tests revealed presence of locations where cracks did not occur without a roof deck but did occur when the deck was installed. A simulation was therefore attempted using the method presented here to analyze factors contributing to the decrease in fatigue strength due to this change in condition.

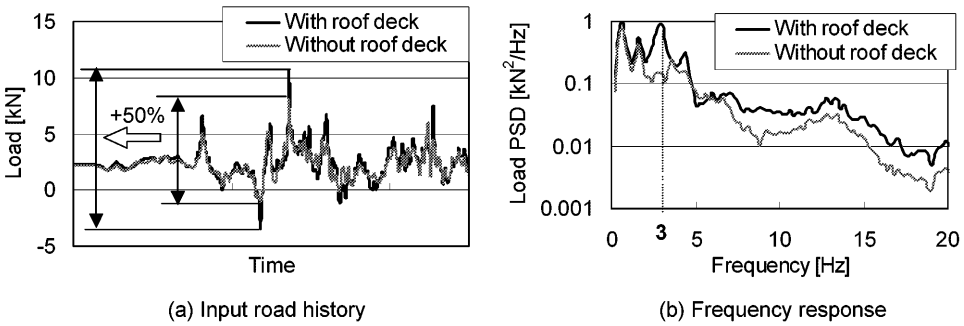

(a) Input road history (b) Frequency response

Fig. 15 Comparison of front mount force between roof deck installed cab and uninstalled cab

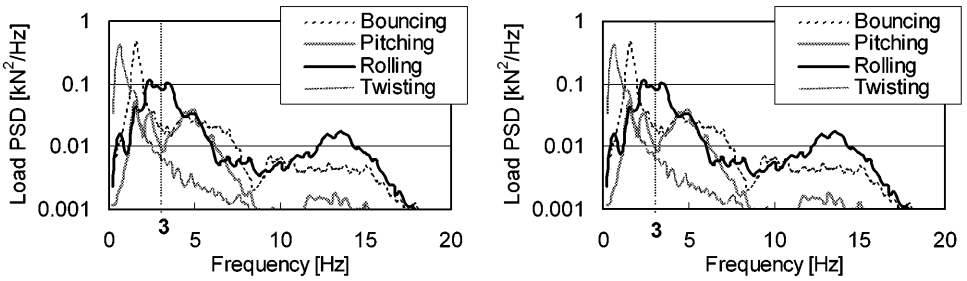

(a) Without roof deck (b) With roof deck

Fig.16 Comparison of component force frequency characteristic between roof deck installed cab and uninstalled cab

5.1 Effects of roof deck on input loads

The team first studied the difference in input loads on the cab between the two conditions, with and without the roof deck. **Fig. 15** shows the results of analyzing the input load history and the frequency response at one of the front cab mounts under the two conditions. The load history graph shows that when the cab is installed with the roof deck, the vibration amplitude increases by approximately 50 % as compared with the case without the roof deck and the frequency response graph shows that resonance occurs at around 3 Hz frequency.

The cab is supported by mounts at four locations, and so it should be appropriate to break down the vertical input loads on the cab into four component forces – bouncing, pitching, rolling, and twisting[5] – in order to study the causes of the above-mentioned findings. The frequency characteristics of each component force are shown in **Fig. 16**. The graph indicates that only rolling inputs have a peak frequency of 3 Hz when the cab is installed with the roof deck although there are no peak frequencies without the roof deck. There are no other component forces that have peak frequencies around 3 Hz. This means that installing the roof deck significantly increases rolling inputs.

5.2 Effects of roof deck on fatigue life

Next, the team studied the effects the change in input load discussed above might have on the fatigue life. The distribution of damage in a location on the cab was compared between when the location was under the roof deck load and when it was free from the load. The results showed that when the deck was installed, the magnitude of the largest damage was 20 times that

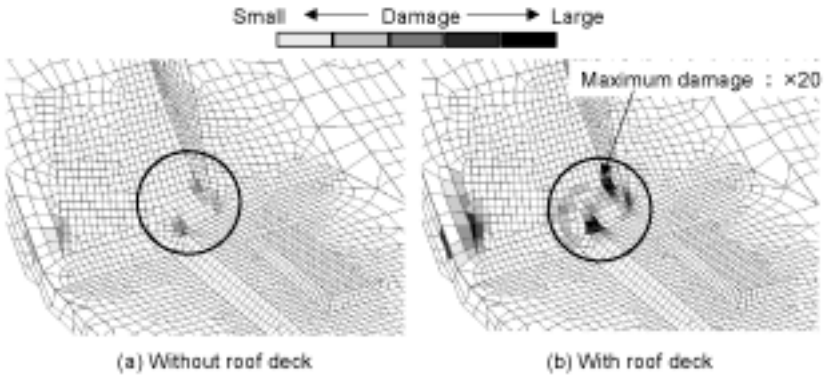

Fig. 17 Comparison of damage distribution between roof deck installed cab and uninstalled cab

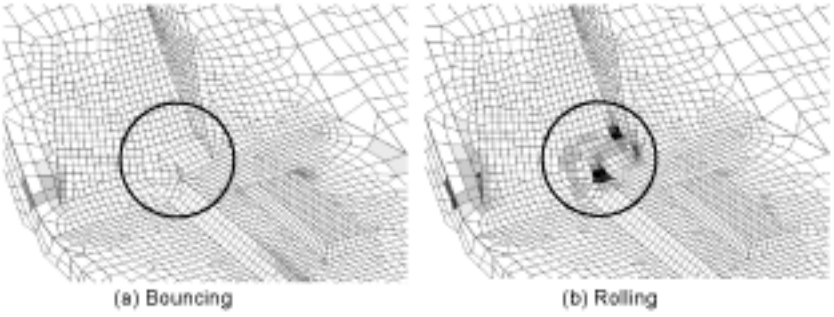

Fig. 18 Damage distribution by each component force

of the cab with no deck installed (**Fig. 17**). In order to investigate the contribution of the above-mentioned component forces to the damage at that location, a fatigue life simulation was conducted for each of the input component forces. The results are shown in **Fig. 18**. The calculation result indicates that bouncing input has little contribution but rolling input has a significant contribution to the damage. In other words, the fatigue strength of the location is largely influenced by rolling inputs.

The results of studies on the causes of cracks in a cab on which a roof deck is installed are summarized as follows:

(1) Installing the roof deck significantly increases rolling inputs.
(2) Rolling inputs contribute significantly to the fatigue strength of the investigated location.

These two facts may explain the causes of cracks.

6. Summary

This paper discussed a fatigue strength prediction method that was developed to simulate the bench durability test and examined the cases of its application. The results yielded through the research are summarized below.

(1) Multi-body simulation using an elastic body model enabled cab input loads to be calculated with sufficient accuracy for practical application.
(2) The fatigue life simulation that supported stress (strain) history allowed the locations of cracks to be predicted both in non-welded panel sections and spot welds, although the prediction was not sufficiently accurate in quantitative terms for spot welds.
(3) The study using the CAE simulation method on the effects caused by installing on the cab, a roof deck on fatigue life revealed the mechanism of changes in the input mode and changes in the crack life that resulted from the difference in the test condition.

In future studies, the team will seek to improve the accuracy of the fatigue life simulation, with the ultimate objective of building a CAE simulation system that can predict the fatigue strength under rough-road durability test conditions.

References

(1) K. Koibuchi: "Fatigue Life Prediction and it's Software", speech collection for JSAE symposium "New Proposals for Future Fatigue Endurance Evaluation of Vehicle Bodies", JSAE, 2000
(2) T. Sakamoto: "Development of Engine Rubber Mount with Hydrauic Damping", Journal of JSAE, Vol. 36, No. 12, 1982
(3) A. Rupp, K. Storzel and V. Grubisic: Computer Aided Dimensioning of Spot-Welded Automotive Structures, SAE Technical Paper 95071, 1995
(4) LMS FALANCS Theory Manual Version 2.9
(5) Y. Kondo, H. Ono and K. Hamano: "Study of Load Applied to Vehicle Body during Rough-Road Driving", Mitsubishi Motors Technical Review, NO. 1, 1988


Shinichi CHIBA


Kimihiko AOYAMA


Kenji YANABU


Hideo TACHIBANA


Katsushi MATSUDA


Masashi UCHIKURA

NEW TECHNOLOGIES

Development of New 2.4 Litre, Four-Cylinder, MIVEC Engine

Shinichi MURATA* Hiroshi TANAKA* Shigetsugu INOUE*
Takeshi INOGUCHI* Toshihiko OKA** Yasunori KUTSUNA**

Abstract

A new 2.4 litre, four-cylinder, SOHC engine was developed for compact passenger cars. This engine has a Mitsubishi Innovative Valve timing Electronic Control system (MIVEC) and incorporates design refinements such as an expanded bore and a reduced cylinder-block height. Despite being an MPI engine running on unleaded regular gasoline, it therefore delivers power and fuel consumption close to those of a premium-gasoline-fueled, DOHC, GDI* engine with continuously variable valve timing. In addition, MIVEC helps to give this new MPI engine lower exhaust emissions and smaller dimensions than a GDI engine.

***Key words**: Gasoline Engine, Variable Valve Timing System*

1. Introduction

Development of automotive technologies that address environmental and energy-related concerns is increasingly important, but demand for improvements in performance – a factor in the fundamental appeal of automobiles – is as strong as ever. When new engines are developed, variable valve timing is typically employed as a means of satisfying these conflicting requirements(1).

At the same time, automakers have a growing need to make engines lighter and more compact as a means of realizing better passive safety and greater freedom in the areas of packaging and exterior design.

All of these issues are reflected in a 2.4 litre, in-line, four-cylinder, SOHC engine recently developed by Mitsubishi Motors Corporation (MMC) for compact passenger cars. In the development program, a light, compact SOHC engine was fitted with a newly developed MIVEC system (a technology that provides multiple selectable cam profiles and thus permits control over in-cylinder flows). In addition, the combustion chambers, cylinder block, and other elements of the engine's basic structure were refined. The resulting design realizes strong in-cylinder flows and concomitantly high combustion stability, which in turn ensures superior fuel consumption and emissions performance. At the same time, it ensures maximal air intake volumes and concomitantly superior power.

Key technologies and structural features of the new engine are outlined in this paper.

2. Development targets

As a standard-setting solution to current and future needs, the new engine was developed to have the following characteristics:

(1) class-leading power and fuel consumption using unleaded regular gasoline (a reflection of users' economic priorities);
(2) sufficiently low exhaust emissions for '75 %-level reduction' classification on the basis of Japan's 2000 exhaust emissions standards; and
(3) low weight and compact dimensions.

3. Major specifications

The major specifications of the newly developed engine, whose model code is 4G69, are shown in **Table 1**, and external and cross-sectional views of the engine are shown in **Fig. 1**. In tests conducted in-house, the engine achieved maximum output of 121 kW and maximum torque of 217 Nm (**Fig. 2**). And in studies of fuel consumption, the engine achieved 10·15-mode figures in the same range as those of in-cylinder-direct-injection engines (including those produced by other companies), thus showing that it could exceed Japan's 2010 fuel-consumption standard by an ample margin (**Fig. 3**).

4. MIVEC system

4.1 Purpose of MIVEC system

The MIVEC system provides the engine with intake cams for a low-speed mode (in which the two intake valves of each cylinder have a different lift) and intake cams for a high-speed mode (in which both intake valves have equally high lift), and it selects the cams as necessary. The valve lift curves and the corresponding objectives are shown in **Fig. 4**.

When the engine speed is relatively low, the valve-lift difference boosts in-cylinder flows, thereby stabilizing combustion and realizing low fuel consumption, low emissions, and high torque. When the engine speed

* RV Powertrain Team, RV Segment Competence Center, Car Research & Dev. Office, MMC
** Basic Powertrain Dev. Dept., Car Research & Dev. Office, MMC

Table 1 Engine specifications

Engine model	4G69 MIVEC	4G64 GDI-V
Cylinder layout	In-line 4	
Bore x stroke (mm)	87.0 x 100	86.5 x 100
Displacement (L)	2.378	2.350
Compression ratio	9.5	10.8
Fuel supply	Port injection	In-cylinder direct injection
Fuel type	Regular	Premium
Valvetrain	SOHC; 16-valve; Cam profiles switching	DOHC; 16-valve; continuous cam phasing
Performance	121 kW/6000 min^{-1} 217 Nm/4000 min^{-1}	121 kW/5700 min^{-1} 230 Nm/3500 min^{-1}
Exhaust emissions compliance	75 %-level reduction of Japan's 2000 emissions standard	25 %-level reduction of Japan's 2000 emissions standard

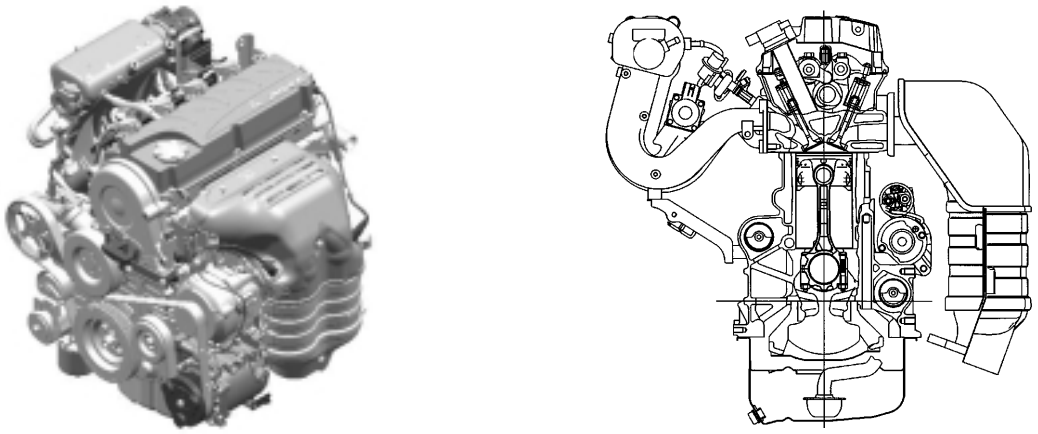

Fig. 1 Views of 4G69 engine

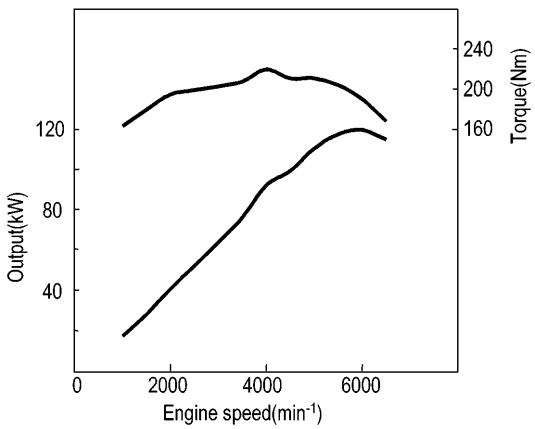

Fig. 2 Engine performance curves

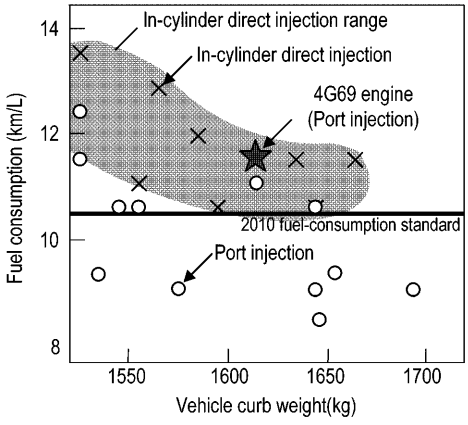

Fig. 3 10·15-mode fuel consumption

becomes relatively high, increases in the valve-open duration and valve lift yield relatively large air intake volumes and increased output.

4.2 Structure of MIVEC system

To enable adoption of the MIVEC system without revision of the basic structure of the existing SOHC cylinder head, a new cam profiles switching mechanism (an evolution of existing DOHC MIVEC technology) was employed. As shown in **Fig. 5**, the valve mechanism for each cylinder incorporates a low-lift cam and corresponding rocker arm for one intake valve; a medium-lift cam and corresponding rocker arm for the other intake valve; a high-lift cam, which is centrally located between the low-lift cam and medium-lift cam; and a T-shaped lever, which follows the high-lift cam. When the

Mode	Item	Power	Fuel consumption	Exhaust emissions (cold starting)
Low-speed	Improved combustion stability by means of reduced internal EGR	○	○	○
	Improved combustion stability by means of boosted in-cylinder flows		○	○
	Minimized friction by means of low valve lift		○	
	Improved volumetric efficiency by means of reduced spitback	○		
High-speed	Improved volumetric efficiency by means of exhaust dynamic effects	○		
	Improved volumetric efficiency by means of high valve lift	○		

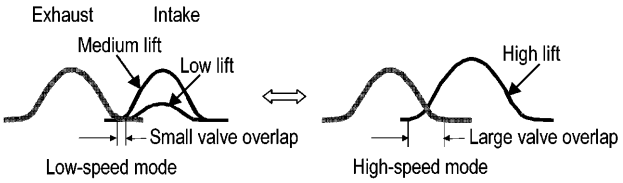

Fig. 4 Aims of MIVEC system

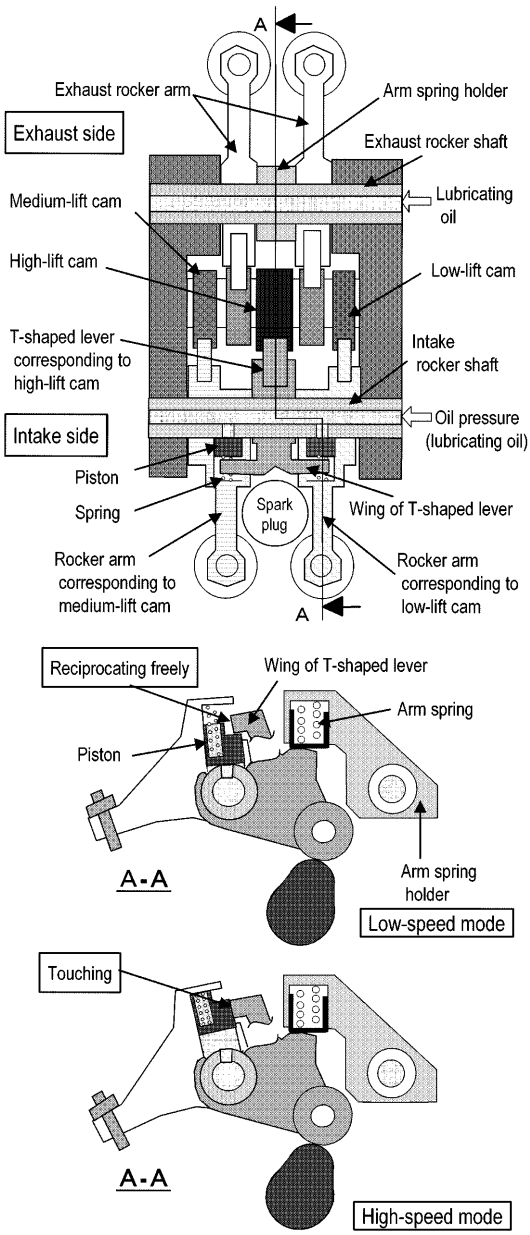

Fig. 5 Structure of MIVEC system

engine speed is relatively low, the wing of the T-shaped lever reciprocates without acting upon anything; the intake valves are respectively actuated by the low-lift cam and medium-lift cam. When the engine reaches a predetermined higher speed, pistons in the rocker arms are moved by hydraulic pressure such that the T-shaped lever pushes the back of each rocker arm; both valves are thus actuated by the high-lift cam. The rocker-arm shape and valve-lift curves were optimized through repeated behavior-structure analysis and tests conducted using the computer-analysis model shown in **Fig. 6**.

Cam profiles switching occurs at an engine speed of 3500 min^{-1} (the speed at which the torque curve yielded by the low-speed-mode cams intersects with the torque curve yielded by the high-speed-mode cam). The MIVEC system does not include a timing mechanism for cam profiles switching, so the pistons occasionally bounce back off the wing of the T-shaped lever (instead of fitting in front of it) when oil pressure is applied. High-speed-mode valve actuation thus begins with the subsequent cylinder in the engine's firing order. An accumulator incorporated into the profiles switching oil passage limits the rate of piston bounceback to 0.6 % for all four cylinders and thus promotes durability.

4.3 Benefits of MIVEC system

(1) Power

The 4G69 large-displacement four-cylinder engine has a long-stroke design for compactness. With a long-stroke design, valve-diameter increases are precluded by limits imposed by the bore. The flow velocity of intake air is thus extremely high, so increases in valve lift and port flow contribute greatly to increases in air intake volume. With the 4G69 engine, increased air intake volume was achieved by increase in valve opening area and limitation of in-cylinder flows, both of which are yielded by the high-speed cam. The resulting beneficial effect on maximum power is comparable with that yielded by the intake-air cooling and high compression ratio of a GDI engine. A breakdown of the improvement in maximum power is shown in **Fig. 7**.

(2) Fuel consumption

In operating ranges where the engine uses the low-speed cams, strong in-cylinder flows yield a homogeneous air-fuel mixture and concomitantly high combustion stability. External exhaust-gas recirculation (EGR) was thus adopted as a means of minimizing fuel consumption (**Fig. 8**). In-cylinder flow and flow coefficient typically have a tradeoff relationship, but both were maximized by means of computer analysis (**Fig. 9**) and testing based on know-how gained in GDI development.

(3) Exhaust emissions

Strong in-cylinder flows also permit a lean air-fuel

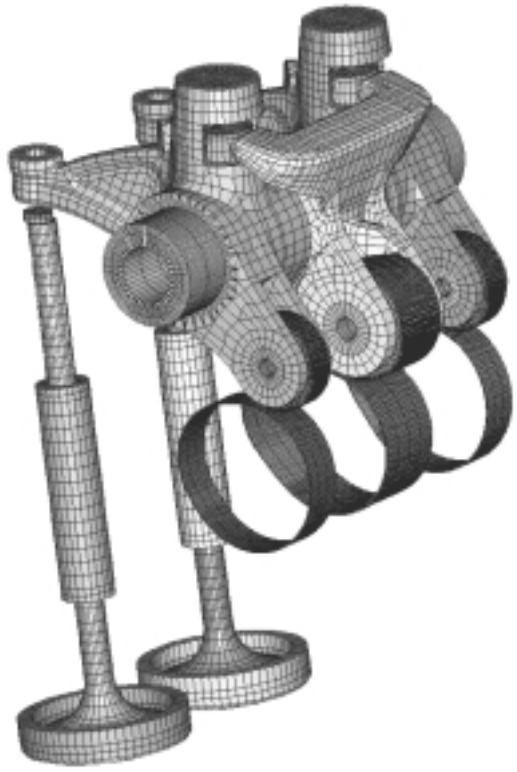

Fig. 6 Finite-element model of valvetrain

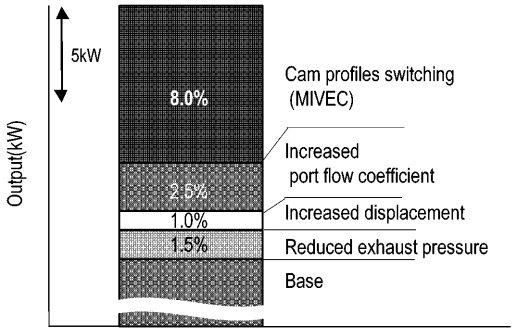

Fig. 7 Factors contributing to improved power

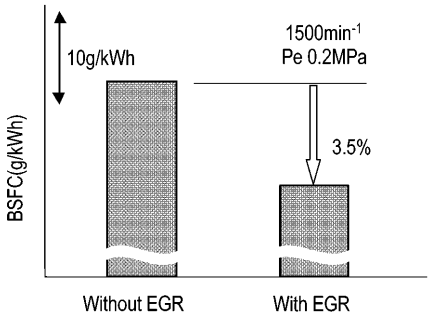

Fig. 8 Effect of EGR on fuel consumption

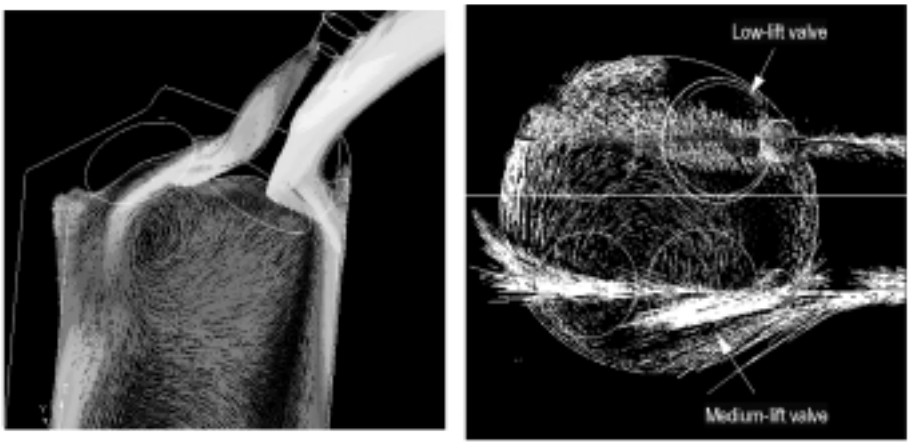

Fig. 9 In-cylinder-flow analysis

mixture and retarded ignition timing during cold starts, thereby enabling rapid exhaust-catalyst warmup (**Fig. 10**). To minimize performance losses (mainly torque losses at low engine speeds) caused by exhaust interference between cylinders, a dual-outlet exhaust manifold incorporating a front catalyst was adopted.

Consequently, exhaust emissions for '75 %-level reduction' classification on the basis of Japan's 2000 exhaust emissions standards were achieved and the potential for compliance (provided an underfloor catalyst and other items are added later) with California's Super Ultra Low Emission Vehicle standard was realized.

5. Refinement of engine parts other than valvetrain

The basic structure of the newly developed engine is the same as that of a 2.0-litre turbocharged engine used in the World Rally Championship. Durability- and reliability-related know-how gained from rallies was used to refine the new naturally aspirated engine as detailed hereafter.

5.1 Main moving parts

The pistons, connecting rods, and crankshaft were newly designed, becoming approximately 8 % lighter

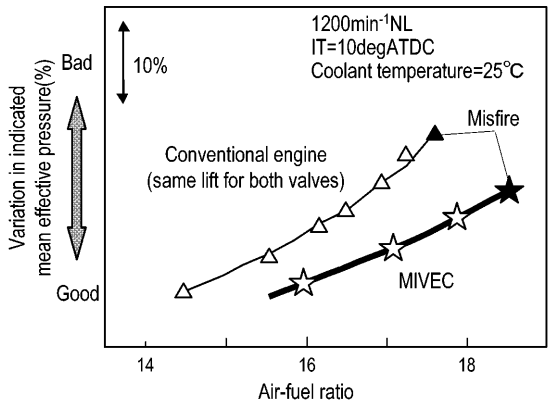

Fig. 10 Effect of MIVEC system on stability

than those of the 4G64 GDI engine. Notably, the pistons' compression height was reduced by 6 mm and the cylinder-block height was reduced accordingly. These revisions not only reduced the weight of the pistons and cylinder block but also positioned each piston's center of gravity closer to the piston pin, thereby reducing friction and piston slap.

5.2 Cylinder block and cooling system

A material thickness of 6 mm between bores (the smallest such dimension of any 2.4 litre engine) was established, permitting a 0.5 mm bore increase and concomitantly higher output performance. Also, the shape of the water holes in the top deck was optimized to enhance cooling and minimize bore deformation. Further the cooling system was given extensive improvements including a higher-efficiency water pump, a reduced water-jacket depth in the cylinder block, and an increased coolant flow velocity in the cylinder head.

5.3 Lightness and compactness

Compared with the 4G64 GDI engine, the newly developed engine was made 50 mm shorter (from top to bottom) and, including the exhaust system, more than 23 kg lighter. Its compactness and lightness make it advantageous for employment in vehicles.

6. Summary

In line with the development targets, the newly developed engine has great commercial potential. We plan to continue our development efforts, employing the engine in new vehicles to realize products that are attractive to customers.

Finally, we wish to express our gratitude to the staff of Daiwa Seiko Co., Ltd. and all other personnel, both inside and outside Mitsubishi Motors, who gave valuable assistance in the development of the new engine and its MIVEC system.

References

(1) Moritani et al: Current and Future Trends in Valve Technology, Journal of JSAE, Vol. 56, No. 2, p. 22 – 26 (2002)

(2) K. Hatano et al: Development of a new multi-mode variable valve timing engine, SAE paper No. 930878 (1993)


Shinichi MURATA


Hiroshi TANAKA


Shigetsugu INOUE


Takeshi INOGUCHI


Toshihiko OKA


Yasunori KUTSUNA

NEW TECHNOLOGIES

Development of 6M61CNG Engine for Medium-Duty Trucks

Shoji TANAKA* Masato YOSHIDA* Toshihiro KOKUBUN*
Tetsuhisa UESUGI** Toshiyuki KODAMA**

Abstract

Mitsubishi Fuso Truck & Bus Corporation has been developed a new CNG (Compressed Natural Gas) engine, in-line 6-cylinder 6M61CNG, for medium-duty trucks. This engine has been developed based on the 6M61 diesel engine. With its newly designed fuel supply system, intake system and ignition system, the engine successfully obtained ULEV (Ultra Low Emission Vehicle) level certification under the Low Emission Vehicle Certification System, proving that the exhaust emissions of the engine were reduced to at least 75 % of the 2003 regulation limit, as well as achieved the best output performance in this class.

Key words: *Compressed Natural Gas, Alternative Fuel, Spark Ignition Engine, Emission*

1. Introduction

Strong pressure for reductions in automotive exhaust emissions in urban areas has recently prompted local governments and other bodies to promote the introduction of low-emission vehicles that use alternative fuels. Among such vehicles, those that run on compressed natural gas (CNG) are attracting attention. Against this background, Mitsubishi Fuso Truck & Bus Corporation (MFTBC) recently developed the 6M61CNG engine for medium-duty trucks. Based on a diesel engine, this new CNG engine incorporates newly designed fuel-supply and intake systems that help it realize class-leading output together with emissions that are low enough for Ultra Low Emission Vehicle (ULEV) certification. It was launched in July 2002 as a powerplant for 2002-model Mitsubishi Fuso FIGHTER trucks (**Fig. 1**).

The 6M61CNG engine received ULEV approval under Japan's 7LG certification system (this is operated seven local governments in the Kanto region: the metropolitan of Tokyo, the prefectures of Kanagawa, Saitama, and Chiba and the cities of Yokohama, Kawasaki, and Chiba) in November 2002.

An overview of the 6M61CNG engine is given in this paper.

2. Development targets

Based on the highly evaluated 6M61 diesel engine, which was launched in Japan in 1999, the 6M61CNG engine was developed to have the following characteristics:

(1) Low exhaust emissions

For minimal pollution, MFTBC targeted exhaust emissions low enough for ULEV certification (at least 75 % lower than those permitted by 2003 regulations).

(2) High output performance

MFTBC aimed for the 6M61CNG engine to have the highest levels of output and torque in the class.

Fig. 1 CNG FIGHTER garbage-vehicle

(3) High reliability

MFTBC aimed to realize sufficient quality and durability to ensure breakdown-free operation throughout the vehicle's service life.

(4) Suitability for special-purpose vehicles

Garbage-collection vehicles and van-body vehicles account for approximately 90 % of CNG-fuelled medium-duty trucks, so MFTBC took steps to ensure compatibility with special-purpose vehicles (mainly garbage-collection vehicles and refrigerated vehicles).

3. Major specifications

For CNG-fuelled operation, the 6M61CNG engine differs from the 6M61 diesel engine mainly in its fuel-supply system, intake system, and ignition system, which were all newly designed.

The engine's major specifications are shown in **Table 1**. External views of the engine are shown in **Fig. 2**. And a schematic diagram of the engine is shown in **Fig. 3**.

Highly pressurized fuel from the CNG tank has its pressure reduced in three stages from 20 MPa to atmospheric pressure before being supplied to the engine.

* Engine Design Dept., Research & Dev. Office, MFTBC
** Engine Testing Dept., Research & Dev. Office, MFTBC

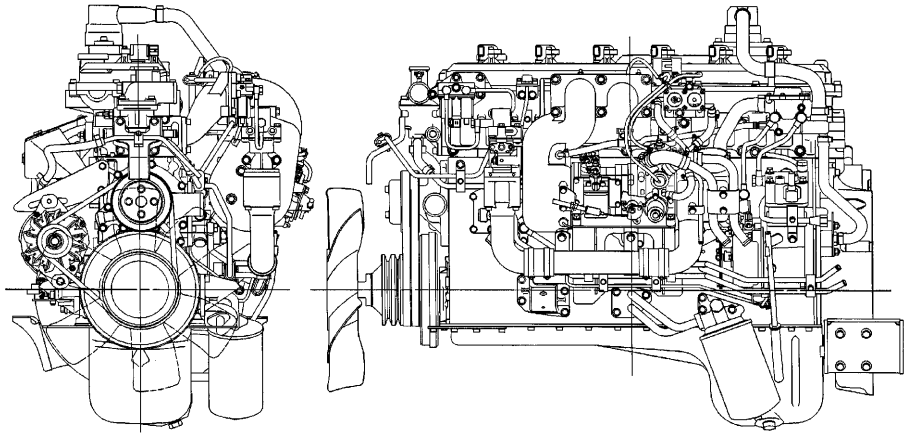

Fig. 2 External outline of 6M61CNG engine

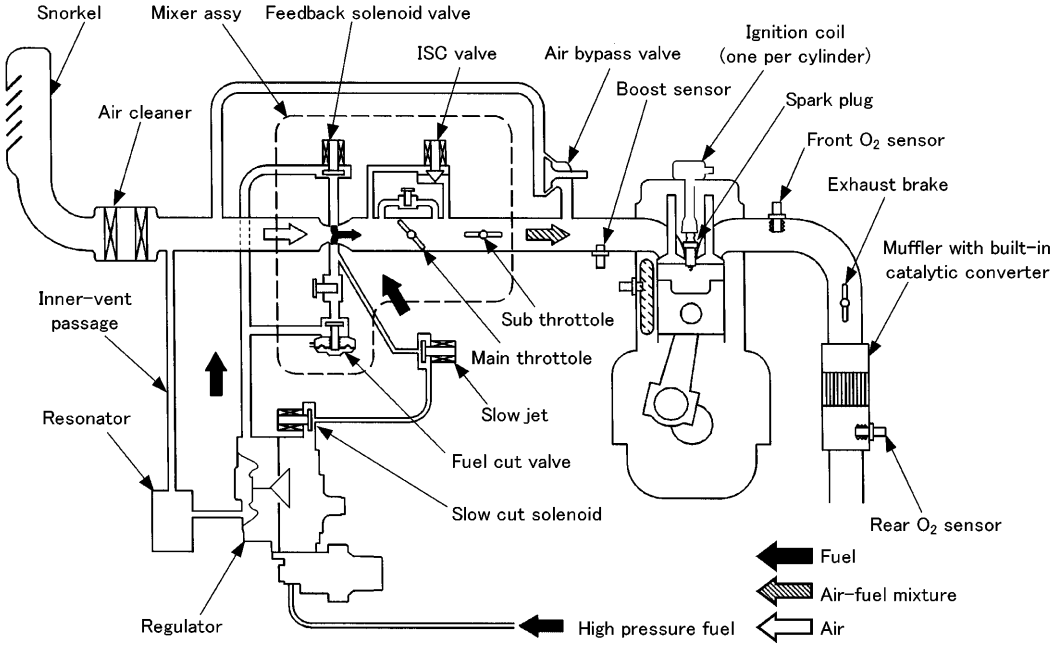

Fig. 3 Schematic diagram of 6M61CNG engine

The base engine was an 8.2-litre, six-cylinder, direct-injection diesel engine for medium-duty trucks. For CNG-fuelled operation, a speed sensor was fitted in the location formerly occupied by an injection pump and spark plugs were fitted in the locations formerly occupied by injection nozzles. The compression ratio was set at 12 to minimize the risk of knocking. The intake system was fitted with a boost sensor to enable ignition-timing correction, and the exhaust system was fitted with a muffler incorporating a three-way catalytic converter and an O_2 sensor to enable control over the air-fuel ratio.

For auxiliary braking, the exhaust brake of the diesel-engine model was retained.

4. Technical features

4.1 Performance and exhaust emissions

With the 6M61CNG engine, an electronically controlled mixer-type fuel-supply system, various other advanced technologies, and optimal tuning of all parts together enable low exhaust emissions and class-leading output performance.

Exhaust-emission limits imposed by Japan's 2003 regulations are shown in **Fig. 4**. Thanks partly to stoichiometric combustion under all speed and loading conditions and partly to the three-way catalytic converter, nitrogen-oxide (NOx) emissions and hydrocarbon (HC) emissions are low enough for ULEV certification, i.e., at least 75 % lower than those permitted by the 2003 regulations.

(1) Fuel-supply system

The fuel-supply arrangement is a mixer type in which fuel is drawn into the cylinders by the intake vacuum in a venturi section. This arrangement is advantageous in terms of simplicity and reliability.

With a mixer arrangement, the fuel supply can, unless appropriate steps are taken, become unstable if

Table 1 Engine specifications

Model	6M61CNG	6M61-2 diesel
Type	4-cycle	
No. of cylinders	6	
Valve mechanism	OHC; 4 valves per cylinder (two intake; two exhaust)	
Displacement (L)	8.201	
Bore x stroke (mm)	ϕ 118 x 125	
Max. output (kW/min^{-1})	140/2900	154/2900
Max. torque (Nm/min^{-1})	608/1000	559/1700
Compression ratio	12.0	19.0
Ignition method	Spark ignition	Compression ignition
Fuel-supply arrangement	Regulator + mixer	Injection pump + injectors
Emission-control arrangement	Three-way catalytic converter	None
Exhaust brake	Included	

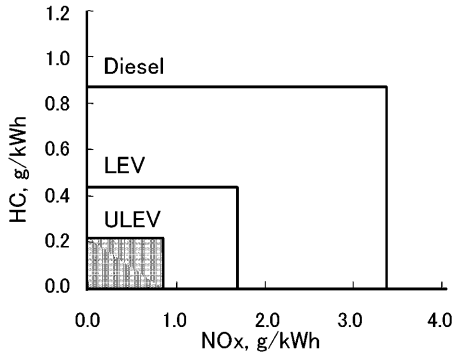

Fig. 4 Japan's 2003 exhaust-emission regulations

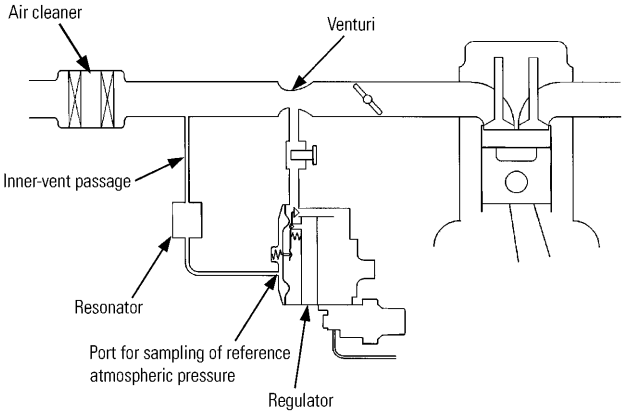

Fig. 5 Schematic of inner-vent system

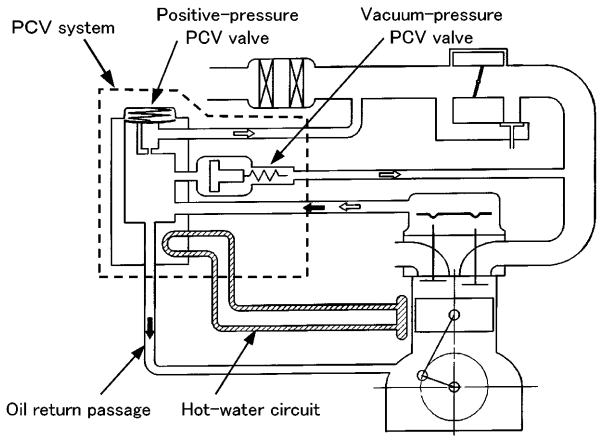

Fig. 6 Schematic of PCV system with hot-water

the venturi is affected by clogging of the air cleaner and/or by airflow generated by the vehicle's movement. Consequently, an inner-vent system, which samples the reference atmospheric pressure of pressure-regulated fuel in the intake passage between the air cleaner and the mixer and counteracts the abovementioned effects, was adopted. This system is shown in **Fig. 5**.

For minimal exhaust emissions and maximal fuel economy, output, and driveability, the air-fuel ratio is continuously adjusted in accordance with signals from the O_2 sensors and other sensors. Changes in the air-fuel ratio are achieved through adjustment of the fuel-injection amount by duty control (based on the signals) of a feedback solenoid on the mixer.

A slow jet, which supplies the engine with fuel at a pressure of 0.03 MPa (the pressure that results from the regulator's second stage of pressure reduction), was adopted as an auxiliary fuel-injection device for maximal idling stability.

Further, a sub throttle was incorporated downstream of the main throttle to serve as a wide-open-throttle (WOT) governor for overspeed prevention during WOT operation.

(2) Positive crankcase ventilation (PCV) system

A closed PCV system was adopted for compliance with regulations on crankcase emissions.

A schematic diagram of the PCV system is shown in **Fig. 6**. This system incorporates positive-pressure and vacuum-pressure PCV valves, which keep the pressure in the crankcase constant and thus ensure the reliability of seals and other parts. It also incorporates a hot-water circuit, which prevents moisture in blowby gases from condensing.

(3) Intake and exhaust systems

To maximize the energy absorbed during operation of the exhaust brake, an air bypass valve, which bypasses the throttle when the throttle is completely closed, was adopted. As a result, the highly evaluated exhaust-brake performance of the original diesel-engine medium-duty vehicle is largely replicated.

(4) Ignition system

A low-tension ignition system was adopted to maximize ignition-system reliability. A schematic diagram of this system is shown in **Fig. 7**. An ignition coil is directly mounted on the spark plug for each cylinder, and an electronic control unit (ECU) effects ignition control in accordance with the appropriate firing order and ignition timing. This arrangement is an effective means of minimizing radio-interference noise and ignition-energy losses.

Further, spark plugs with iridium center electrodes, which are highly resistant to erosion, were adopted for maximal ignition stability.

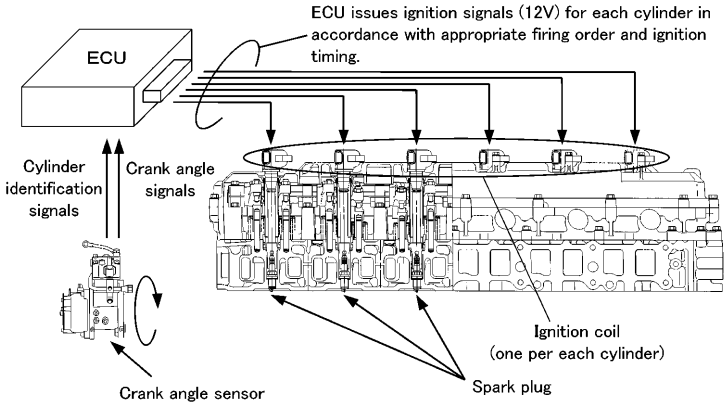

Fig. 7 Schematic of low-tension circuit spark

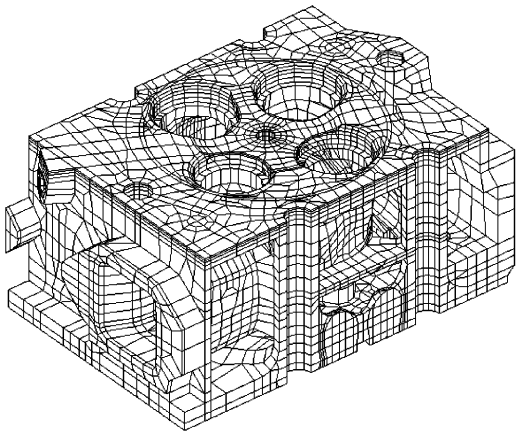

Fig. 8 Finite element model of CNG cylinder head

4.2 Reliability

Since all-stoichiometric combustion causes high combustion and exhaust temperatures, adequate high-temperature strength was ensured by the following design revisions:

Alloy cast iron was adopted for the cylinder head, and a shape that maximizes the cylinder head's thermal fatigue strength was determined through analysis of the heat deformation of flame-contact surfaces using the finite-element-method (FEM) model shown in **Fig. 8**.

A special heat-resistant cast steel with superior high-temperature strength, superior high-temperature proof stress, and superior resistance to oxidation was adopted for the exhaust manifold.

The engine valves were thermally sprayed with a Triballoy® that offers excellent wear resistance at high temperatures, and a cobalt-molybdenum-chromium sintered alloy was adopted for the valve seats.

4.3 Application to special-purpose vehicles

To meet the great need for special-purpose vehicles that have the low emissions and low noise of CNG vehicles, application-specific measures were taken as follows:

(1) Garbage-collection vehicles

To enable adjustment of the idling speed to suit garbage-collection equipment from various manufacturers, the engine was provided with a fast idle mechanism that opens and closes the throttle using a vacuum actuator while the garbage-collection equipment is running.

(2) Refrigerated vehicles

To prevent the loading applied to the engine by the refrigeration equipment from causing unwanted engine-speed fluctuations while the engine is idling, the engine was provided with an idle speed control (ISC) valve that keeps the engine running at an appropriate target speed.

5. Summary

With its various design enhancements, the 6M61CNG engine meets all of MFTBC's development targets and has high commercial viability. Its availability in medium-duty commercial vehicles means that MFTBC is able to offer CNG engines in every commercial-vehicle category (light-duty, medium-duty, and heavy-duty). The development team aims to further refine the new engine in line with feedback from users and other relevant parties.


Shoji TANAKA


Masato YOSHIDA


Toshihiro KOKUBUN


Tetsuhisa UESUGI


Toshiyuki KODAMA

NEW TECHNOLOGIES

Development of High-Performance Lithium-Ion Batteries for Hybrid Electric Vehicles

Nobuaki TAKEDA* Sadao IMAI*
Yusuke HORII** Hiroaki YOSHIDA‡**

Abstract

In view of the need to protect the global environment and save energy, there has been strong demand for the development of electric vehicles (EV) and hybrid electric vehicles (HEV). Aiming at downsizing, weight reduction, improvement of input and output performance as well as the charging/discharging efficiency of batteries, Mitsubishi Motors Corporation has been developing new, high-performance manganese based lithium-ion batteries, suitable for EV and HEV respectively, and proved their excellent performance. This paper introduces the battery mainly for HEV application.

Key words: *Battery, Electric Vehicle, Hybrid Vehicle, Electric Motor, Energy Regeneration*

1. Introduction

To make electric vehicles (EVs) and hybrid electric vehicles (HEVs) viable for general use, manufacturers must increase energy efficiency (and thus reduce fuel consumption and, with regard to HEVs, exhaust emissions) while delivering driving performance and ease of use comparable with those of conventional-engine vehicles. Improvements in propulsion-battery performance are thus crucial[(1)].

Mitsubishi Motors Corporation (MMC) and Mitsubishi Fuso Truck & Bus Corporation (MFTBC) were quick to identify lithium-ion (Li-ion) batteries as a potential means of meeting these requirements. In conjunction with Japan Storage Battery Co., Ltd., MMC and MFTBC are engaged in development of high-performance manganese-based Li-ion batteries suitable for EVs and HEVs.

Compared with lead-acid batteries and nickel-metal-hydride (Ni-MH) batteries, Li-ion batteries are superior in terms of specific energy (the amount of available energy per unit of mass or volume) and in terms of specific power (the amount of available output per unit of mass or volume). As a result, they are seen as the most promising batteries for secondary-battery applications.

MMC's and MFTBC's involvement in battery development have yielded a number of achievements: A Mitsubishi EV set a Guinness world record by covering more than 2000 km in 24 hours[(2)], and another completed a 780 km circuit of Shikoku (one of Japan's main islands) with only one charge along the way, further highlighting the growing possibilities of EVs as a means of mobility[(3)]. Also, a Mitsubishi Fuso series-hybrid heavy-duty bus (the first such bus in Japan) has been running successfully on public routes since June 2002. MFTBC has also applied its battery technology to a parallel hybrid propulsion system for the CANTER light-duty truck. This paper describes the superior performance of Li-ion batteries developed for HEVs.

2. Characteristics of Li-ion batteries

Small Li-ion batteries are widely used in mobile telephones, notebook computers, video cameras, and other electronic products owing to their high energy density. Lithium cobalt oxide is used as a positive-electrode material in these small Li-ion batteries. This material has excellent characteristics, but the high price of cobalt makes it too costly for the large batteries used in vehicles. In batteries developed for vehicles, therefore, lithium manganese oxide (a material based on manganese, which is relatively inexpensive and has a limited environmental impact) is used instead. The charging and discharging reactions in a battery of this type are shown in **Fig. 1**.

Manganese-based Li-ion batteries also have the following important characteristics for application to vehicles:

- Their energy efficiency and charging/discharging efficiency are high.
- A high single-cell voltage (three times that of Ni-MH batteries and twice that of lead-acid batteries) means the number of cells in a battery can be relatively small (advantageous with regard to numbers of parts and connections between terminals).
- The state of charge (SOC) can be sensed easily, so charging durations can be managed and driving ranges can be accurately predicted.
- Charging and discharging reactions produce relatively little heat, so a simple cooling system is adequate and operation is possible in a wide range of ambient temperatures.

* Electronics Engin. Dept., Research & Dev. Office, MFTBC
** Vehicle Research Dept., Research & Dev. Office, MFTBC
‡** Advanced Electrical/Electronics Dept., Car Research & Dev. Office, MMC

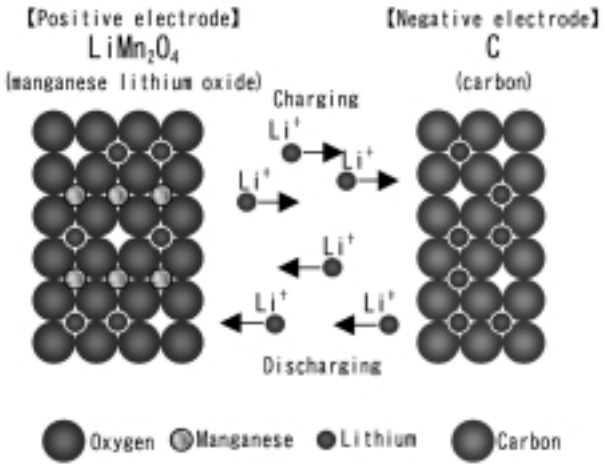

Fig. 1 Schematic of a Li-ion battery

Fig. 2 Mitsubishi ECLIPSE-EV prototype

3. Application to vehicles

3.1 EV batteries

With EV batteries, achieving longer per-charge driving ranges is the primary focus of attention. Since external chargers are needed with EVs, achieving shorter charging durations is also crucial. The LEL80MP battery, which has high specific energy and permits high-current charging, was thus developed. To verify the extent to which the LEL80MP battery could extend total driving ranges by means of longer per-charge driving ranges and shorter charging durations, the battery was fitted in a Mitsubishi FTO-EV prototype and subjected to repeated driving and charging cycles for 24 hours. At the end of the 24-hour period, the vehicle had covered a distance of 2142.3 km, which was recognized as a Guinness world record. Also, a Mitsubishi ECLIPSE-EV prototype (**Fig. 2**) equipped with the LEV95P battery, which has even better capacity and input/output characteristics, completed a 780 km circuit of Shikoku with only one charge along the way, thus indicating a driving range comparable with that of a conventional-engine vehicle. The LEV95P battery's specifications are shown in **Table 1**.

Table 1 Specifications of LEV95P cell

Voltage	(V)	3.75
Capacity	(Ah)	95
Size (W x L x H)	(mm)	94 x 170 x 114
Mass	(kg)	3.5
Specific energy	(Wh/kg)	102
Specific power*	(W/kg)	1060
Specific recharge power*	(W/kg)	280

* : with 50 % SOC after 30 s

3.2 HEV batteries

High output performance is a key requirement of HEV batteries. With a truck, bus, or other heavy-duty HEV, however, large amounts of regenerative braking power make input (charging) performance equally important. The specific power, specific recharge power, specific energy, and battery capacity must be carefully established to match the output required by the motor, the regenerative braking performance, and the hybrid system configuration (series or parallel).

3.2.1 Series HEVs

(1) Overview of AEROSTAR NONSTEP HEV bus

In June 2002, a Mitsubishi Fuso AEROSTAR NONSTEP heavy-duty bus fitted with a series hybrid drive system became the first bus of its kind to enter service on public routes in Japan. A hybrid-series drive system with a diesel-engine generator was adopted for this vehicle. One merit of this system is that it permits the use of compact drivetrain parts and thus gives a high degree of layout freedom, which in turn permits a maximal non-step floor surface (a key requirement for passenger accommodation on a public-service bus). Another reason is that it represents a low-pollution drive arrangement that can be adopted nationwide without new infrastructure facilities. The vehicle in public service is based on one exhibited at the 2000 Tokyo Motor Show. With the Li-ion battery's energy-recovery performance improved and a cooled exhaust-gas recirculation system and an oxidation catalyst added to the engine's intake and exhaust systems, it gives 43 % higher fuel efficiency and 60 % lower nitrogen-oxide emissions than an AEROSTAR NONSTEP bus with a conventional powertrain.

Since only the electric motor is used for propulsion, the battery is subjected to frequent high-current inputs and outputs. Particular importance was thus attached to low internal resistance when the battery was developed. The battery is mounted on the roof of the vehicle. A perspective view of the vehicle is shown in **Fig. 3**, and the vehicle's specifications are shown in **Table 2**.

(2) Battery performance requirements

In establishing the battery specifications, we studied data on actual operation in typical urban situations and determined the battery's required input/output performance in accordance with the required driving and braking forces. Assuming motor efficiency of 90 %, the required battery output power was then calculated as

Table 2 Specifications of AEROSTAR NONSTEP HEV bus

Vehicle			KL-MP37JM (modified)
Capacity (persons)			68
Vehicle dimensions	Overall length	(mm)	10955
	Overall width	(mm)	2490
	Overall height	(mm)	3095
Motor	Type		Induction
	Max. output	(kW)	90 x 2
Generator	Type		Permanent-magnet synchronous
	Max. output	(kW)	40
Engine	Fuel		Diesel fuel
	Displacement	(cc)	8201

Table 3 Specifications of LEC33H and LEC24H

Cell model		LEC33H	LEC24H
Nominal voltage	(V)	3.6	
Capacity	(Ah)	33	24
Size (W x L x H)	(mm)	45 x 109 x 192	
Mass	(kg)	1.9	
Specific energy	(Wh/kg)	62	45
Specific power*	(W/kg)	1440	1580
Specific recharge power*	(W/kg)	460	1000
Number of cells in battery		180	170
Total voltage	(V)	648	612
Total output*	(kW)	450	460
Total input*	(kW)	150	300

* : with 50 % SOC after 10 s

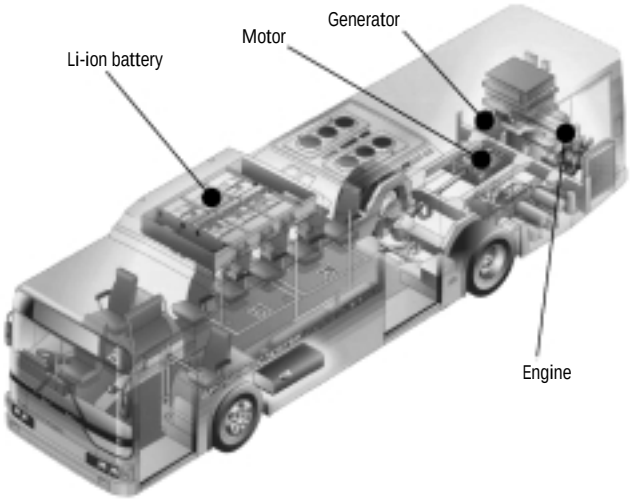

Fig. 3 Perspective view of AEROSTAR NONSTEP HEV bus

Fig.4 LEC33H and LEC24H single cell

172 kW and the required battery recharge power as 176 kW. To permit recovery of all braking energy (a key factor in the pursuit of high efficiency with the vehicle), a target of at least 176 kW was established for recharge power and output power.

With regard to the total voltage, a 650 V-class motor of the type typically used with streetcars was specified keep the current to a minimum during high-power charging and discharging. The voltage range was set to meet the inverter's requirements.

The battery was mounted on the roof to maximize the non-step floor area, so the battery's mass and size were reduced to the greatest extent permitted by the recharge and output power targets and by the required voltage range.

(3) Battery specifications

In accordance with the aforementioned conditions, the LEC33H Li-ion battery was developed and subjected to various evaluation tests in the AEROSTAR NONSTEP HEV prototype that was exhibited at the 2000 Tokyo Motor Show. The results indicated adequate battery capacity but also showed that a better brake feeling could be achieved if the battery's low-temperature input/output characteristics were improved. The LEC24H battery, an improved version resulting from steps taken to optimize ion conduction for higher input and output capability, was thus adopted for use on public routes. A single cell is shown in **Fig. 4**, and the batteries' specifications are shown in **Table 3**.

In consideration of voltage fluctuations that occur during vehicle acceleration and deceleration and of the required balance of output and capacity, the battery's rated voltage was set at 612 V (rather than the 648 V used with the prototype vehicle). Significantly improved input and output performance made it possible for the propulsion motors to be powered by the battery alone (as with an EV). It was thus possible to significantly reduce exhaust emissions, fuel consumption, and noise and to improve vehicle's dynamic performance.

3.2.2 Parallel HEVs

(1) Overview of CANTER HEV

Series hybrid drive systems are idea for public-service buses, which are driven at relatively low speeds in urban areas. By contrast, parallel hybrid drive systems are suitable for trucks, which are subjected to a wide range of operating conditions. A new parallel hybrid drive system was developed for the popular CANTER light-duty truck, in which it was combined with a small-displacement, low-emission engine and a next-generation mechanical automatic transmission. The result was a highly practical light-duty hybrid truck that realizes low exhaust emissions and low fuel consumption and is easy to drive. The CANTER HEV was exhibited at

Table 4 Specifications of CANTER HEV

Vehicle		CANTER HEV
Dimensions	Overall length (mm)	6235
	Overall width (mm)	1885
	Overall height (mm)	2820
	Wheelbase (mm)	3350
Maximum payload (kg)		2800
Engine		Newly developed low-emission diesel engine
Transmission		Electronically controlled mechanical automatic transmission
Motor	Type	Permanent-magnet synchronous
	Max. output (kW)	35

Table 5 Specifications of LEV3H cell

Cell type		LEV3H
Nominal voltage	(V)	3.6
Capacity	(Ah)	3
Size (W x L x H)	(mm)	109 x 19 x 85.5
Mass	(kg)	0.33
Specific energy	(Wh/kg)	33
Specific power*	(W/kg)	2000
Specific recharge power*	(W/kg)	1500
Number of cells in battery		80
Total voltage	(V)	288
Total output*	(kW)	48
Total input*	(kW)	36

* : with 50 % SOC after 10 s

the 2002 Tokyo Motor Show. A perspective view is shown in **Fig. 5**, and major specifications are shown in **Table 4**.

(2) Battery specifications

With a parallel hybrid drive system, the battery is used mainly for engine assistance when the vehicle starts moving and accelerates and for recovery of braking energy when the vehicle decelerates. With a relatively small vehicle, high charge/discharge performance is thus more important than battery capacity. With a truck, however, the higher vehicle weight means that quantities of charge/discharge energy are relatively large, so battery capacity is also crucial. Consequently, the LEV3H battery, which has the high specific energy of a Li-ion battery (and thus exploits the motor's performance potential) and at the same time has a good balance of weight and capacity, was adopted for the parallel hybrid drive system. A single cell is shown in **Fig. 6**, and the battery's specifications are shown in **Table 5**.

4. Test results

4.1 Specific power and specific energy

The relationship between specific power and specific energy for each of the Li-ion batteries mentioned in the preceding section is shown in **Fig. 7**[4][5]. As shown, the newly developed Li-ion batteries each offer good performance (those for EVs having high capacity and those for HEVs having high output).

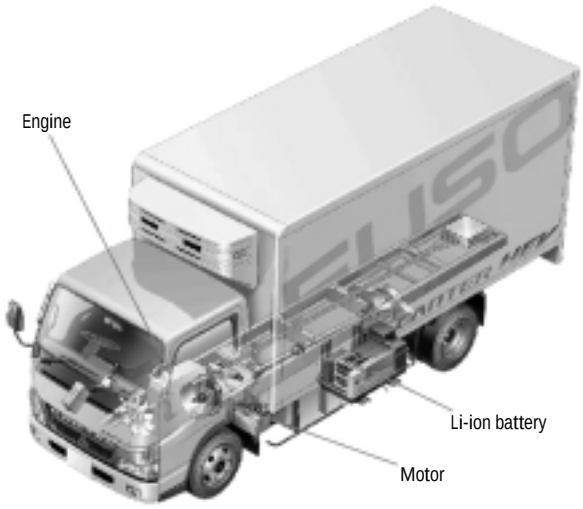

Fig. 5 CANTER HEV

Fig. 6 LEV3H single cell

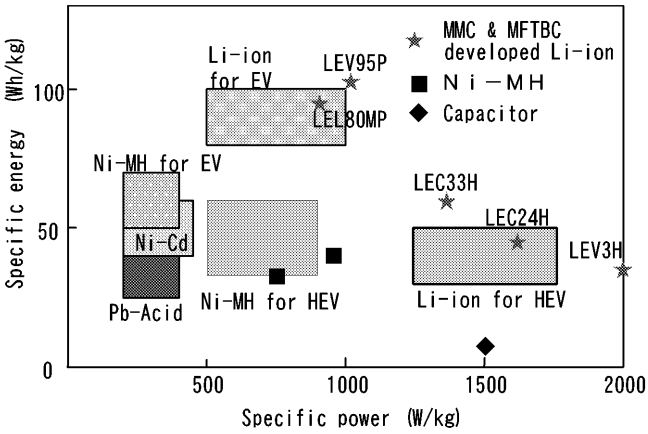

Fig. 7 Relationship between specific power and specific energy

4.2 Durability

For verification of battery durability, charge/discharge patterns that simulate driving conditions involving harsh acceleration and deceleration are employed in ongoing bench tests. Results for a LEC24H cell are shown in **Fig. 8**. Even after testing equivalent to 300000 km of operation in an actual vehicle, this cell

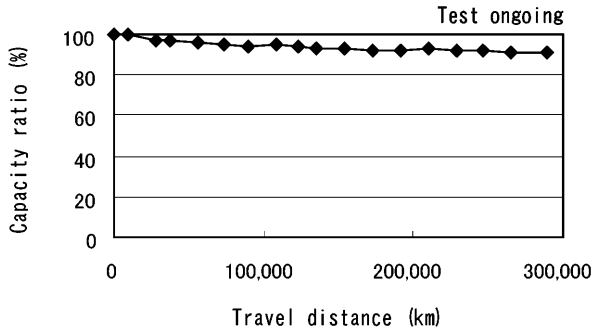

Fig. 8 Results of bench test

retains adequate capacity, thus indicating adequate durability. Questions remain over the appropriateness of estimating deterioration from discharge capacity with batteries used in HEVs, so a method for estimating deterioration with reference to charge/discharge performance is under development.

4.3 Safety and reliability

To prevent a Li-ion battery from deteriorating, the cell voltages must be managed such that the battery is neither excessively discharged nor excessively charged. Consequently, each battery unit is equipped with a control unit that transmits battery-status data and battery-failure data (determined from cell voltages, cell temperatures, and other factors) to a vehicle controller via a controller area network communication system. To enable efficient battery utilization, the control unit incorporates a cell balancer that corrects voltage differences between cells. It also controls a cooling fan mounted on each battery module.

Further, the ability to withstand the abuse items listed in **Table 6** is confirmed to ensure that the battery does not catch fire or cause any other hazard even if it becomes excessively charged or discharged in the event of a control-system fault or becomes damaged in the event of a collision. Evaluation is conducted with a 100 % SOC at room temperature.

5. Summary

The superior characteristics of Li-ion batteries were verified through achievement of EV driving ranges comparable with those of conventional-engine vehicles and through adoption of Li-ion batteries in the AEROSTAR NONSTEP HEV and CANTER HEV.

Battery characteristics significantly influence vehicle performance. With EVs, high-performance Li-ion batteries are essential for longer per-charge driving ranges. And with HEVs, they are a vital means of increasing charging and discharging efficiency, reducing fuel consumption and exhaust emissions, and eliminating the need for external charging (thus enabling easy maintenance).

With the Li-ion batteries described in this paper, MMC and MFTBC not only achieved high performance but also achieved cost savings by using a positive-electrode material based on manganese, which is inexpensive and exists in abundance.

Bearing in mind the need for an optimal balance of battery performance, battery durability, and control-system functionality, MMC will continue working with Japan Storage Battery Co., Ltd. to develop higher-performance batteries and to promote their widespread adoption.

Table 6 Abuse test item (single cell)

Item	Details
External short circuit	Wire with resistance of 0.5 mΩ is connected between positive and negative terminals for at least six hours.
Excessive discharging	Cell is discharged to 250 % of rated capacity.
Excessive charging	Cell is charged to 250 % of rated capacity.
Nail penetration	Nail with diameter of 5 mm is driven into center of cell at right angles and left for at least six hours.
Vibration	Cell is subjected to vibration test compliant with JIS D 1601 standard.

References

(1) Japan Electric Vehicle Association: JEVA Electric Vehicle Forum, 2000
(2) N. Furukawa, M. Ozaki, M. Koike, T. Fukunaga, and Y. Tanaka: EV24h Travel Distance Record Challenge, EVS-17, 2000
(3) Yoshida, Sugiura, Maeda, Furukawa, Hashiguchi, and Hayakawa: Can EV Boast Mobility ?, Mitsubishi Motors Technical Review, NO. 14, 2002
(4) Japan Electric Vehicle Association: JEVA Electric Vehicle Forum, 1999
(5) GS Technical Handbook: Lithium Ion Rechargeable Battery


Nobuaki TAKEDA


Sadao IMAI


Yusuke HORII


Hiroaki YOSHIDA

NEW TECHNOLOGIES

Development of Super AYC

Yuichi USHIRODA* Kaoru SAWASE* Naoki TAKAHASHI*
Keiji SUZUKI* Kunihiro MANABE*

Abstract

The AYC (Active Yaw Control) system installed on the LANCER EVOLUTION IV in 1996 greatly improved the cornering performance of 4WD vehicles by controlling the torque difference between right and left tires, thus equalizing the load on each of the four tires. Following the improved performance of the EVOLUTION series, further improvement of AYC functions has been desired for sports driving. We have therefore developed a new Super AYC, which increases the degree of control and improves the cornering performance as well as traction performance.

Key words: *Vehicle Dynamics, Differential Gear*

1. Introduction

The AYC system[1] directly controls the yaw moment acting on a vehicle by creating left-right differences in the driving and braking forces acting on the vehicle's rear wheels. Concomitantly uniform distribution of tire loading between the four wheels enhances the vehicle's cornering performance. Further, the system's operation does not conflict with the driver's acceleration and braking inputs since torque transfers depend only on the torque difference between the left and right wheels and cause almost no change in the total driving and braking forces of the four wheels. Users with any level of driving skill can thus enjoy system's benefits. The system has been highly evaluated since its initial adoption in the Mitsubishi LANCER EVOLUTION IV in 1996.

The AYC's control processes have been fine-tuned a number of times to enhance cornering performance in line with the LANCER EVOLUTION's year-by-year evolution. As the dynamic performance potential of the vehicle has been increased, however, the system's capacity has become inadequate to fully exploit it. The need for a system permitting higher levels of cornering performance and traction performance has become particularly critical for motorsport applications.

To address this situation, Mitsubishi Motors Corporation has developed the Super AYC, which is capable of creating greater torque differences, i.e., greater torque transfers, between the left and right wheels, thereby providing the car with higher cornering performance and higher traction performance. This report describes the technical features of the Super AYC.

2. Optimum torque transfer amounts

Early in development of the Super AYC, target torque transfer amounts were determined by means of simulations using an analytical technique known as the 'dynamic square' method[2].

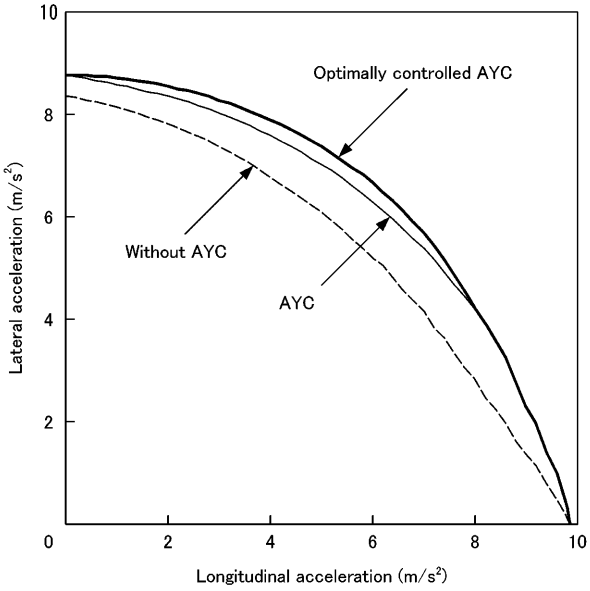

Fig. 1 Acceleration cornering performance

Fig. 1 shows the simulated maximal acceleration cornering performance obtained using an AYC model containing no torque transfer amount limitations on the assumption that the torque difference between the left and right wheels is optimally controlled in accordance with vehicle conditions. It is compared with the acceleration cornering performances of vehicles with and without the AYC. Each of the curves represents the maximum lateral acceleration at which driving is possible with a given longitudinal acceleration rate condition.

The optimally controlled AYC can provide a cornering performance augmentation domain 25 % larger than that provided by the AYC. Since this optimally controlled AYC requires a torque transfer amount 1.8 times as large as the AYC's torque transfer amount, this amount was taken as the target and research was conducted to identify methods for achieving this target.

* Powertrain Dev. Dept., Car Research & Dev. Office, MMC

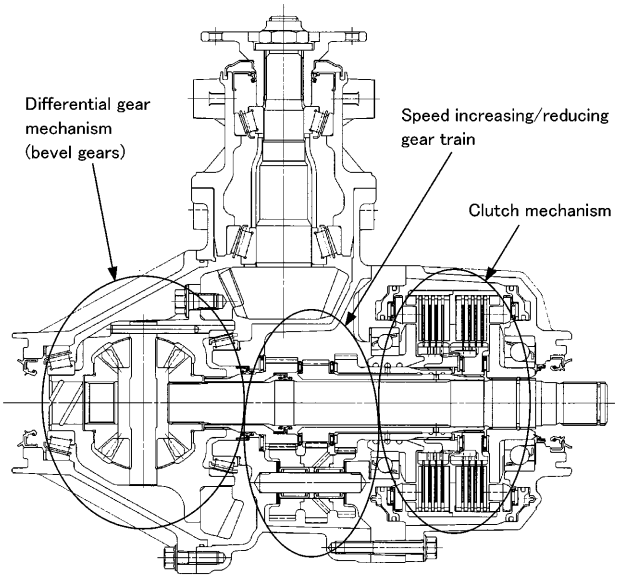

Fig. 2 Cross-sectional view of AYC

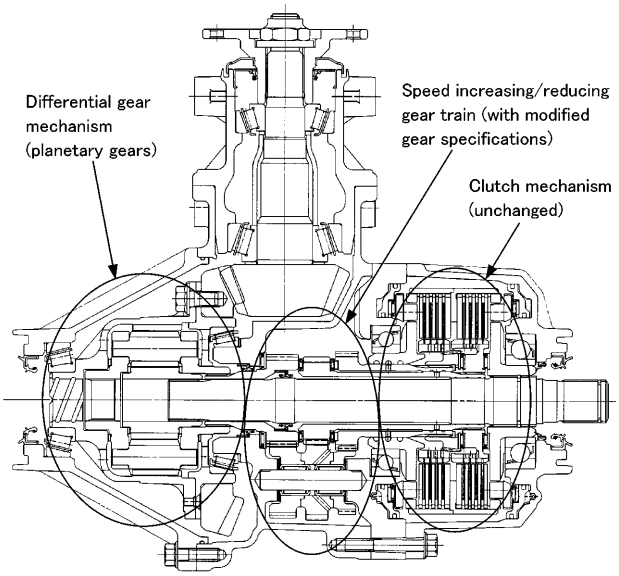

Fig. 3 Cross-sectional view of Super AYC

3. Methods for increasing torque transfer amount

The AYC is a case-to-shaft torque transfer system including a speed increasing/reducing gear train and a clutch mechanism between the input shaft and right axle shaft of the differential gear section (**Fig. 2**).

One conceivable method for increasing the torque transfer amount is to increase the clutch-transmitted torque by, for example, increasing the number of clutch plates, increasing the clutch friction area diameter, or increasing the pressure receiving area of the piston. But attaining the target torque transfer amount by this method would necessitate an increase in clutch size and modification of many clutch components. In addition, the strength of the speed increasing/reducing gear train would have to be increased to accommodate the increased clutch-transmitted torque.

The method actually selected for the Super AYC to increase the torque transfer amount while keeping the size increase and related component modifications to a minimum is a shaft-to-shaft torque transfer arrangement that transmits torque between the left and right axle shafts. This arrangement potentially allows a torque transfer amount twice as large as that allowed by the original system, and it was realized simply by means of a change in the differential mechanism from bevel gears to planetary gears and by modification of the specifications of the speed increasing/decreasing gear train. (**Fig. 3**).

4. Torque transfer mechanism

The mechanism by which the torque transfer amount is increased with the shaft-to-shaft arrangement is discussed hereafter.

Table 1 shows the respective torque paths of the original AYC and Super AYC. The symbols used in this table are interpreted as follows: Ti = input torque; Tl = left wheel torque; Tr = right wheel torque; Tcl = left clutch torque; Tcr = right clutch torque; ρl and ρr = speed increasing/reducing gear ratios when the left clutch and right clutch, respectively, are used.

First, the torque difference ΔT between the left and right wheels is calculated for the previous, case-to-shaft AYC. When the left clutch torque Tcl is made active and the torque is transferred to the left wheel,

$$\begin{aligned} Tl &= (1/2) \cdot (Ti + \rho l + Tcl) \\ Tr &= (1/2) \cdot (Ti + \rho l + Tcl) - Tcl \\ \Delta T &= Tl - Tr = Tcl \end{aligned} \quad (1)$$

When the right clutch torque Tcr is made active and the torque is transferred to the right wheel,

$$\begin{aligned} Tl &= (1/2) \cdot (Ti - \rho r \cdot Tcr) \\ Tr &= (1/2) \cdot (Ti - \rho r \cdot Tcr) + Tcr \\ \Delta T &= Tr - Tl = Tcr \end{aligned} \quad (2)$$

From equations (1) and (2), it can be seen that the clutch torque in the AYC is equal to the torque difference between the left and right wheels.

In the shaft-to-shaft "Super AYC", when the left clutch torque Tcl is made active and the torque is transferred to the left wheel,

$$\begin{aligned} Tl &= (1/2) \cdot Ti + \rho l \cdot Tcl \\ Tr &= (1/2) \cdot Ti - Tcl \\ \Delta T &= Tl - Tr = (\rho l + 1) \cdot Tcl \end{aligned} \quad (3)$$

When the right clutch torque Tcr is made active and the torque is transferred to the right wheel,

$$\begin{aligned} Tl &= (1/2) \cdot Ti - \rho r \cdot Tcr \\ Tr &= (1/2) \cdot Ti + Tcr \\ \Delta T &= Tr - Tl = (\rho r + 1) \cdot Tcr \end{aligned} \quad (4)$$

Table 1 Torque flow of AYC

	Torque transfer to left wheel	Torque transfer to right wheel
AYC	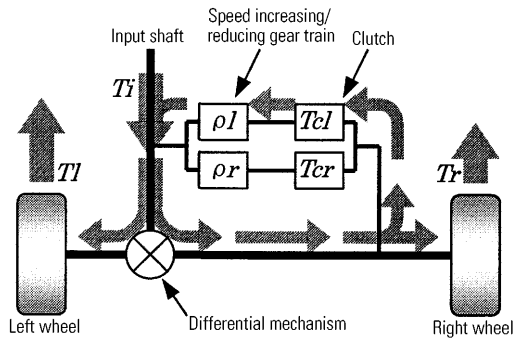	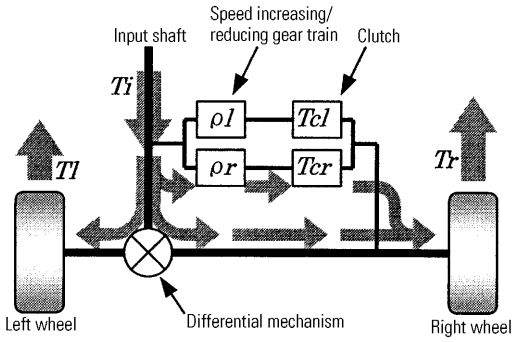
Super AYC	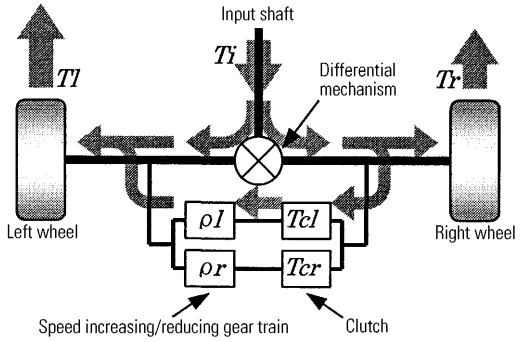	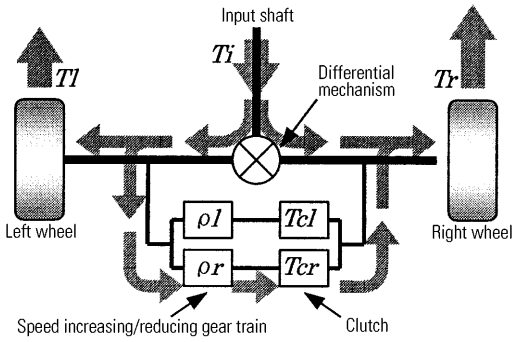

From equations (3) and (4), it can be seen that the torque difference ΔT of the Super AYC depends on the speed increasing/reducing gear ratio values ρl and ρr.

There follows a discussion of the speed increasing/reducing gear ratios ρl and ρr. In the Super AYC, two pseudo left-axle-connected shafts are formed, one having a speed equivalent to the left axle shaft speed reduced by the gear ratio ρl of the speed increasing/reducing gear train (which is connected to the left axle shaft) and the other having a speed equivalent to the left axle speed increased by the gear ratio ρr of the speed increasing/reducing gear train. A left clutch is provided between the former pseudo shaft and the right axle shaft, and a right clutch is provided between the latter pseudo shaft and the right axle shaft. Since these slip-coupled clutches are capable of transmitting torque from the high-speed side to the low-speed side, engaging the left clutch during straight-ahead driving enables the torque to be transferred to the left axle shaft and engaging the right clutch during straight-ahead driving enables the torque to be transferred to the right axle shaft. Also during cornering, torque transfer to the left wheel and torque transfer to the right wheel are both possible (albeit not simultaneously) as long as the speed difference between the left and right wheels is smaller than the amount of increase or decrease of speed created by the speed increasing/reducing gear train, but when the speed difference between the left and right wheels becomes so large that the speed difference at the clutch exceeds zero and reverse rotation starts taking place, torque transfer is possible to only one of the wheels.

With the Super AYC, the gear ratios of the speed increasing/reducing gear train are set so that torque transfer is possible to both the left and right wheels within the range where the speed difference between the left and right wheels does not exceed 20 % of the input shaft speed. This range corresponds to a turning radius of 7.5 m or greater.

The gear ratios of the speed increasing/reducing gear train when the vehicle is making a turn within this range are calculated as follows:

If Ni is the input shaft speed, Nl is the left wheel speed, and Nr is the right wheel speed, the relationship between these speeds is expressed by

$$Nl + Nr = 2Ni \quad (5)$$

When the vehicle is making a right turn ($Nl > Nr$) with the left-right wheel speed difference at 20 % of the input shaft speed, the following relationships must hold true for the left clutch speed difference to be zero.

$$Nl - Nr = 0.2Ni \quad (6)$$
$$Nr = Nl / \rho l \quad (7)$$

From equations (5), (6), and (7), $\rho l = 1.22$.

Similarly, when the vehicle is making a left turn ($Nl < Nr$) with the left-right wheel speed difference at 20 % of the input shaft speed, the following relationships must hold true for the right clutch speed difference to be zero.

$$Nr - Nl = 0.2Ni \quad (8)$$

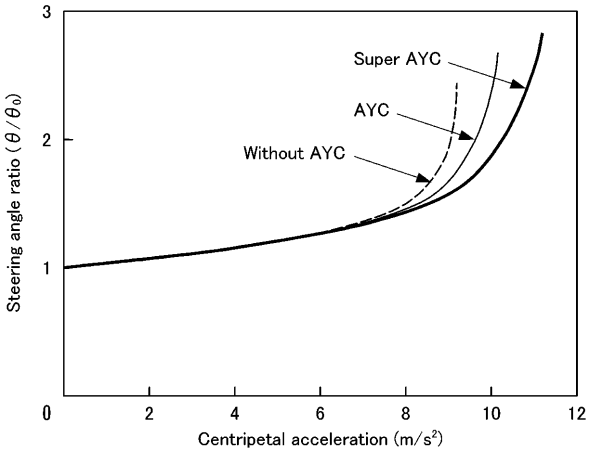

Fig. 4 Constant-radius cornering characteristics

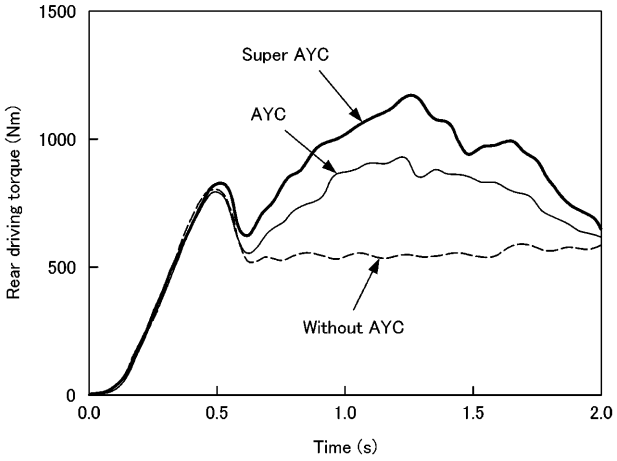

Fig. 5 Rear driving torque at start on split-μ road surface

$$Nr = Nl / \rho r \quad (9)$$

From equations (5), (8), and (9), $\rho l = 0.82$.

From the ρl and ρr values and equations (3) and (4), the left-right wheel torque difference ΔT of the Super AYC is determined as follows:

When the left clutch is engaged: $\Delta T = 2.22\ Tcl$
When the right clutch is engaged: $\Delta T = 1.82\ Tcr$

Although the left-right wheel torque difference for the left clutch torque is not identical to that for the right clutch torque, the target torque transfer amount (1.8 or more times as large as that of the conventional AYC) has been achieved.

5. Control outline

AYC control processes consist of feedback control, whereby the actual wheel speeds are made close to a reference left-right speed difference (which is determined from the steering wheel angle and vehicle speed), and feedforward control, which ensures that the system responds well to the driver's inputs.

These two control methodologies were carried over from the AYC to the Super AYC, but refinements (mainly in the feedback control) were made to realize a more natural operating feel together with improved cornering performance.

6. Verification of system's effects using actual vehicles

The effects of the Super AYC's superior torque transfer capability were verified using actual vehicles.

Fig. 4 shows the cornering characteristics of the vehicles while tracing a circle with a constant 30 m radius and at the same time gradually increasing in speed. The larger torque transfer amount of the Super AYC evidently yielded superior outer-limit cornering performance. **Fig. 5** shows the total rear wheel driving torque during a standing start on a split-μ road surface. The greater torque transfer capability of the Super AYC system evidently yielded higher rear wheel driving torque and superior traction performance.

7. Summary

By means of a change in the torque transfer method, the conventional AYC was transformed with minimal component modification into a new system capable of providing a sufficient torque transfer amount to meet demand for higher cornering performance and traction performance.

The development team will continue working to develop new powertrain systems in pursuit of further improvements in vehicles' dynamic performance.

References

(1) Sawase et al: Development of Active Yaw Control System, Journal of JSAE, Vol. 50, No. 11, 1996
(2) M. Kato et al: Study on Vehicle Dynamics in Marginal Condition Using Dynamic Square Method, IPC-8, 9531020, 1995


Yuichi USHIRODA


Kaoru SAWASE


Naoki TAKAHASHI


Keiji SUZUKI


Kunihiro MANABE

NEW TECHNOLOGIES

Development of Magnet Compound Type Seat-Suspension

Satoshi KAWAZOE* Akio YASUDA** Shinji YAMAGUCHI**

Abstract

Small trucks have severely limited freedom of layout in the cab interior, so the space for the suspension to be installed under the seat is also limited. As the conventional seat suspension utilizing coil springs and torsion bars does not have a sufficient working stroke, the setting has been rather hard with a high spring constant. Recently, we have successfully developed a new seat suspension that offers softer, better riding comfort, yet it occupies even less space than the conventional type suspension. This was achieved by utilizing the combination of a magnetized coil spring with non-linear spring characteristics and a torsion bar with linear spring characteristics. This paper introduces the new seat suspension.

Key words: *Truck, Seat, Riding Comfort, Magnet*

1. Introduction

As anyone who has played with magnets as a child is aware, unlike poles attract each other and like poles repel each other, the attraction or repulsion becoming stronger as the poles are brought closer together. The attraction and repulsion between poles is fundamental to devices that work using magnetism.

The performance available from permanent magnets was dramatically increased in 1984 with the development of a magnetic material made from neodium (Nd), iron (Fe), and boron (B). Since then, Nd – Fe – B permanent magnets have been used for an increasingly wide range of purposes in electrical appliances, medical equipment, automobile engines, and other products (**Fig. 1**[(1)]).

Permanent magnets also have possibilities for seat -suspension. Vibration-absorption arrangements for seat-suspension conventionally employ either compressed air or metal springs. Air-suspension generally allows a low spring constant, and it allows easy compensation for weight differences between users by means of adjustment of the pressure in the air-suspension chamber. On the downside, air-suspension is costly and requires considerable space for installation. And with light-duty trucks, which generally lack on-board compressed-air supplies, it cannot be used unless a dedicated source of compressed air is also provided.

Seat-suspension employing metal springs (typically coil springs and/or torsion bars) also has shortcomings: Since the spring characteristics are linear, a location that does not provide space for an adequate stroke generally necessitates a high spring rate, resulting in a relatively hard ride.

Mitsubishi Fuso Truck & Bus Corporation avoided these limitations with the magnetic spring arrangement that it recently developed for seat-suspension: Non-linear characteristics provided by the magnetic spring are combined with the linear characteristics of auxiliary metal springs, permitting a low spring rate that yields a comfortable ride despite a short stroke.

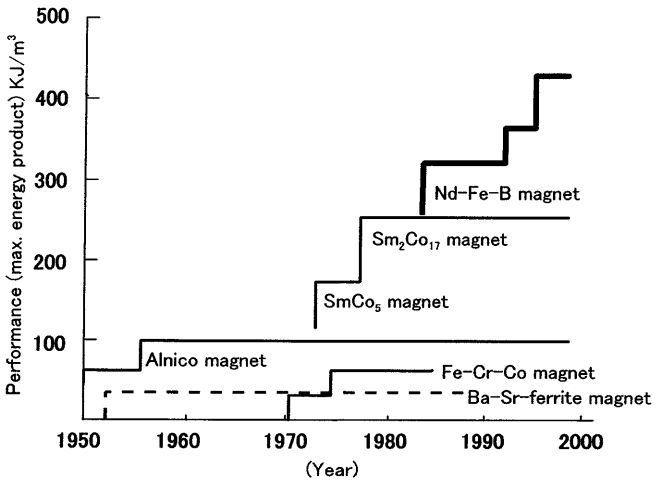

Fig. 1 Development of permanent magnet

2. Development goals

For maximal headroom in the new Mitsubishi CANTER, the hip point was set 15 mm lower than in previous models. Since the space available under the seat was reduced as a result, it was not possible to achieve a comfortable ride by using a conventional coil-spring seat-suspension system. A magnetic seat-suspension system whose non-linear spring characteristics permit both compact dimensions and superior ride comfort was thus developed.

* Cab Design Dept., Research & Dev. Office, MFTBC
** Function Testing Dept., Research & Dev. Office, MFTBC
** Vehicle Research Dept., Research & Dev. Office, MFTBC

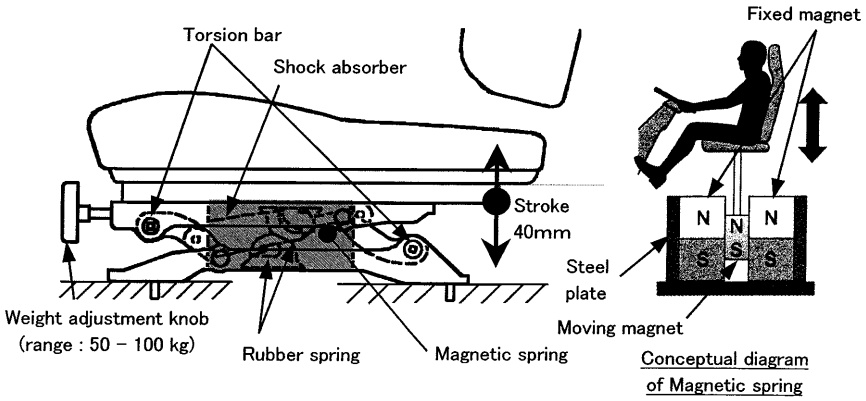

Fig. 2 Structural outline

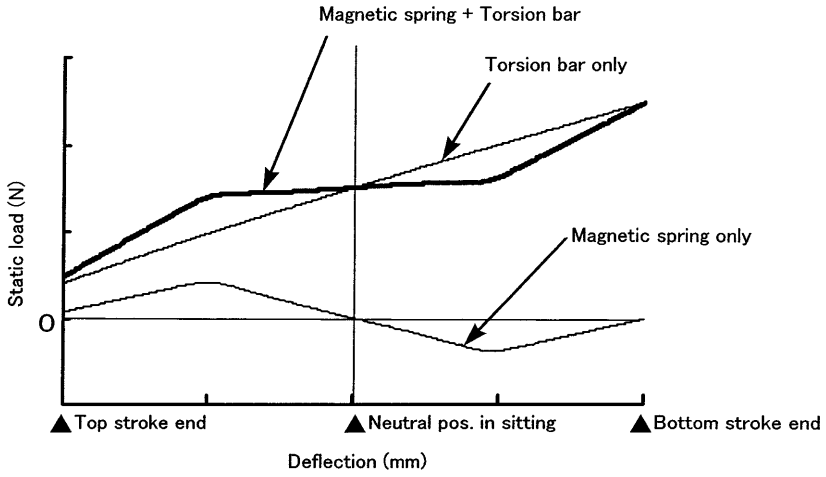

Fig. 3 Static load – deflection characteristic

Table 1 Specification comparison

		Magnetic suspension	Coil-spring suspension
Method of vibration absorption & damping		Magnetic spring + Torsion bar + Shock absorber	Coil spring + Torsion bar + Shock absorber
Spring constant	(N/mm)	7.8 – 8.8	14.8 – 15.8
Overall stroke	(mm)	40	60
Downward stroke	(mm)	25	40
Damping force of shock absorber	(N/0.3 m/s)	Extension: 686 Compression: 1372	Extension: 1029 Compression: 1764
Weight adjustable range	(kg)	50 – 100	50 – 90
Mass of unit	(kg)	10.0	9.5

3. Structure and characteristics

A magnet attached to the seat (moving magnet) moves up and down between left- and right-hand floor-mounted magnets (fixed magnets), producing spring forces of particular non-linear characteristics (**Fig. 2**).

Magnetic forces balance when the seat occupied by the driver is at the neutral point. At a seat position higher or lower than the neutral point, the magnetic spring produces an upward or downward non-linear force, respectively. The magnetic spring is combined with two torsion bars (auxiliary springs) to enable a low spring constant (and a concomitantly soft ride) when the seat is occupied (**Fig. 3**).

To soften the shock caused by bottoming at the end of the stroke, rubber springs are located on the left- and right-hand links (one upper rubber spring and one lower rubber spring on each side). The torsion bars permit stepless adjustment for driver-weight variations in a range from 50 kg to 100 kg.

The specifications of the magnetic seat-suspension system and the specifications of a conventional coil-spring seat-suspension system are compared in **Table 1**. As shown, the spring constant in the vicinity of the neutral point is approximately 50 % lower, i.e., softer, with the magnetic system.

4. Results of evaluation

4.1 Results of bench tests

For a ride-comfort comparison, the magnetic seat-suspension system and a conventional coil-spring seat-suspension system for light-duty trucks were each set on a bench-mounted shaker and subjected to displacement inputs corresponding to vehicle operation at 70 km/h on Metropolitan Expressway in Japan. As shown in **Fig. 4**, the magnetic system yielded both lower resonant frequency (see ① in **Fig. 4**) and lower peak transmissibility (see ② in **Fig. 4**) than the coil-spring system. The magnetic system also comprehensively suppressed transmissibility in the 3 – 15 Hz range (see ③ in **Fig. 4**). (Vibration in this frequency range is particularly easy to feel.)

The two seat-suspension systems were also subjected to displacement inputs corresponding to vehicle

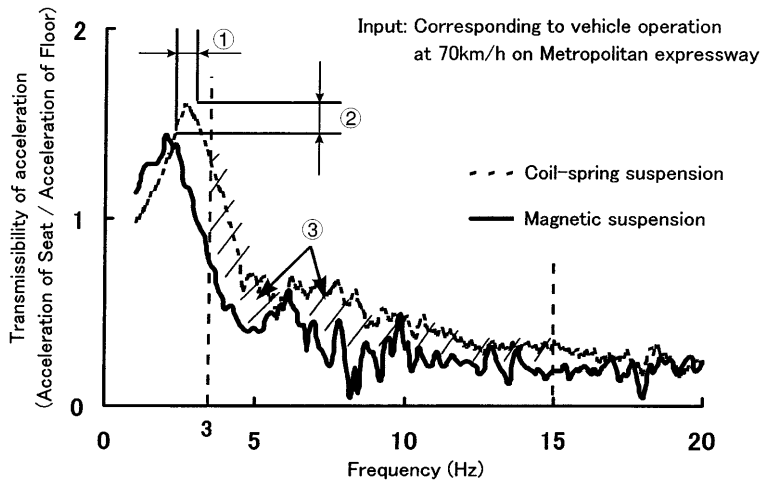

Fig. 4 Bench test of riding comfort (1)

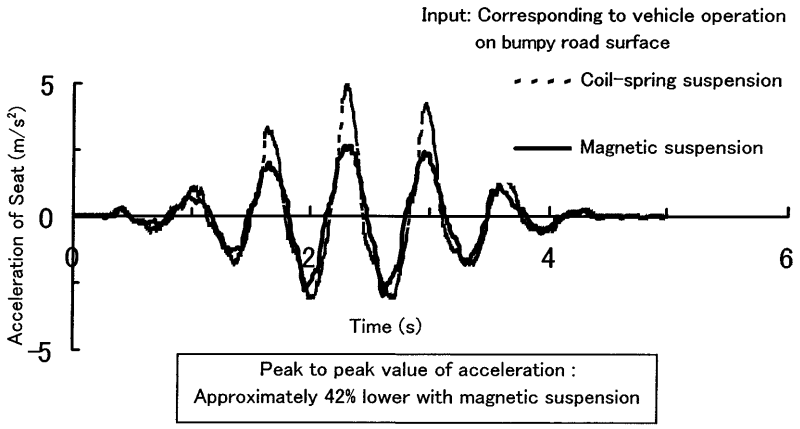

Fig. 5 Bench test of riding comfort (2)

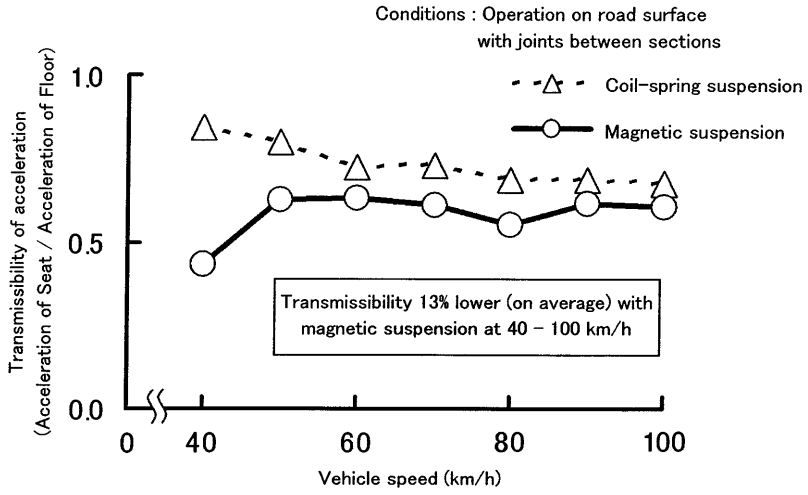

Fig. 6 Vehicle test of riding comfort

operation on bumpy road surfaces, and compared in terms of acceleration. As shown in **Fig. 5**, peak-to-peak values were approximately 42 % lower with the magnetic system and there was no deterioration in damping.

With regard to durability, magnetic spring and related links, torsion bars, and shock absorbers in the magnetic system remained free of abnormalities after 500000-cycle vibration tests.

4.2 Results of vehicle tests

The acceleration transmissibility at every vehicle speed was measured with each suspension system on a road surface with joints between sections (the kind of surface found on elevated roads), and the results were compared. As shown in **Fig. 6**, the average acceleration transmissibility of the magnetic system at speeds in the 40 – 100 km/h range was 13 % lower than that of the coil-spring system.

The results of evaluation of ride feeling during actual vehicle operation can be summarized as follows: ① On a smooth road surface, the magnetic system gave a sense of smooth movement over the entire stroke by lower spring constant and lower friction, resulting in superior ride comfort. ② On a road surface with joints between sections, the magnetic system's seat acceleration was lower, resulting in superior ride comfort. ③ On a bumpy road surface, bottoming could occasionally be felt toward the end of the magnetic system's stroke, but damping was good and there was no abrupt shock. Overall, the magnetic system's ride feeling was always comparable to or better than that of the coil-spring system.

5. Resolution of concerns

The use of permanent magnets gave rise to concern about leakage of magnetic flux, so the extent of leakage was verified.

The magnetic spring is constructed such that the permanent magnets are covered by steel plating. Magnetic flux flows within the plating, so the plating effectively forms a shield that minimizes leakage. As shown in **Table 2**, it was confirmed that leaking magnetic force did not exceed 0.33 mT (3.3 gauss) (well below the reference value of 0.5 mT (5 gauss) for cardiac pacemakers[2]). It was thus confirmed that leakage had no health effects.

It was also confirmed that tools, bolts, nuts, and other metallic items did not stick to the magnetic spring. Not even a paper clip weighing approximately 0.3 g was attracted strongly enough to stick. Further, a cover

Table 2 Measured value and reference value of magnetic force

	Location of measurement	Result
Measured leakage of magnetic flux	Upper surface of Cushion pad	Max. 0.13 mT (1.3G)
	Front surface of Suspension	Max. 0.27 mT (2.7G)
	Side surface of Suspension	Max. 0.33 mT (3.3G)
	Devices	Reference value
(Reference data) Devices affected by magnetism	Bank card, Wristwatch	Not more than 2.0 mT (20 G)
	Magnetic tape, CPU	Not more than 1.0 mT (10 G)
	Cardiac pacemaker	Not more than 0.5 mT (5 G)

mT: millitesla; G: gauss

made of non-woven fabric was fitted over the entire magnetic spring to keep foreign objects out.

With regard to deterioration of the permanent magnets over time, measurements taken by the magnet manufacturer showed that the demagnetization coefficient after 10 years was no greater than 1 %. It was thus confirmed that deterioration in magnetic-spring performance was not an issue. Further, a nickel coating was applied to the magnets to prevent rust from forming on them. After 500 hours of salt-spray testing, it was confirmed that no rust had formed and that no change in magnetic force had occurred.

6. Summary

A magnetic seat-suspension system for trucks (the first such system) was developed and was adopted in the new Mitsubishi CANTER. The system is standard equipment in some models, and it has received a generally favourable evaluation at dealer presentations, press test drives, and other events. In accordance with customers response, we intend to enhance the system and pursue reductions in size, weight, and cost.

In closing, we wish to express our gratitude to the staff of the departments and companies that co-operated in the development program.

References

(1) NEOMAX magnet catalog, Sumitomo Special Metals Co., Ltd.

(2) Masafumi Okamoto: Magnetic Shielding with Compound Magnetic Material, Hyomen Gijutsu (Journal of The Surface Finishing Society of Japan), Vol. 42 (1991)

Satoshi KAWAZOE

Akio YASUDA

Shinji YAMAGUCHI

NEW TECHNOLOGIES

Development of Aluminum Frame for Heavy-Duty Trucks

Kenji KARITA* Yoichiro KOHIYAMA* Toshihiko KOBIKI*
Kiyoshi OOSHIMA** Mamoru HASHIMOTO‡**

Abstract

Aluminum was successfully used as the material for the chassis frame, a main structural member of heavy-duty trucks, to significantly reduce the truck weight and so allow the payload to be increased. A variable-section extrusion technology was used to mold the side rails of the aluminum frame (the first of its kind in the world). The shape and configuration of the aluminum frame design were optimized while maintaining strength and rigidity equivalent to those of a standard steel frame by using computer-aided-engineering analysis. Using the aluminum frame thus developed, a super-lightweight bulk truck was developed and exhibited at the 2002 Tokyo Motor Show.

Key words: *Aluminum Frame, Load Efficiency Improvement*

1. Introduction

With a view to meeting market demands for lower truck weights, Mitsubishi Fuso Truck & Bus Corporation has been working on development of an aluminum chassis frame for heavy-duty trucks since 1995 in collaboration with Mitsubishi Materials Corporation and Mitsubishi Aluminum Co., Ltd. Following the resolution of various technical obstacles, the development program has advanced to the point at which the goal – commercial production of aluminum frames – is in sight. This report describes the development targets and technical features of a recently produced prototype aluminum frame. It also gives an overview of a recently built super-lightweight bulk truck that has a cab-and-chassis configuration incorporating an aluminum frame and is fitted with an aluminum tank that was made by Mitsubishi Materials Corporation and has a class-largest capacity of 17 m^3.

2. Targets of development

The aluminum frame was developed for application to high-rigidity and fixed-payload vehicles such as tank lorries, which are subject to keen demand for weight reduction. Weight-reduction targets aimed at higher fuel economy and loading efficiency were set both for the frame and for the overall vehicle. Rigidity and strength comparable with those of a current steel frame were also targeted. The strategy employed for their achievement was optimization of the overall vehicle design.

(1) Weight reduction targets
- Aluminum frame: at least 300 kg lighter than steel frame
- Super-lightweight bulk truck: at least 1500 kg lighter than steel-frame truck

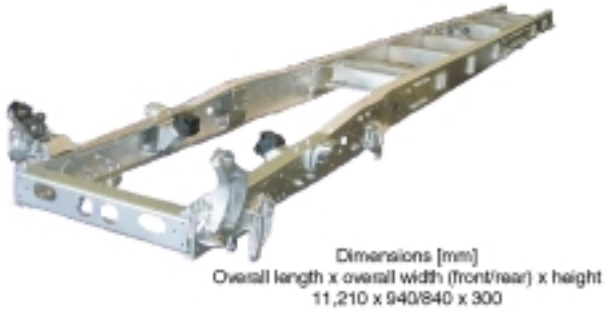

Fig. 1 Aluminum frame

3. Major specifications

The major specifications and appearance of the aluminum frame are shown in **Fig. 1**. The major specifications of the super-lightweight bulk truck are shown in **Table 1**, and the appearance of the truck is shown in **Fig. 2.**

4. Technical features

4.1 Reduced weight and improved fuel consumption

Weight reductions were implemented in chassis components that accounted for 65 % of cab-and-chassis weight and in the bulk tank mounted on the chassis. Also, super-single tires (**Fig. 3**), whose rolling resistance is 10 % lower than that of conventional tires, were specified for improved fuel consumption.

[Main weight-reduction items]

(1) Adoption of aluminum chassis frame (weight reduction achieved: 320 kg)

(2) Adoption of super-single tires with aluminum wheels (**Fig. 3**) as well as other aluminum parts including fuel tank (weight reduction achieved: 200 kg)

* Vehicle Dev. & Design Office, Research & Dev. Office, MFTBC

** Technical Center, Automotive Products Dev. Dept., Extrusion Div., Mitsubishi Aluminum Co., Ltd.

‡* Aluminum Fabricating Sec., Mitsubishi Materials Corporation

Table 1 Major specifications of super-lightweight bulk truck

Overall length x overall width x overall height (mm)		11270 x 2490 x 3430
Wheelbase (mm)		7040
Gross vehicle weight (kg)		24930
Bulk tank capacity (m^3)		17
Maximum payload (kg)		15800
Crew		2
Engine		6M70 (T2)
Piston displacement (cc)		12882
Maximum output (kW/min^{-1})		257/2200
Maximum torque (Nm/min^{-1})		1520/1200
Transmission		M130S7D
Tires	Front	295/70R22.5
	Rear	435/45R22.5 (super single)

Fig. 2 Super-lightweight bulk truck, SUPER GREAT FU (exhibited at 2002 Tokyo Motor Show)

(3) Adoption of aluminum bulk tank: (weight reduction achieved: 1000 kg)
These measures reduced weight by approximately 1.5 tons in total, allowing the payload to be increased by the same amount and concurrently realizing a 3 % improvement in fuel consumption.

4.2 Variable-section extrusion

Variable-section extrusion technology was adopted to form the side rails, which constitute major parts of the aluminum frame. This technology was originally developed by Mitsubishi Aluminum Co., Ltd.

Unlike standard extrusion technology, which forms products of a uniform section using only stationary dies, the variable-section extrusion technology uses movable dies in addition to stationary dies as shown in **Fig. 4**. The variable-section extrusion system changes the positions of the movable dies using a drive unit, thus varying the section of the product as the material passes through the dies.

This technology is suitable for side rails, whose sectional shape needs to differ from area to area. Its single-piece forming capability eliminates the need for welding and thus ensures increased accuracy and rigidity in the frame.

Extrusion-formed, high-rigidity channel-section beams and box-section beams were adopted as the

Fig. 3 Super-single tires

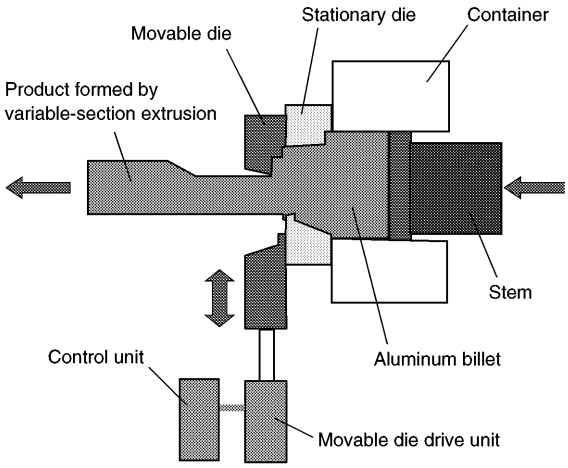

〈Variable-section extrusion mechanism〉

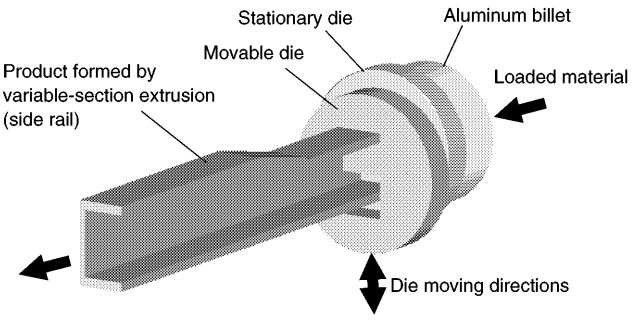

〈Computer-generated image of variable-section extrusion〉

Fig. 4 Variable-section extrusion

crossmembers connecting the left- and right-hand rails. Mitsubishi Materials Corporation assembled the side rails and crossmembers, successfully producing a frame with dimensional accuracy as high as that of a steel frame.

4.3 Rigidity

Each heavy-duty truck shipped from the factory in cab-and-chassis form is completed by a body builder in accordance with the customer's order. The truck's frame must be sufficiently strong and rigid to bear the load of the body constructed on it and to thus assure a vehicle service life over a million kilometers. Any significant deficiency in the frame's rigidity can detract

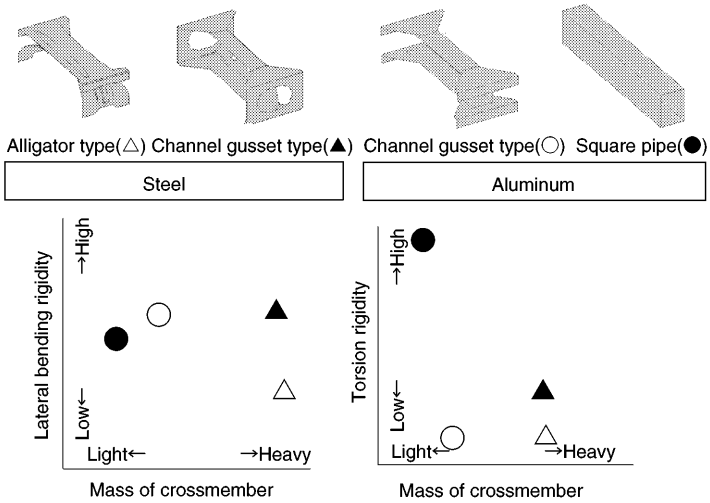

Fig. 5 Rigidity of crossmember

Fig. 6 Stiffness test of aluminum frame

from the vehicle's handling stability and cause the body structure to be subjected to concomitantly increased input loads, resulting in premature wear of body components. The rigidity of the aluminum frame was assured by the following features:

- Rigidity of vertical bending:
  The thicknesses of the side rails' flanges and webs were optimized taking advantage of the variable-extrusion method.
- Rigidity of lateral bending and torsion:
  Aluminum channel-section crossmembers that are highly resistant to lateral bending were combined with extrusion-formed box-section crossmembers that are highly resistant to torsion (**Fig. 5**).

The results of rigidity tests (**Fig. 6**) conducted on the aluminum frame indicated rigidity comparable with that of the current, time-proven steel frame.

In addition, computer-aided-engineering (CAE) analysis was conducted using the model shown in **Fig. 7** for optimal matching of the frame and tank, resulting in overall vehicle rigidity equivalent to that of the current steel-frame bulk truck (**Fig. 8**).

4.4 Strength and durability

The adoption of aluminum in place of steel as a truck-frame material necessitated various strength-related studies since it resulted in a reduction of about one half in tensile strength and a reduction of about one thirds in vertical modulus of elasticity.

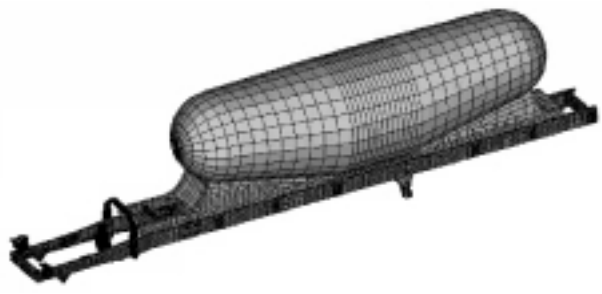

Fig. 7 Analysis model of aluminum frame with tank

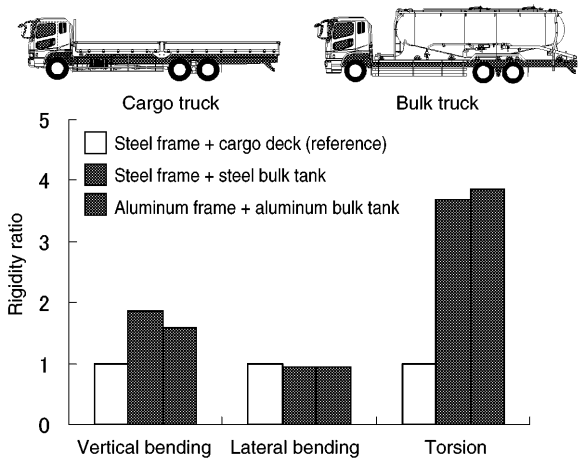

Fig. 8 Rigidity of entire vehicle

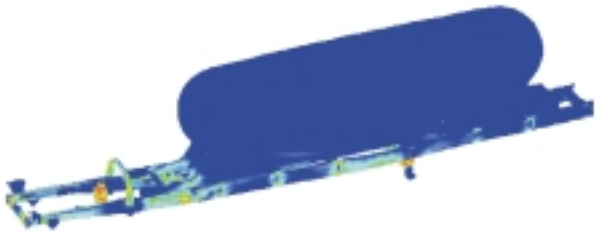

Fig. 9 Stress distribution during vehicle-turning

To ensure adequate strength in the aluminum frame and aluminum bulk tank mountings, CAE analysis of the entire vehicle was conducted with assumed conditions corresponding to harsh inputs caused by steering maneuvers. The analysis results were reflected in the aluminum frame design, resulting in strength equivalent to that of a steel frame (**Fig. 9**).

The aluminum frame was also subjected to a bench test (**Fig. 10**), which proved that the frame was sufficiently strong and durable to resist large, local load inputs in the vicinity of the rear suspension.

To compensate for inferior local strength in fastener areas, the unit surface pressure of each nut was reduced using a large washer (which also helped to prevent the

Fig. 10 Strength test of aluminum frame

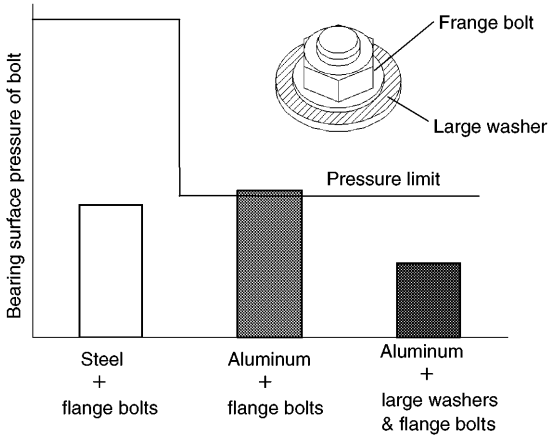

Fig. 11 Strength of bolting locations

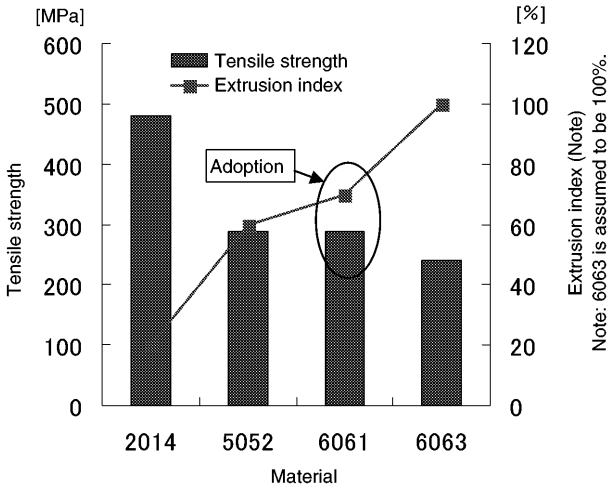

Fig. 12 Tensile strength and extrusion index of aluminum material

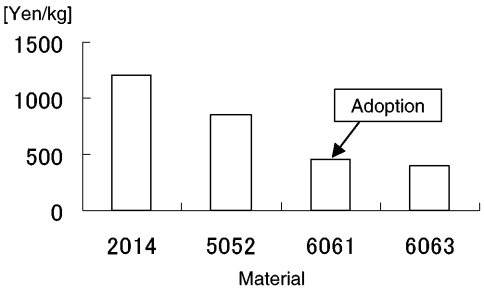

Fig. 13 Costs of aluminum materials

bolt from coming loose) (**Fig. 11**). These fasteners were dacrotized to prevent contact corrosion.

4.5 Material

The material selected for the frame is 6061-T6, which is well balanced in terms of extrusion formability, strength, and cost (**Figs. 12** and **13**). This material has been used for the crossmembers of certain heavy-duty trucks since 1998.

5. Summary

Collaborative development with Mitsubishi Materials Corporation and Mitsubishi Aluminum Co., Ltd. yielded an aluminum frame that satisfies the weight-reduction target and has sufficient strength and rigidity. Remaining technical issues will be addressed to enable commercial adoption of the aluminum frame. Finally, the authors wish to express their gratitude to all of the people inside and outside the company who gave valuable suggestions and assistance.

References

(1) Japan Light Metal Association: Aluminum Handbook
(2) Akira Yamamoto: Theory and Calculation of Screw Fastening


Kenji KARITA


Yoichiro KOHIYAMA


Toshihiko KOBIKI

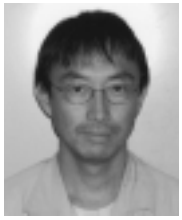
Kiyoshi OOSHIMA


Mamoru HASHIMOTO

NEW TECHNOLOGIES

Quality Assurance of Completed Engines Using Motoring Tests

Masaya YAMANA* Satoru YOSHIDA*

Abstract

Although the quality of a completed engine ready for shipping is traditionally assured by adopting the firing run at the final process of the engine assembly line, we have recently introduced a new inspection procedure by motoring, without combustion, in order to improve the quality as well as working environment.

This paper outlines our new philosophy of "In-process quality control" to identify and promptly respond to quality troubles, which we established when deploying quality assurance for motoring. It also describes the new quality assurance process we have developed for the ignition system.

Key words: *Cold Test, Motoring Test, Engine Quality, Engine Assembly Line*

1. Introduction

For assuring the quality of its line-assembled engines, Mitsubishi Motors Corporation (MMC) has so far used both the in-process quality assurance inspection implemented in each component assembling process and the completed engine quality assurance inspection consisting of firing-run tests that are performed using gasoline on finally assembled engines under the same conditions as the engines on actual vehicles.

However, the need to upgrade product quality while meeting environmental protection requirements and improving the working environment raises technical challenges that cannot be solved by simply refining the firing-run testing system. Rather, a new quality assurance method to replace the firing-run test method is required.

The motoring test system is a new engine quality assurance inspection system that drives a completed engine using an electric motor, analyzes measurement data from externally located sensing devices using a computer, and determines the quality of the engine. MMC has adopted this system in its 4G9 and 4G6 engine assembly lines. This report outlines the motoring test system and also the new inspection system that was developed for assuring the quality of the ignition system.

2. Role of operation testers in engine assembly lines

The quality assurance inspections in an engine assembly line are classified into the following two categories (**Fig. 1**).

(1) In-process work quality assurance inspection that directly checks the quality of fastening, press-fitting, insertion and other value-adding operations involved in the assembly of two or more parts in a process of the assembly line.

(2) Assembly functional quality assurance inspection that indirectly checks for water/oil leakage, friction, malfunction, noise, vibration, and other defects caused by inappropriate or improper assembly of components.

Just as the in-process work quality assurance is important for promptly detecting product defects and reducing man-hours for repairs, the assembly functional quality assurance is crucial to enable the manufacturer to assure body assembling shops and markets of the quality of its products.

Operation testers play their role in the assembly functional quality assurance inspection mentioned above.

3. Problems of firing-run test in quality assessment

In the firing-run test, there are typically the following problems with regard to quality assessment.

(1) Since the test identifies defects in an engine by symptoms such as rough idling and hesitation, it cannot provide means for determining defects quantitatively and locating causes easily.

(2) Since the test can provide only a secondary or indirect means for evaluating combustion, the information provided is influenced by factors that are not related to the engine itself but contribute to combustion such as atmospheric temperature, coolant temperature, and oil temperature, which could lead to varying judgments.

(3) One engine model has about 200 or more variations depending on vehicle models and their markets. During the firing-run test of a variation, a special computer designed for shared use by five variations is used rather than using the specific engine com-

* Power Train Production Engin. Dept., Car Research & Dev. Office, MMC

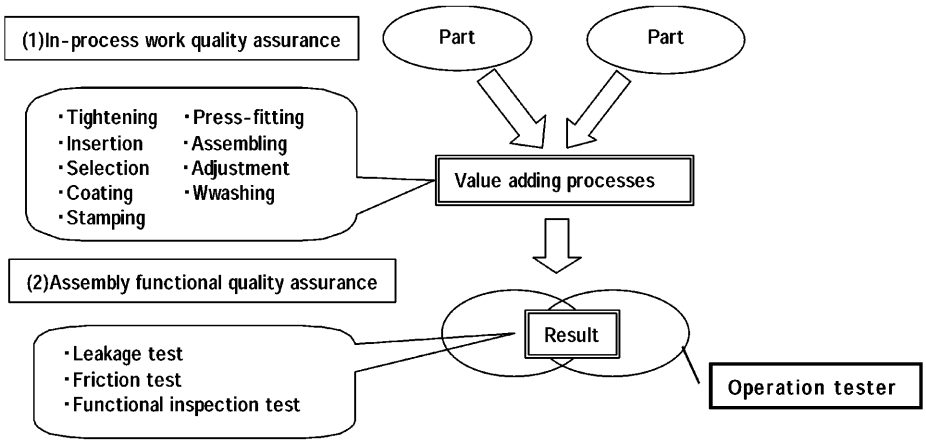

Fig. 1 In-process work quality assurance and assembly functional quality assurance

puter for the variation. In addition, since the computer program is modified to enhance engine startability, some engine variations may operate in the operation tester in conditions significantly different from those in actual vehicles. Therefore, the detected operational quality levels may not be exactly the same as shown on actual vehicles.

4. Outline of motoring test

The motoring test has started being employed in place of the firing-run test in the automotive industry not only because of the reasons stated in section 3 above but also due to environmental reasons (noise, exhaust emissions, etc.).

Expecting expanded application in the future, MMC introduced the motoring test to the assembly functional quality assurance process in the production lines of its major gasoline engines, namely the 4G9 (1800 – 2000 cc) and 4G6 (2000 – 2400 cc).

4.1 Merits of motoring test

Typical merits of the motoring test are as follows:

(1) The motoring test makes it easier to locate the causes of a defect since it can analyze the problem factors that influence the function and performance of the engine and directly set the responsible factor items.
(2) The motoring test can acquire primary data directly, not through combustion, which prevents measurement data from being affected by external conditions.
(3) The motoring test does not use individual engine computers, thus avoiding variation in sensing accuracy between engine models.
(4) The motoring test involves no gasoline combustion and thus no exhaust emissions.
(5) When included in a newly constructed assembly line, the motoring test helps to reduce utility costs including gasoline and coolant.

4.2 Establishment of motoring test process

(1) Selection of inspection items

Part of the analyses conducted by the motoring test mentioned in paragraph 4.1 (1) is shown in **Fig. 2**.

The motoring test could theoretically measure a huge number of items, but doing so could lead to some inspection items being measured twice or more and thus loss of overall process efficiency. For this reason, inspection items were assessed as follows.

Using the matrix shown in **Fig. 2**, inspection items were determined for each defect, and then each of the inspection items is given one of the three sensing accuracy levels from "1" (low) to "3" (high). In addition, weights representing importance of inspection derived from past experience were assigned to individual causes of each defect. Using the weight and sensing accuracy numbers, the importance of each inspection item was rated using the following equation:

$$\text{Weight} \times \text{Sensing accuracy} = \text{Importance of inspection}$$

Since only the inspection-item-based assessment could miss necessary inspection items, each defect cause was also assessed for importance. Using the results of the dual assessments, the number of inspection items was reduced from the initial 14 to 12 without sacrificing quality assurance level.

(2) Allocation of inspection process

The inspection process allocation should have close relevance to inspection items. The philosophy we adopted in selecting inspection items was "quality completion process", the objective of which is to find defects as early as possible and to prevent defective in-process items from entering the downstream processes, thus minimizing losses. To implement this concept, quality assurance must be implemented after every process in which integration of a specific function is completed, rather than performing all functional inspections collectively in the final process.

Through the analyses and studies mentioned above, the inspection items and inspection process allocation were determined as shown in **Fig. 3**.

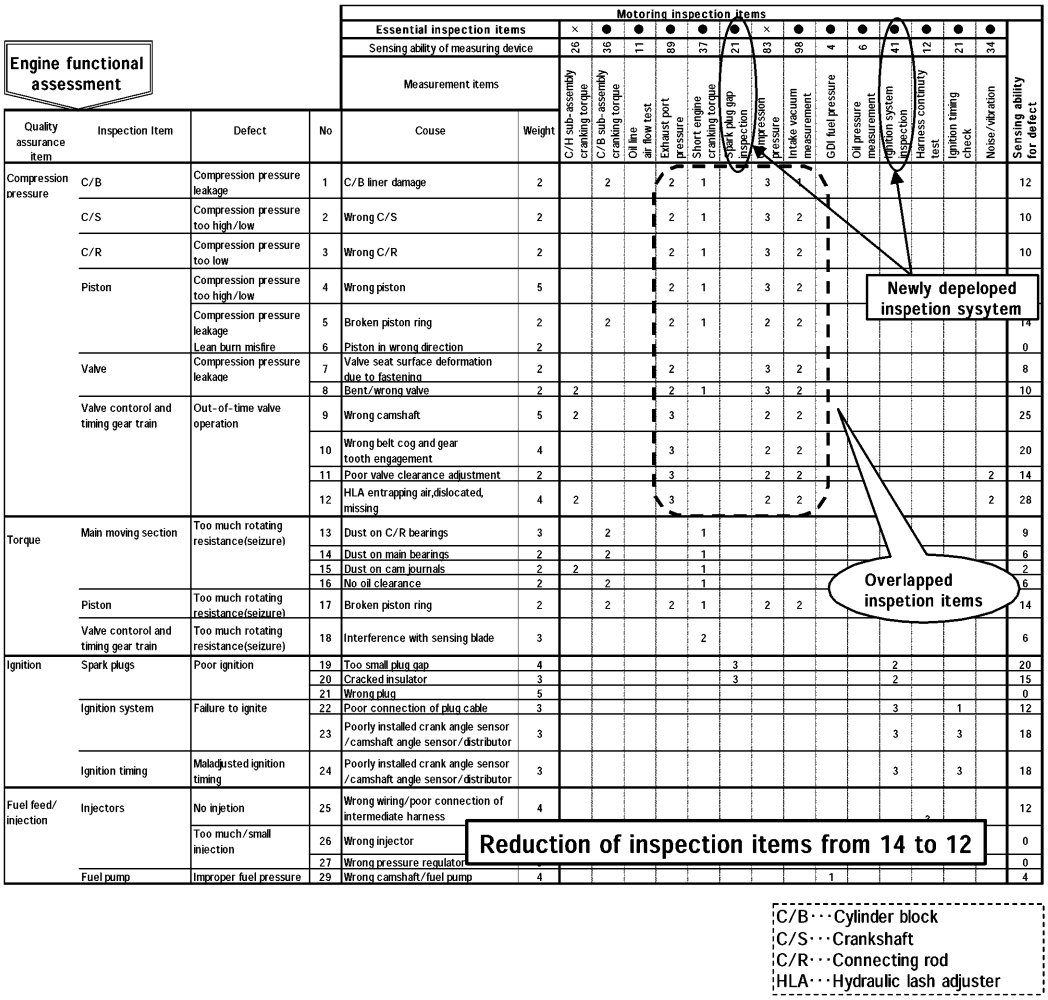

Fig. 2 Grading inspection items based on functional quality assurance levels (part of grading table)

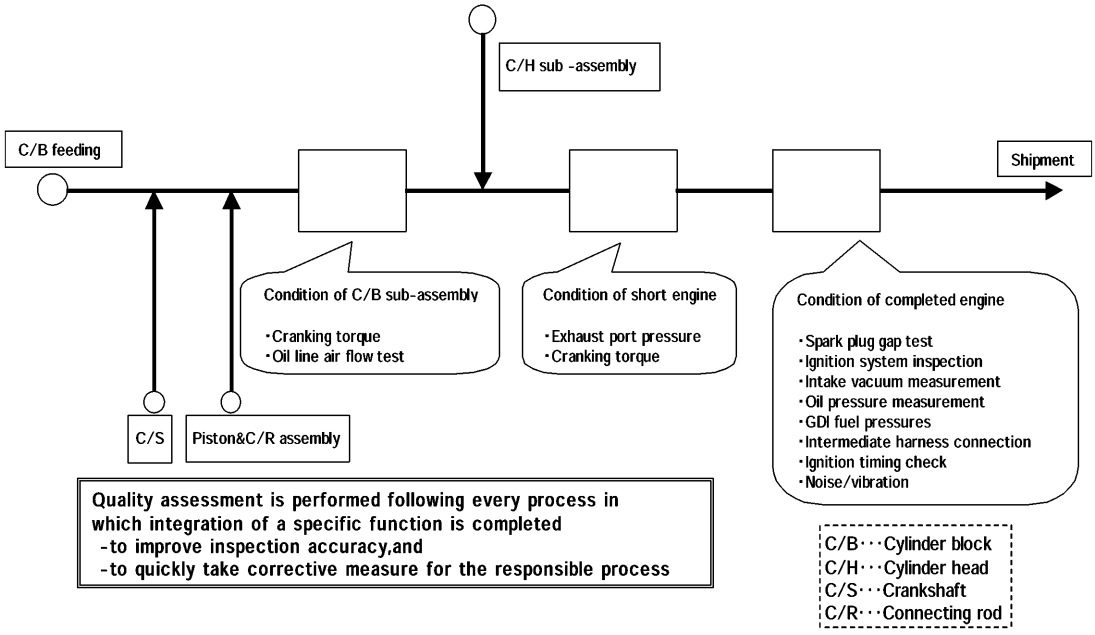

Fig 3 Motoring test items allocated to process stages

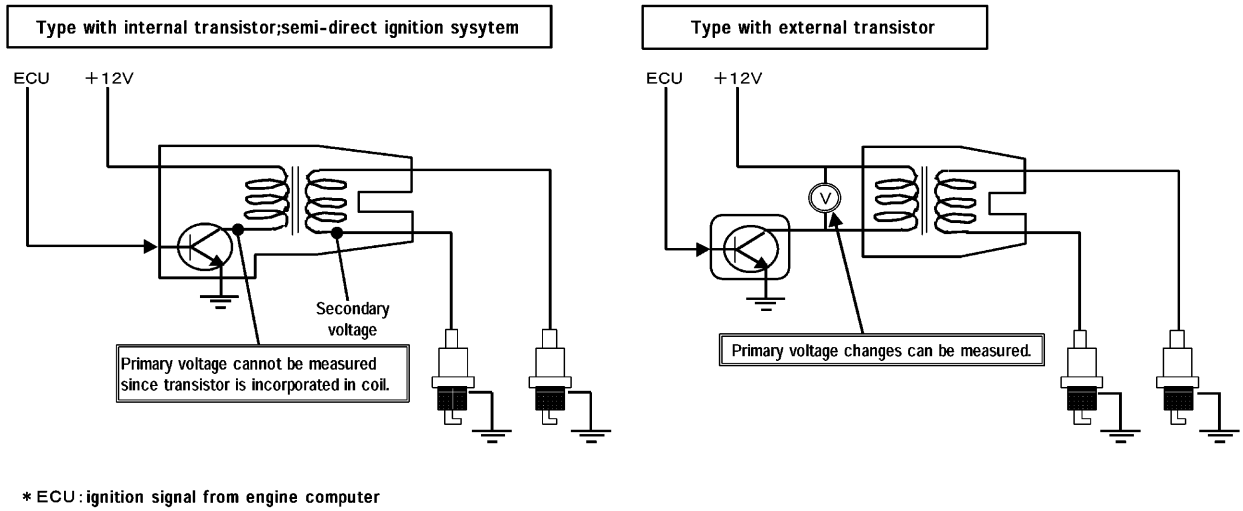

Fig. 4 Ignition coils with internal transistor and external transistor

5. Development of ignition system inspections

As a result of assessing the inspection items mentioned in section 4.2, it was found that the motoring test was able to identify the causes of almost all defects to accuracy levels equivalent to or higher than those by firing-run tests.

Only the ignition system, however, required a new method to be developed for evaluating functional quality in place of the firing-run test. The newly developed inspection system for the ignition system is described below in detail.

5.1 Functional quality assurance items

The following two conditions must be satisfied in order to assure the functional quality of the ignition system.

(1) Outputs of the crankshaft angle sensor and camshaft angle sensor are normal.
(2) Ignition-related cables and spark plugs are correctly installed and sparks (discharges) of correct energy take place in spark plugs when the ignition system is completed.

Condition (1) can be checked by evaluating output waveforms of the sensors. Condition (2), however, involved a problem to be solved before it could be checked, i.e., the way to detect too narrow spark plug gaps, which are typical defects that can occur when installing spark plugs.

5.2 Problems to be solved

Development of a system for inspecting the ignition system involved the following two major problems:

(1) Today's engines use ignition coils with internal transistors (**Fig. 4**). Ignition coils with external transistors, which were used until several years ago, allowed the quality of the overall ignition system including the spark plug gap to be assured by measuring changes in the primary voltage of the ignition coil and monitoring the discharge time of the spark plugs using waveforms derived from measuring the change in primary voltage.
With ignition coils with internal transistors, on the other hand, it is impossible to measure changes in primary voltage and so the above-mentioned method of checking the state of discharge cannot be used.
(2) Some engines use a semi-direct ignition system in which two spark plugs share a single ignition coil. In these engines, even if the gap of one plug in the pair is too small, the defect cannot be detected as long as the gap of the other plug is normal, because the state of the pair is dominated by the state of the good plug.

5.3 Development of new inspection system

The following solutions were devised to solve the above two problems.

(1) Inspection of internal transistor ignition systems
The ignition coil causes a spark plug to generate sparks utilizing current induced by electromagnetic induction.

This means that the change in the magnetic field resulting from electromagnetic induction can be detected as a voltage change if external coils are placed above the ignition coil as shown in **Fig. 5**. A measuring system using this principle was developed.

Fig. 6 shows a voltage waveform obtained using the newly devised system.

In this waveform, the first high crest corresponds to the start of discharge and the second to the magnetic field change at the end of the discharge. Regarding the period between the start and end of discharge as the discharge time, the discharge time was examined. The results showed that the discharge time measurements given by the new external coil system closely correlated with the measurements obtained by the conventional method that provided discharge time data based on the change in primary voltage of the ignition coil. Following this verification, the system using external

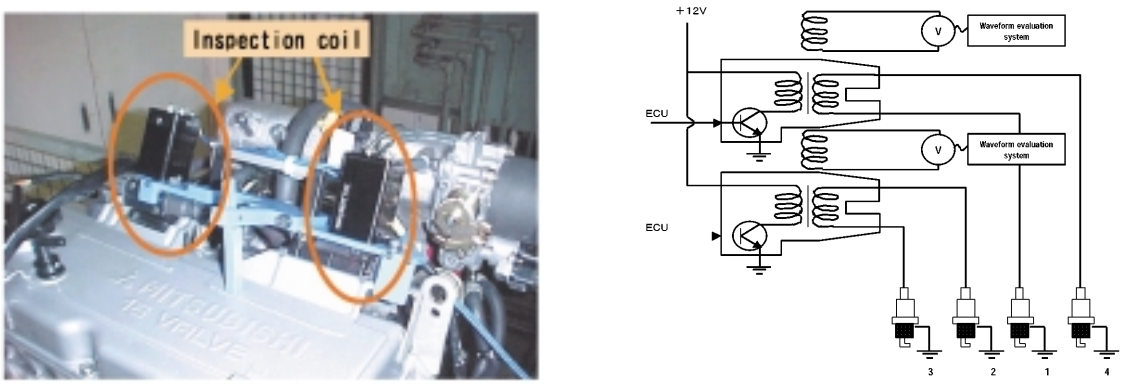

Fig. 5 Ignition system inspection coils applied to 4G9 engine

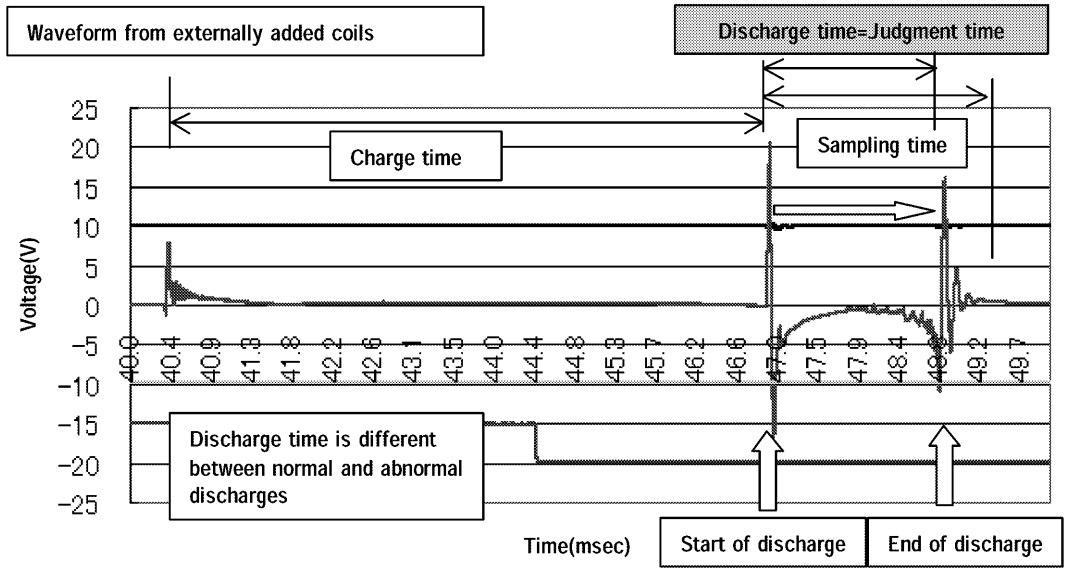

Fig. 6 Waveform obtained from test using external coils

coils was used to inspect the internal transistor ignition system.

(2) Inspection of semi-direct ignition system

With a single spark plug, the narrower the gap between the electrodes, the easier the discharge takes place or the longer the discharge time with smaller voltage applied.

With paired spark plugs of a semi-direct ignition system, the two plugs are connected in series to form a single circuit. As a result, the discharge time of both the plugs is governed by that of the plug with the wider plug gap without any influence of the plug with the smaller gap when they are caused to release sparks in open air, making it difficult to detect improper plug gaps.

Regarding the characteristics of electric discharge, it is known that the plug gap is correlated to atmospheric pressure around the electrodes during discharge. An attempt was made to solve the above problem by using this fact.

During measurement of the time between the discharge start point and discharge end point shown in **Fig. 6**, the engine under test was motored and both the plugs were caused to discharge simultaneously on the compression stroke when the pressure around one of the plugs was high.

The discharge time measurements were classified into three categories: long, medium, and short. These measurements were analyzed to know how the discharge time varied depending on whether both plug gaps were normal or only one plug gap was abnormal. The result is shown in **Fig. 7**.

As indicated, the discharge time of a defective plug with too small a gap was longer than that of a good plug and was classified as “medium”. Since the plug with correct gap paired with it on the same circuit was placed in atmospheric pressure, its discharge time was almost equal to that of the defective plug, or “medium”, so the condition of this pair could be discriminated from that of a good plug pair.

Thus, individual spark plugs can be examined by inspecting the ignition system while the engine is being motored.

	Normal gap (#1 cylinder)		Normal gap (#4 cylinder)		Measurement result	Judgment
	Pressure during discharge	Discharge time	Pressure during discharge	Discharge time		
Both are good	**Compression stroke (high)**	**Short**	**Exhaust stroke(low)**	Medium	**short**	OK
	Exhaust stroke(low)	Medium	Compression stroke (high)	**Short**	**short**	OK

	Normal gap (#1 cylinder)		Too small gap(#4 cylinder)		Measurement result	Judgment
	Pressure during discharge	Discharge time	Pressure during discharge	Discharge time		
One is bad	**Compression stroke (high)**	**Short**	**Exhaust stroke(low)**	Long	**Short**	OK
	Exhaust stroke(low)	Medium	Compression stroke (high)	**Medium**	**Medium**	NG

Fig. 7 Determination of good and bad spark plugs

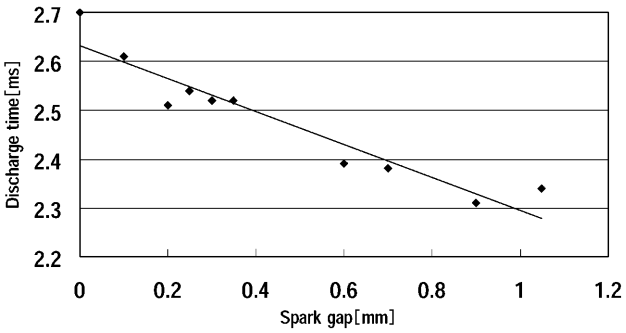

Fig. 8 Spark gap and discharge time

5.4 Validity of the theory

Since the solutions discussed in paragraphs (1) and (2) are considered theoretically to be applicable to the quality assurance process of the overall ignition system including the spark gap of individual plugs, they were tested using actual engines to evaluate their validity.

The results are shown in **Fig. 8**. The graph shows the correlation between the spark gap and discharge time, indicating that the discharge time gets longer as the spark gap becomes narrower.

The test therefore proved that the new inspection system can be used to assure the quality of the overall ignition system to an accuracy equivalent to or higher than that offered by the conventional firing-run tests.

6. Summary

The motoring-test-based pre-shipment quality assurance system discussed in this report has been applied to the 4G9 engine assembly line, and engines inspected by the system started being shipped in September 2001.

Incorporating the newly developed ignition system inspection technologies and re-defined test items, this quality assurance system is now working well in the 4G9 engine assembly line, and is detecting even those defects that were difficult to detect with the conventional firing-run-test-based system.

The motoring test system applied to the 4G6 engine assembly line is an advanced version of the 4G9 engine's system that can accommodate quality assurance inspection of not only the 4G6 engines for current vehicle models but also the new engines for future vehicle models.

We wish to thank the staff of the production department, quality assurance department, and many other people of the company who offered advice and cooperation in the development and application of the motoring-test-based quality assurance system.

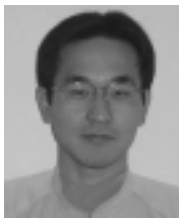

Masaya YAMANA

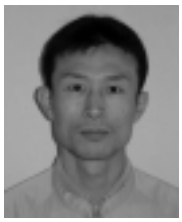

Satoru YOSHIDA

NEW TECHNOLOGIES

New Method to Produce Quality Parts Using 3D Coordinate Measuring Machine

Junichi TAKAHASHI* Takuma IKEDA*

Abstract

Traditionally, efforts to improve production preparation for stamping parts using information technology have focused on the processes before stamping die fabrication, and by mostly applying techniques of CAD (Computer Aided Design), CAM (Computer Aided Manufacturing) and CAE (Computer Aided Engineering). However, in order to improve work efficiency further and ensure the dimensional accuracy of parts at an early stage, it is important to use CAT (Computer Aided Testing) technology, which enables the accuracy of a part to be evaluated properly against CAD data.

This paper introduces a new approach to ensure the accuracy of parts using CAT and its expected development in the future.

Key words: *CAT, Quality Improvement, Based on CAD Data*

1. Computer aided testing

CAT is employed in the following two industrial production areas:

(1) Verification of various characteristics of parts and products at the development stage
(2) Quality control of products in production preparation and manufacturing processes

3D contact measuring systems known as coordinate measuring machines (CMMs) are some of the most widely used CAT systems in the automobile-manufacturing field. They are generally used in the area (2) described above, mainly for assessing deviation of products from their specifications using the process capability index (*Cp*) and other indices. **Fig. 1** shows a CMM system used by Mitsubishi Motors Corporation (MMC) for body accuracy measurement. In addition to CMMs of the type shown in **Fig. 1**, MMC recently introduced portable non-contact 3D measuring systems for use in a new quality control system for press-formed sheet metal parts.

2. Major defects in press-formed sheet metal parts

The types of defects that occur most frequently in press-formed sheet metal parts can be broadly classified into two types: those whose magnitude is easy to determine (for example, cracks and wrinkles that can be caused by press forming) and those whose magnitude is difficult to quantitatively determine despite their significant effects on the accuracy of parts (for example, springback and twist) (**Fig. 2**). Defects in the latter category can be caused by a combination of different factors, so quality assurance measures taken to prevent them involve repeated trial-and-error testing.

Fig. 1 CMM system

3. Features of recently introduced CAT system

MMC introduced the CAT system into the sheet metal press forming process with the aim of assuring accuracy in parts and with the aim of efficiently assessing deviation from specifications.

To ensure selection of the system most appropriate for achieving the objectives, the following requirements were established for system capabilities

(1) Allows product measurements to be evaluated against product's CAD data in terms of absolute values.
(2) Allows the magnitude of defects to be ascertained both quantitatively and visually.
(3) Allows causes of defects to be assessed individually and measures against them to be devised.
(4) Allows measurement and assessment to be per-

* Body Production Engin. Dept., Car Research & Dev. Office, MMC

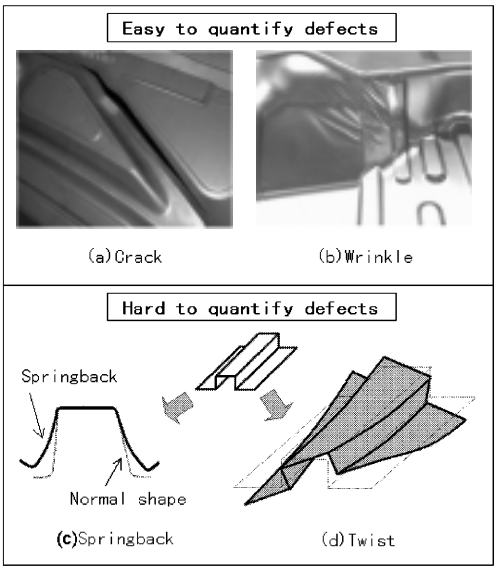

Fig. 2 Defect figuration of sheet metal parts

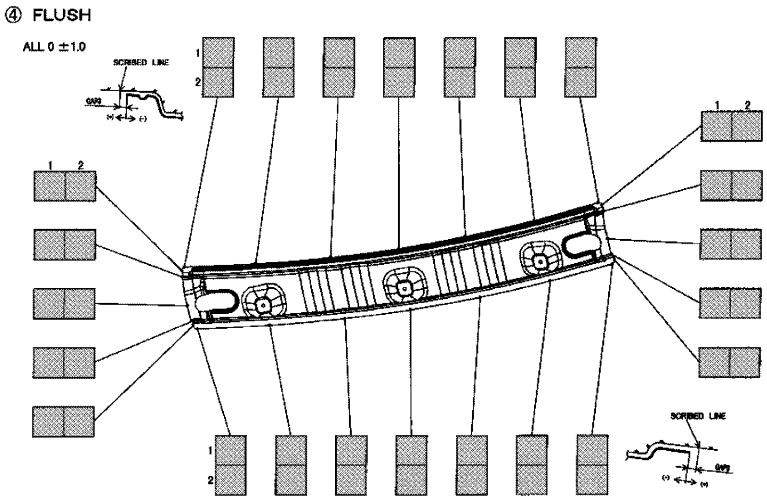

Fig. 4 Consequence of inspection report

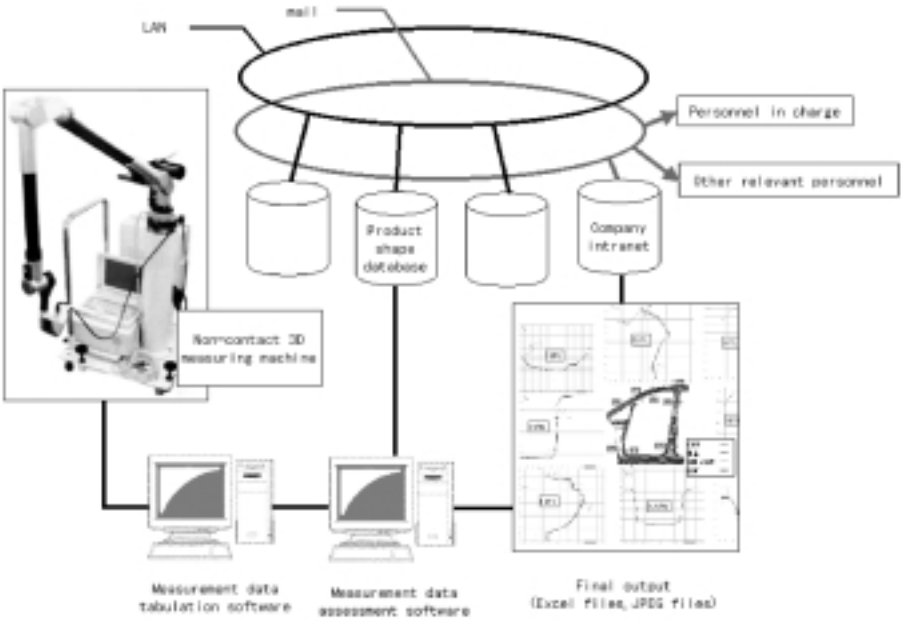

Fig. 3 System architecture of CAT

formed easily.

The adopted CAT system architecture is shown in **Fig. 3**.

The selected 3D measuring system consists of a measuring machine with multiple-joint arms and laser sensors. The system is of portable design for good mobility and is capable of scanning the shapes of objects under measurement without touching the objects.

The system includes measurement data tabulation software and measurement data assessment software. Running them in parallel enables real time assessment of measurement results.

The system receives the CAD data of the product under measurement via a local area network, and it evaluates the measurement data by comparing them with the CAD data in terms of absolute values.

The final evaluation data are stored as Excel or JPEG files and are transmitted to the personnel in charge and to other relevant personnel via the company's intranet.

4. Example of application of CAT system

Examples of application of the system to measurement of actual parts is described hereafter.

For comparison purposes, a conventional inspection sheet is shown in **Fig. 4**. The conventional, previously used inspection process involves placing a sheet metal part on a test jig, measuring the part using a vernier caliper and other gauges, and handwriting the results on the inspection sheet. Although it is possible to detect an accuracy defect at any edge of a product using the conventional method, it is extremely difficult to quantitatively ascertain the reason(s) for such a defect.

Fig. 5 shows the results of an investigation into an accuracy defect conducted using the CAT system. Shown in part **(a)** of **Fig. 5** are the system-produced measurement data of an inner rear roof rail compared with the CAD surface data. The red portions indicate the areas where there were large differences between the measurement data and the CAD data. The visual representation made the nature of the accuracy defect

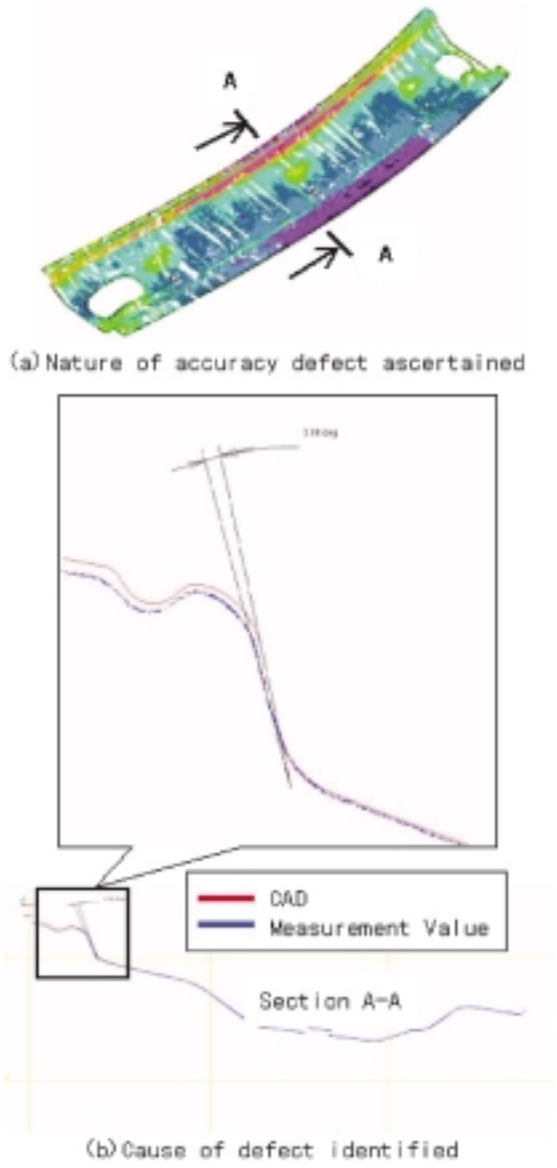

Fig. 5 Case example of application for CAT

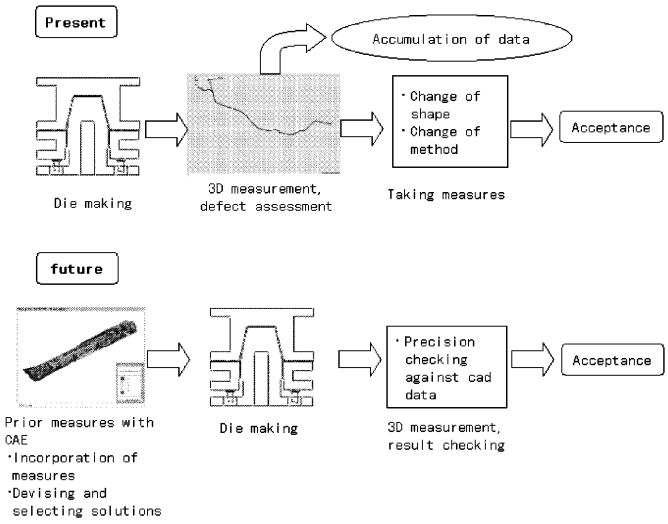

Fig. 6 Simultaneous use of CAE

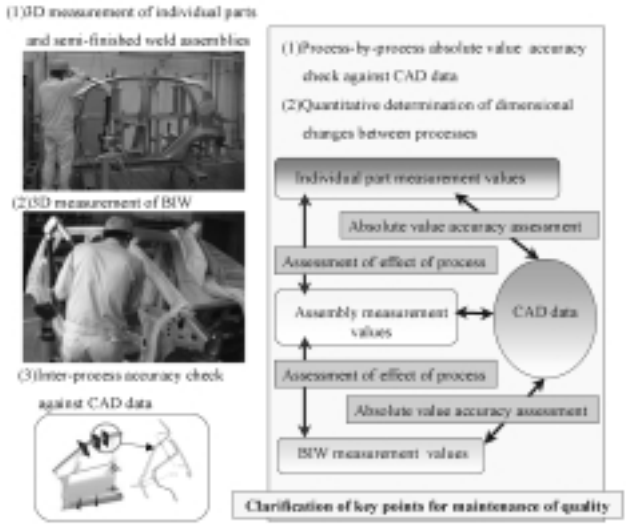

Fig. 7 BIW quality improvement activities

easy to ascertain.

Once the nature of the accuracy defect had been ascertained, section analysis was carried out to identify the cause of the defect (part **(b)** of **Fig. 5**). The section analysis revealed that the cause of the accuracy defect was an angular deviation in the wall (verifiable, thanks to the new system, both visually and quantitatively).

As shown by this example, the system, by providing information on the cause of a defect, allows effective and concrete countermeasures to be quickly devised.

5. Future expansion of system

(1) Use of CAT system and computer-aided engineering (CAE)

Although the CAT system is currently used as a means of ensuring accuracy in parts, initial steps have been taken to enable defect data accumulated by the system to be used for improvement of accuracy in CAE analysis. The envisaged result is transformation of the CAT system into a system (like the one shown in **Fig. 6**) that uses CAE technology to predict possible defects and to take measures against them before they actually occur.

(2) Assuring accuracy in body in white (BIW)

Although this paper has thus far described employment of the CAT system to ensure accuracy in sheet metal parts, MMC's ultimate objective is to use the system to ensure 100 % accuracy in the overall BIW. Early achievement of the required BIW accuracy level is vital at the production preparation stage, and early identification of accuracy defects and implementation of countermeasures are vital after the beginning of volume production. To this end, it is essential not only to assure accuracy in individual sheet metal parts but also to find key control points among a variety of processes and properly manage these points to ensure accuracy in

internally and externally sourced welded assemblies and in the overall BIW.

The new COLT is the first vehicle with which MMC has used the CAT system to track accuracy changes in each process and thereby clarify important control points for maintaining accuracy. Activities for improvement of BIW quality are shown in **Fig. 7**.

The activities are centered on determining absolute error amounts in each individual part, welded assembly and BIW production process through direct comparison of measurement data with CAD data. Analysis of absolute values of errors in chronological order enables clear identification of the parts of processes that significantly affect accuracy in the vehicle body. Through these activities, MMC will be able to offer products with unprecedentedly high quality.

6. Summary

Amid hollowing out of the manufacturing sector in Japan, MMC cannot achieve advantages over competitors simply by employing information technologies in existing processes. Rather, MMC must use information technologies to revolutionize the processes by which it produces automobiles. The activities described in this paper reflect the kind of thinking necessary for success.


Junichi TAKAHASHI


Takuma IKEDA

New System for COLT Production

Koichi KAKU* Takeshi ANDO**

1. Introduction

The new COLT is the first car that Mitsubishi Motors Corporation (MMC) has developed in close co-operation with DaimlerChrysler. It is a global-strategy car and a symbol of the new MMC. In terms of product attributes, the COLT is intended to offer class-leading quality, well-balanced performance, and exceptional freedom of choice with respect to interior and exterior appearance and equipment. To realize these attributes at the highest possible level, the production department adopted the motto 'For production, the customer is No. 1.' and worked, as shown in **Fig. 1**, toward the three following goals:

(1) Delivering quality that satisfies all customers
(2) Realizing performance that satisfies all customers
(3) Realizing freedom of choice that satisfies all customers

This paper describes related work performed at the Okazaki plant, where the COLT is produced. It also describes efforts to reduce costs at the Okazaki plant through the introduction of state-of-the-art technologies.

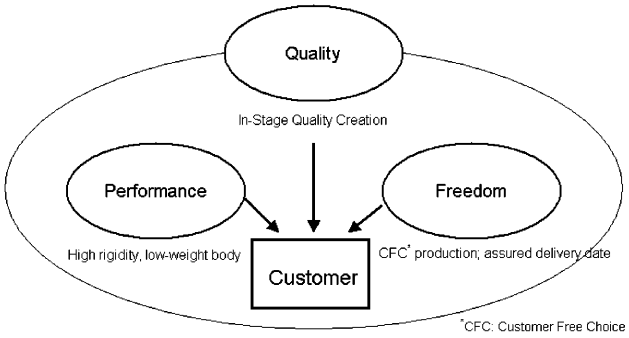

Fig. 1 Concept of customer-oriented car production

2. Delivering quality

To deliver quality that satisfies all customers, MMC adopted the Quality Gate concept employed by DaimlerChrysler. With this concept of quality management applied to the development of a new vehicle model, a 'gate' (a point at which a strict quality audit is conducted) is established at every critical point in every process from conception and design to production and shipping; quality in each process is maximized to enable the audit at each gate to be passed. To realize the Quality Gate concept on the production lines, MMC created a unique production-quality-assurance system. Quality-assurance measures taken at the development and production-preparation stages and following the transition to production are described hereafter.

2.1 Quality assurance at development and production-preparation stages

The COLT's styling was conceived in Europe. The production department conducted productivity studies to determine how to achieve high productivity while giving priority to full realization of styling features intended by the designer (notably a front mask that expresses the Mitsubishi identity and a distinctive one-motion body form in which side airdams and overfenders are incorporated into the side panels).

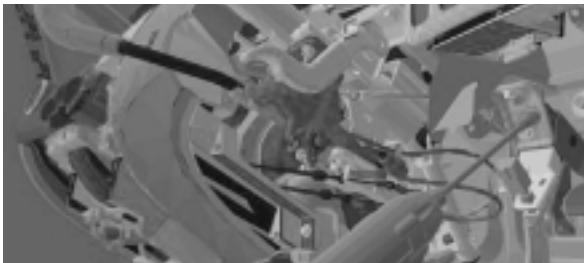

Fig. 2 Analysis of brake-pedal installation on virtual car

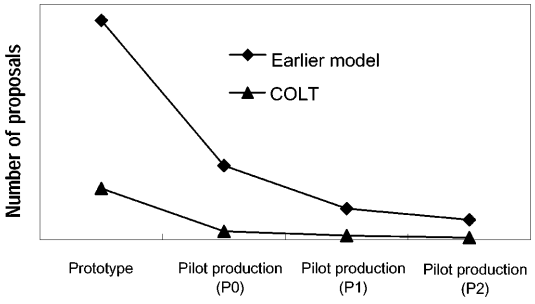

Fig. 3 Number of proposals from design to production

Further, CATIA, a software package that handles three-dimensional data, was used for all aspects of the

* Car Production Project, Car Production planning & Engin. Office, Global Production Headquarters, MMC
** Production Dept., Nagoya Plant, MMC

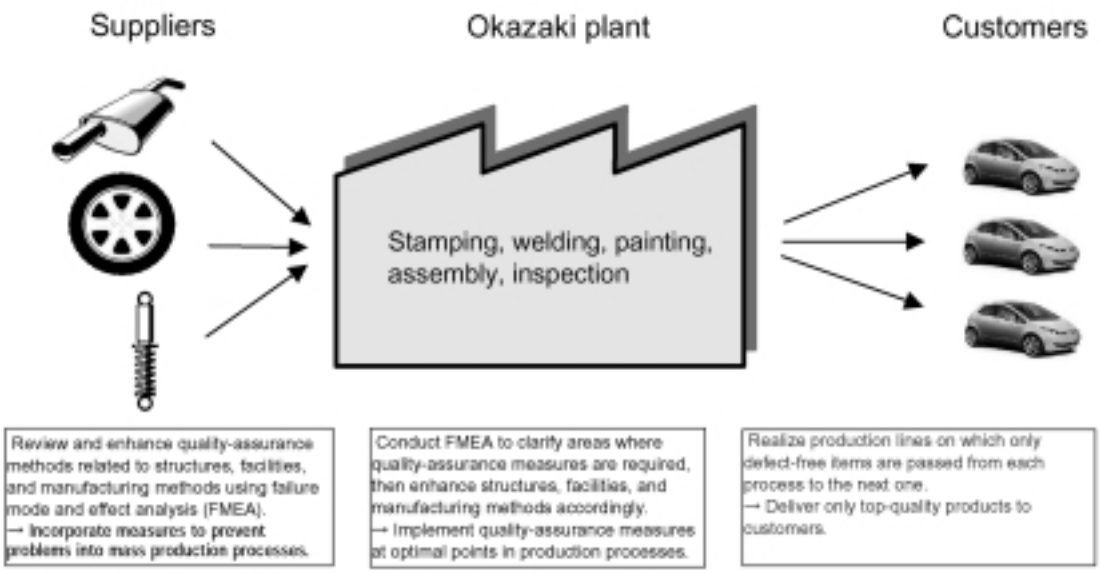

Fig. 4 In-Stage Quality Creation

COLT's development. Prior to fabrication of a physical prototype cars, all vehicle data were entered into a computer and used to create a virtual car, i.e., a digital prototype. The digital prototype was used for design confirmation by the development department. In addition, it enabled potential production problems to be verified through virtual assembly of parts in accordance with process sequences used on the actual production lines. **Fig. 2** shows an image from a study of brake-pedal installation.

Also, all production tasks (from welding to assembly) for the prototype cars were performed by skilled production workers, enabling the benefits of their experience and know-how to be reflected in production processes. Proposals for needed improvements identified at this stage were provided to the development department via a Quality Information Pool (a system that synthesizes quality-related information and was put to full use for the first time with the COLT), greatly shortening the time between proposals and their implementation and verification.

As a result of these steps, the number of potential production problems that needed to be addressed at the development stage was, as shown in **Fig. 3**, significantly smaller with the COLT than with earlier vehicle models. The COLT thus embodies high quality and is easy for workers to build.

2.2 Quality assurance in production processes

With the COLT, the Quality Gate concept was applied in a seamless manner to every aspect of the car (from individual parts produced and delivered by part manufacturers through production, shipping, and final customer delivery by MMC). The system for ensuring that customers receive only products that have undergone quality assurance in all processes is known as In-Stage Quality Creation (ISQC). Having been introduced at the Okazaki plant, ISQC is to be introduced at all other MMC plants. ISQC enabled a shift away from a quality-control system based primarily on checking of finished articles toward a quality-control system that improves production processes such that only correct articles can be produced. **Fig. 4** shows the thinking behind ISQC. Specific measures taken to realize ISQC are described below.

(1) Quality assurance with supplier-sourced parts

Breaking free of previous purchasing practices, MMC employed a global purchasing strategy to select the best suppliers for the COLT. In co-operation with these suppliers, MMC assured quality in all major functional and safety-related parts by means of the following steps:

① Design and process failure mode and effective analysis
② Confirmation of implementation of critical control points in quality check process charts
③ Confirmation of compliance of mass production processes with quality check process charts
④ Confirmation of results of reliability tests; confirmation of securing of process capability

The system yielded by these steps ensures that only quality-assured parts are used.

(2) Quality assurance at Okazaki plant

To ensure satisfactory quality in production processes in accordance with ISQC, the production lines at the Okazaki plant were revised to ensure that only satisfactory items are passed from each process to the next one. Measures taken on each line are shown in **Table 1**, and the locations of processes in which quality is checked are shown in **Fig. 5**.

3. Realizing performance

The COLT's body structure ensures safety and incorporates weight-saving measures that help to realize well-balanced running performance and fuel economy. Production-related measures necessitated by the new body structure are described hereafter.

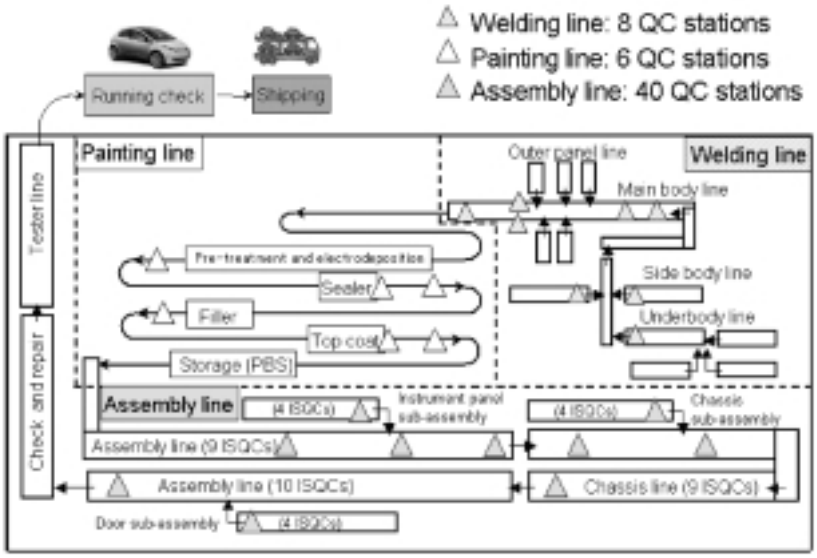

Fig. 5 Locations of processes in which quality is checked

Table 1 Quality-control commitments at Okazaki plant

Welding line	• All critical control points (approximately 150) are measured and assured in-line within the cycle time. • Critical dimensions and accuracy are assured with gauges. • All control points (approximately 600) are automatically measured and assured at random.
Paint line	• Quality-control points are specified, then equipment and process improvements are incorporated into mass-production processes. • Operation control points are specified, and confirmation and assurance are performed in the assurance process (particularly for sealing related to water leakage and rust)
Assembly line	• Approximately 5000 failure modes are predicted, then structure, equipment, and process modifications for defect prevention are incorporated into mass-production processes. • Assurance items (approximately 1000) are specified, and all items are confirmed and assured. • New In-Stage Quality Creation processes are established to ensure that only defect-free items are passed from each process to the next. • Expanded use is made of transmitter-equipped torque wrenches and nut runners for assurance of tightening torques. • Expanded use is made of checking devices for bar-coded parts to prevent assembly mistakes. • Expanded use of modular construction permits quality assurance on a module-by-module basis.
Inspection line	• Data on finished vehicles and on in-line inspections and repairs are electronically entered into the Mitsubishi Inspection Data Control System such that inspection results are handled as electronic data. Thus, inspection reliability, management streamlining, and vehicle quality are improved.

3.1 Measures for production of new body structure

The COLT is built on a new platform that was made possible by MMC's alliance with DaimlerChrysler. In this platform, a straight-frame construction is combined with octagon-section front side members for greatly superior energy absorption. In fact, the results of in-house tests indicate class-leading crash-safety performance.

The new body is built at the Okazaki plant on the same flexible line as the bodies of models such as the CHARIOT GRANDIS, GALANT, and PAJERO iO. As an example of facilities used for multi-model mixed production on the flexible line, the four-face rotatable fixture of a flexible welding system is shown in **Fig. 6**. This fixture has a unique jig for one vehicle model on each face, making it possible for the body sides and underbodies of four vehicle models to be fitted together at a single station. The jig for the COLT was subjected to a trial in a separate location prior to installation and was then installed on weekends. The overall flexibility of the production line (MMC began introducing and refining flexible production processes with earlier vehicle models) made it possible for MMC to prepare for COLT production during weekends and holidays with no line stoppages. Further, computer-aided-design (CAD) simulation of part-to-part interference and other aspects of the equipment (**Fig. 7**) made possible a significantly shortened trial period.

3.2 Weight-minimizing measures

The COLT's body in white is outstandingly light and rigid compared with others in the class, so it contributes to well-balanced performance and to outstanding fuel economy.

Production-related technologies used for body lightness include tailored blanks and fabrication of bumpers from optimally thin material. These technologies are described hereafter.

(1) Tailored blanks

To maximize rigidity in performance-critical areas (main members and joints) and minimize weight in all other areas, tailored blanks (blanks that are formed by welding together of appropriately positioned thick steel plates and thin steel plates before being pressed). Employment of tailored blanks for the front side members, front floor assembly, and other structural mem-

Fig. 6 Flexible welding line using four-face rotatable fixture

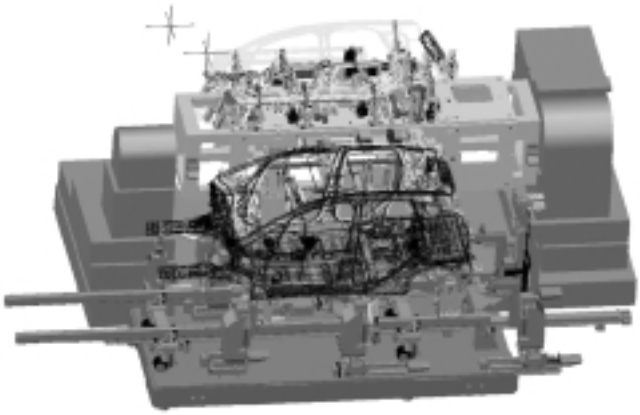

Fig. 7 CAD simulation of four-face rotatable fixture

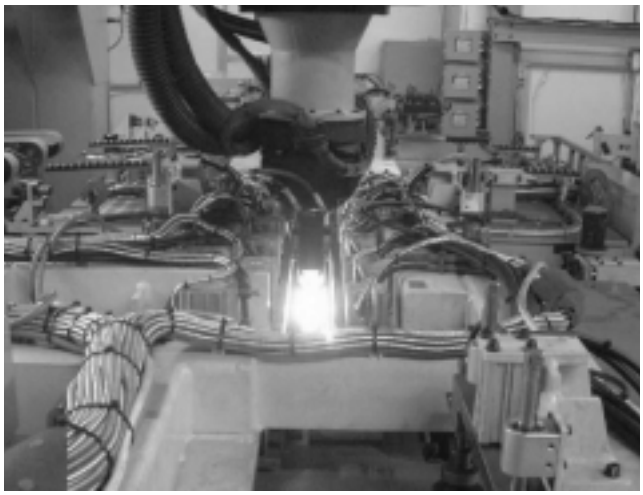

Fig. 8 Laser welding of steel plates

bers yields lightness and energy absorption and thus contributes to superior crash-safety performance. By way of example, tailored blanks (together with other structural rationalization measures) realized a weight saving in the front floor assembly of 6.2 kg per vehicle. Tailored blanks are also adopted for the front doors, rear doors, and tailgate, further helping to realize a body that is low in weight and cost. Further, a yttrium alminum garnet (YAG) laser, which permits laser energy to be transmitted via optical fiber, is employed for the welding. This technology yields great flexibility. Laser welding of steel plates is shown in **Fig. 8**.

(2) Thin-material, high-rigidity bumpers

Bumpers conventionally require material of 2.5 mm in thickness. With the COLT, however, the use of high-rigidity material and the use of flow-analysis techniques to create a rigid shape enabled the material to be made as thin as 2.0 mm with no compromise in rigidity. The overall benefits are a weight saving of 1 kg per vehicle and relatively low cost.

4. Realizing freedom of choice

To provide customers with freedom of choice, the new Customer Free Choice sales system was adopted for the COLT. This system allows customers to freely combine trim and equipment (based on three basic packages) to suit their individual lifestyles and needs. It also enables MMC to schedule production and shipping in such a way that each customer knows exactly when an ordered car will be delivered. Measures taken at the Okazaki plant to enable scheduled completion dates to be honored without fail are detailed hereafter.

Table 2 Key points for streamlined process

Welding line	• A dedicated in-line repair line is established, so streamlining is maintained as bodies are repaired and passed to the subsequent process. • Bodies to be subjected to verification of weld quality and bodies to be subjected to accuracy measurement are reflected in production scheduling. They are checked and measured off-line then introduced into the line in as scheduled.
Paint line	• Added measures against defects (measures to minimize substrate pimples, measures to minimize sealer defects, measures to improve finish quality, etc.) and added processes that ensure quality (two primer and sealer processes and 10 top coat processes) maximize the percentage of defect-free off-line vehicles. • Lines are as straight as possible (with minimal points of divergence and converge) for streamlining.
Bumper line	• A newly established bumper plant is located next to the body assembly line. • Number of in-process materials is minimized using assembly ON information to start painting, thereby minimizing flaws on materials from material handling.

4.1 Honoring scheduled completion dates without fail

Realization of ISCQ increased the percentage of defect-free off-line vehicles, thus enabling production to take place in a completely streamlined manner. Since production can take place exactly as planned, there are no sequence mixups to cause production delays. Nevertheless, a vehicle progress tracking system, which issues an alert corresponding to any vehicle whose production is delayed and enables the progress of production of each vehicle to be monitored using a web browser, was introduced. These factors together enable vehicles to be produced such that scheduled completion dates are honored without fail. Measures that keep processes streamlined on each line are shown in **Table 2**.

5. Measures for cost minimization

With the COLT, steps were taken to minimize various costs through the introduction of advanced technologies. The aforementioned tailored blanks and thin-material, high-rigidity bumpers, while helping to minimize weight and maximize rigidity, are examples of measures yielding cost savings. Other examples are described hereafter.

5.1 World-standard low-cost body

With the COLT, product structures and manufacturing methods that are compatible with base-grade steel plate that can be procured almost anywhere in the world were realized by means of structural studies, computer-aided-engineering technologies, and thorough proving trials. It was thus made possible for the body to be made from the least expensive base material available in Japan.

Fig. 9 Installation of instrument-panel module

5.2 Expanded use of modular construction

To minimize the amount of main-line work and minimize physical demands imposed on line workers, MMC uses instrument-panel modules, door modules, and other modules. With the COLT, the number of parts included in instrument-panel modules was increased and modular construction was adopted for the corners and head lining, resulting in further improved productivity and reduced costs. Installation of an instrument-panel module is shown in **Fig. 9**.

6. Summary

Measures were taken to realize consistently customer-focused production. The goal could not be achieved by the production department alone; it was achieved through concurrent activities with the development department, purchasing department, information-technology department, and other departments inside the company and through partnerships with part manufacturers outside the company.

Finally, we wish to take this opportunity to express our gratitude to all personnel inside and outside the company who contributed to successful launch of the COLT.

Koichi KAKU

Takeshi ANDO

Exciting EVs!

Hiroaki YOSHIDA* Akira MAEDA* Nobuya FURUKAWA*
Hiroyasu SUZUKI* Katsuhiko SUGIURA*

Introduction

As part of its work on technologies for electric vehicles (EVs) and hybrid electric vehicles (HEVs), Mitsubishi Motors Corporation (MMC) conducts research aimed at realizing usable high-capacity manganese lithium-ion batteries and lightweight motors that are suitable for real-world conditions. In 2002, MMC took part in competitions that allowed it to present its latest technologies to the public and assess their performance: With its ECLIPSE EV prototype, MMC conducted a demonstration drive as part of the Shikoku EV Rally Festival (the biggest EV rally held on public roads in Japan). This demonstration drive covered 815 km from MMC's Tokyo headquarters to Niihama City on the island of Shikoku, and it enabled MMC to assess the ECLIPSE EV prototype's high-speed practicality. And with its FTO EV prototype, MMC took part in the Suzuka EV Race and the Japan EV Festival Tsukuba Time Trial, thereby gaining opportunities to assess the FTO EV prototype's high-power-output performance. This paper gives an overview of the two vehicles, and it describes the competitions and the results thereof.

1. Vehicle overview

ECLIPSE EV (**Fig. 1**, **Table 1**, **Table 2**)

To allow existing charging facilities to be used along the route of the demonstration drive, the ECLIPSE EV's charging arrangement was changed from conductive to inductive.

FTO EV (**Fig. 2**, **Table 1**, **Table 2**)

The FTO EV has a body lighter than that of the ECLIPSE EV and running performance comparable with that of the ECLIPSE EV. For competition use, its suspension system, braking performance, and cooling performance were improved.

2. Competitions

2.1 Shikoku EV Rally Festival demonstration drive

The Shikoku EV Rally Festival demonstration drive was a test of long-distance EV operation using, as far as possible, existing commercial charging stations.

The ECLIPSE EV began the demonstration drive when it left MMC's Tokyo headquarters at 06:30 on Thursday August 22nd 2002. Having received three battery charges along the 815 km route, it reached its destination, Niihama Technical College (located in Ehime Prefecture on the island of Shikoku), at 15:10 the follow-

Fig. 1 ECLIPSE EV

Table 1 Vehicle specifications

	ECLIPSE	FTO
Overall length (mm)	4450	4320
Overall width (mm)	1750	1735
Overall height (mm)	1310	1300
Curb weight (kg)	1515	1440
Seating capacity (persons)	2	
Drive system	Front-wheel drive	
Transmission	Five-speed manual	
Max. speed (km/h)	180 minimum	

Table 2 Main component specifications (common to ECLIPSE EV and FTO EV)

Motor	Type	Permanent-magnet synchronous
	Supplier	Mitsubishi Heavy Industries, Ltd.
	Max. output (kW)	100
	Max. torque (Nm)	250
	Cooling method	Liquid
	Dimensions (mm)	ϕ 300 x 200
	Weight (kg)	47
Controller		IGBT PWM inverter
Batteries	Type	Lithium-ion
	Supplier	Japan Storage Battery Co., Ltd.
	Capacity (Ah)	95
	Total voltage (V)	14.8
	Dimensions (mm)	388 x 175 x 116
	Weight (kg each)	14.5
	Number on board	24 (series-connected)

* Advanced Electrical/Electronics Dept., Car Research & Dev. Office, MMC

Fig. 2 FTO EV

Table 3 Lengths of route sections

Route section	Length (km)
Start to Fujikawa service area	146
to Hamamatsu	248
to Yoro service area	402
to Kyoto EV charging station	512
to Kobe EV charging station	580
to Kamiita service area	700
to Niihama Technical College	815

ing day, Friday August 23rd. Expressways accounted for more than 95 % of the route.

The route is shown in **Fig. 3**, and the length of each route section is shown in **Table 3.** During the drive, the ECLIPSE EV's status was remotely monitored in real time by means of a car location system and displayed on the Internet.

The average vehicle speed (in km/h) and electric power consumption (in km/kWh) in each route section are shown in **Fig. 4**.

(1) Charging (Fig. 5)

The inductive method of charging (**Fig. 6**) was adopted. With this method, power is transferred to the vehicle by means of electromagnetic induction; alternating current with a high frequency (hundreds of kilohertz) flowing in a coil on the charger side induces a current in a coil on the vehicle side when brought near it. The coils are separately encased in plastic. Since there is no galvanic contact between the conductors, the risk of electric shocks is minimal; users can perform charging tasks safely even in rainy weather. Given these merits, inductive charging is seen as a valuable means of enabling charging stations to accommodate passenger cars of multiple makes and models.

Fig. 3 Demonstration drive route

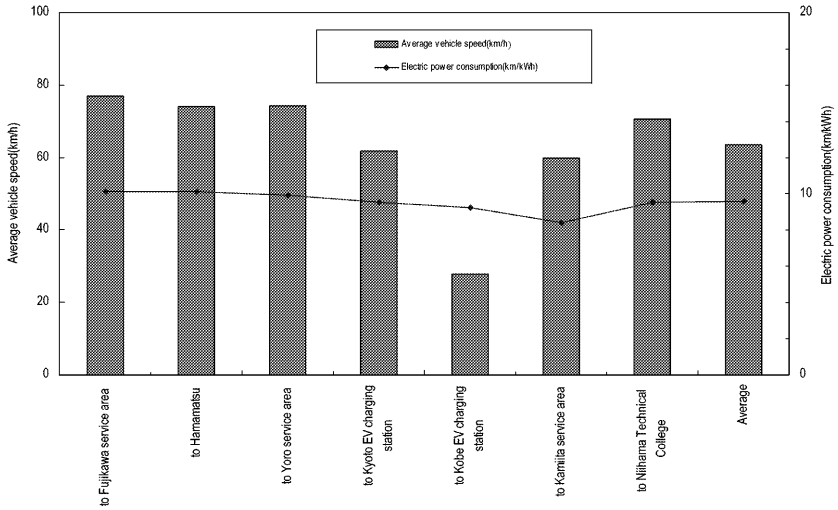

Fig. 4 Average vehicle speed and electric power consumption in each route section

Charging stations in Japan are currently all based on conventional chargers, i.e., not quick chargers, and have maximum power output of approximately 6 kW. With this output, increasing the ECLIPSE EV's state of charge from zero to 100 % takes approximately seven hours. With the current infrastructure, economic considerations will likely preclude the introduction of charger with higher output. If EVs are to become a common means of inter-city travel, however, increases in charger performance or increases in EV energy efficiency (to enable EVs to cover inter-city distances with lower battery drainage) are desirable.

With regard to the current charging infrastructure, no inductive charging stations exist between Kanagawa Prefecture and Kyoto Prefecture so an inductive charger was temporarily installed at an MMC dealership in Hamamatsu City, Shizuoka Prefecture. Even with a gasoline-engine vehicle, the distance between Tokyo and Kyoto is just about the greatest that can be driven

Fig. 5 Commercial EV charging station in Kobe

Fig. 6 Inductive charging

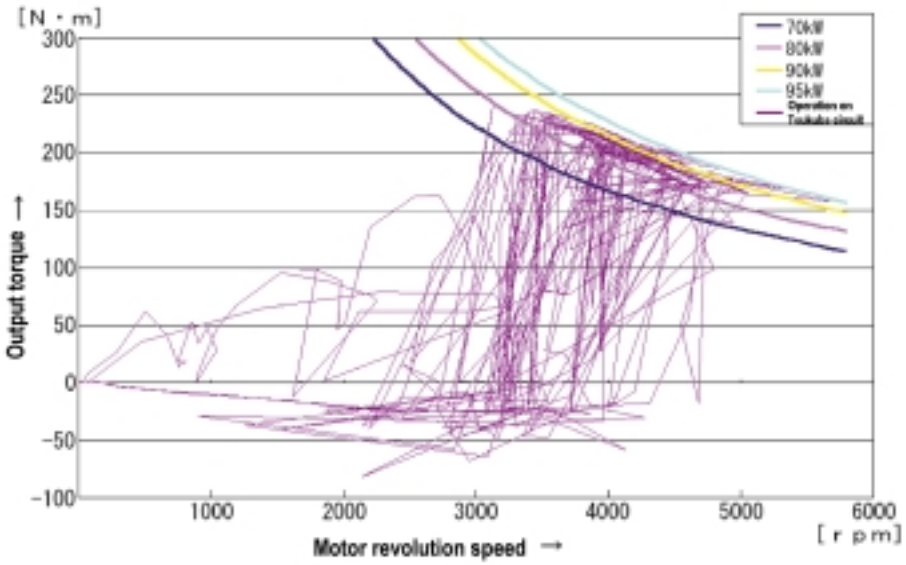

Fig. 7 Motor output characteristics while driving on Tsukuba circuit

without a fuel stop. With the ECLIPSE EV's level of performance, then, charging stations located with approximately the same density as gasoline stations would probably be adequate for inter-city travel.

(2) Results

As shown in **Fig. 4**, electric power consumption (this corresponds to the fuel consumption of a vehicle with an internal combustion engine) was an average of 10 km/kWh. The price of electricity at the Kobe charging station used during the demonstration drive was ¥30 /kWh, so the cost of 'fuel' was approximately one third of the cost of gasoline – a great saving.

The vehicle was trapped in traffic jams between the Kyoto charging station and the Kobe charging station, but its electric power consumption did not deteriorate significantly at that time (**Fig. 4**) because an EV (in contrast to a vehicle with an internal combustion engine) uses no power to run items other than accessories while stationary. The absence of superfluous energy consumption is another advantage of EVs.

2.2 Participation in EV races

EVs tend to be seen as advantageous in only economic and environmental terms, but appropriate use of their battery and motor properties can also yield running performance better than that of vehicles with internal combustion engines. MMC entered the FTO EV in races with a view to assessing its performance potential.

(1) Enhancements for race use

Given the likelihood of continuous operation with maximum power output, it was deemed that cooling performance would not be adequate with an inverter arrangement identical to that of the ECLIPSE EV. Consequently, the capacity of the inverter heat sink was increased and the coolant pump was replaced with a

larger one.

To reduce the vehicle's weight, the existing lithium-ion batteries were replaced with compact, lightweight, higher-energy-density, 40 Ah batteries. The weight saving was approximately 200 kg.

(2) Results

① Second in class in Suzuka EV Race

The Suzuka EV Race took place on July 27th 2002 on the east course of the Suzuka circuit. Owing to insufficient inverter cooling performance, the expected output was not obtained during high-speed, high-output operation. Although the FTO EV achieved a fast lap time of 1 minute 7.84 seconds (thus beating the previous year's course record of 1 minute 8.33 seconds), its total time for five laps (5 minutes 44.86 seconds) placed it second in the class.

② Second in class in Tsukuba Time Trial

The Tsukuba Time Trial took place on November 4th 2002 on the Tsukuba circuit. In preliminary testing, the aforementioned vehicle improvements helped realize a lap time in the order of 1 minute 12 seconds (better than that of a high-power gasoline-engine vehicle). In the actual time trial, however, poor track conditions resulted in a less satisfactory lap time of 1 minute 14.07 seconds.

③ Issues arising from race results

In the two races, it was observed that motor output was concentrated near the maximum level. (By way of example, **Fig. 7** shows the motor output characteristics observed during operation on the Tsukuba circuit.) The need for improvements in output characteristics and stability in this range was thus confirmed. The motor's mechanical strength and the batteries' internal resistance were also identified as critical factors. Future development targets were thus clarified.

3. Summary

Race participation with the ECLIPSE EV and FTO EV enabled the performance of lithium-ion batteries and lightweight motors to be assessed and enabled outstanding issues to be clarified. MMC will pursue further advances (including cost reductions) with a view to realizing practical EVs.

Reference

(1) Yoshida, Sugiura, Maeda, Furukawa, Hashiguchi, Hayakawa: Can EV Boast Mobility?, Mitsubishi Motors Technical Review, NO. 14, 2002


Hiroaki YOSHIDA


Akira MAEDA


Nobuya FURUKAWA


Hiroyasu SUZUKI


Katsuhiko SUGIURA

Development of Quiescent Combustion System (MIQCS) for Low Exhaust Emissions and Low Fuel Consumption with Heavy-Duty Diesel Engine

Hiroshi JOTAKI* Kazutoshi MORI*
Kenji SAKAI* Seiji OKADA**

Abstract

As standards on exhaust emissions from diesel-engine vehicles are rapidly tightened around the world, development efforts aimed at simultaneously reducing exhaust emissions and fuel consumption continue apace[1][2].

Development of a new-generation direct-injection engine by Mitsubishi Fuso Truck & Bus Company (MFTBC) is one of such efforts. A key technology of this engine is the Mitsubishi Innovative Quiescent Combustion System (MIQCS), which was developed through a combustion-based approach involving a detailed study of intake-port characteristics, fuel-injection characteristics, and combustion-chamber shapes, observation and analysis of air flows and sprayed fuel flows, and simulation of combustion. In light of significant benefits achieved in this attempt to minimize exhaust emissions and fuel consumption, the MIQCS development team was awarded the Technical Development Prize of the Society of Automotive Engineers of Japan's (JSAE's) 52nd Technical Awards in 2002.

The MIQCS system is used in the turbocharged and intercooled engine (see Table 1 below) used in Mitsubishi Fuso heavy-duty trucks that went on sale in February 2000.

Table 1 Engine specifications

Engine model	6M70TI (turbocharged and intercooled)
Bore x stroke	ϕ 135 mm x 150 mm (six-cylinder, in-line, 12.9 L displacement)
Fuel injection	Common-rail system

1. Concept of combustion

Combustion in a diesel engine consists of two combustion phases: (1) pre-mixed combustion that occurs when fuel injected into a cylinder evaporates into a gas and is ignited by compression, and (2) diffusive combustion in which incompletely vaporized injected fuel droplets burn. When the pre-mixed combustion is vigorous, thermal efficiency is concomitantly high but nitrogen oxides (NOx) are produced in concomitantly large quantities. And when the diffusive combustion progresses slowly, black smoke emissions increase and thermal efficiency decreases in proportion to the length of the combustion period. The key to simultaneously decreasing exhaust emissions and fuel consumption in a diesel engine is, therefore, to realize a two-phase combustion process in which the pre-mixed combustion is optimally limited and the diffusive combustion is optimally promoted (**Fig. 1**). To achieve this ideal type of combustion, it is essential, through proper control of the spacial dispersion and mixing with air of fuel that has been injected at high pressure into the cylinder and atomized into small droplets, to create a uniformly lean mixture that enables homogeneous combustion with a low flame temperature.

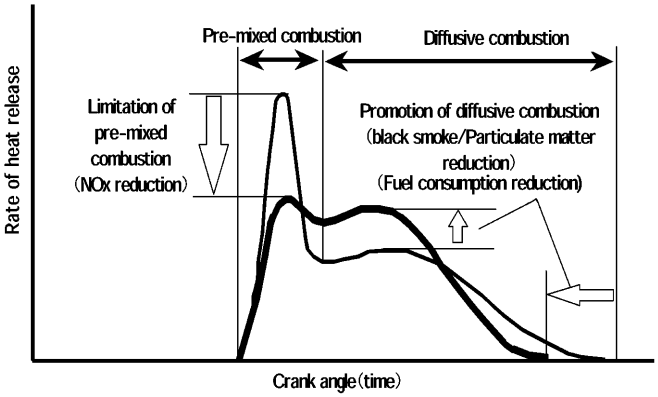

Fig. 1 Control of combustion process

2. Comparison and selection of combustion systems

Most direct-injection diesel engines used in heavy-duty trucks sold in Japan use the swirl-supported combustion system (SSCS). This system employs in-cylinder swirl and squish flows and other air flows to promote mixture of the fuel spray with air prior to combustion.

* Engine Research Dept., Research & Dev. Office, MFTBC
** Engine Design Dept., Research & Dev. Office, MFTBC

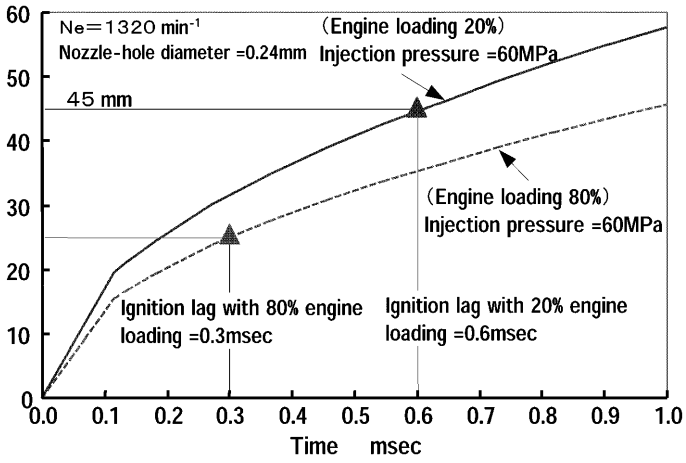

Fig. 2 Predicted spray penetration

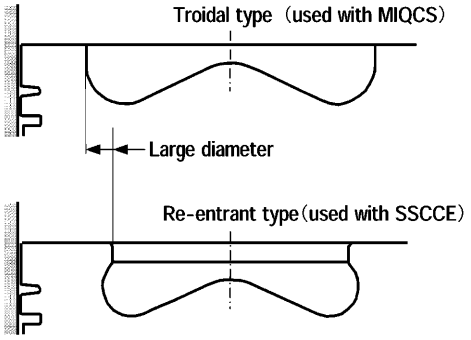

Fig. 3 Cross section of combustion bowl shapes

By contrast, the quiescent combustion system (QCS)[3] utilizes the energy of a high-pressure fuel spray as the primary means of promoting mixture of the fuel spray with air before combustion. In the QCS, a combination of a low-swirl-ratio intake port and a large-diameter combustion bowl limits in-cylinder air flow, thus enabling high thermal efficiency to be obtained. For this reason, the QCS is widely used in large marine engines[4]. Conventionally, however, the QCS cannot be used to optimize the combustion characteristics of a heavy-duty truck's diesel engine though the engine's entire operating range.

Since the in-cylinder swirl flow is weak with the QCS, any sprayed fuel that adheres to the wall of the combustion bowl prior to combustion fails to mix with the air, resulting in significant emissions of black smoke and hydrocarbons. To prevent this undesirable condition, the diameter of the combustion bowl must be made greater than the distance by which the spray tip penetrates during the ignition-lag period (**Fig. 2**) and transient in-cylinder air flow must be properly controlled. A toroidal combustion chamber (**Fig. 3**), which meets these requirements, was selected for the MIQCS.

Sufficient air volume was ensured by selection of a port arrangement with two intake valves and two exhaust valves per cylinder. In addition, the intake-port layout was devised so as to minimize interference between the two intake-valve flows (**Fig. 4**).

For selection of an appropriate in-cylinder swirl ratio

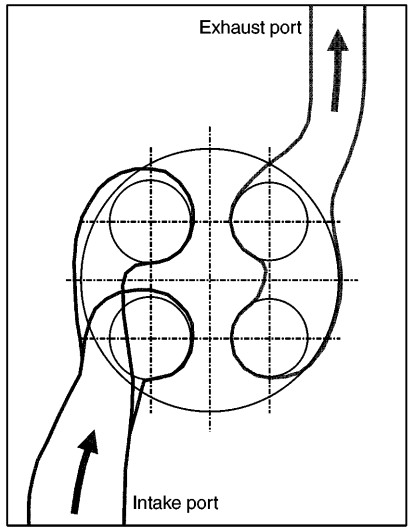

Fig. 4 Port layout

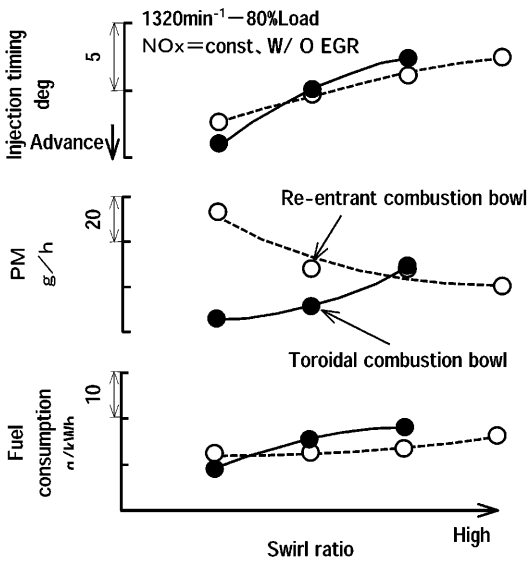

Fig. 5 Influence of swirl ratio and combustion bowl shape on emissions and fuel consumption

for the MIQCS, comparison was made of the effects of various swirl ratios with the re-entrant-type combustion chamber for the conventional SSCS and the large-bowl-diameter, toroidal-type combustion chamber for the MIQCS (**Fig. 5**). Decreases in the swirl ratio caused fuel consumption to decrease with both combustion-chamber types. The same decreases in the swirl ratio caused PM emissions to increase with the re-entrant type combustion chamber and to decrease with the large-bowl-diameter, toroidal-type combustion chamber. Consequently, a large-bowl-diameter toroidal-type combustion chamber with a low-swirl-ratio intake ports was identified as the optimum choice for simultaneous minimization of fuel consumption and PM emissions.

Since the QCS depends primarily upon the fuel-injection energy to mix the fuel with the air, a high injection pressure is necessary. With marine engines and with the diesel engines of non-Japanese heavy-duty

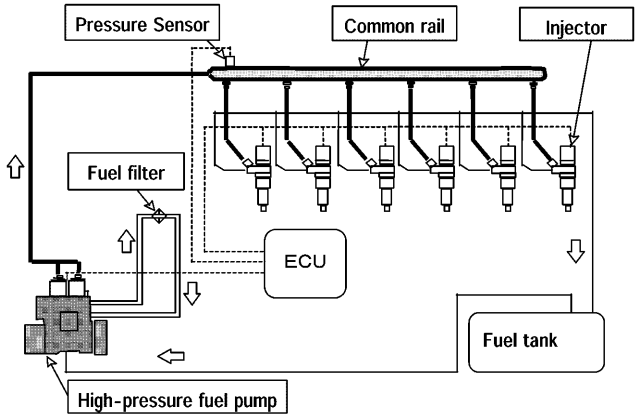

Fig. 6 Common-rail system

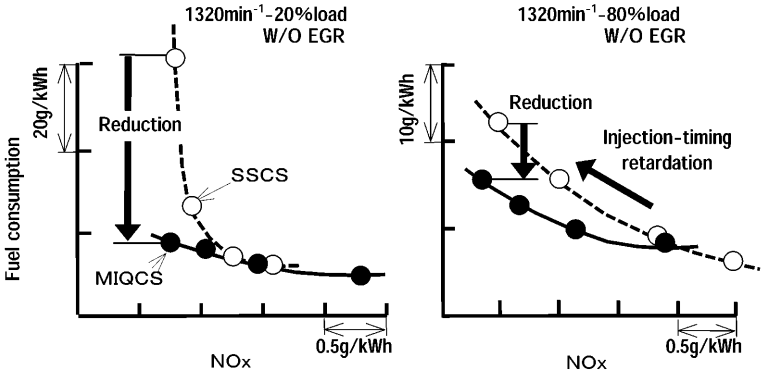

Fig. 7 Comparison between MIQCS and SSCS for overcoming Nox and fuel consumption trade-off

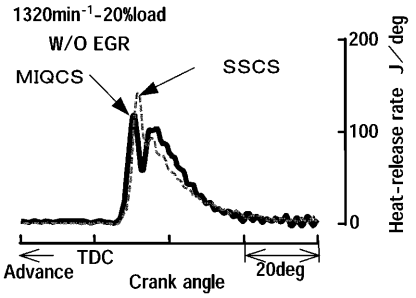

Fig. 8 Comparison of heat-release rates with MIQCS and SSCS

vehicles, manufacturers often use high-pressure fuel-injection systems[5] such as jerk-type electronic unit injectors (EUIs) or unit pumps (PLDs). EUIs and PLDs offer high maximum injection pressures, but the injection pressure depends on the engine speed. Consequently, the injection pressure is insufficient for mixing fuel with air during low-speed operation.

In light of the abovementioned factors, the common-rail system (CRS)[6] shown in **Fig. 6** was selected for fuel supply with the MIQCS. The CRS offers a sufficiently high injection pressure even during low-speed engine operation, thus enabling low exhaust emissions and low fuel consumption over the whole range of operating conditions, and it permits the injection pressure and injection timing to be controlled independently of the engine speed.

With the combined benefits of the low-swirl cylinder head, large-bowl-diameter toroidal combustion chamber, and CRS, the MIQCS offers advantages over the SSCS particularly in terms of the trade-off between NOx emissions and fuel consumption at the low end of the NOx-emissions range (**Fig. 7**).

3. Clarification of MIQCS combustion phenomena

To clarify the reasons for the superiority of the MIQCS over the SSCS in terms of NOx-reduction characteristics, the two combustion systems' heat-release rates were compared (**Fig. 8**).

The MIQCS was found to have a relatively short ignition-lag period, a relatively low pre-mixed-combustion peak, and a relatively short combustion period, thus realizing the concept of ideal two-stage combustion. These characteristics explain the MIQCS's ability to simultaneously minimize NOx emissions and fuel consumption.

Flame-temperature analyses performed using the two-color method[7] as part of the observation of in-cylinder combustion revealed that high-temperature combustion occurred in the combustion bowl with the SSCS and that relatively low-temperature combustion occurred throughout the cylinder with the MIQCS (**Fig. 9**). Further, the results of flame-area analyses revealed that the MIQCS's area of high-temperature combustion (with temperatures in excess of 2800 K) was approximately half that of the SSCS. Since high-temperature combustion contributes greatly to NOx formation, the relatively small flame area can be considered one of the reasons for the low NOx emissions of the MIQCS (**Fig. 10**).

In-cylinder temperatures and NOx-generation amounts were investigated by means of numerical analyses performed using the KIVA-II computer program[8]. The results showed that the region of high-temperature combustion (with temperatures higher than 2550 K) occurring in the first half of the combustion cycle was smaller with the MIQCS than with the SSCS and that the rate of NOx formation was relatively low with the MIQCS in the same period (**Fig 11**). Further, the results of the numerical analyses showed that combustion in the second half of the combustion cycle was more vigorous with the MIQCS than with the SSCS. Recombustion of soot promoted by combustion that remains vigorous late in the cycle can be interpreted as one reason for the MIQCS's relatively low emissions of black soot.

4. Real-world potential of MIQCS

As suggested by the results of basic tests and combustion analyses, the MIQCS is capable of simultane-

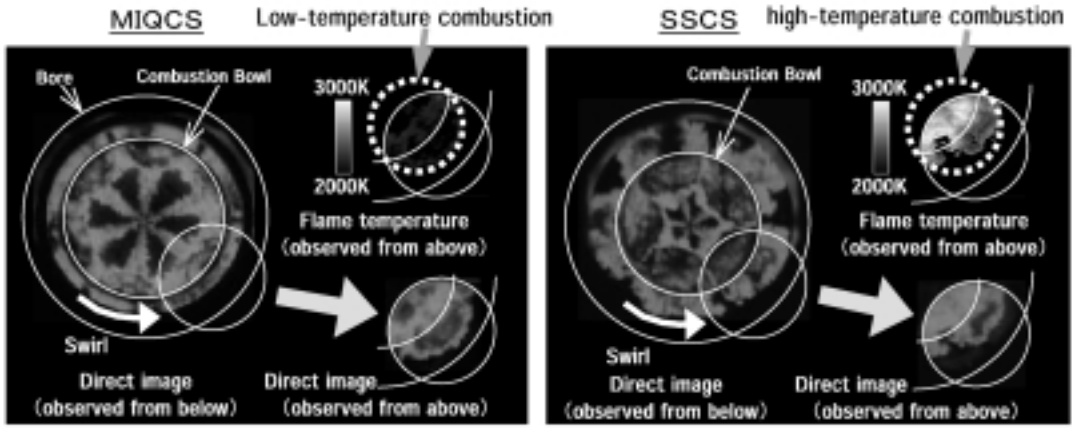

Fig. 9 Combustion images and flame temperature for MIQCS and SSCS

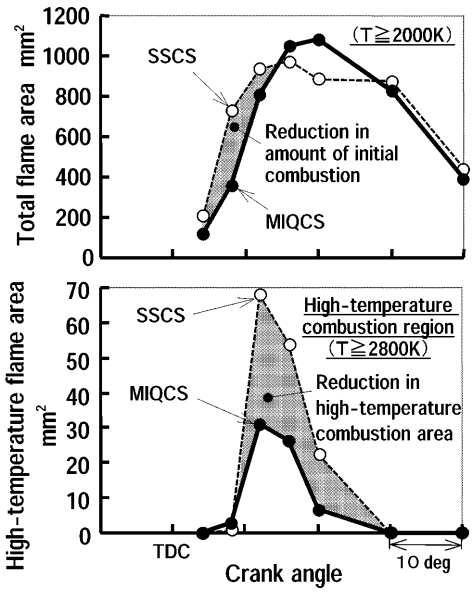

Fig. 10 Comparison of flame area for MIQCS and SSCS

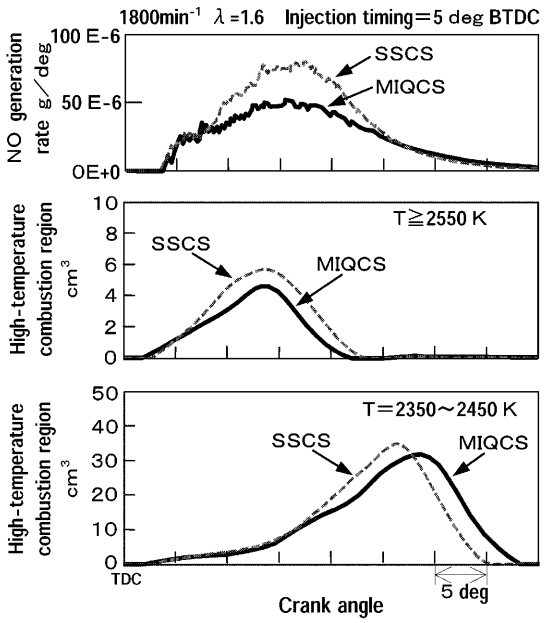

Fig. 11 Comparison of combustion process by CAE

ously reducing exhaust emissions and fuel consumption. To enable the real-world potential of this technology to be ascertained, the MIQCS was combined with an exhaust-gas recirculation (EGR) system[9] in an engine and optimized through subjection of the engine to testing under full-load conditions and in Japan's 13-mode diesel-engine test cycle.

In the full-load test, The MIQCS achieved lower fuel consumption than the SSCS at all engine speeds and its maximum thermal efficiency was as high as 45 %. The MIQCS also achieved a significant reduction in fuel consumption at the output point. Clearly, the MIQCS proved an extremely effective means of minimizing fuel consumption.

The MIQCS also achieved lower black-smoke emissions than the SSCS at all engine speeds. (Its superiority in this regard was greatest toward the high end of the speed range.) Since black smoke is the main contributor to particulate matter (PM), the MIQCS is clearly an effective means of minimizing PM emissions (**Fig. 12**).

Further, the results of comparison made of the exhaust emissions of the MIQCS and SSCS in Japan's 13-mode test cycle showed that the MIQCS realized lower PM emissions and fuel consumption than the SSCS with any given level of NOx emissions. Its emission levels were low enough to satisfy Japan's 1998 – 1999 exhaust-emission standards, and its fuel consumption was lower than that of already-marketed engines that comply with Japan's 1994 exhaust-emissions standards (**Fig. 13**).

Toward the lower end of the NOx-emission range, the MIQCS's merits with respect to reduction of fuel consumption and PM emissions were found to be significant, indicating great potential for use in future ultra-low-emission, low-fuel-consumption engines.

5. Resource savings and greenhouse-gas reductions

Reduced fuel consumption by vehicles using MIQCS engines also means reduced carbon-dioxide (CO_2)

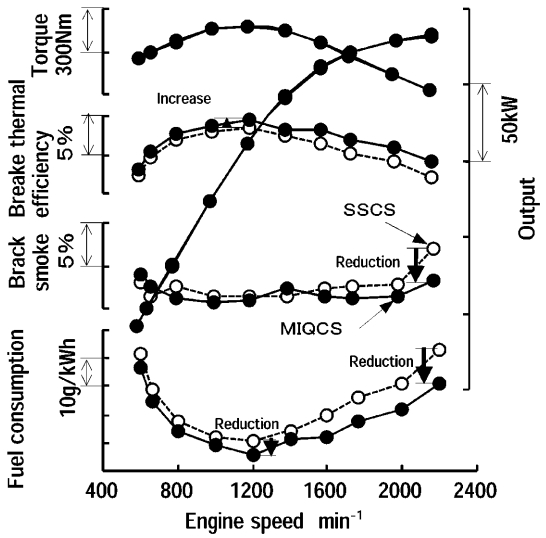

Fig. 12 Full-load performance

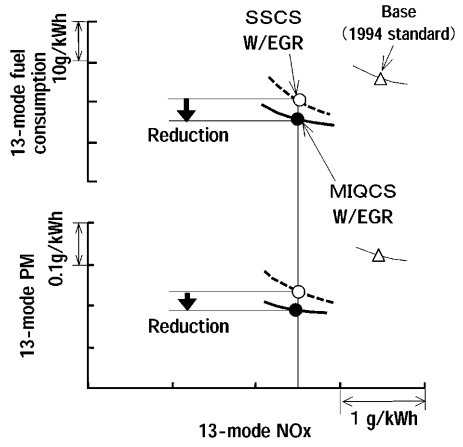

Fig. 13 Exhaust emissions and fuel consumption in Japan's 13-mode test cycle

emissions. If all the Mitsubishi-made heavy-duty trucks currently used in Japan were replaced with trucks equipped with MIQCS engines, the conceivable reduction in diesel-fuel consumption would be approximately 320000 kiloliters per year and the conceivable reduction in CO_2 emissions would be 860000 tons per year (a significant contribution to efforts to slow global warming) (**Table 2**).

6. Summary

The MIQCS, a new combustion system developed for new-generation direct-injection diesel engines, was adopted in the diesel engines of MFTBC heavy-duty trucks that are now on the market. The MIQCS not only realizes significantly reduced air-polluting NOx and PM emissions but also enables greatly reduced fuel consumption and concomitantly reduced CO_2 emissions (a vital achievement with respect to environmental protection).

Research and development for further advancement of the MIQCS will be conducted in pursuit of ways to take even greater advantage of diesel engines' inherent fuel economy (their greatest merit) while further reducing exhaust emissions toward zero.

Table 2 Achievable reductions in resource consumption and CO_2 emissions

	Reduction in diesel-fuel consumption	Reduction in CO_2 emissions
One truck	Approx. 1600 L/year	Approx. 4.3 tons/year
All Mitsubishi heavy-duty trucks	Approx. 320000 kL/year	Approx. 860000 tons/year

Assumptions for calculations: One truck covers 120000 km per year, and 200000 Mitsubishi heavy-duty trucks are currently in use in Japan.

References

(1) K. Mori, et al.: "Worldwide Trends in Heavy-Duty Diesel Engine Exhaust Emission Legislation and Compliance Technologies", SAE Paper No. 970753
(2) P. Zelenka, et al.: "Cooled EGR a Key Technology for Future Efficient HD Diesels", SAE Paper No. 980190
(3) W. P. Cartellieri, et al.: "Swirl Supported or Quiescent Combustion for 1990's Heavy-Duty DI Diesel Engines – An Analysis", SAE Paper No. 880342
(4) K. Kunberger: "New Medium-Speed Diesel Designed to Combine Economy with Ecology Features", Diesel & Gas Turbine Worldwide (July – August 1993)
(5) M. Schitter, et al.: "Leistungsmerkmale der neuen Nutzfahrzeugmotoren OM 501 LA und OM 502 LA von Mercedes-Benz", MTZ (Vol. 57 No. 11)
(6) Y. Yamaki, et al.: "Heavy duty diesel engine with common rail type fuel injection system", IPC-8 (No. 9530139)
(7) H. Nakajima, et al.: "The Analysis of Flame in DI diesel Engine – Part 3: Measurement and Analysis of Flame Temperature", JSAE Vol. No. 945
(8) R. J. Donahue, et al.: "Cylinder-Averaged Histories of Nitrogen Oxide in a DI diesel with Simulated Turbocharging", SAE Paper No. 942046
(9) S. Kohketsu, et al.: "EGR Technologies for a Turbocharged and Intercooled Heavy-Duty Diesel Engine", SAE Paper No. 970340


Hiroshi JOTAKI


Kazutoshi MORI


Kenji SAKAI


Seiji OKADA

Theoretical Analysis of Tire Acoustic Cavity Noise and Proposal for Improvement Technique

Hiroshi YAMAUCHI*

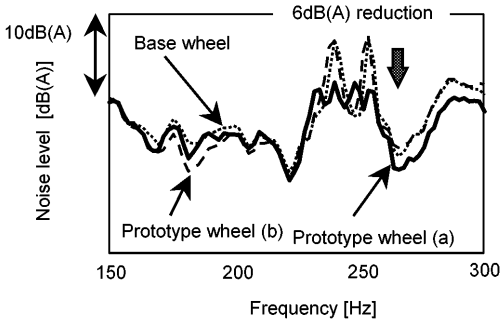

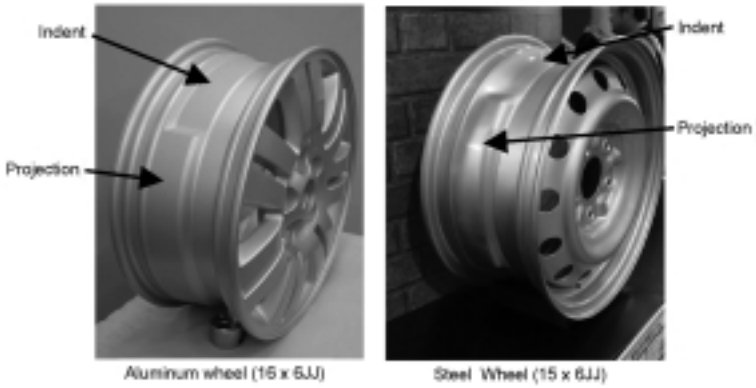

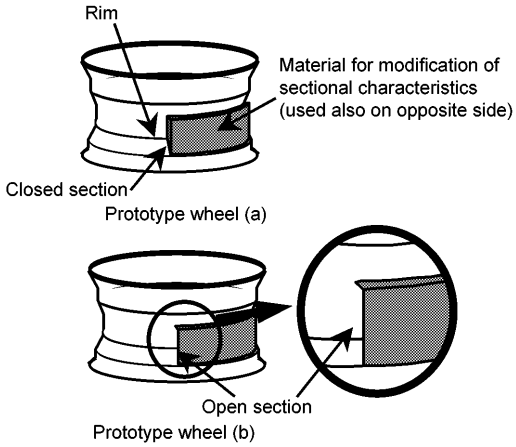

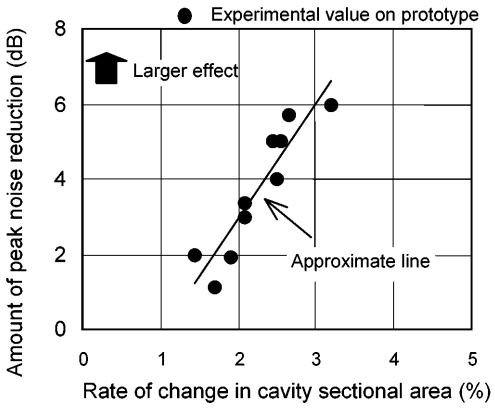

The author of "Theoretical Analysis of Tire Acoustic Cavity Noise and Proposal for Improvement Technique" received for his paper the Asahara Prize Science Promotion Award of the Society of Automotive Engineers of Japan's (JSAE's) 52nd Technical Awards, presented in 2003. The selection committee expressed high praise for the new technology, describing it as, "a valuable technology for improvement of human-automobile-environment interaction; one that is well matched to contemporary demands for creation of a human-friendly environment; and one that has significant potential for adoption in all vehicles".

The paper first shows that the mechanism by which tires generate annoying road noise during driving can be explained by an original theory that the author deduced from basic principles (not relying on existing theories). It then proposes a new wheel structure embodying the theory, discusses several prototype wheels based on the structure, and shows the results of experiments performed on the prototypes.

In the proposed wheel structure, small indents and projections are formed on the tires and wheels to cause the sectional form of the tire's inside cavity to vary circumferentially. Appropriate location of the indents and projections makes it possible to limit deterioration of ride quality to a minimum.

A detailed study of the proposed wheel structure with regard to cost and weight is now being conducted as part of moves toward volume production. Should volume production be realized, the new-structure wheels will enable customers to enjoy unprecedented ride comfort in their vehicles.

Hiroshi YAMAUCHI

* Vehicle Proving Dept., Car Research & Dev. Office, MMC

NEW PRODUCTS

New COLT

In November 2002, Mitsubishi Motors Corporation (MMC) entered the rapidly growing subcompact segment with the launch of the New COLT, a next-generation subcompact car in which a superior balance of performance, fuel economy, and environmental compatibility is complemented by a class-eclipsing level of refinement.

1. Targets

When choosing an automobile or any other product, today's discerning consumers look for the added touch of refinement that elevates one particular brand or model above the rest of the class. The New COLT was developed accordingly; it meets the needs of discerning car-buyers by combining three vital attributes: class-eclipsing quality that's reflected in every aspect of the New COLT's look and feel; a superior balance of on-road performance characteristics; and great freedom of choice with regard to trim and equipment.

2. Features

- Quality

(1) Exterior

A 'one-motion form' that flows smoothly from the front bumper to the end of trailing edge of the roof maximizes occupant space within modest exterior dimensions (a particularly important accomplishment in a subcompact car) and helps to give the New COLT a fresh, dynamic, and truly distinctive look. Four-bulb headlamps with deeply contoured reflectors behind clear lenses contribute to a front mask that embodies real refinement and functional aesthetics.

The overall front-end architecture embodies MMC's new design identity, which reflects MMC's confidence in the future. The New COLT is offered with a wide range of 10 body colours, six of which were newly created for this car.

(2) Interior

Since the cabin is the part of the New COLT that users will most often see and touch, it was developed with an unrelenting focus on quality and comfort.

Consequently, the interior design combines contours and textures in a way that creates a refined, relaxing environment with a clean, contemporary look. Major instrumentation takes the form of a distinctive, easy-to-read three-dial meter cluster. The center panel has flush surfaces that give it a highly evolved look and feel, and it positions the audio, air-conditioning, and other controls where they are easiest to use. On each side of the cabin, the smooth lines of the instrument panel flow seamlessly into those of the door trim, creating a strong sense of continuity. There is a choice of two interior colour schemes: 'cool', which uses a blueish-grey key colour to evoke a high-tech, sporty image, and 'warm', which uses two-tone brown and beige to convey a sense of chic elegance.

(3) Packaging

The New COLT offers plenty of interior space; a long wheelbase of 2,500 mm permits a cabin length of 1,705 mm (one of the greatest in the subcompact category), and shoulder room is ample at 1,340 mm. A column-mounted shift lever and a foot-operated parking brake further enhance legroom for front-seat occupants and permit easy movement from one side of the cabin to the other.

(4) Handy storage spaces

In terms of convenience and ease of use, the New COLT eclipses the class. Two types of front seat – bench and separate – are available. In models with the bench seat, the passenger-side squab of the seat conceals a locker that has a capacity of 6.1 liters (sufficient for five 500 ml beverage bottles) and is ideal for storing handbags and other personal items out of sight. The squab automatically locks in the raised position, and its underside is fitted with hooks that can be used to secure luggage. In models with separate front seats, the space between the driver's seat and passenger seat is occupied by a multi-purpose tray, which incorporates movable, detachable cup holders and can be fitted with a choice of genuine Mitsubishi accessories including a center console and MiniDisc holders.

• Performance

(1) Newly developed MIVEC* engines

For an optimal combination of high output, low fuel consumption, and low exhaust emissions, New COLT models are equipped with newly developed 1.3- and 1.5-liter MIVEC engines. Each new engine combines a short-stroke design, optimally shaped intake ports, and the variable intake-valve timing made possible by the MIVEC to achieve capable performance with minimal fuel consumption throughout the rev range.

*Mitsubishi Innovative Valve timing Electronic Control system

(2) CVT* control for smooth running

Each engine is mated to a CVT in which a minimal pulley-piston diameter, minimal oil-pump delivery, and optimal tuning of torque-converter lockup control ensure efficient transmission of engine power for enjoyably smooth running.

*continuously variable transmission

(3) Class-topping performance

Integral control of the newly developed MIVEC engines and CVT helps to realize off-the-line acceleration and passing acceleration that are among the best in the class.

(4) Superior fuel consumption and emissions performance

The inherent efficiency of the MIVEC engines and CVT and the integral engine and CVT control are complemented by a high-efficiency air-conditioner unit and other measures aimed at maximizing fuel consumption during day-to-day urban driving. Also, measures to minimize the MIVEC engines' hydrocarbon emissions are complemented by a dual manifold catalytic converter employing a trimetal catalyst for further enhanced emission-reduction performance. As a result, all New COLT models comply with Ultra Low Emission Vehicle standards.

(5) Newly developed platform

A new platform with straight side rails was jointly developed by MMC and DaimlerChrysler for shared use. Minimal offsets in the frame layout enhance body rigidity and strength and contribute to superior collision safety. Also, the front side members each have an octagon section at the front end and figure-of-eight section at the rear end for efficient impact-energy absorption and an optimal frame-distortion mode. These frame-related measures are complemented by high-rigidity pressed doors and other strength-enhancing measures. Consequently, the results of in-house tests with a 64 km/h offset frontal impact, a 55 km/h full-width frontal impact, and a 55 km/h side impact correspond to a Japan New Car Assessment Program rating of five stars.

(6) Newly developed suspension system

A newly developed MacPherson-strut suspension arrangement is employed at the front. A completely flat front crossmember maximizes mounting rigidity, thus helping to realize nimble handling. Plus, optimized spring positioning and strut damping characteristics, input-splitting upper insulators, and other measures ensure a smooth ride. An H-type torsion-beam suspension arrangement is employed at the rear. The space it occupies is minimized by location of the coil springs under the rear floor side members and by location of the shock absorbers as close as possible to the periphery of the body. The cabin is concomitantly spacious.

• Freedom of choice

With the New COLT, MMC has introduced a Customer Free Choice system that enables customers to select interior and exterior appearance and equipment as desired. Three basic packages are offered as a starting point for selections, and customers can modify them by combining exterior and interior colors, seat types, and equipment specifications while deleting items they do not require. As a result, customers can each have a New Colt that's exactly tailored to their individual tastes and lifestyles.

3. Major specifications

The major specifications of the New COLT are shown in the following table.

Specifications \ Model		2WD	
		Mitsubishi UA-25A	Mitsubishi UA-27A
Overall length	(mm)	3,870	
Overall width	(mm)	1,680	
Overall height	(mm)	1,550	
Vehicle weight	(kg)	1,010	1,020
Minimum turning radius	(m)	4.7	
10·15-mode fuel consumption	(km/L)	20.0	18.0
Engine model		4G19 1.3 L MIVEC	4G15 1.5 L MIVEC
Valve mechanism and number of cylinders		DOHC; 16-valve; four cylinders	
Maximum output	(kW (PS)/min^{-1})	66 (90) /5,600	72 (98) /6,000
Maximum torque	(Nm (kg-m)/min^{-1})	121 (12.3) /4,250	132 (13.5) /4,250
Transmission		INVECS-III CVT (continuously variable transmission)	
Suspension	Front	MacPherson struts (with stabilizer)	
	Rear	Torsion beam (with stabilizer)	
Tires		175/65R14 · 185/55R15	

([A&B Product Dev. Project], Car Research & Dev. Office, MMC: T. Tanaka, M. Tanaka, Ishiwata)

NEW PRODUCTS

LANCER CARGO

– Japan domestic version –

Demand for passenger-car-based commercial vehicles remains steady in Japan. Until recently, Mitsubishi Motors Corporation (MMC) was represented in this segment by the LIBERO CARGO. This vehicle had been on the market for more than 10 years, however, so MMC needed to offer a vehicle with higher levels of environmental compatibility, safety, and economy to meet today's needs. MMC's response was the LANCER CARGO, a new commercial vehicle that's more appealing in every way. It was launched in January 2003.

1. Targets

MMC began its LANCER CARGO program by conducting research that yielded an accurate picture of today's usage trends and user requirements for light commercial vehicles. Based on its findings, MMC worked to develop a vehicle that would increase MMC's market share by virtue of a low purchase price, low running costs, and superior reliability and ease of use-all attributes for which there is strong demand.

2. Features

(1) Business-oriented exterior design

To ensure that minor knocks on the bumpers are not conspicuous and that bumper replacement costs are minimal, the plastic used for the bumpers is material color black rather than painted. The front grille is also same kind of color and has a unique design that gives prominence to a large Mitsubishi three-diamond emblem. At the rear, an enlarged tailgate opening ensures easy cargo-handling. A newly designed tailgate with concomitantly broad surfaces is complemented by newly designed rear lamp units that have smaller dimensions for reduced cost and incorporate a high-brilliance silver coating for good visibility. The space above each rear lamp unit is occupied by a quarter end garnish that further emphasizes the vehicle's originality.

(2) Roomy cabin and cargo area

A cab-forward design and long wheelbase like those of the LANCER WAGON yield superior spaciousness for people and cargo. Other features shared with the LANCER WAGON include high seating positions, which facilitate occupant ingress and egress, and a low dashboard and low belt line, which together promote visibility and a sense of openness.

To ensure suitability for business use, the LANCER CARGO was designed differently from the LANCER WAGON in several respects: The spare tire was moved from the cargo area to a position under the cargo-area floor, and the cargo-area floor was made flat. The rear seat was moved forward to make the cargo area longer. And cargo loading and unloading were made easier by elimination of the luggage-floor box (located on the cargo-area floor in the LANCER WAGON), by lowering of the cargo-area floor to a height of 550 mm (measured from the ground), and by lowering of the top surface of the rear bumper.

(3) Class-topping fuel economy

In developing the LANCER CARGO, MMC placed particular emphasis on fuel economy, which is a major factor in purchase decisions. This emphasis is reflected in powertrain specifications: The two-wheel-drive, automatic-transmission version (the top-selling version of the LANCER CARGO) is offered with a continuously variable transmission (the first to be used in a light commercial vehicle), and the four-wheel-drive (4WD) version has an INVECS-II four-speed automatic transmission. Each automatic transmission is mated to a simple 1.5-liter, SOHC, four-valve-per-cylinder, MPI engine, resulting in class-topping 10·15-mode fuel consumption. Further, emphasis was placed not only on catalog-figure fuel consumption but also on fuel consumption achieved in practical use (an important factor in running costs); several driving patterns typical of light commer-

cial vehicles were determined through a study of practical use and were used as references in the development program. The overall result is fuel economy that's superior to that of competing vehicles (including those with five-speed manual transmissions).

(4) Driving performance for business needs

The LANCER WAGON's proven four-wheel independent suspension system (this has a MacPherson-strut arrangement at the front and a multi-link arrangement at the rear) is employed also in the LANCER CARGO. To deal with the significant cargo weights and cargo-weight fluctuations associated with cargo-carrying applications, the body and suspension system were strengthened and the suspension system was retuned. Particular attention was paid to ensuring good handling stability when the vehicle is carrying cargo and good ride comfort when it is moderately loaded. Further, the 4WD system is the unique in the class to have a center differential fitted with a viscous coupling unit. This technology promotes stability when the vehicle is driven laden on gradients and on snow-covered roads.

(5) Safety and environmental compatibility

The LANCER CARGO has a Reinforced Impact Safety Evolution body structure like that of the LANCER WAGON. Consequently, it achieved Japan New Car Assessment Program ratings almost identical to those of the LANCER WAGON for occupant protection in a 64 km/h offset frontal impact, in a 55 km/h full-width frontal impact, and in a 55 km/h side impact. Passive safety is promoted by driver and front-passenger airbags (these are fitted as standard equipment), by impact-absorbing pillar trim (this mitigates secondary-impact head injuries), and by seatbelt pretensioners and force limiters (these are fitted as standard equipment).

With regard to environmental compatibility, every version of the LANCER CARGO is certified as an Ultra Low Emission Vehicle (U-LEV) owing to exhaust emissions that are at least 75 % lower than those permitted by Japan's 2000 standards. Every version also complies with Japan's 2010 standards for fuel consumption. By virtue of these two environmental credentials, the LANCER CARGO qualifies for favourable treatment under Japan's system of 'green' tax incentives.

3. Major specifications

The LANCER CARGO lineup and major specifications are shown in the following table.

Specifications \ Model				LANCER CARGO		
				UB-CS2V		
				E, G		
				2WD		4WD
				5 M/T	CVT	4 A/T
Seating capacity			(persons)	2 (5)		
Dimensions	Overall length		(mm)	4,440		
	Overall width		(mm)	1,695		
	Overall height		(mm)	1,455		
	Wheelbase		(mm)	2,600		
	Tread	Front	(mm)	1,470		
		Rear	(mm)	1,470		
	Ground clearance		(mm)	155		
	Cargo-area length		(mm)	1,740 (1,045) ( ): dimension with five occupants		
	Cargo-area width		(mm)	1,360 (1,400) ( ): dimension with five occupants		
	Cargo-area height		(mm)	905		
Engine	Model			4G15		
	Displacement		(cc)	1,468		
	Valve mechanism; number of cylinders			SOHC 16-valve; four cylinders		
	Maximum output		{kW (PS)/min^{-1} Net}	66 (90) /5,250		
	Maximum torque		{Nm (kgf·m) /min^{-1} Net}	133 (13.6) /3,750		
	Fuel supply system			ECI-MULTI (electronically controlled fuel injection)		
Chassis	Steering			Rack and pinion (power-assisted)		
	Suspension	Front		MacPherson struts		
		Rear		Multi-link		
	Brakes	Front		Ventilated discs (13-inch)		
		Rear		Leading/trailing drums (9-inch)		
	Tires			165/R13-6PRLT		

([C & D Product Dev. Project], Car Research & Dev. Office, MMC: Ikeda, Uchida, Aiba)

NEW PRODUCTS

New LANCER EVOLUTION VIII

– Japan domestic version –

Since its debut in 1992, the LANCER EVOLUTION series has evolved through participation in the World Rally Championship and other leading motorsport events around the world. The latest version, the LANCER EVOLUTION VIII, was launched in February 2003. This version marks the LANCER EVOLUTION's introduction in North America, where it will be a flagship model for the revitalized Mitsubishi Motors Corporation (MMC).

1. Targets

With the LANCER EVOLUTION VIII, know-how gained in motorsport competitions was fed back into the development process to bring the design even closer to perfection. New technologies and new interior and exterior styling features were adopted in pursuit of a car that looks and feels even faster and more refined.

2. Features

(1) Interior and exterior: a new fusion of style and functionality

The front bumper and hood reflect the new MMC design identity in forms that were airflow-optimized for better aerodynamics and cooling performance. And the rear spoiler, whose shape evokes the perpendicular lines of jet-fighter wings, is made entirely of light, rigid carbon-fiber-reinforced plastic – a world first on a production four-door sedan. These new features combine a sharper, aggressive look with functionality needed for motorsport success.

In the cabin, dark titanium-finish panels and carbon-fiber "EVOLUTION" emblems give enhanced style and presence. At the same time, functionality is enhanced by new features including a small, spherical, leather-covered shift knob whose size, shape, and hardness were optimized for easy operation in high-G conditions and to minimize the risk of hand damage during high-intensity sports driving.

(2) World-class performance for a 2.0-liter sedan

The engine is based on the 2.0-liter turbocharged engine of the LANCER EVOLUTION VII. Increased boost pressure at mid-range engine speeds (3,000 – 5,000 rpm) yields higher maximum torque. Also, a newly developed six-speed manual transmission with 2nd – 4th ratios similar to those of the previously used close-ratio transmission provides a gear range that accommodates a wide range of driving conditions by permitting both superior acceleration and superior high-speed performance. And to accommodate the higher engine torque and improve reliability, the water pump has an increased capacity and the pistons, connecting rods, transmission, propeller shaft, and other parts of the powertrain incorporate strength-increasing measures.

(3) Extended handling limits and higher ride quality

MMC's unique all-wheel-control technologies (these maximize tire performance by actively controlling each wheel's driving and braking forces to match tire loading, which constantly varies with longitudinal and lateral load shifts and changes in road-surface conditions) were further improved for the LANCER EVOLUTION VIII: A newly developed Super Active Yaw Control system transfers twice the previous amount of torque between the left and right wheels and thus generates bigger yaw moments, which translate into extended cornering limits. In addition, increased limited-slip-differential effectiveness yields increased traction during high-G cornering maneuvers, resulting in increased motorsport competitiveness.

Higher body rigidity is yielded by reinforcements in areas including the front and rear suspension mountings and the base of each center pillar and by more extensive spot welds. In the suspension system, higher rigidity is yielded by newly shaped rear-axle-hub mounting bolts. Also, improved damping response yielded by thicker rods in the rear shock absorbers combines with reduced unsprung weight yielded by lighter

aluminum wheels, resulting in extended performance limits and improved ride quality.

(4) Performance-enhancing aerodynamics with optimal front/rear lift balance

Openings in the front bumper were eliminated wherever possible, leaving only those essential for cooling, and the air outlet in the hood was made larger for more efficient airflow. These design revisions together minimize air resistance and front lift. Also, the engine undercover was revised (with an airdam added at the front and a venturi section added in the center) to generate more downforce and an increased flow of cooling air to the powertrain. Further, the rear spoiler is, thanks to the adoption of carbon-fiber-reinforced plastic, stiffer and thinner with a more effective wing section that generates more downforce without increasing drag. The new aerodynamic features all promote handling stability during high-speed driving.

(5) Reduced weight

In the GSR variant, the weight increase resulting from adoption of the six-speed manual transmission is offset by weight reductions in areas including the engine, driveshaft, exhaust manifold, and body; the vehicle is approximately the same weight as the corresponding LANCER EVOLUTION VII variant with the same equipment and fuel load. The RS variant, which has a five-speed manual transmission, is approximately 20 kg lighter than the corresponding LANCER EVOLUTION VII variant with the same equipment and fuel load.

3. Major specifications

Major specifications of LANCER EVOLUTION VIII are shown in the following table.

Specifications \ Model				LANCER EVOLUTION VIII	
				Mitsubishi GH-CT9A	
				Full-time 4WD	
				6 M/T (GSR, RS)	5 M/T (RS)
Seating capacity			(persons)	5	
Dimensions	Overall length		(mm)	4,490	
	Overall width		(mm)	1,770	
	Overall height		(mm)	1,450	
	Wheelbase		(mm)	2,625	
	Tread	Front	(mm)	1,515	1,500
		Rear	(mm)	1,515	1,500
	Ground clearance		(mm)	140	
Engine	Model			4G63 Turbo	
	Displacement		(cc)	1,997	
	Valve mechanism and number of cylinders			DOHC; 16-valve; four cylinders	
	Maximum output		{kW (PS)/min^{-1}Net}	206 (280)/6,500	
	Maximum torque		{Nm (kgf·m)/min^{-1}Net}	392 (40.0)/3,500	
	Fuel supply system			ECI-MULTI (electronically controlled fuel injection)	
Running equipment	Steering			Rack and pinion (power-assisted)	
	Suspension	Front		MacPherson-strut	
		Rear		Multi-link	
	Brakes	Front		Ventilated discs (17-inch)	Ventilated discs (15-inch)
		Rear		Ventilated discs (16-inch)	Ventilated discs (15-inch)
	Tires			235/45ZR17	205/65R15

([C & D Product Dev. Project], Car Research & Dev. Office, MMC : Kato, Fujii, Kometani)

NEW PRODUCTS

eK-SPORT

– Japan domestic version –

On September 2, 2002, Mitsubishi Motors Corporation (MMC) launched the eK-SPORT, a sporty variant of the eK-WAGON minicar that it launched in October 2001.

1. Targets

In developing, the eK-SPORT, MMC worked toward the following main targets:

(1) a new identity appealing specifically to sports-oriented young people (as opposed to an identity derived from that of the eK-WAGON, which is intended to appeal to a wide range of customers irrespective of gender and age);
(2) increased levels of running, turning, and stopping performance for an exhilarating drive befitting the vehicle's 'SPORT' badge; and
(3) superior quality reflected in styling and quietness in a higher class than those of conventional sport-minicar models.

2. Features

Created in line with a 'stylish sport wagon' product concept and aimed mainly at customers in the 20 – 30 age group, the eK-SPORT reflects a new vision for the sport-minicar genre. It's available in two versions: "R" (with an intercooler-turbocharged engine) and "Z" (with a naturally aspirated engine). Major features are as follows:

(1) Distinctive exterior styling

Rather than taking the conventional approach of creating a sporty appearance using a profusion of accessories, MMC pursued simplicity, paying exceptionally close attention to colors and materials and cleverly combining subtle contours to achieve a new look that's simple but distinctive and sporty but refined.

Other exterior features include high-intensity discharge headlamps, which are offered as a factory-fitted option.

(2) Refined interior appointments

While the imaginatively designed storage spaces and other utility-oriented features of the eK-WAGON are retained, a stronger sense of sportiness and refinement is yielded by exclusive features including a black-based color scheme; hybrid instrumentation with an analogue tachometer and a digital speedometer; a leather-wrapped three-spoke steering wheel; and front and rear sports seats that give superior comfort and hold.

(3) Superior performance

In the "R" version, superior low-speed torque and excellent response across the entire rev range are delivered by a 660 cc, three-cylinder, 12-valve, intercooler-turbocharged engine with ECI-Multi fuel injection. The engine is mated to an electronically controlled four-speed automatic transmission, resulting in smooth, natural-feeling acceleration.

The "Z" version has the same 12-valve, ECI-MULTI engine as the eK-WAGON. In two-wheel-drive form, it qualifies for 'green' tax exemptions by complying with Japan's 2010 fuel-consumption standards.

Every vehicle in the eK-SPORT lineup is certified as a LEV.

(4) Sharp handling and dependable braking

The suspension system of the "R" version is based on that of the eK-WAGON but is tuned for nimbler handling and better roadholding and stability befitting the eK-SPORT's more dynamic identity. Exclusive features including reinforced suspension mountings, a performance rod, and a rear stabilizer further enhance handling stability and realize a flat ride.

For superior braking performance, the "R" version is equipped as standard with 14-inch ventilated front disc brakes and an antilock braking system with brake assist and electronic braking-force distribution.

(5) Quietness like that of larger cars

A forged crankshaft, revised engine mountings, and extensively applied sound-insulating and sound-absorbing materials on engine-compartment and floor surfaces effectively suppress the transmission of vibra-

tion and noise, making the eK-SPORT one of the quietest vehicles in the class.

(6) Wide range of colors

The eK-SPORT is available in a range of 10 colours. The main display color is a refined silver metallic that emphasizes the metallic impression created by the eK-SPORT's body contours.

3. Major specifications

The major specifications of the eK-SPORT are shown in the following table.

Specification \ Model				eK-SPORT			
				Z		R	
				2WD	4WD	2WD	4WD
				3 A/T		4 A/T	
Dimensions	Overall length		(mm)	3,395			
	Overall width		(mm)	1,475			
	Overall height		(mm)	1,550		1,570	
	Wheelbase		(mm)	2,340			
	Tread	Front	(mm)	1,295		1,300	1,295
		Rear	(mm)	1,295			
	Cabin length		(mm)	1,830			
	Cabin width		(mm)	1,220			
	Cabin height		(mm)	1,280			
	Vehicle weight		(kg)	800	850	850	900
	Minimum turning radius		(m)	4.4			
Engine	Model			3G83		3G83 (with intercooled turbocharger)	
	Displacement		(cc)	657			
	Valve mechanism and number of cylinders			SOHC; 12-valve; three cylinders			
	Maximum output		(kW (PS)/min^{-1} Net)	37 (50) /6,500		47 (64) /6,000	
	Maximum torque		(Nm (kg·m)/min^{-1} Net)	62 (6.3) /4,000		93 (9.5) /3,500	
	Fuel supply system			ECI-MULTI (electronically controlled fuel injection)			
Running equipment	Steering			Rack and pinion (power-assisted)			
	Suspension	Front		MacPherson struts			
		Rear		Three-link rigid axle with torque arm			
	Brakes	Front		Discs (13-inch)		Ventilated discs (14-inch)	
		Rear		Leading/trailing drums (7-inch)			
	Tires			155/65R13		155/55R14	165/55R14

([A&B Product Dev. Project], Car Research & Dev. Office, MMC: Morii, Nishino, Sasakura, Masuda)

NEW PRODUCTS

New CANTER

A new generation of Mitsubishi Fuso CANTER (payload two-ton class) and CANTER GUTS (payload 1.5-ton class) light-duty trucks went on sale in June 2002 following a full model change in eight years and seven months.

1. Targets

With their high payload potential and superior durability and reliability, CANTER cab-over-engine trucks have earned an excellent international reputation. The latest generation of CANTER trucks – the result of a full model change – will consolidate this reputation. Developed as a new global standard for light-duty trucks, it reflects Mitsubishi's "Global Fit" concept in unprecedented levels of cab roominess, ride comfort, safety, and environmental performance.

2. Features

(1) Cab design with "round cubic" theme

The design keynote is a "round cubic" form that identifies the new-generation CANTER trucks as members of the same family as Mitsubishi Fuso's heavy-duty and medium-duty trucks. Key elements of the family identity are an inverted-trapezoid grille, forward-sloping side windows, and side character lines. Distinctively styled headlamps further complement the new look and, on higher-powered models, employ discharge headlamp for superior night-time visibility.

(2) Class-leading driveability and cab traversability

A dash-mounted shift lever (a world first in a mass-produced cab-over-engine truck) minimizes driver effort by realizing short, easy shift strokes. A fold-down armrest (standard in DX- and higher-grade vehicles) further enhances the driveability by permitting a comfortable driving position and by making the dash-mounted shift lever even easier to use. The new CANTER's day-to-day usability is further boosted by superior cab traversability (the ease with which users can move from one side of the cab to the other), which is realized by a parking-brake lever that remains below the height of the seat squabs when the parking brake is engaged.

(3) Class-leading roominess

More-upright A-pillars and a more spreaded side tumble in the cab design are complemented by more-compact instruments that make the instrument panel 40 mm shorter (from front to rear) than that of the previous-generation CANTER. The result is class-leading roominess and legroom. Interior spaciousness is particularly outstanding in wide-cab models since the cab extends 100 mm further forward than that of corresponding previous-generation models and has a 20 mm-higher roof. In all models, increased tilt and telescope ranges for the steering wheel and an increased slide range for the seat allow greater freedom in adjustment of the driving position. Together with an optimized pedal layout, these improvements help to minimize driver fatigue.

(4) Class-leading ease of getting in and out

The more-upright A-pillars combine with newly shaped steps and fenders to get in and out easier than with the previous-generation CANTER. Cab access is particularly easy with wide-cab models because longer steps allow users to get in and out in a near-upright position.

(5) Class-leading collision safety

FUSO-RISE collision-safety technology is newly employed to ensure that the vehicle effectively absorbs and dissipates impact energy and maintains an adequate survival zone for occupants within the limited space in the cab-over-engine structure. Major features

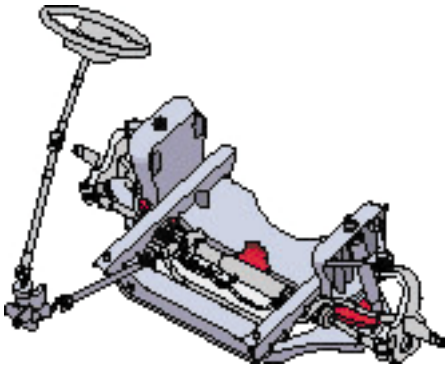

include energy-absorbing material in the front main sills that support the cab, a parallel-cross structure (incorporating impact beams) in the doors, and closed-section front chassis rails. Together with an impact-absorbing instrument-panel frame, these features realize the highest level of collision safety in the class.

(6) Class-leading braking performance

Standard equipment in higher-powered models includes a Power-ABS system (the first in the class), which supplements conventional antilock-braking-system functionality with brake-pedal power assistance and with a function that apportions braking force to individual wheels in accordance with the front and rear axle loads. All-wheels disc brakes (standard on higher-powered CANTER models and on the CANTER GUTS) further enhance braking performance.

(7) Class-leading ride comfort

A further evolution of the CANTER's highly appraised independent front suspension delivers the ideal balance of ride comfort and handling stability. Plus, greatly expanded availability of the independent front suspension means these benefits can be enjoyed in about 70 % of models.

(8) Environmental performance

Newly added enclosure covers on the engine and transmission combine with radial tires and other technologies to ensure that all models comply with Japan's 2000/2001 noise regulations. Certain models comply with Japan's 7LG* and 6LG** certification systems for low-emission vehicles and with an increasingly stringent Tokyo Metropolitan Government environmental ordinance. In addition, extensive use of recycled and recyclable materials gives all models a recyclability rate in excess of 90 %.

*Seven local governments in the Kanto region

**Six local governments in the Kansai region

3. Major specifications

Major specifications are shown in the following table.

Specifications \ Model				FE70EB11	FE82EE32
				Standard cab	Wide cab
				Payload two-ton; low bed	Payload three-ton; low bed
Dimensions	Overall length		(mm)	4,690	6,180
	Overall width		(mm)	1,695	2,120
	Overall height		(mm)	1,970	2,235
	Wheelbase		(mm)	2,500	3,350
	Tread	Front	(mm)	1,390	1,665
		Rear	(mm)	1,235	1,560
	Length of loading bed		(mm)	3,120	4,350
	Bed height		(mm)	820	910
Weights	Maximum payload		(kg)	2,000	3,000
	Gross vehicle weight		(kg)	4,415	5,915
Engine	Model			4M51 (1)	4M51 (2)
	Displacement		(cc)	5,249	
	Maximum output		{kW (PS)/min^{-1} Net}	103 (140)/3,200	114 (155)/3,200
	Maximum torque		{Nm (kgf·m)/min^{-1} Net}	333 (34.0)/1,600	373 (38.0)/1,600
Running equipment	Transmission			5 M/T	6 M/T
	Suspension	Front		Independent	
		Rear		Rigid axle	
	Brakes	Front		Disc	
		Rear		Drum	Disc
	Tires			205/65R16	225/70R16

(Vehicle Dev. & Design Office, Research & Dev. Office, MFTBC: Yoshikawa)

INTERNATIONAL NETWORK

Mitsubishi Motors North America
6400 Kattella Avenue, Cypress
CA 90630–0064, U.S.A.
Phone: 714–372–6000
Telefax: 714–373–1020

Mitsubishi Motors R & D of America, Inc.
3735 Varsity Drive Ann Arbor
MI 48108, U.S.A.
Phone: 734–971–0900
Telefax: 734–971–0901

Mitsubishi Motor Sales of Caribbean, Inc.
Carretera No. 2, Km 20.1 Barrio
Candelaria Toa Baja, PUERTO RICO
Phone: 787–251–8715
Telefax: 787–251–3720

Netherlands Car B.V.
Dr. Hub van Doorneweg 1,
6121 RD Born, THE NETHERLANDS
Phone: 31–46–489–4444
Telefax: 31–46–489–5488

Mitsubishi Motors Europe B.V.
Douglassingel 1
1119 MB Schiphol-Rijk
THE NETHERLANDS
Phone: 31–20–6531862
Telefax: 31–20–6531883

Mitsubishi Motor Sales Europe B.V.
Douglassingel 1
1119 MB Schiphol-Rijk
THE NETHERLANDS
Phone: 31–20–4468111
Telefax: 31–20–4468135

Mitsubishi Motors Sales Nederland B.V.
Diamantlaan 29
2132 WV Hoofddorp, THE NETHERLANDS
Phone: 31–23–5555222
Telefax: 31–23–5540620

Mitsubishi Motor Sales Sweden AB
Box 8144 s-163 08 Spanga, SWEDEN
Phone: 46–8–474–5400
Telefax: 46–8–621–1794

MMC Automotive Espana S.A.
Trvesia de Costa Brava no. 6–5a planta
28034 Madrid, SPAIN
Phone: 34–91–3877400
Telefax: 34–91–3877458

Mitsubishi Motor R & D Europe GmbH
Diamant-strass 1 65468
Trebur 2
GERMANY
Phone: 49–6147–9141–0
Telefax: 49–6147–3312

Mitsubishi Motor Sales Danmark A.S.
Provestensvej 50 DK 3000
Helsingor, DENMARK
Phone: 45–4926–6700
Telefax: 45–4926–6767

Mitsubishi Motors de Portugal, S.A.
Povos 2601 Vila Franca de Xira codex,
PORTUGAL
Phone: 351–63–2006100
Telefax: 351–63–2006232

Mitsubishi Motors Australia, Ltd.
1284 South Road, Clovelly Park
South Australia, 5042, AUSTRALIA
Phone: 8–8275–7111
Telefax: 8–8275–6841

Mitsubishi Motors New Zealand, Ltd.
Todd Park, Heriot Drive
Porirua, NEW ZEALAND
Phone: 4–237–0109
Telefax: 4–237–4495

MMC Sittipol Company, Ltd.
69–69/1–3 MUII Phaholyothin Road,
Tambol Klongneung, Ampur Klongluang,
Phathumthanee, 12120, THAILAND
Phone: 2–908–8000
Telefax: 2–908–8280

Mitsubishi Motors Philippines Corporation
Ortigas Avenue Extention,
Cainta, Rizal, Manila, PHILIPPINES
Phone: 2–658–0109
Telefax: 2–658–0006

P.T. Mitsubishi Krama Yudha Motors and Manufacturing
Petukangan 3, J1 Raya Bekasi
Km–21 Pulo Gadung, Jakarta Timur
Jakarta, INDONESIA
Phone: 021–460–2908
Telefax: 021–460–2915

Mitsubishi Fuso Truck of America, Inc.
100 Center Sq. Road, Bridgeport
New Jersey 08014, U.S.A.
Phone: 856–467–4500
Telefax: 856–467–4695

Mitsubishi Trucks Europe – Sociedade
Add. Apartado 7
Tramagal 2200
Abrantes Codex, PORTUGAL
Phone: 351–41–899800
Telefax: 351–41–899875

MITSUBISHI MOTORS CORPORATION

- **Head Office**
  16–4, Kohnan 2-chome, Minato-ku, Tokyo 108–8410, Japan
  Phone: +81–3–6719–2111
  Telefax: +81–3–6719–0034

- **Design Center**
  Tama Design Center
  1–16–1, Karakida, Tama-shi, Tokyo 206–0035, Japan
  Phone: +81–423–89–7307

- **Engineering Offices**
  Car Research & Development Office
  1, Nakashinkiri, Hashime-cho, Okazaki-shi, Aichi Pref. 444–8501, Japan
  Phone: +81–564–31–3100
  [Tokachi Proving Ground]
  22–1, Osarushi, Otofuke-cho, Kato-gun, Hokkaido 080–0271, Japan
  Phone: +81–155–32–7111

- **Plants**
  Nagoya Plant
  [Nagoya Plant – Oye]
  2, Oye-cho, Minato-ku, Nagoya-shi, Aichi Pref. 455–8501, Japan
  Phone: +81–52–611–9100
  [Nagoya Plant – Okazaki]
  1, Nakashinkiri, Hashime-cho, Okazaki-shi, Aichi Pref. 444–8501, Japan
  Phone: +81–564–31–3100
  Kyoto Plant
  [Kyoto Plant – Kyoto]
  1, Uzumasa Tatsumi-cho, Ukyo-ku, Kyoto-shi 616–8501, Japan
  Phone: +81–75–864–8000
  [Kyoto Plant – Shiga]
  2–1, Kosunacho, Kosei-cho, Koga-gun, Shiga Pref. 520–3212, Japan
  Phone: +81–748–75–3131
  Mizushima Plant
  1–1, Mizushima Kaigandori, Kurashiki-shi, Okayama Pref. 712–8501, Japan
  Phone: +81–86–444–4114

MITSUBISHI FUSO TRUCK & BUS CORPORATION

- **Engineering Office**
  Research & Development Office
  10, Ohkura-cho, Nakahara-ku, Kawasaki-shi 211–8522, Japan
  Phone: +81–44–587–2000
  [Kitsuregawa Research & Development Center]
  4300, Washijuku, Kitsuregawa-machi, Shioya-gun, Tochigi Pref. 329–1411, Japan
  Phone: +81–28–686–4711

- **Plant**
  Kawasaki Plant
  [Kawasaki Plant – Kawasaki]
  10, Ohkura-cho, Nakahara-ku, Kawasaki-shi 211–8522, Japan
  Phone: +81–44–587–2000
  [Nakatsu Plant – Nakatsu]
  4001, Nakatsu Aza Sakuradai, Aikawa-cho, Aikou-gun, Kanagawa Pref. 243–0303, Japan
  Phone: +81–462–86–8111
  [Oye Bus Plant – Oye]
  3998-16, Minami, Motohoshizaki-cho, Minato-ku, Nagoya-shi, Aichi Pref. 455-0025, Japan
  Phone: +81–52–611–9155

Printed in Japan

This review is printed on recycled paper (100% recycles paper, 83% whiteness) with soybean oil ink

Printed in Tokyo, Japan

ISSN 0915-3802